UNIVERSITÉ DE STRASBOURG

ÉCOLE DOCTORALE DE PHYSIQUE ET CHIMIE PHYSIQUE

IPCMS CNRS/UDS

THÈSE présentée par :

Alexandre CHEMINAL

soutenue le : **17 Avril 2015**

pour obtenir le grade de : **Docteur de l'université de Strasbourg**

Discipline/ Spécialité : Physique

Processus de conversion d'énergie ultra-rapide dans des protéines photo-sensibles et nanostructures organiques à visée photovoltaïque

THÈSE dirigée par :

[Pr. HAACKE Stefan] Professeur, CNRS/Université de Strasbourg

RAPPORTEURS :

[Pr. KUKURA Philipp] Associate Professor, University of Oxford

[Pr. MOSER Jacques Edouard] Professeur , Ecole Polytechnique Fédérale de Lausanne

---

AUTRES MEMBRES DU JURY :

[Dr. GINDENSPERGER Etienne] chargé de recherche, CNRS/Université de Strasbourg



Alexandre CHEMINAL, Strasbourg August 30, 2015

Remerciements

Je tiens tout d'abord à remercier Stefan pour m'avoir permis de réaliser cette thèse dans son équipe à l'IPCMS et pour la confiance qu'il m'a accordé tout au long de mon travail de thèse.

Un grand merci à toute l'équipe BioDyn, anciens comme nouveaux. En premier lieu à Jérémie, pour ses questions qui font progresser toujours plus loin dans la réflexion, et pour son dynamisme et sa bonne humeur. Ensuite, aux anciens, Thomas Gelot et Thomas Roland qui ont su nous transmettre leur savoir faire, et ce dernier pour les bons moment passés dans la super coloc à côté de la cathédrale avec ce cher (vieux) Thierry Achard.
Un grand merci à Li pour sa disponibilité et ses attentions, et à Moussa pour nos discussions, physiques et philosophiques, et sa motivation. Et également au passage une très bonne santé à la petite Diarra et à ses futurs frères et soeurs?
Un grand merci également à Sébastien Harlepp pour les séminaires doctorants et pour ses conseils et discussions tout au long de la thèse, et à Julien Nillon pour ses conseils en matière de NOPA et d'optique non linéaire.
Et aussi bonne chance aux derniers arrivés: Anastasia et Damianos.

Merci à Olivier Crégut, pour sa disponibilité et le partage interactif de son (immense) savoir faire en optique et en programmation (et j'en passe); à Gauthier Dekynt pour les développements mécaniques et la réalisation des pièces nécessaire au bon fonctionnement des manips, mais également à Jean Pierre Vola, pour ses conseils et son aide précieuse pour les questions d'électronique.

Un grand merci à Laure Biniek pour son temps passé à prendre et à m'expliquer les clichés de diffraction électronique et de TEM, à Nicolas Leclerc pour son aide avec le TB2 et à Thomas Heiser, Patrick Lévêque, Roni Bechara, Juliane Reuthers et les autres membres du consortium RhinSolar.

Egalement merci au personnel administratif de l'IPCMS: Estelle Brunette, Sophie Siegel et José Radmacher pour leur aide pour les questions administratives.

Merci aussi à ceux que j'ai oublié de citer ici mais qui j'espère se reconnaitront.

Enfin un grand merci à mes parents pour leur soutien tout au long de ma scolarité, et surtout à Adeline, ma chérie ¡3 qui m'a soutenu et supporté tout au long de cette longue étape de 3 ans et quelque.

Résumé en français

1. Introduction

Cette thèse porte sur l'étude de phénomènes de conversion d'énergie photonique. Cette conversion est possible dans les systèmes organiques absorbant l'énergie de photons à travers une excitation électronique. L'énergie est stockée dans le matériau sous forme d'un état excité. Cette énergie est alors transformée, plus ou moins efficacement, à travers des réactions photochimiques, en d'autres formes d'énergie.

Ces cascades réactionnelles, dans des matériaux biologiques ou artificiels, permettent de réaliser différentes fonctions à partir de l'énergie des photons absorbés. L'efficacité du système de conversion d'énergie photonique est définie par la probabilité d'obtenir l'énergie finale sous la forme recherchée. Les systèmes photochimiques les plus efficaces sont donc ceux pour lesquels le chemin réactionnel remplissant la fonction recherchée est dominant.

La spectroscopie ultra-rapide permet de sonder les états électroniques impliqués dans les photoréactions à l'échelle de la femtoseconde. Les techniques associées permettent de suivre les populations de ces états et de comprendre les cinétiques réactionnelles et les transferts d'energie ou de charge entre les différents états du système. Ces états électroniques sont caractérisés par leurs spectres d'absorption ou d'émission. Les mesures de spectroscopie résolue en temps permettent d'obtenir, à l'échelle de la femtoseconde, l'évolution temporelle de ces signatures spectrales.

Cette thèse porte sur l'utilisation des techniques de spectroscopie ultrarapide pour étudier la conversion d'énergie photonique dans des

systèmes organiques. Ces techniques permettent d'observer les états fondamentaux et excités des molécules à l'échelle des photoréactions. Elles sont utilisées ici afin de comprendre les transferts d'énergie et de charge intra- et inter-moléculaires donnant lieu aux processus photochimiques recherchés.

Dans cette optique, deux systèmes différents sont étudiés. L'un est une protéine photosensible réalisant une photo-isomérisation, l'autre est une nanostructure organique servant de couche active pour des cellules photovoltaïques. La protéine photosensible a pour fonction la transformation de l'énergie photonique en mouvement à l'échelle moléculaire, tandis que la couche active photovoltaïque organique sert à transformer l'énergie photonique en énergie électrique.

Pour ces deux systèmes, l'environnement a un impact sur la photochimie et donc l'efficacité du processus recherché. L'étude de ces deux systèmes photosensibles par spectroscopie ultrarapide a pour objectif de mettre en évidence et de caractériser le rôle du milieu environnant sur la photochimie/photophysique de ces systèmes.

2. Etude de l'usage du BODIPY TB2 comme "petite molécule" donneuse d'électrons dans des cellules photovoltaïques

Le BODIPY TB2 est une molécule dérivée du colorant BODIPY (DiPyrromethene de Bore). Elle possède un fort coefficient d'extinction, est soluble dans les solvants chlorés et s'organise sous forme d'agrégats, la rendant intéressante en tant que petite molécule dans la réalisation de cellules solaires en fine couche active déposée par spin-coating.

Cette petite molécule peut être utilisée comme donneur d'électrons dans des cellules solaires photovoltaïques organiques. En cellule solaire, elle est combinée avec l'accepteur standard PCBM (Phényl-C61-Butanoate de Méthyle). Le mélange des deux molécules est déposé sur un substrat couvert d'une couche d'ITO (Oxyde d'Indium et d'éTain) et de PEDOT:PSS (Poly-EthylèneDiOxydeThiophène : Poly-Styrène sulfonate de Sodium). De telles cellules donnent des conversions de puissance solaire en puissance électrique allant jusqu'a 4.7% [**42**].

Le but de cette étude et d'étudier les facteurs limitant l'efficacité de conversion dans la couche active de telles cellules.

L'efficacité des cellules solaires organiques dépend fortement de la morphologie de la couche active ainsi que de sa nanostructuration [**32**]. En effet, ces deux facteurs limitent la diffusion des excitons vers les interfaces donneur-accepteur ou les charges sont séparées. Cette séparation se produit à travers un transfert de charge depuis les molécules donneuses (TB2) vers les molécules acceptrices (PCBM). Après transfert de charge, les deux charges peuvent se séparer en vainquant leur attraction Coulombienne, et ainsi participer au courant. Dans le cas contraire, elles peuvent se recombiner, au détriment du fonctionnement de la cellule. La nanomorphologie influe également sur la délocalisation des charges et leur percolation jusqu'aux électrodes. C'est donc un paramètre important pour le transport des charges photogénérées.

Afin d'étudier l'effet de la morphologie de la couche active sur l'efficacité, différents films ont été produits, en variant la quantité de PCBM dans la couche active ainsi qu'en changeant les conditions de recuit du film, conduisant a une variété de nanomorphologies de la couche active.

Les différents films sont caractérisés par spectroscopie classique et ultrarapide ainsi que par spectro-électro-chimie, afin de déterminer les spectres caractéristiques des différents états électroniques impliqués dans leur photochimie et la dynamique de leurs populations, ainsi que par microscopie électronique en transmission et par diffraction électronique, afin de déterminer la nanomorphologie des films.

La combinaison de ces techniques permet de déterminer précisément la photochimie de ces différentes couches actives et leur lien avec la nanomorphologie, l'objectif étant de mettre à jour les phénomènes limitant la génération efficace de charges libres pouvant être extraites. Les autres facteurs limitant l'efficacité, tels que le transport de charge et la collection de charge aux électrodes, ne sont pas étudiés dans ce travail.

2.1. Morphologie

La morphologie des différents films est caractérisée par diffraction électronique et par microscopie électronique en transmission. Les films purs de TB2 et de PCBM permettent d'avoir une référence pour l'ensemble des mélanges. Leurs structures sont connues dans la littérature.

Les films de TB2 sans recuit ne présentent pas de phase cristalline et sont principalement amorphes. Après recuit, des cristaux sont formés, ce qui est indiqué par la présence d'anneaux de diffraction similaires à ceux présents dans les clichés de diffraction électronique sur cristal unique, ainsi que par un shift vers le rouge du maximum d'absorption. Ils indiquent la présence de phases cristallines dans les films de TB2 recuits, sous forme d'agrégats à caractère dominant J.

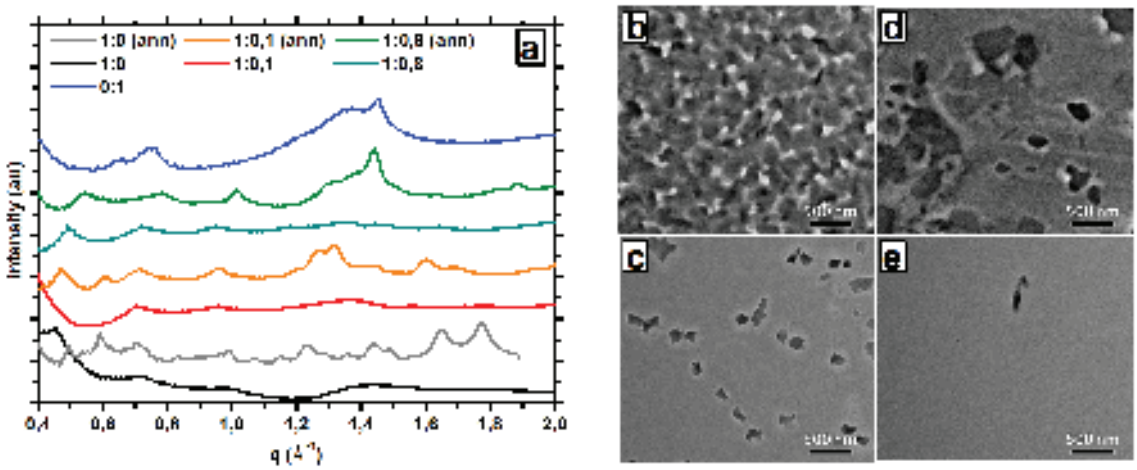

Figure 1.: Distribution radiale moyennée sur les angles de diffraction électronique pour différents mélanges déposés sur des substrats de silice fondue. Images de microscopie électronique en transmission des films de mélange 1:0.1 recuit et brut (b et c) et de films de mélange 1:0.8 recuit et brut (d et e).

Les films de mélange TB2/PCBM étudiés montrent que les films non recuits sont amorphes (absence de pics de diffraction életronique étroits, figure 1a). Le cas des films recuits est plus complexe et indique que l'augmentation de la fraction de PCBM dans les films réduit l'agrégation du TB2. Cet effet est aussi observé dans les spectres d'absorption, dans

lesquels le pic s'absorption caractéristique des agrégats de TB2 est réduit quand la fraction de PCBM est augmentée.

Ainsi, la morphologie des couches actives étudiées dépend des conditions de recuit, permettant l'aggrégation du TB2 sous forme d'agrégats J. L'agrégation du TB2 est réduite par l'ajout d'une proportion plus importante de PCBM dans le film.

2.2. Influence de la morphologie sur la génération de charges

L'étude des couches actives de mélange TB2/PCBM pour un rapport massique de 1 pour 0.5 avec et sans recuit permet d'étudier l'influence de la morphologie. En effet, pour ces deux couches actives, la première présente des agrégats de TB2 alors que la seconde est un mélange homogène et amorphe.

Film brut

Le film brut de mélange TB2/PCBM au rapport massique de 1 pour 0.5 est préparé par spin-coating sur un substrat de verre recouvert d'ITO. La photochimie est étudiée pour une excitation sélective du TB2 à 800nm. Dans cette région spectrale, l'absorption du PCBM est négligeable au vu du très faible coefficient d'extinction molaire du PCBM devant le TB2.

Des mesures de quenching de fluorescence en fonction du contenu en PCBM indiquent un fort quenching de la fluorescence du TB2 avec l'ajout de PCBM, à contenu en TB2 constant. Cela indique la présence de nouveaux chemins réactionnels depuis l'état excité du TB2. Le phénomène attendu est un transfert de charge ou d'électron vers le PCBM.

Les mesures d'absorption transitoire présentent de nouvelles bandes d'absorption photoinduites en comparaison avec le film de TB2 brut.

Ces nouvelles bandes d'absorption sont localisées autour de 600nm et 1050nm, et sont associées avec la signature négative du dépeuplement de l'état fondamental du PCBM (observé à 340nm). Le dépeuplement de l'état fondamental du TB2 (autour de 450nm et 775nm) a également une durée de vie plus longue que dans le cas du TB2 seul, passant de quelques picosecondes à plus d'une centaine de picosecondes. Cela indique donc une excitation du PCBM indirecte par le biais de l'état excité du TB2 et la formation de nouvelles espèces à longue durée de vie impliquant le TB2 et le PCBM. Le temps de formation des ces nouvelles espèces est de l'ordre de la centaine de femtosecondes (deux constantes de temps de formation à 80 et 700fs).

Une analyse globale des données permet d'extraire les spectres associés aux déclins des données d'absorption transitoire. Trois constantes de temps sont supérieures à la picoseconde et les spectres associées comportent les contributions positives caractéristiques des espèces photoproduites. Celui associé à la constante de temps de 8ns est très similaire à la différence d'absorption cation moins état fondamental du TB2. Ce dernier à été mesuré par spectroéléctrochimie en film. Cette constante de temps est donc associée aux charges séparées dans le film. La signature de l'anion du PCBM n'est pas observée, ce qui peut être expliqué par le faible coefficient d'extinction de cette espèce, mais aussi par l'ambipolarité du TB2.
Les spectres associés deux autres constantes de temps de 8.5ps et 165ps présentent à la fois les absorptions photoinduites à 600 et 1050nm, et les signatures caractéristiques du dépeuplement de l'état fondamental du TB2 et du PCBM. Ces constantes de temps sont par conséquent attribuées à des états à transfert de charge. La forme différente des absorptions induites et la présence du dépeuplement de l'état fondamental du PCBM suggèrent qu'il s'agit d'états à transferts de charges liés à l'interface. La constante de temps la plus courte correspond à une montée du signal au voisinage du maximum de la signature du cation libre du TB2 à 1000nm. Elle est donc attribuée à une combinaison de séparation de charges depuis les états de transfert de charge à l'interface, et d'une contribution de recombinaison de charge à l'interface en 8.5ps.

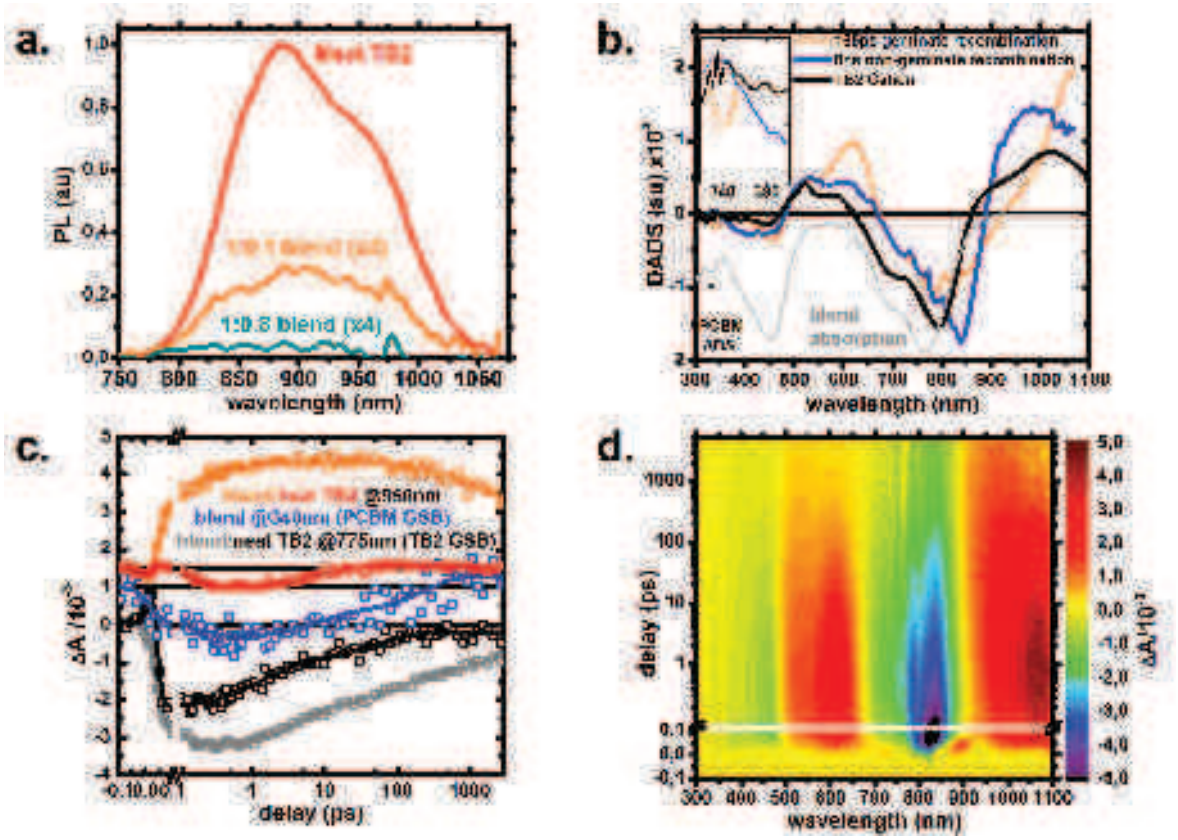

Figure 2.: Résultats de l'étude du mélange TB2/PCBM à rapport massique de 1 pour 0.5. Panneau a: quenching de la fluorescence du TB2 en fonction de la quantité de PCBM à contenu en TB2 fixe. Panneau b: Spectres associés aux déclins attribués aux principales espèces chargées dans le film, et spectre de différence du cation du TB2 obtenu par spectroélectrochimie. La fenêtre montre le grossissement de la région du dépeuplement de l'état fondamental du PCBM. Panneau c: cinétiques d'absorption transitoire caractéristiques du dépeuplement de l'état fondamental du TB2 pour le film pur et le mélange, comparaison des cinétiques dans l'infrarouge et cinétique du dépeuplement de l'état fondamental du PCBM dans le mélange. Panneau d: carte 2D des données d'absorption transitoire pour le mélange excité à 800nm.

La constante de temps plus longue, est attribuée à la recombinaison géminée des états à transfert de charge interfaciaux en 165ps.

Ni les données de spectroscopie transitoire, ni les calculs de rayon de Förster à partir des spectres d'émission du TB2 et d'absorption du PCBM ne permettent de distinguer le processus de formation des espèces chargées. Il s'agit donc globalement d'un transfert de charge, soit directement depuis le TB2 vers le PCBM (transfert d'électron) soit d'un transfert d'énergie depuis l'état excité du TB2 vers l'état excité du PCBM suivi d'un transfert de trou depuis le PCBM vers le TB2.

Les données de spectroscopie résolue en temps sont donc en bon accord avec les mesures de fluorescence statique, et indiquent un rapide quenching de l'état excité du TB2 initialement excité à une échelle inférieure à la picoseconde par la formation d'espèces chargées. La formation des espèces chargées par transfert de charge à lieu avec deux constantes de temps de 80 et 700fs. Les espèces chargées sont produites avec un rendement proche de 100%, et 75% des charges séparées sont produites à cette échelle de temps. Parmi les espèces chargées produites, environ deux tiers le sont sous la forme d'états à transfert de charge liés à l'interface TB2/PCBM. Ces dernières se recombinent pour moitié en 165ps, le reste se recombine ou se sépare sous forme de charges libres en 8.5ps. Les charges séparées ont une durée de vie de l'ordre de 8ns qui est limitée par la recombinaison (recombinaison non géminée) en l'absence d'électrodes pour collecter ces dernières.

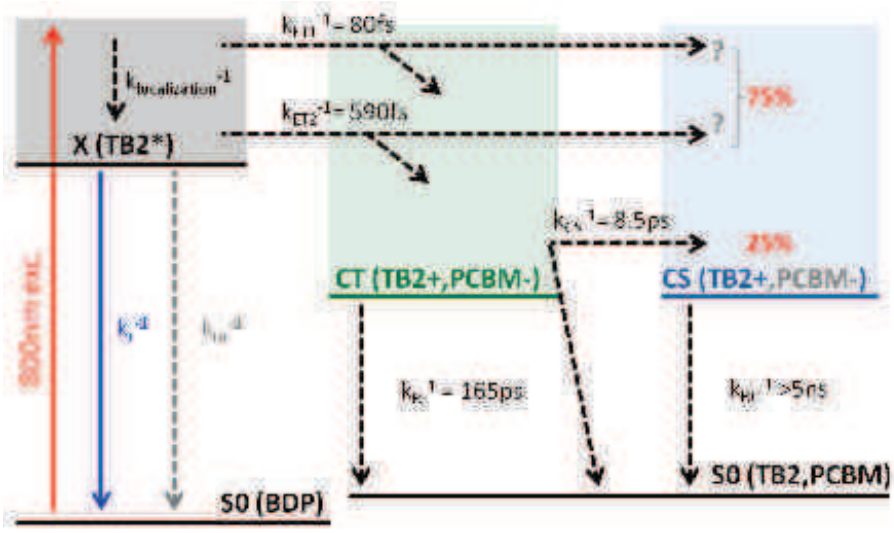

Figure 3.: Schéma réactionnel du film brut de mélange TB2/PCBM au rapport massique de 1 pour 0.5. CT: état à transfert de charge à l'interface donneur-accepteur; CS: charges séparées; X: excitons dans le TB2.

Film recuit

Le film recuit de mélange TB2/PCBM au rapport massique de 1:0.5 est produit de la même façon que le film brut, mais subit un recuit de 10min à 110^{o}C. De la même façon que pour le film brut, une excitation sélective du TB2 est possible à 800nm.

Les mesures de quenching de fluorescence en fonction du contenu en PCBM montrent un quenching plus faible que dans le cas des films bruts, avec l'augmentation du contenu en PCBM. De nouveaux chemins réactionnels dépeuplent l'état excité du TB2 mais moins efficacement que dans le cas des flms non recuits.

Les mesures d'absorption transitoire présentent une évolution spectro-temporelle différente du film non recuit. En particulier, les importantes absorptions photoinduites à 600 et 1050nm sont absentes. De plus, une contribution négative significative est présente aux longueurs d'onde de fluorescence du TB2 dans les premières picosecondes, indiquant la présence d'états excités du TB2 à longue durée de vie. Ces signaux d'émission stimulée évoluent avec une absorption photoinduite large au-

tour de 600nm, attribuée à l'absorption des états excités.
Des mesures de fluorescence résolues en temps par échantillonnage optique non-linéaire en somme de fréquence (fluorescence up-conversion) permettent d'étudier spécifiquement l'état excité du TB2 par sa cinétique de fluorescence. La décroissance du signal de fluorescence se produit avec trois temps caractéristiques, indiquant trois classes d'états excités du TB2 seul recuit 10min à 110^oC. Ces déclins exponentiels sont de 500fs (44% du signal en amplitude), 2.6ps (43%) et 22.5ps (15%). Les cinétiques de fluorescence du mélange massique 1 pour 0.5 présentent les mêmes temps de vie avec des amplitudes similaires, cependant l'amplitude du signal est plus faible (39% de l'amplitude du signal de fluorescence du TB2 seul recuit). Cela indique donc qu'environ 60% de la population d'états excités du TB2 ont été dépeuplés à une échelle de temps inférieure à la résolution temporelle du montage expérimental (100-200fs). En outre la population restante évolue de la même façon que dans le film de TB2 pur. Le quenching des états excités du TB2 est donc seulement partiel.

L'analyse globale fournit les spectres associés aux déclins exponentiels du signal d'absorption transitoire. Un de ces spectres, associé à une constante de temps de 305ps, est très similaire au spectre des espèces chargées dans les films non recuits, mais son amplitude est faible, et ne représente que 10% de l'amplitude du signal des états à transfert de charge dans les films non recuits. Cette contribution n'est pas suffisante pour expliquer le quenching de la population excitée du TB2.
Le spectre associé au déclin de plus de 5ns, et représentant les espèces au temps de vie les plus longs, est très similaire à la dérivée du spectre d'absorption de la couche active. Ce type de signal spectroscopique est caractéristique d'un effet Stark quadratique, un signal d'électroabsorption dû à la présence de dipoles électriques dans le film et qui est associé à la séparation à grande distance des charges [**33,58**], indiquant la présence de porteurs de charge délocalisés, les polarons. Les cinétiques aux extrema de ce signal indiquent que ces derniers sont formés dans les premières centaines de femtosecondes après excitation, ce qui est en bon accord avec les mesures de fluorescence résolue en temps. Un second

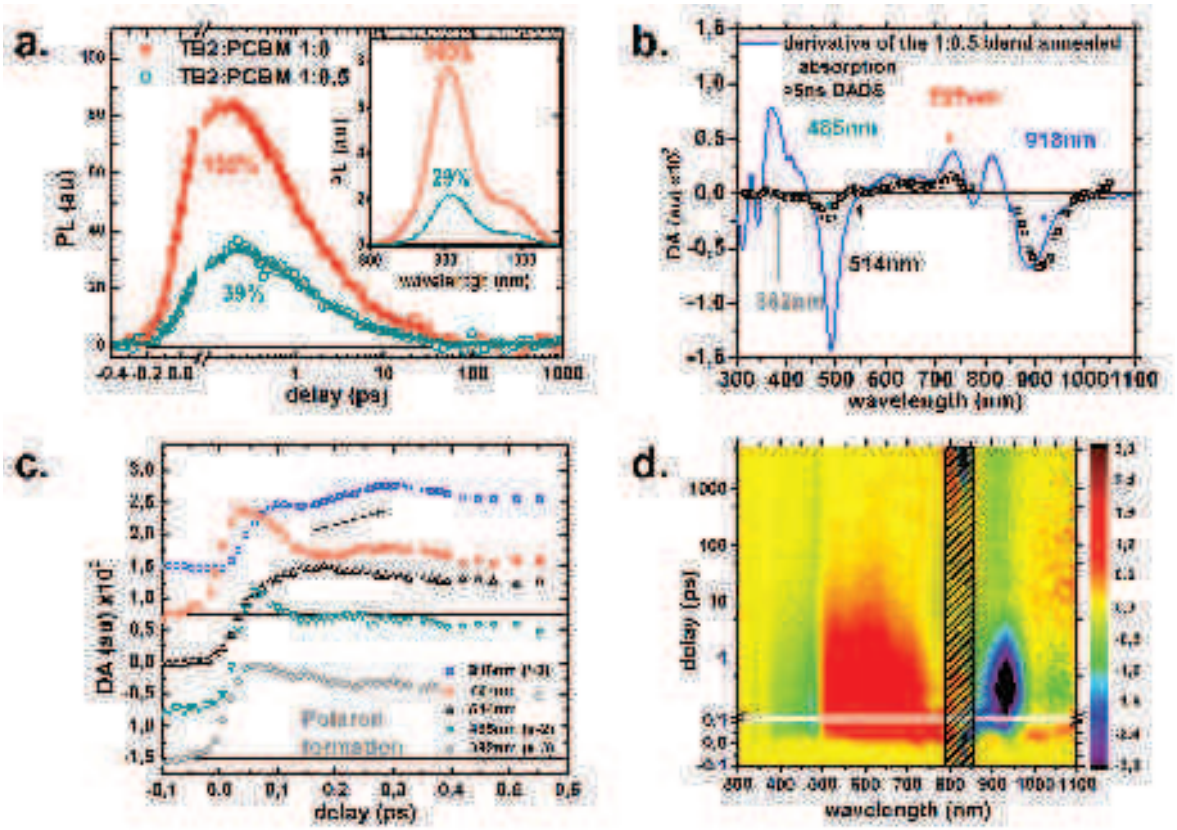

Figure 4.: Résultats obtenus sur les films recuits de mélange TB2:PCBM au rapport massique de 1:0.5. Panneau a: fluorescence résolue en temps du TB2 dans un film recuit de TB2 pur et en mélange. La fenêtre montre le quenching de la fluorescence du TB2 par l'ajout de PCBM. Panneau b: spectre associé au déclin des espèces à longue durée de vie dans les données d'absorption transitoire, comparé à la dérivée première du spectre d'absorption du mélange. Panneau c: cinétiques d'absorption transitoire aux longueurs d'onde caractéristiques indiquées dans le panneau b. Panneau d: carte 2D des données d'absorption transitoire du mélange recuit excité à 800nm.

temps de formation est également observé à l'échelle de 20ps, qui correspond à la durée de vie d'une des classes de population excitonique. Des signatures similaires sont présentes dans les films de TB2 seul recuit, indiquant que les polarons peuvent se former en l'absence de PCBM. Cependant, la quantification du nombre de polarons formés est impossible en l'absence d'observation directe à travers une bande d'absorption caractéristique.

Ainsi, dans le cas des films recuits, la formation globale d'espèces chargées est moins efficace que dans les films bruts. Un tiers des excitons se recombinent et ne participent pas à la formation de charges. Cependant, les porteurs de charges créés dans le films sont plus délocalisés et ont une durée de vie plus longue que dans le cas des films bruts. La principale différence entre les films recuits et non recuits est la présence d'agrégats de TB2, qui favorisent la formation de porteurs délocalisés au détriment d'une formation efficace de porteurs de charges. Cette observation suggère que la taille des agrégats ne permet pas de séparer efficacement les charges aux interfaces.

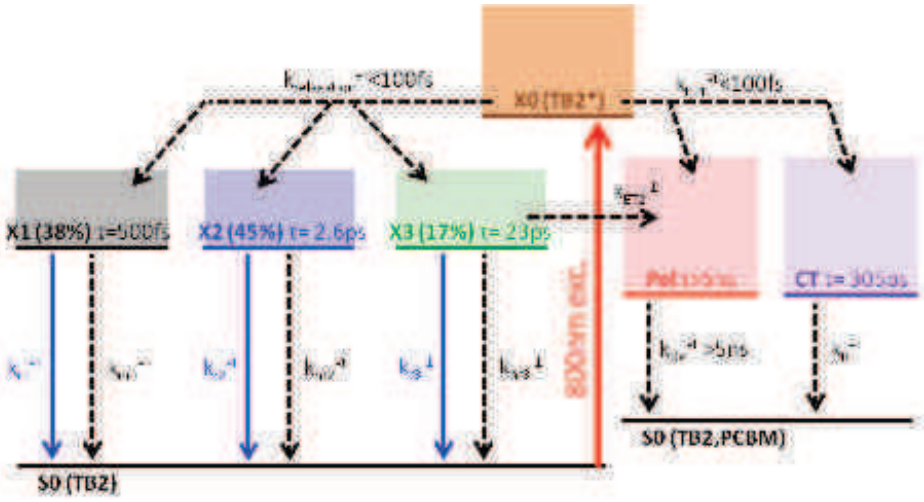

Figure 5.: Schéma réactionnel du mélange recuit de TB2/PCBM au rapport massique de 1:0.5. X: exciton dans le TB2; Pol: polarons; CT: états à transfert de charge et charges séparées localisées.

3. *Anabaena* Sensory Rhodopsin: une protéine photoisomérisante naturelle bistable

La protéine *Anabaena* sensory Rhodopsin (ASR) est une protéine de rétinal. C'est une protéine transmembranaire, composée d'une structure d'acides aminés formant 7 hélices, qui ancrent la protéine dans la membrane, et à laquelle est attachée une molécule de rétinal par le biais d'une base de Schiff. Cette protéine sert de photorécepteur à la cyanobactérie *Anabaena* [**70**].

La particularité de cette protéine parmi les protéines de rétinal [**69**] est qu'elle possède le rétinal sous deux formes de façon stable à température ambiante : sous forme de l'isomère *13-cis* du rétinal, ou sous forme *all-trans*.
Ces deux formes de rétinal se convertissent mutuellement en l'autre sous l'action des photons incidents. Ainsi, selon la composition spectrale du rayonnement incident, un échantillon d'ASR en solution va former un équilibre statistique entre les deux formes. En l'absence de rayonnement incident, la composition est dominée par l'isomère *all-trans* (environ 100%), à travers une relaxation thermique possédant une demie-vie d'environ 3h. Sous illumination avec une LED orange (590nm), un équilibre favorable au *13-cis* se forme (63% *13-cis*). L'accumulation de l'une ou l'autre forme de rétinal dans l'ASR est donc possible en fixant les conditions d'illumination de l'échantillon.

La bistabilité de l'ASR fait de cette protéine un système intéressant pour l'étude de l'isomérisation. En effet, l'isomérisation permet de transformer l'énergie lumineuse en mouvement à l'échelle moléculaire. Le développement et la synthèse de photoswitches moléculaires requiert une compréhension approfondie de ce phénomène et des paramètres contrôlant son efficacité [**97**]. De tels photoswitches sont des composant essentiels pour la réalisation de nano-robots et nano-actuateurs pour des application physiques ou biologiques. Cependant, pour réaliser de tels systèmes, il est nécessaire d'avoir des photoswitches efficaces. L'ASR permet d'étudier l'isomérisation de deux formes du rétinal dans le même

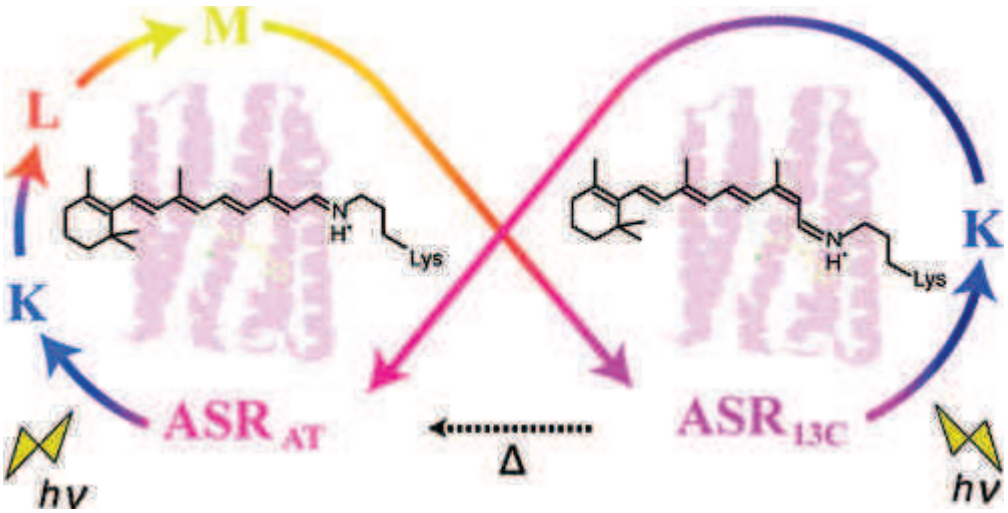

Figure 6.: Schéma du photocycle de l'ASR.

environnement. L'interaction des deux isomères avec la protéine conduit à deux dynamiques d'isomérisation différentes offrant des rendements différents, comme l'ont montré le groupe de S. Ruhmann par des mesures d'absorption transitoire et le groupe de H.Kandori par des mesures du rendement quantique d'isomérisation.

Le but de cette étude est d'étudier en détail la dynamique d'isomérisation et le rendement quantique des deux isomères du rétinal dans l'ASR, afin de comprendre les facteurs clés régissant le rendement d'isomérisation.

Pour ce faire, les échantillons d'ASR sont illuminés à l'aide d'une LED orange (orange-adapted) ou laissés dans le noir (dark-adapted) afin d'accumuler l'un ou l'autre des isomères. Une caractérisation par HPLC permet de déterminer le contenu en isomères des échantillons, ce qui permet de séparer les contributions de chaque isomère dans la photochimie de l'ASR.

3.1. Dynamique des états excités

Les échantillons d'ASR orange et dark-adapted sont mesurés par spectroscopie résolue en temps avec une excitation à 560nm permettant une

excitation depuis l'état fondamental vers le premier état excité avec un faible excès d'énergie. De telles expériences ont déjà été réalisées et permettent de conforter les présentes observations [**112**].

La caractérisation du contenu en isomères permet de séparer les contributions de chaque isomère dans les mesures de spectroscopie résolue en temps. Ces mesures mettent en évidence une durée de vie de l'état excité de l'isomère *13-cis* plus rapide que pour l'isomère *all-trans*.

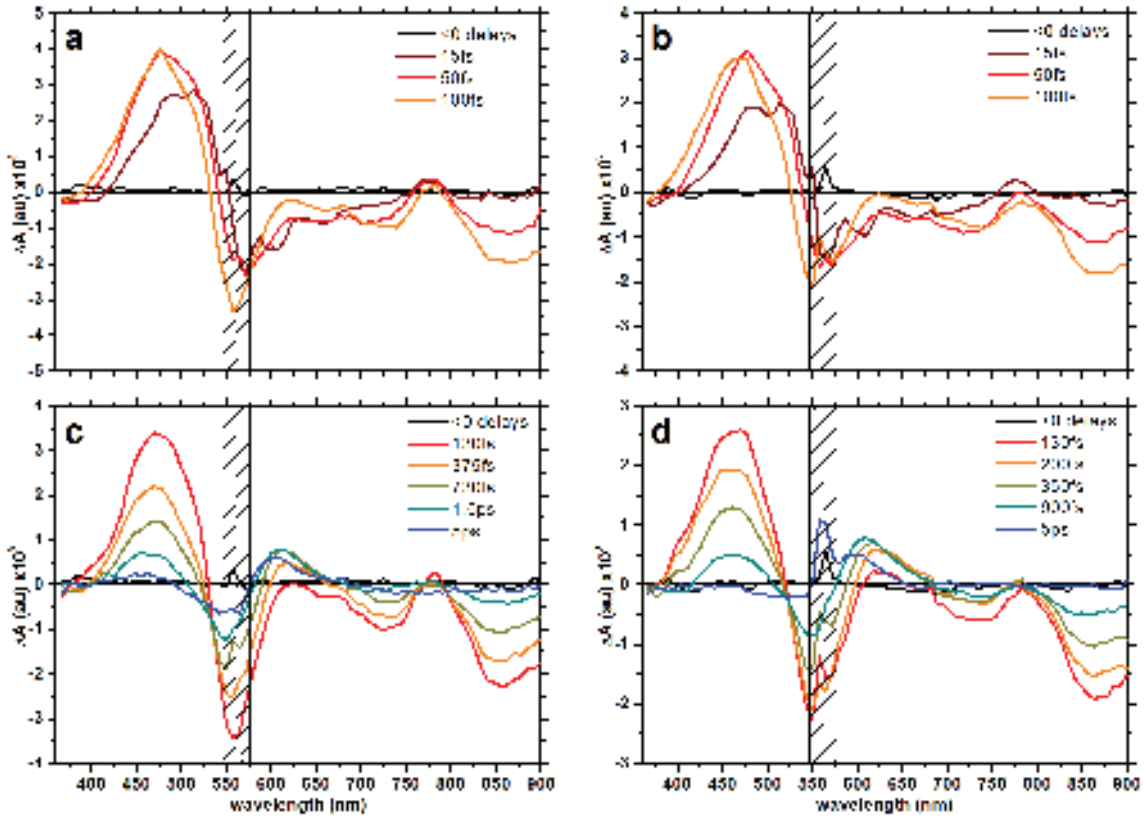

Figure 7.: Evolution spectrale aux temps courts des signaux d'absorption transitoire de l'ASR DA et OA (a et b, respectivement). Evolution pour les temps plus longs pour l'asr DA et OA (C et d, repsctivement). La région spectrale du laser de pompe est masquée en raison du faible rapport signal à bruit. Les délais sont indiqués sur les graphes.

La dynamique des deux isomères de rétinal dans l'ASR est similaire dans l'ensemble, et se caractérise par la formation d'un état excité ab-

sorbant dans la gamme de 400-500nm, et responsable du signal positif dans les données d'absorption résolue en temps dans les premières picosecondes après excitation avec un pulse de longueur d'onde 560nm. Ces résultats sont présentées en figure 7. Cette ESA (AbSorption d'état Excité) est accompagnée du signal de SE (Emission Stimulée) dans la zone de 600-900nm, qui correspond à la fluorescence de l'état excité. L'ESA et la SE possèdent une dynamique spectrale caractérisée par un décalage vers le bleu du maximum de la bande d'ESA et un décalage vers le rouge de la bande de SE, indiquant une relaxation vibrationnelle dans l'état excité dans les 100 premières femtosecondes après excitation. Ensuite, la population de l'état excité diminue et le signal est caractérisé principalement par le GSB (déplétion de l'état fondamental), négatif et centré sur 560nm, indiquant que toute la population excitée ne retourne pas à l'état fondamental, et par une bande d'absorption photoinduite centrée sur 615nm et indiquant la présence d'un photoproduit. Cette bande d'absorption, assimilée à l'espèce J de la photochimie de la bactériorhodopsine effectue un décalage vers le bleu en quelques picosecondes, ce qui indique la relaxation vibrationnelle du photoproduit pour former l'état K, forme relaxée du rétinal isomérisé dans la protéine non relaxée.

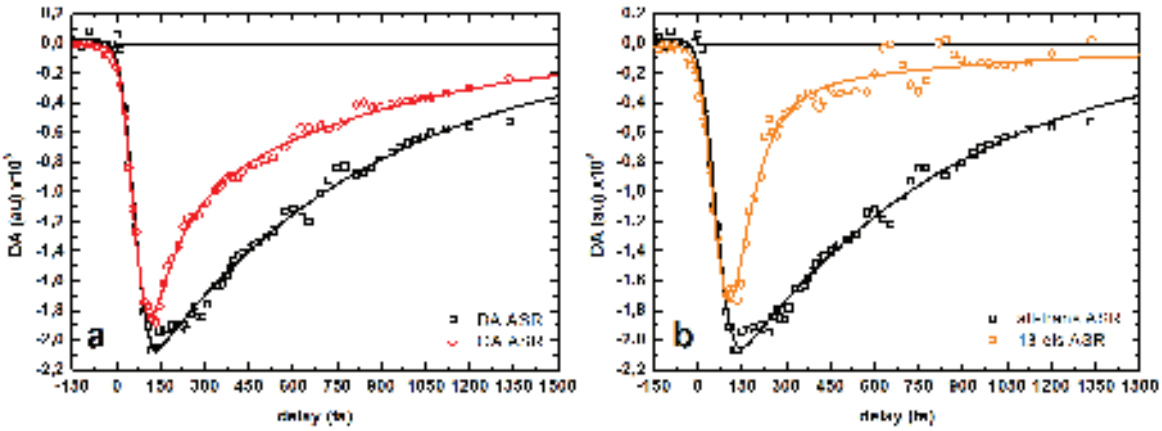

Figure 8.: Traces cinétiques de la SE a 875nm pour l'ASR orange et dark adapted (OA et DA, a) et pour les isomères purs (b). Les lignes sont des fits bi-exponentiels.

Ces mesures indiquent également une différence importante entre les cinétiques des deux isomères. En effet, les cinétiques de SE mesurées à 875nm, où ce dernier signal est exempt de contributions d'autres états, et présentées en figure 8, indiquent un déclin bi-exponentiel des traces pour l'ASR OA et DA. Ces mêmes constantes de temps se retrouvent dans les cinétiques des isomères purs, et indiquent une durée de vie de l'état excité de 110fs pour l'isomère *13-cis* et 770fs pour l'isomère *all-trans*. Cela confirme les mesures similaires effectuées par S. Ruhman. Une tendance similaire se retrouve pour la formation de l'état J à partir de l'état excité pour les deux isomères, indiquant une cinétique plus rapide pour l'isomère *13-cis*.

La cinétique plus rapide de l'isomère *13-cis* est en accord avec des calculs de chimie quantique par le groupe de M.Olivucci indiquant l'absence de barrière à l'état excité sur le chemin réactionnel de cet isomère. D'autre part, l'isomère *all-trans* présente une telle barrière, en bon accord avec la cinétique plus lente de ce dernier.

3.2. Cohérence de l'état excité de l'ASR 13C

La courte durée de vie de l'état excité de l'isomère *13-cis* est du même ordre de grandeur que la relaxation vibrationnelle de cet état depuis la zone de Franck-Condon (figure 9,a). Cette évolution suggère une évolution de la population excitée sous forme d'un paquet d'onde, préservant la cohérence des états ainsi générés. Cette observation est soutenue par l'observation d'oscillations d'une période de 500fs dans les résidus des fits multi-exponentiels des données (figure 9,b), présentant une amplitude significativement supérieure au niveau de bruit [**110**]. Ces oscillations sont similaires à celles observées dans la Rhodopsine. Ces oscillations présentent une phase différente selon la région spectrale. Elles indiquent la présence d'une cohérence vibrationnelle pour des temps supérieurs à la durée de vie de l'état excité, mettant en avant la préservation de la cohérence dans l'état fondamental.

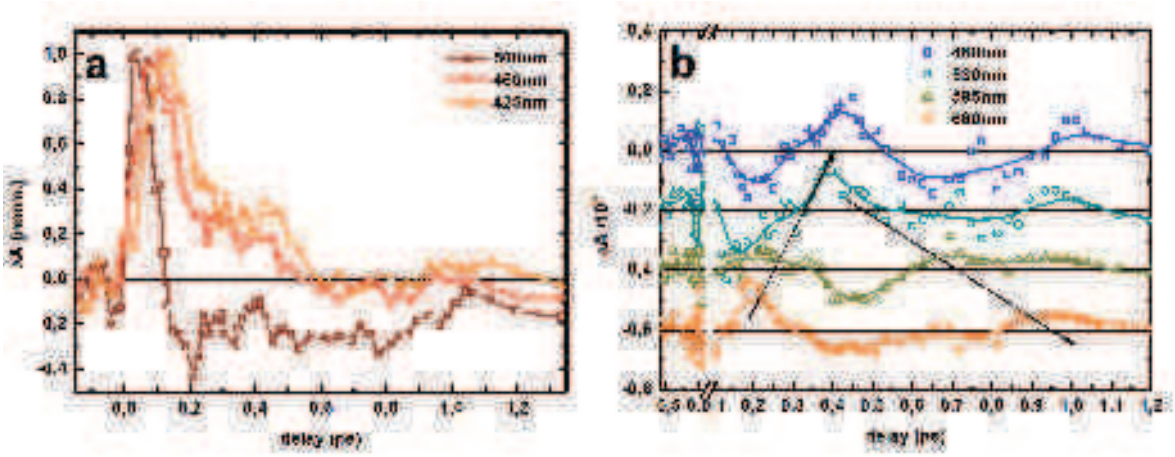

Figure 9.: Traces cinétiques de l'état excité de l'ASR *13-cis* à différentes longueurs d'onde et normalisées à leur maximum, mettant en avant le shift vers le bleu de ce signal (a). (b) résidus des régressions non linéaires des cinétiques de l'ASR OA par un modèle de déclin multi-exponentiel présentant des oscillations au dessus du niveau de bruit. Le décalage de phase entre les oscillations est indiqué par des flèches.

3.3. Efficacité quantique d'isomérisation

Aux temps longs, supérieurs à 15ps après excitation, le signal est stationnaire. L'état excité est dépeuplé et le signal n'est composé que des contributions du GSB, indiquant un non retour à l'état fondamental, et la signature positive du photoproduit relaxé K. Connaissant la densité d'excitation, la concentration de la solution, le chemin optique et le spectre de ces deux états, le rendement quantique d'isomérisation peut être calculé. Le spectre de l'état K est obtenu par extrapolation des spectres des états K des deux isomères obtenus par Kandori à basse température (130K). Ces spectres sont fittés puis décalés vers le rouge et élargis pour tenir compte de la relaxation de la protéine à température ambiante ainsi que de l'élargissement inhomogène (figure 10).

Les régressions linéaires obtenues (figure 10, b) indiquent un rendement quantique d'isomérisation de pour l'isomère *13-cis* et pour l'isomère *all-trans*. Ces valeurs sont significativement plus faibles que celles obtenues par d'autres méthodes par Kandori *et al.*[**120**]. Au vu de l'incertitude

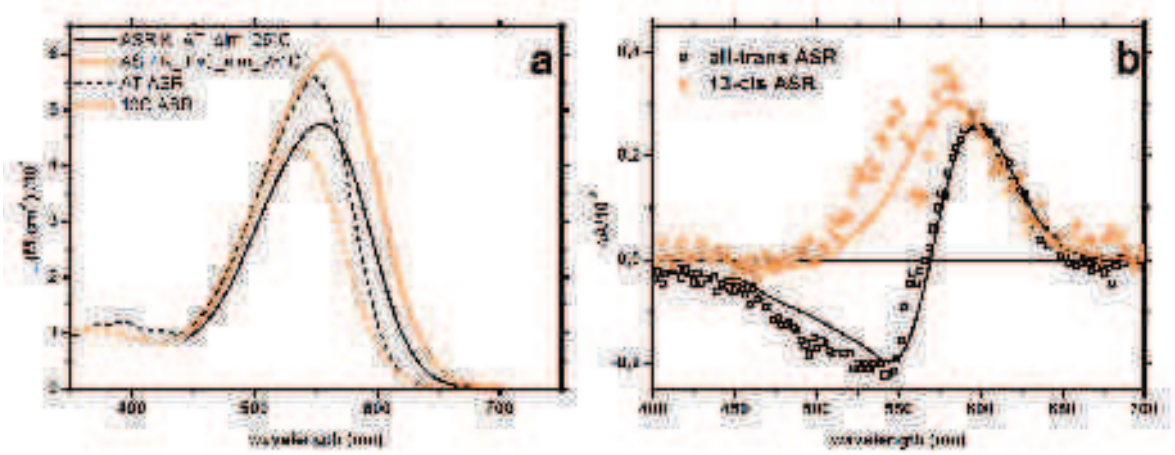

Figure 10.: Coefficients d'extinction molaire de l'état fondamental des deux isomères de rétinal dans l'ASR ainsi que ceux de l'état K calculés pour uen température ambiante (a). (b), régression linéaire du signal stationnaire aux temps longs permettant de calculer le rendement quantique d'isomérisation.

relative due à la détermination de la densité d'excitation, il convient de comparer également l'efficacité quantique d'isomérisation relative des deux isomères, qui permet de s'affranchir du calcul de la densité d'excitation. La valeur ainsi trouvé pour le rendement quantique d'isomérisation relatif est de $\pm$ contre $\pm$ pour les mesures du groupe de Kandori, indiquant en effet un contraste plus important entre les efficacités d'isomérisation des deux isomères.

La détermination du rendement quantique d'isomérisation par cette méthode permet d'estimer le rendement juste après l'isomérisation. Les résultats obtenus par cette méthode sont différents de ceux obtenus par des méthodes statiques, qui utilisent l'interconversion des deux isomères dans une solution continuement éclairée. La méthode présentée ici est plus précise car elle empêche la ré-excitation des protéines, et assure une excitation de la protéine et de son chromophore depuis l'état fondamental relaxé.

La combinaison des mesures de durée de vie d'état excité et de rendement quantique d'isomérisation permet de mettre à défaut les prédictions de type Laudau-Zener utilisées pour décrire l'isomérisation de la Rhodop-

sine et de l'Isorhodopsine, et affirmant que l'isomérisation était d'autant plus efficace que la durée de vie de l'état excité est courte. Les résultats présentés ici montrent que non seulement l'isomérisation du chromophore *all-trans* est plus efficace malgré une durée de vie de l'état excité plus courte, mais aussi, en combinaison avec les simulations de chimie quantique, que la durée de vie de l'état excité était imposée par la topologie de l'état excité avant l'intersection conique entre l'état excité et l'état fondamental, et par conséquent n'est pas pertinente pour l'estimation du rendement quantique d'isomérisation.

4. Conclusion

Les résultats obtenus sur les deux systèmes photochimiques organiques mettent en évidence le rôle critique qu'exerce l'environnement de ces systèmes sur les réactions.
L'utilisation combinée de techniques de spectroscopie statique et résolue en temps permet de comprendre précisément la photochimie de ces systèmes. En combinaison avec une approche systématique permettant d'isoler les différents facteurs environnementaux, l'effet de ces derniers peut être étudié.

Dans le cas de la protéine ASR, les résultats présentés ici indiquent que la combinaison de la forme du rétinal et de son interaction avec les acides aminés environnants de la protéine conduisent à des réactions très différentes au sein d'une même protéine. En particulier, la durée de vie des états excités de chaque isomère ainsi que le rendement quantique d'isomérisation, déterminés ici simultanément dans les mêmes conditions, sont significativement différents. En outre, ces résultats supportent l'idée que la dynamique de l'état excité et le rendement d'isomérisation sont deux quantités non correlées. De plus, la dynamique de l'isomère *13-cis* du rétinal dans l'ASR diffère significativement de celle de l'isomère *all-trans* non seulement par sa vitesse supérieure, mais aussi par son caractère cohérent depuis l'excitation jusqu'a la formation du photoproduit.

Dans les couches actives pour le photovoltaïque organique, composées de mélange de BODIPY TB2 avec du PCBM, les études photophysiques permettent d'obtenir des informations précieuses sur le rôle de la morphologie de la couche active sur les processus de génération de charge.
En particulier, l'agrégation du TB2 sous la forme d'agrégats à caractère principal J dans les films change la nature des porteurs de charges. Les films ne présentant pas d'agrégation conduisent à la formation de charges libres localisées, tandis que les films présentant des agrégats de TB2 forment des charges libres délocalisées sous la forme de polarons, ayant une durée de vie plus longue. Toutefois, la taille des agrégats de TB2 dans les couches actives étudiées, identiques à celles utilisées dans les meilleures cellules solaires produites à base de ce matériau, limite les processus de génération de charge.
Le contrôle de la morphologie et en particulier le contrôle de la taille des agrégats de TB2 dans la couche active est donc nécessaire pour améliorer les processus de génération de charges libres.

Contents

Part I.

Introduction

1. Photonic energy conversion

Photons are the most commonly found form of energy in the universe. The photons Earth recieves from the Sun is the primary form of energy supplying life on our planet. It is the particule associated with the exchange of electromagnetic energy between atoms and molecules surrounding us. Once it interacts with matter, it can be absorbed and transformed into electrostatic energy (electronically excited states, ...) and then into molecular movement (conformationnal change, phonons -heat-) or back into photons (luminescence), and usually in a combination of all, depending on the material it interacts with.

Advanced materials design at the molecular scale in natural and synthetic structures allows to specifically enhance specific transformation pathways. For instance Rhodopsin, a natural protein, converts more than 67% of absorbed photon energy into conformationnal change of the molecule (isomerization of the retinal chromophore) and is the first step of a cascade chemical reaction, optimized by nature and leading to vertebrate vision. Efficient synthetic fluorophores such as Rhodamines can convert more than 90% of absorbed photon energy into luminescence, and are designed and used as amplification media in dye lasers or as photon counters.

Since chemistry allows to synthetize molecules with various properties, understanding the properties giving rise to a specific enhancement of a conversion path would allow to craft efficient molecules for a given conversion application.

Stimulated absorption of a photon occurs in a sub-femtosecond timescale, and the desexcitation of the electronically excited states can be as short

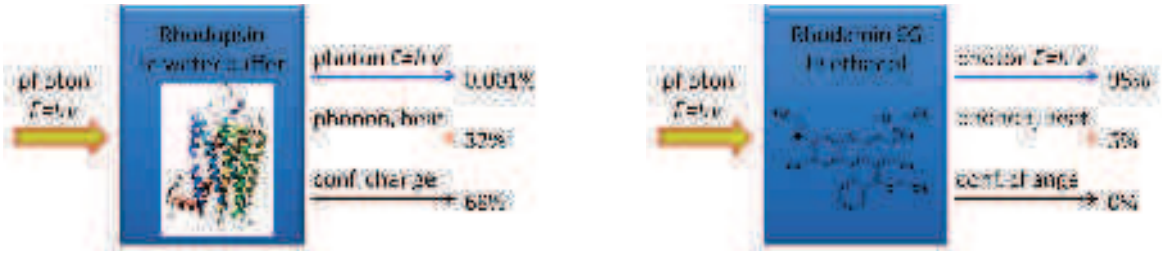

Figure 1.1.: Photonic energy conversion for two molecules upon photon absorption: rhodopsin, a protein found in mammals and responsible for vision and rhodamine 6G, a synthetic dye used in dye lasers.

as a few femtoseconds. The observation of energy conversion thus usually requires techniques with sub nanosecond time resolution.

In this thesis, worked through at the Institut de Physique et Chimie des Matériaux de Strasbourg, we study the photo-generation of charges in organic nanostructures used for conversion of photonic energy into electric energy, in donor molecules for organic photovoltaïc applications as well as the conformationnal change via photoisomerization of a molecule in a light-sensitive protein using ultrafast spectroscopies. Our purpose is to enlight the comprehension of those two phenomena and more specifically the relation between these materials properties and structure with the efficiency of the energy conversion. This would provide a basis of knowledge for the synthesis of efficient photon energy converters for a wide range of applications.

2. Transient spectroscopies

The time resolved spectroscopy techniques allows to perform spectroscopic characterizations as a function of time. These techniques are widely used to characterize the photochemisrty and photophysics of a wide range of physical and chemical systems. Different techniques can be used depending on the desired spectroscopic information, the time resolution, the photon energy range and the complexity of operating the experiment.

2.1. Interest of femtosecond transient spectroscopies

Since we study here systems reacting with visible light, its absorption and emission are typically located in the near UV to near infrared. In addition, the photophysics and chemistry of the studied systems occurs on the femtosecond (retinal isomerization) to the nanosecond (CT states lifetime) timescales. We thus need instrumentation with femtosecond resolution and nanosecond time range.
The femtosecond time range implies the use of femtosecond lasers as photon sources to access the required time resolution. In addition, the femtosecond timescale sampling over the desired time range requires most of the time fully optical techniques, since electrical ones are usually limited to the nanosecond delays.
Finally, the transient absorption measurements measures many different transitions, and the signals are often overlapping, hindering a correct understanding of the photophysics. The use of transient fluorescence techniques are very useful in this case to characterize specificly the excited state populations through its emission.

In this work, UV to near infrared femtosecond transient absorption spectroscopy was used in combination with femtosecond time resolved fluorescence up conversion in and streak camera (picosecond resolution), to characterize the photophysics of the different systems studied.

2.2. Experimental setups

The use of femtosecond lasers allows to exploit the diversity of non linear optics phenomena to generate the different excitation and probe beams, optical time gates, ... needed in femtosecond transient spectroscopies. Indeed, our femtosecond laser power souce is a Ti:Sapphire oscillator with regenerative amplifier providing 0.5mJ, 40fs long pulses of 800nm wavelength at 5kHz. Performing transient spectroscpies requires the use of tuneable sources and broadband sources. The high peak energy of the laser source allows to produce very high peak electric fields, resulting in non linear phenomena in selected materials of interest.

2.2.1. Non linear optics

Non linear optics describes the propagation of high energy optical beams in materials. In the case of high electric fields, the propagation of electromagnetic waves can no longer be described by regular optics. The intensity of the electric fields polarizes the materials and modifies its properties. In this case, the approximation of a linear relationship between the electric field and the polarization is no longer valid, and one should take into account the higher orders in the expansion of the polarization $\vec{P}$ in function of the electric field $\vec{E}(\omega)$:

$$\vec{P}(\omega_1, \ldots, \omega_i) = \epsilon_0 \sum_i \chi^{(i)} \vec{E}(\omega_1) \ldots \vec{E}(\omega_i) \tag{2.1}$$

Where the tensor $\chi^{(i)}$ is the order i electric susceptibility of the material, for an electromgnetic wave of pulsation ω away from the materials resonances (transparent).
Depending on the electromagnetic waves and the materials properties, different non linear processes may be observed.

Sum frequency generation (SFG): This phenomenon is a second order ($\chi^{(2)}$) process occuring in non centrosymmetric materials where too electromagnetic waves interact in the material to form a third one if the phase matching condition are verified. This condition should be verified by the wave vectors of the electromagnetic waves:

$$\vec{k}_1 + \vec{k}_2 = \vec{k}_3$$

The produced electromagnetic wave intensity is proportionnal to the intensity of both incident waves. Because of the energy conservation, the resulting electromagnetic wave has a pulsation ω_3 such as:

$$\omega_3 = \omega_1 + \omega_2$$

This non linear process can be used to produce new wavelength beams for spectroscopy.

Second harmonic generation (SHG:) This phenomenon is a special case of SFG where $\vec{k}_1 = \vec{k}_2$, in that case, the phase matching conditions gives $2 \times \omega_1 = \omega_3$. This phenomenon is used to double the frequency of laser beams, for instance to generate a 400nm pump beam from the 800nm source laser using a BBO (Baryum $\beta-$ Borate) crystal.

Optical parametric amplification (OPA): This $\chi^{(2)}$ process, allowing to transfer the intensity of the pump wave $\vec{k}_1$ to the seed wave $\vec{k}_2$, amplifying the latter. The phase matching condition results in the production of an additionnal wave $\vec{k}_3$ termed as "idler':

$$\vec{k}_1 = \vec{k}_2 + \vec{k}_3$$

It also allows to tune the signal wavelength by selecting a specific phase matching conditions in the family of propagating waves verifying the latter condition. This non linear process allows to amplify laser beams of weak intensity to use it as photon energy tuneable pump beams for instance. A derivative version of OPA is NOPA (non-collinear optical parametric amplification), where the beams are not collinear which allows to acces a wider range of phase matching conditions, but also to a spectrally broader amplification [1]. Important parameter optimization and NOPA description can be found here [2].

White light generation (WLG): White light generation is a $\chi^{(3)}$ process, which is a consequence of beam self-phase modulation. This is a complex phenomenon leading to the broadening of the laser pulses when propagating in transparent media [3, 4]. This phenomeneon depends on the focus of the input laser beam, repetition rate and intensity of the laser, nature of the material used [5] (example for solid state media, as used in this work). For instance, the 800nm beam from the source laser, when focused in a calcium fluoride crystal, gives raise to a coherent laser pulse extending from 290 to 900nm. This supercontinuum generation is used to produce probe beams for the simultaneous measurement of transient absorption signals over a large spectral band.

2.2.2. Streak camera

The streak camera is an ensemble of a streak tube and a CCD camera allowing to separate temporally incident photons as a function of its delay with regard to a reference clock signal. When clocked to the frequency of an excitation pusled laser, while detected the fluorescence photons from an excited sample, it allows to time resolve the fluorescence.

The streak tube is an electronic device that amplifies the incident photons, and then to separate it spatially as a function of its arrival time. It consists in a photocathode that converts the incident photons into electrons (photoelectric effect). These electrons are then amplified by a photomultiplier stage and propagates to the streak chamber. In this chamber is applied a vertically oscillating electric field between two plates, synchronized to the clock signal, that acelerates the electrons in the vertical direction. Since the amplitude of the oscillating electric field depends on time, different arrival time of electrons will result in a different vertical deflection. This results in a vertical spread of the electrons, the position of those determined by its arrival time. The slope of the oscillating electric field is calibrated and allows to tune the time window, fine tuning of the phase of the oscillating electric field with respect to the

clock allows to offset the time delays. Finally, the output of the chamber hosts a phosphor screen converting the incident vertically spread electrons back into photons, that are detected by the output CCD. The horizontal direction of the system can be used to sample an other spatial information. The latter could be any physical observation transposed as an horizontal spread of the incident photons. For time resolved fluorescence measurement, one may use the output beam of a spectrometer to get spectral information. The spectrometer allows indeed to convert the information about photon energy into an horizontal spreading of photons. Note that the spectral sensitivity range is limited by the spectral response of the photocathode.

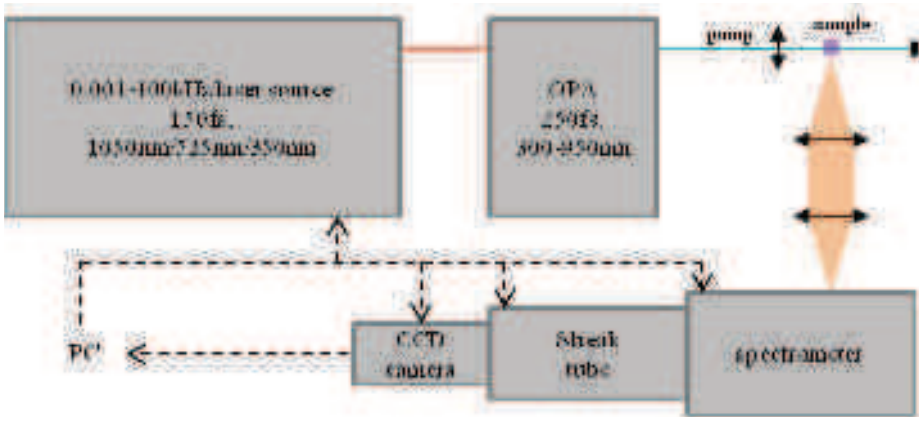

Figure 2.1.: Schematics of the streak camera based transient fluorescence setup.

In the end, the streak camera is mounted at the image focal plan of a spectrometer. It is synchronized to a source laser (Tangerine, Amplitude technologies) pumping a home made OPA [6] to have a tunable excitation. The output of the OPA is focused in the sample of interest, whose fluorescence is focused on the entrance slit of the imaging spectrometer, as depicted in figure 2.1. The CCD camera at the output of the streak tube measures the amount of fluorescence photons I with a given arrival time in the vertical pixels y_n and with a given photon energy in the horizontal pixels x_n, as depicted in equation 2.2. The corresponding data consists in a matrix of time resolved fluorescence spectra $F(\lambda, t)$ with a selected range and resolution in time and photon energy depending on the experimental settings:

$$I(x_n(\lambda), y_n(t)) = F(\lambda, t) \tag{2.2}$$

The streak tube, the CCD and the spectrometer are controlled by a computer allowing to set the experimental settings (synchronization, time window, spectral window, amplification) and to read the CCD camera (time integration, reading mode). The electronically generated delays allows time resolutions down to 5-7ps, and time ranges from nanosecond to miliseconds.

2.2.3. Transient absorption

The transient absorption (TA) experiment is an optical setup using the Ti:Saphhire based source as an input and which optical output is focused on the entrance slit of an imaging spectrometer, mounted with a CCD in the image focal plane. A wide variety of setups can be used, depending on the time resolution, pump wavelength, probe window and detection range [5, 7] (for femtosecond time resolutions and UV-visible pump and detection windows).

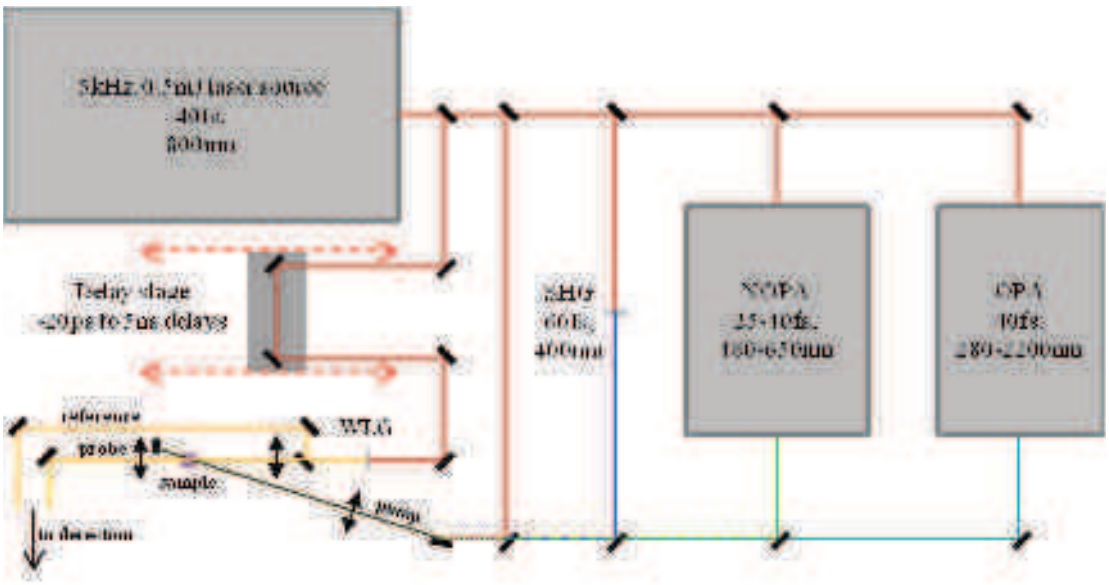

Figure 2.2.: Schematics of the transient absorption setup.

Our transient absorption setup uses a probe beam focused in a 2mm thick calcium flouride or 4mm thick YAG window to generate a white light continuum spanning respectively from 290 to 900nm or 500 to 1100nm, after passing through a computer controlled delay line. This probe beam is splitted into a probe beam focused in the studied sample to probe its absorption, and a reference beam used to correct the white light beam power density spectrum fluctuations. Note that the calcium fluoride window is continuously translated at approximately 1Hz to prevent the window from thermic damage. The pump beam is either used directly as a 800nm, 40fs pump or injected in a non linear stage to generate the desired pump frequency. 400nm, 60fs pulses can be generated by SHG in a BBO crystal, 480 to 650nm, 25 to 40fs long pulses generated in a home made NOPA or 280 to 2000nm, 40fs long pulses generated by an OPA (TOPAS, Light Conversion, note that only wavelengths from 535 to 560nm obtained by sum frequency of the signal with the idler have been used in this work). The so generated pump beam is focused in the sample so that the pump beam is larger than the probe beam at the probe focal point, and overlapped. A schematics of the setup is pictured in figure 2.2.
The probe and reference beams are vertically spaced and passes through an imaging spectrometer mounted with a CCD camera, so that the top of the CCD recieves the reference, and the bottom part the probe beam. A sequence of integrated probe and reference beams with and without excitation is generated by chopping the pump pulses with a mechanial chopper wheel, and used to calculate the change in the transmitted probe light when the sample is excited. This sequence is repeated for different pump-probe delays by changing the probe path with the delay line. This results in a measure of the difference absorption of the sample as a function of the photon wavelength and pump-probe delays:

$$\Delta A(x_n(\lambda), y_n(t)) = \Delta A(\lambda, t) = log\left[I(\lambda, t)\right]_{with\ pump} - log\left[I(\lambda, t)\right]_{without\ pump} \tag{2.3}$$

The transient absorption data measured should correspond to the change in concentration with respect to the initial concentration of the different species n involved in the photochemical process observed, and charac-

terized by their molar absorption spectra:

$$\Delta A(\lambda, t) = l \times \sum_n \epsilon_n(\lambda) \Delta c_n(t) \tag{2.4}$$

Where l is the optical path length, $\Delta c_n(t)$ the temporal evolution of the variation in the concentration of species n with regard to its concentration before excitation and $\epsilon_n(\lambda)$ its molar absorption coefficient. Note that $\Delta c_n(t)$ can be negative since ground states can be depopulated by the pump pulse. Ideally, knowing all the species involved in the photochemical system measured, along with its molar absorption spectra, would allow to quantitatively estimate the concentration evolution in the system, and obtain the yield of interconversion between species. However, noise and vibrational relaxations changing the spectrum of the same electronic state as well as the incapability to obtain the spectrum of certain states prevents from doing it, and the complexity of the often overlapping absorption spectra of the species makes transient absorption hard to decipher in some cases.

2.2.4. Transient fluorescence

Femtosecond transient fluorescence (TF) measurements are performed using an optically gated fluorescence up conversion setup. This setup is used to measure the fluorescence dynamics of TB2, which can be efficiently quenched in the presence of PCBM. This quenching results in sub-picosecond fluorescence lifetimes, that can not be resolved using the streak camera setup, the latter having a time resolution of approximately 6ps. Optical gating of the fluorescence allows to go down to hundred femtoseconds time resolution.

The optically gated time resolved fluorescence experiment uses the $\chi^{(2)}$ non linear optical phenomena of either sum or difference frequency generation in solid media, usually BBO. A schematic of the eperiment is depicted in figure 2.3. The fluorescence is triggered by excitation of the samples with a femtosecond laser. It is then collected and focused in the BBO crystal. The optical gate is a high energy pusled laser beam, passing through a controllable delay line, is then focused in the BBO crystal,

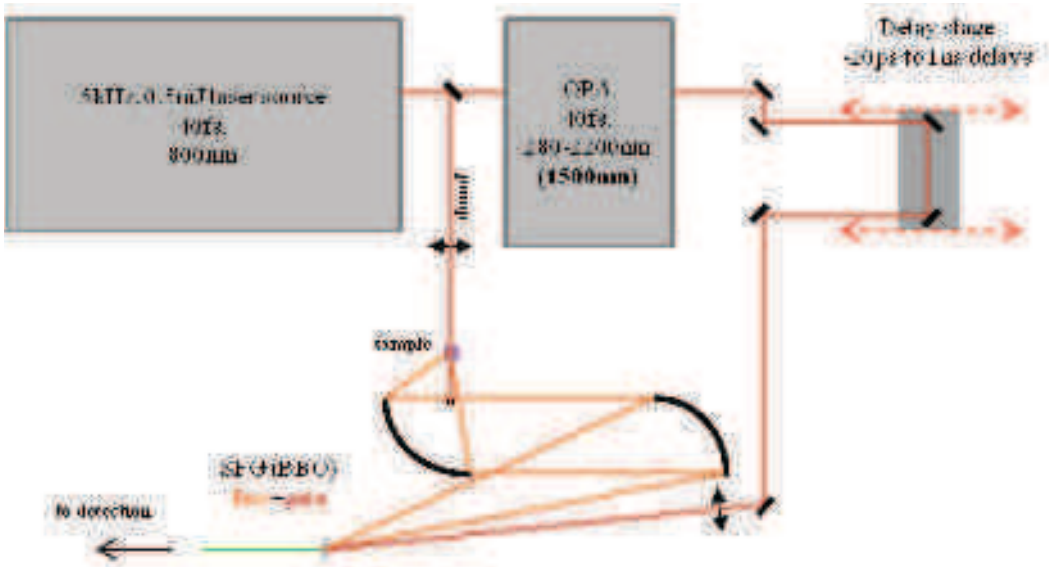

Figure 2.3.: Schematics of the optically gated transient fluorescence up conversion setup.

so that fluorescence and gate beams overlap. Depending on the phase matching conditions, which can be tuned by changing the orientation of the BBO crystal, one can process to the sum or difference frequency of the latter beams. The resulting beam is then collimated and focused on the entrance slit of a spectrometer mounted with a Pelletier cooled CCD. The signal intensity as a function of the wavelength is then acquired. The arrival time of the gate pulses is controlled by the delay line. The CCD and delay line are computer controlled and allows to measure the converted fluorescence spectra as a function of the delay.

The up conversion configuration uses the phase matching conditions on the wavevectors $\vec{k}$:

$$\vec{k}_{fluo} + \vec{k}_{gate} = \vec{k}_{signal}$$

Where $\vec{k}_{gate}$ is constant in intensity. The resulting signal intensity is proportionnal to the product of the intensities of the interacting gate and fluorescence signals. Since the fluorescence signal is longer than the gate pusle duration, only the fluorescence photons present in the BBO crystal at the same time than the gate ones can be converted. As a result, the signal intensity is proportionnal to the number of fluorescence pho-

tons interacting with the gate photons, and consists in a time correlated number of fluorescence photons emitted at the wavelength verifying:

$$\lambda_{signal} = \left(\frac{1}{\lambda_{fluo}} + \frac{1}{\lambda_{gate}} \right)^{-1}$$

For this experiment, since the TB2 fluorescence is emitted in the near infrared (800-1100nm), we use a up conversion configuration, so that the resulting sum frequency signal is located in the visible wavelengths to have a good sensitivity with the CCD (silicon sensor). The setup used is described here [8] and is inspired by the historical experiment of Shah [9]. In this work, we use a 800nm pump wavelength from the source laser and a 1500nm, 40fs long pulses with 40μW intensity gate from the TOPAS OPA. The crystal used is a 400μm thick BBO crystal with a θ=46^o orientation. The fluorescence and gate beams are 8.7^o tilted in the same plan. The crystal is 1.75^o tilted with respect to the gate in a type II negative phase matching condition. Integration time is 5s. The resulting up converted signal spans from 550 to 575nm, which corresponds to a fluorescence window of 870 to 930nm. The time resolution is about 200fs (FWHM of the IRF), and the spectral resolution about 10nm. The spectral window of fluorescence converted depends on the phase matching conditions, defining the spectral acceptance of the sum frequency phenomenon. The time resolution is limited by the group velocity mismatch and the wavefront tilting of the fluorescence and gate beam [10, 11]. The crystal thickness is a trade of between the latter phenomena and the yield of the sum frequency mixing.

Finally, the data measured by the system is the intensity spectrum I of the source signal dispersed on the horizontal pixels of the CCD x_n as a function of the delay between pump and gate:

$$I(x_n(\lambda_{signal}), t) \propto F(\lambda_{fluo}, t)$$

2.2.5. Noise managment

The transient spectroscopies used in this work are performed so that the molecules studed are probed under a linear regime of excitation, which usually corresponds to an excitation density of less than 10%. The samples usually have an OD of 0.1 to 0.4, so that the probe beam can be significantly transmitted in the case of transient absorption, and to have low re-absorption of fluorescence in the case of transient fluorescence. This results in small concentrations of excited molecules, and as a consequence, the difference absorption signals lies in the order of 10^{-3} OD, and transient fluorescence intensities can be very low in the case of low fluorescence yield molecules.

To have a good signal to noise ratio in the transient fluorescence measurements, one may be sure to match the numerical aperture of the optical system collecting the fluorescence with the one of the spectrometer used. The optics should be appropriate for the transmission of the fluorescence photons, and one should use detection systems sensitive in the spectral region of the fluorescence. Then, for very low fluorescence signals, one should use an appropriate integration time to reach the desired signal level, taking care of any parasitic light source that may enter the detection system, including the scattered pump photons. In the end, the level of noise might be reduced to the dark noise and reading noise of the sensor, which can be characterized and substracted for.

In the case of transient absorption, increasing the signal to noise ration is generally limited by the fluctuations in the pump and probe beam intensities. The fluctuations in the WLG process can be corrected for by the use of the reference beam described previously. This correction is adapted in our case. Note than in shot to shot pump probe setups, this might not be necessary, as pointed out in this review discussing the origin of noise in transient absorption experiments [12]. The correction using reference leads to a noise level of about 3×10^{-3}, resulting in a noise level in the transient absorption signals of about 5×10^{-4} for a 50 shots integration, which can be further reduced by averaging consecutive

experiments.

The stability of the laser source is continuously monitored to work in the best possible conditions. The laser system has typical fluctuations in its intensity due to thermal effects, resulting in a modulation in the signal at a frequency about some Hz. It is important that the measure is done at a significanlty shorter or longer timescale to avoid systematic fluctuations in the transient absorption data recorded.

2.3. Data processing

The data recorded using transient spectroscopies may need to be corrected for unwanted contributions. In addition, the absolute zero delay should be defined accurately before the use of the data. After that, one may want to model the data in order to extract informations about the kinetics of the observed signals and about the species present in the studied samples photochemistry. This review lists the general data processing techniques used to correct and analyse transient spectroscopy data [13].

2.3.1. Solvent correction

Even though solvents and substrates used to carry the molecules of interest are usually transparent for the pump and probe beams, it can generate solvent-specific responses, in particular in transient absorption data. Indeed, the interaction of pump and probe beams in the solvent medium can generate non linear signals such as cross phase modulation. This results in non negative transient absorption signals for delays close to zero. In addition, other contributions, such as stimulated raman scattering (SRS), two photon absorption, ... can happen[14]. All these phenomena, occuring in the vicinity of the zero delays, are usualy referred to as the coherent artifact.

These contributions can be measured in very similar conditions that the sample of interest, performing the same experiment in a raw, with the solvent only, for delays close to time zero. This measurement can be substracted from the sample data, in order to have only transient absorption contributions from the molecule of interest. Note that in order to preserve the signal to noise ratio, one should measure the transient solvent response with a higher signal to noise ratio. Since the coherent artifact happens only close to zero delays, one may only measure this small delays time region and suppose that the solvent signal is zero for longer delays, in order to preserve the signal to noise ratio. Usually, since the pump is resonant with the absorption of the molecule of interest, its average intensity in the excited volume is lower than in the solvent alone. Measuring in the same pump intensity conditions results in an overestimation of the coherent artifact. The substraction of the solvent reponse is weighted by a coefficient α usually comprised between 0.5 and 0.9:

$$\Delta A(\lambda,t)|_{corrected} = \Delta A(\lambda,t)|_{sample\ in\ sovent} - \alpha \times \Delta A(\lambda,t)|_{solvent} \quad (2.5)$$

Note that such a solvent substraction explicitely neglects the influence of the molecule under study on the average spectral intensity of the probe beam, that would also change the amplitude of the coherent artifact. This procedure allows anyway to substancilly reduce the amplitude of the coherent artifact, resulting in neglectable contributions from it in the processed data.

An alternative way to avoid the addition of noise when substracting the coherent artifact is to model it. The coherent artifact is dominated in our case (approximately 40fs long pulses) by electronic signals that can be modeled by a linear combination of the cross correlation function and its derivatives[14] that we model as a gaussian function. Fitting the temporal evolution of the coherent artifact for the measured wavelengths with our model function results in a model data map for coherent artifact:

$$\Delta A(\lambda,t)|_{corrected} \approx \alpha G(t_0,\sigma,t) + \beta G'(t_0,\sigma,t) + \gamma G''(t_0,\sigma,t) \quad (2.6)$$

with:

$$G(t_0, \sigma, t) = \exp\left(-\frac{1}{2}\left(\frac{t - t_0}{\sigma}\right)^2\right)$$

However, to be fully efficient, the transient absorption data measured on the solvent should have a good signal to noise ratio, and this method has to be improved. However, this method is useful to determine the chirp.

2.3.2. Chirp correction

The supercontinuum probe beam spans over a large range of wavelengths. As a result, the group velocity dispersion in the WLG medium may be large. Therefore the low energy part of the probe pulse travels faster than the high energy part, and thus interacts with the pump at different delays that can span over 200fs, usually called "chirp". An example is shown in figure 2.4, where the coherent artefact appears as a coma shaped non zero signal.

The time zero can either be estimated manually as the middle of the coherent artifact signal or using the coherent artefact model presented above. The so determined t_0 delays as a function of the wavelength is fitted by a 3^d order polynome, leading typically to an accuracy of the fit of about 20fs. The transient absorption data kinetics are then accordingly shifted in order to correct for the chirp.

2.3.3. Fitting

To obtain the lifetime of the different phenomena occuring in the studied materials, one may model the data in order to fit the time constants of the system. We make here the assumption that the kinetics of the populations involved in the transient response obeys to simple rate equations model and thus that the population formation and decay can be modeled by decaying exponential functions. The transient absorption data, for instance, should then correspond to exponentially decaying or growing concentrations of the different species involved in the photochemical process observed, such as evidenced by equation 2.4. This

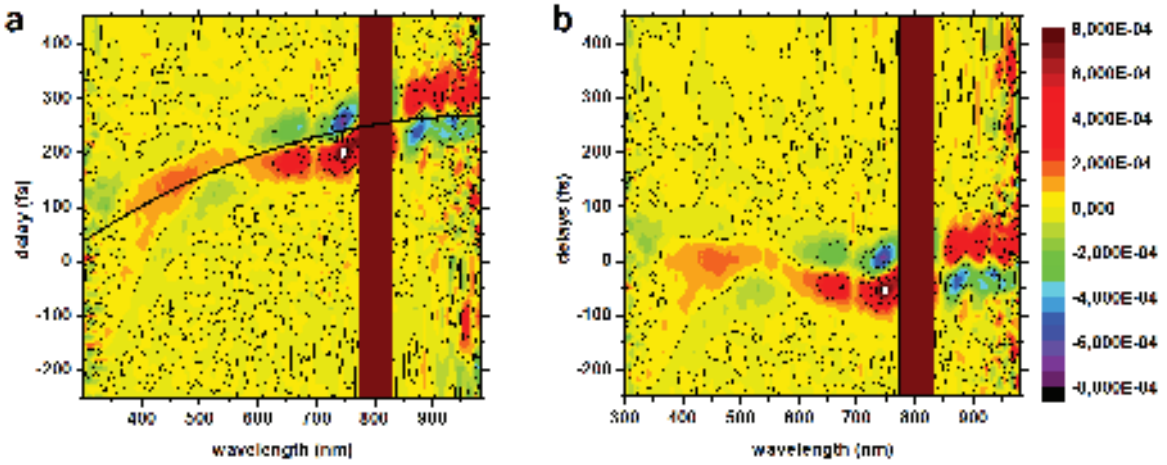

Figure 2.4.: Raw coherent artefact in PCBM cast on ITO/Pedot:PSS substrate, excited out of resonances at 800nm, 300μW in panel a. The thick black line indicates the polynomial fit of the zero delays obtained by modeling the data. The data set is measured with WLG in CaF_2 and is a combination of 3 different data sets sticked together. Panel b presents the chirp corrected data.

model is still valid in the case of transient fluorescence, in this case the molar absorption spectra shoulf be replaced by the fluorescence spectra, and the optical path length removed.
Finally, the measured data is limited by the instrument response function (IRF), which leads to a finite time resolution for short time delays. This instrument response function is accounted for by fitting the data by the convolution of a gaussian IRF of width σ with the sum of exponential decays:

$$\Delta A(\lambda, t) \approx \sum_i a_i exp\left(-\frac{t-t_0}{\tau_i}\right) * \frac{1}{\sigma\sqrt{2\pi}} \exp\left(\left(\frac{t-t_0}{\sigma}\right)^2\right) \tag{2.7}$$

Note that this model explicitly infers that the data are bilinear with respect to time and wavelength, which is not necessarily true, in particular in the case of vibrationnal relasations in excited states and photoproducts. In this case, the decay of the kinetic mght not be due to a decay in this electronic state population, but in the higher energy vibrationnal states of this electronic state.

2.3.4. Data composition

To measure complete transient absorption data from the near UV to the near infrared, one must perform four different experiments leading to four different data sets measured for the same delays but with different wavelength range. To this end, in order to have a good signal to noise ratio over the whole wavelength range, one must change the WLG medium from CaF_2 in the near UV to visible range, to YAG for the near infrared. Changing the crystal used for WLG changes also the position of the zero delay, since the crystal does not share the same optical path length (different refrative index and thickness). After appropriate chirp correction, the different data sets are merged together. The wavelength ranges measured are chosen so that they significantly overlap together. The data sets are combined using the overlap region to match the time delays. The overlap regions are then computed as the average of the two contributing data sets, in order to increase the signal to noise ration in this region. Some data corresponding to the edge of the spectral windows can be removed if its signal to noise ratio is detrimental to the final one.
Finally, one may obtain broadband near UV to near infrared spectral range transient absorption data sets, such as for OPV molecules in this manuscript.

2.3.5. Singular Value Decomposition

The singular value decomposition is a mathematical operation on matrices that allows to decompose a m by n matrix $M_{m,n}$ so that:

$$M_{m,n} = U_{m,m} S_{m,n} V^T_{n,n}$$

Where $U_{m,m}$ and $V_{n,n}$ are orthonormal and $S_{m,n}$ diagonal with its diagonal carrying the singular values in descending order.

The singular values give an indication about the rank of the M matrix. Indeed, only the dominant singular values are necessary to well reproduce most of the M matrix. The other singular values are related

to noise, so that replacing the noise related singular values by zero values, to form the S' matrix and use it instead of the S matrix results in a noise filtering of the so reconstructed M matrix. In case the m direction represents the spectral direction and the n one delays, the U matrix would contain spectral information and the V matrix temporal information. Plotting the diagonal values of the S matrix helps in determining the significant singular values, and thus the rank of the M matrix.

2.3.6. Global analysis and Decay Associated Difference Spectra

After proceeding to the SVD on the data matrix, the temporal V matrix can be used to characterize the dynamics in the data since it contains all the temporal evolution of the whole data set. The $K = S'V^T$ product contains all the major kinetic information of the data set, and consists in a set of kinetics referred to as singular kinetics. Fitting simultaneously these kinetics with the function described in equation 2.7, with shared exponential decays results in a global fitting of the kinetic information of the data set. This fit gives the different lifetimes present in the data as well as the associated amplitudes for the different singular kinetics. The product of the so fitted amplitudes with the spectral matrix U gives the difference spectra associated with the fitted decays in the data set, which are called DADS for decay associated difference spectra:

$$DADS(\lambda, \tau) = U \times \begin{pmatrix} a_{1,\tau_1} & a_{1,\tau_2} & \cdots & a_{1,\tau_i} \\ \vdots & \vdots & \ddots & \vdots \\ a_{k,\tau_1} & a_{k,\tau_2} & \cdots & a_{k,\tau_i} \end{pmatrix}$$

These DADS are interesting since it gives the spectral evolution occuring at the characteristic time τ of the system. It allows to have more information about the interconversion of species in the photochemistry of the studied system.

Part II.

TB2: a BODIPY derivative for use as donor in "small molecule" organic solar cells

3. Organic Photovoltaics

Organic photovoltaics are part of the organic electronics field. Organic electronic consists in using organic materials to build electronic systems. Organic materials refers to molecules mainly constituted by carbon, oxygen and hydrogen atoms.

3.1. Motivations

The world electricity energy production is of great concern since many populated countries are fastly devolopping and therefore will drastically increase the overall world energy demand. In the present energy consumption, renewables accounts for 15.9% , electricity for 17.7% and fossile fuels for the remaining 66.4%. Since electricity can be produced from fossile (79.7% : coal, oil, gas, fission,...) or renewable (20.3% : hydro, wind, geothermal, solar,...) fuels, the final fossile fuels accounts for 80.5% of the world energy consumption [15] and most of these fossile ressources are forecasted to be completely consumed by sooner than the next century (gaz, coal and oil)[16].
To supply the world with energy in a sustainable way, it is clear that one must increase the share of renewable energies. Even though electric energy is currently difficult to store and to transport efficiently in long distances, it is a versatile energy that can easyly be transformed into mechanic energy, radiant energy, heat and chemical energy and is widely used in developped countries. This versatility, together with improvement of eletricity storage and transport and sustainable production makes electricity a key energy for world use.

Since the major (an renewable) source of energy on earth is sun (ap-

proximately $1kW.m^{-2}$ in our lattitudes), production of electric energy from sun is relevant. The most direct way to produce electricity with photons from sun light has been evidenced by Bequerel in 1839 and later explained by Einstein and is named photovoltaic effect[17] which brought the latter a Nobel prize.

First photovoltaic cells for sunlight to electricity conversion appeared in the mid 20th century with efficiencies about 5%, these devices were based on cristalline inorganic semiconductors (Silicon, Germanium). The field of inorganic solar cells evolved since then to reach efficiencies as high as 44.7% for optimized multi-junction Germanium solar cells. Meanwhile, other inorganic materials appeared such as CIGS (Copper Indium Gallium Selenide) and the last technology developped is perovskite solar cells, which already shows promising efficiencies. New cells architectures (tandem cells) have also been developped with the objective to achieve an efficient, cost-effective and easy to process technology. The graph in figure 3.1 illustrates the evolution in time of the different technologies and their record efficiencies.

In the 90s, Grätzell cells or dye-sensitized solar cells were the first organic active material based solar cells, followed in the beginning of the 21th century by the first solid state organic solar cells.
The latter technology uses organic molecules in the active layer. The advantage of organic molecules is the possibility to tune their physical properties (energy level, solubility, agregation,...) at will by changing their chemical composition (substitution of atoms, substitution of side chains, ...). However, structural changes of organic molecules often influences different physical properties at the same time an as a consequence, one commonly have to find a trade off between different properties.

Organic molecules used in photovoltaics are generally designed to be soluble in chlorinated or organic solvents. This allows to process them from solution either by spin-coating, doctor blading, ink jet printing. Small molecules can also be deposited by evaporation in vacuum at rel-

atively low temperatures due to their low boiling point in comparison with inorganic semiconductors. All these processing techniques are compatible with roll-to-roll production and allows production of large areas with high throughput. These techniques are less energy consuming than the production of monocristalline inorganic materials, which make them more eco-friendly.

It is important to point out that organic photovoltaics are not bound to replace inorganic solar cells, and will probably never replace inorganic in some application such as solar panels for use in space. Indeed, the performances of organic solar cells are not yet comparable to those of inorganic ones and some issues such as device lifetime are not sufficient. Still, organic photovoltaics can already have its place on the market of photovoltaic energy where a trade off between efficiency and other performances is acceptable, because of the unique opportunities it offers in comparison to inorganic, such as fabrication on large area flexible substrates, possibility to make semi-transparent solar cells, low weight solar cells. This is very important for versatile or design applications for a cheap price. For some applications, the payback time of organic solar cells can even be shorter than its present limited lifetime.

Therefore, even though solar power plants using organic materials may never exist (thermodynamic solar power plants are more efficient), outcomes from this technology are still important for home scale use and some other niche applications.

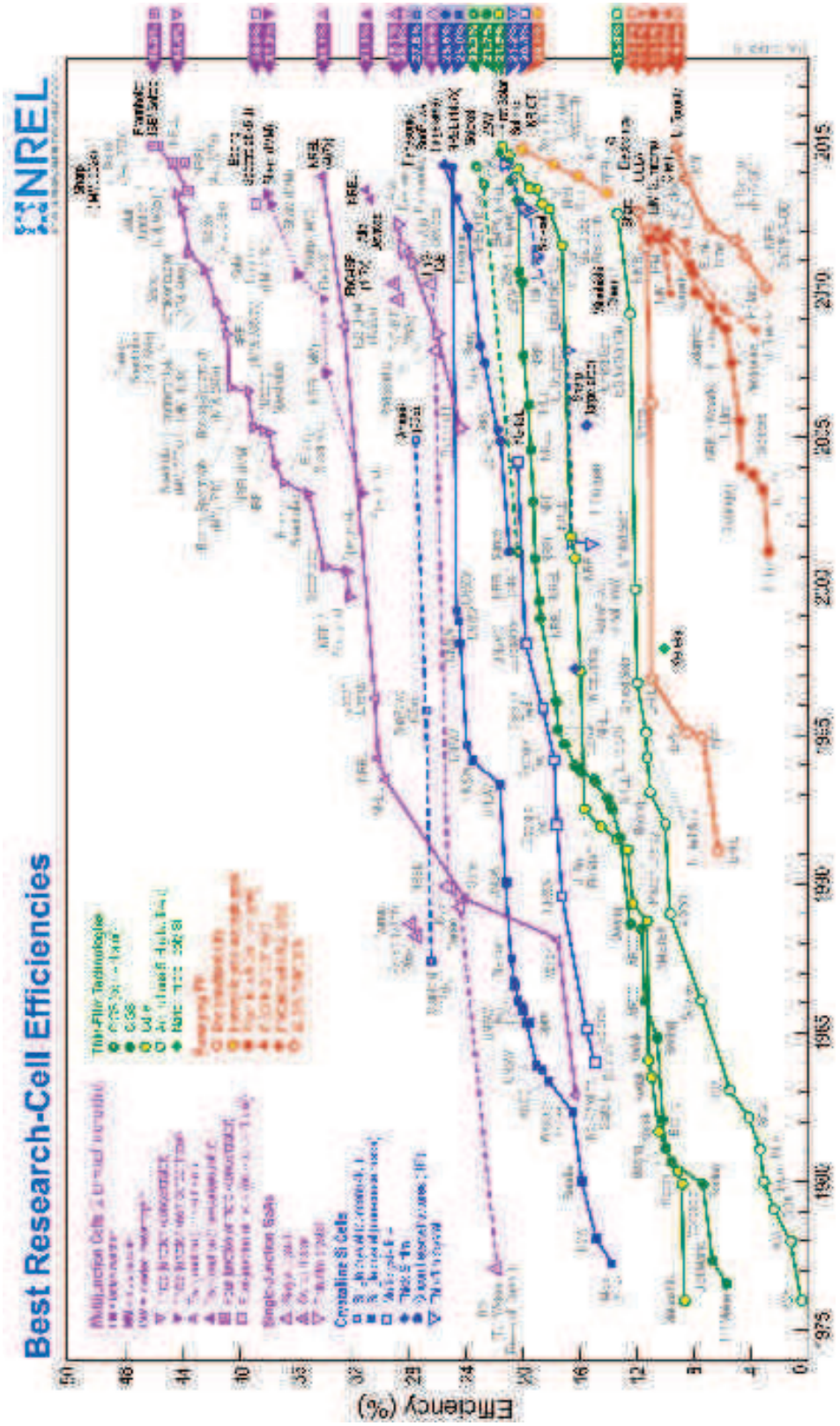

Figure 3.1.: Graph from the National Renewable Energy Laboratory (NREL, www.nrel.gov) showing the lab scale records of different solar cell technologies efficiencies evolution over years.

3.2. Organic semiconductors

The semiconducting character of organic molecules have been evidenced in the XXs. In π-conjugated molecules, where there is an alternation of carbon single and double bonds, the carbon goes from a regular $1s^2 2s^2 2p^2$ electronic configuration to a sp^2 hybridized configuration. The latter configuration corresponds to a mixing of s and p orbitals minimizing the energy of the carbon atom. This results in 3 coplanar sp^2 binding orbitals, referred as σ bonds. The remaining out-of-plane p_z orbitals are orthogonal to the plane. Upon binding with an other carbon atom, the p_z orbitals overlaps creating a π orbital with significant delocalized electron density above and below the plane, this is schematized in figure 3.2. These π-orbitals are the higher energy lying occupied molecular orbitals, refered as HOMO (highest Occupied Molecular Orbital). The lowest energy unoccupied orbitals have also a π character and therefore excitation of conjugated molecules is often referred to as π-π^* transitions.

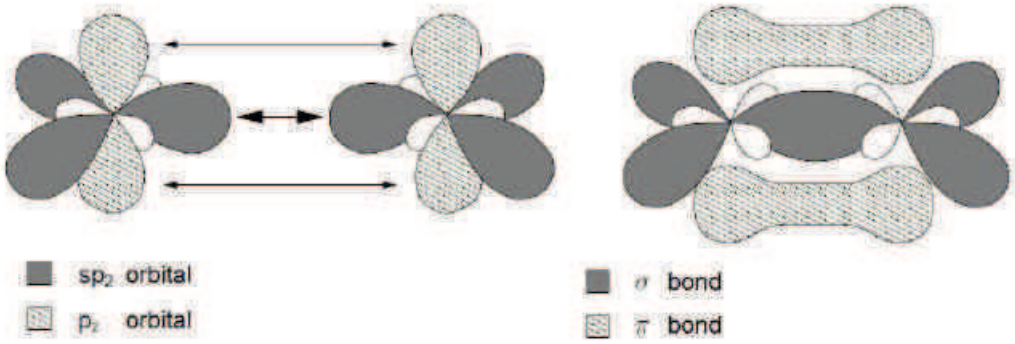

Figure 3.2.: sp^2 hybrisization of carbon atoms. Upon binding (right), a delocalized electronic density is created above and below the plan of the molecule, in the π orbitals.

3.2.1. Examples of organic semiconductors

Organic semiconductors are generally π-conjugated molecules. One can distinguish two main classes of organic semiconductors: polymers and small molecules. Wihtin each class, some main subclasses can be mentioned. Polymers are a repetition of a molecular motif (monomer)

covalently bound together, however one can either repeat the same motif (homopolymer) or alternate different motifs (copolymers). The small molecules class (called small in opposition to long chains of polymers rather than because of their molecular weight which is quite heavy from a chemical point of view) usually contains oligomers (polymers with a small repetition of monomers, typically less than 10) and molecules. These two classes of molecules are displayed with examples in figure 3.3.

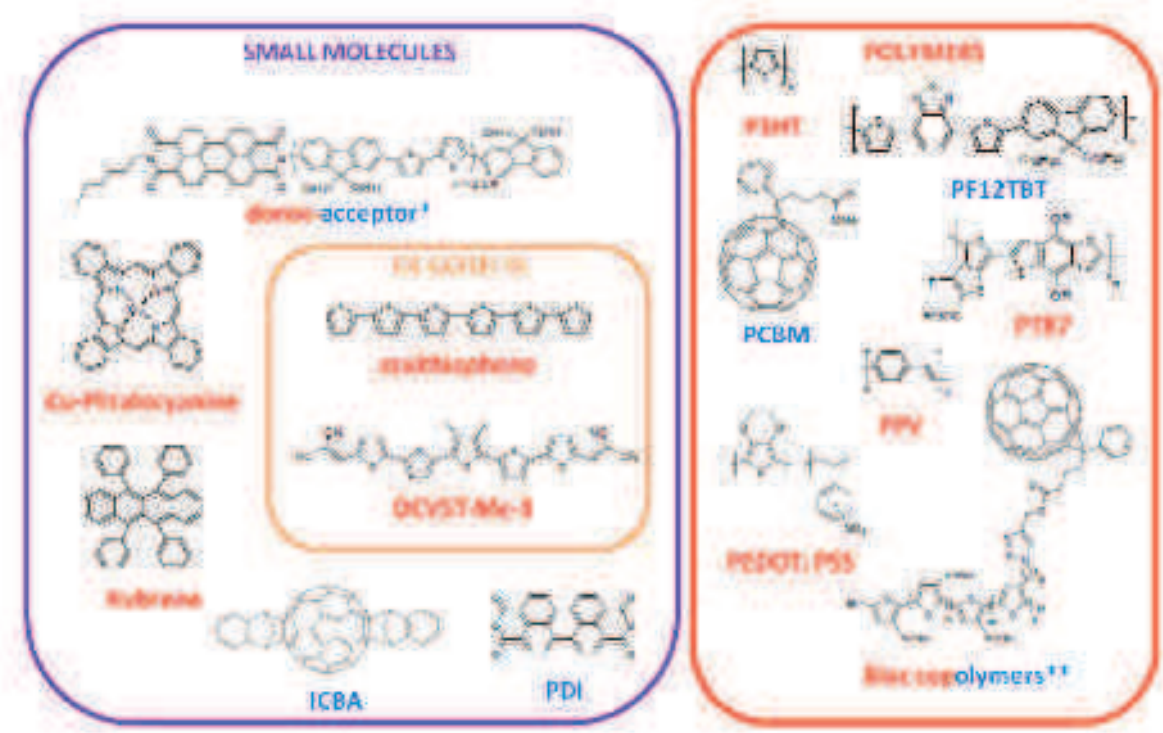

Figure 3.3.: Different type of organic semiconductors used in organic photovoltaics. Donor materials are labeled in red and acceptor in blue. * donor-acceptor small molecule from reference [18]. ** Bloc copolymer from reference[19].

3.2.2. Analogies with inorganics

In inorganic semiconductors, the electrons are fully delocalised, giving rise to well defined energy states whereas in organic semiconductors, delocalisation of electrons is only effective within the molecule in the absence of significant molecular interactions. Even though it is possible to

form relatively well ordered cristalline domains with small molecules, the overall morphology is disordered which makes organic semiconductors intrinsically localised systems. In the end, the band gap or optical gap of an organic semiconducting material can not be described by a band structure, and is defined as the absence of states between the HOMO and the LUMO energy levels of the organic molecule. As a consequence, conductivity in organic materials is much lower than in inorganic semiconductors and metals.

Another significant difference between organic and inorganic semiconductors is the dielectric permittivity which is much lower in organic (ϵ typically in the order of 3) than in inorganic ($\epsilon = 10$ typically) which has a strong influence on the screening of electric field and thus on the nature of excitations in these materials (respectively Frenkel and Wannier-Mott excitons).

3.2.3. Excitons

Excitons are neutral particles resulting from excitation of materials in the condensed phase. Excitons are a bound electron-hole pair in a given material. The two charges are bound together due to the Coulomb interaction V between them:

$$V = \frac{e^2}{4\pi\epsilon_0\epsilon_r r}$$

Where r is the distance between the charges, e the electronic charge, ϵ_0 the vacuum permittivity and ϵ_r the dielectric constant of the material. Since the dielectric constant of organic materials is relatively low ($\epsilon_r \approx 3$) and that the excitons have a small radius (Frenkel excitons, by opposition to large radius Wannier-Mott excitons, see figure 3.4) leading to a small value for r, the energy required to split the exciton is significantly higher than the thermal energy $k_B T$. In case of strong molecular interactions, the exciton may be delocalized over several molecules, but it is insufficient for the exciton to split thermally. However, the delocalization of excitons may be interesting to interact with distant molecules, such as an electron acceptor that may help in splitting the exciton. Delocalized

excitons can be found when molecules form agregates. Since aggregates produces absorption band shifts or splitting [20], the delocalisation of excitons can be evidenced by steady state absorption measurements.
The presence of an exciton on a molecule induces a relaxation of the latter molecule structure. In most conjugated molecules used in OPV, it results by a change in the bond length alternation. This molecular relaxation is included in the definition of exciton.

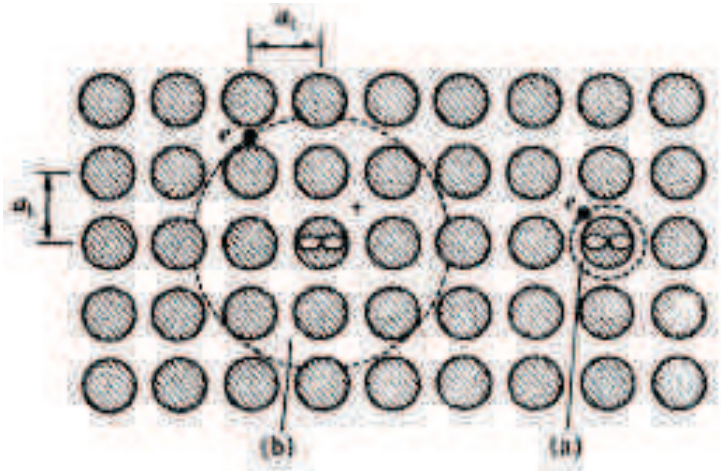

Figure 3.4.: Different classes of excitons. The Frenkel exciton has a smaller radius than the typical lattice constant a_L (a) while the Wannier-Mott excitons has a large radius (b). From [21].

Excitons are neutral particles and are thus insensitive to electric fields. As a consequence, they may diffuse freely in the bulk. Diffusion of excitons occurs through energy transfer (Förster resonance energy transfer -FRET-), which results in the end in a reduction of the exciton's energy. After migration, the exciton may end up trapped in the lowest accessible energy state. Further displacement may only be allowed by thermal activation.

The exciton migration can be limited either by trapping, or by the recombination. The average migration distance during the exciton lifetime is called the diffusion length of the exciton. Diffusion length is usually on the order of 10nm in organic materials. The diffusion length is important in case the exciton has to migrate to trigger photochemical

reactions of interest.

Absorption of a photon in an organic material for organic electronics creates excitons. The lifetime of excitons is determined by the rate of depopulation pathways, including its own lifetime. The expected loss pathway, favorable to organic solar cells yield is the formation of free charges.

3.2.4. Polarons

Free charges in organic materials are much more localized than in inorganic ones. Due to the poor screening of the electric field, the charge carriers generate a potential due to the local excess of charge. This creates a polarization field around the charge, but also deformations of the molecules. The coupling of the charge, its polarization field and the phonons associated with molecular deformations constitutes the polarons.
The delocalization of polarons depends on the delocalization of the charge, and thus on the intermolecular interactions, and on the extension of the polarization fields, which depends on the dielectric constant of the material. As a consequence, two different kind of polarons exists: the small polaron, for which the dimension of the polaron is smaller than the typical lattice dimentions (intermolecular distances) [22], and the large polarons, in the case the extension of the polaron is larger than the typical lattice dimensions [23].
The electron-phonon interaction have a strong influence on the transport of charges. Small polarons transport occurs through hopping while large polarons are favorable to band-like transport [21, 22, 23].
The polarons spectral signature are often a sub bandgap absorption transition.

3.3. Organic Solar cells

Organic solar cells (OSC) are photovoltaic cells where organic materials are used in the active layer. Generally it consists in an active material sandwiched between two electrodes to collect the charges generated in the active layer. Since photons must reach the active area, one of the electrodes must be transparent in the used wavelength range of solar spectrum.
Electrodes are generally made of an evaporated metal, such as gold or aluminium for an opaque and reflective electrode, and Indium Tin Oxyde (ITO) because of their good conductivities as metals and semiconductor respectively. However, organic materials can be used for electrodes, the most commonly used being PEDOT:PSS (poly(3,4-ethilenedioxythiophene) and poly(styrene sulfonate)) as a transparent hole transporting electrode. Advanced electrodes are often used to optimize solar cells such as hole or electron barriers before a metal electrode or structured electrode for photon concentration.

The architecture of the active layer and of the whole solar cell has an influence on the efficiency. The first solar cells where single component planar solar cells and were using the build in field due to the difference in the workfunction energies of electrodes to overcome the Coulomb interaction of electron and charge of the exciton to split it. This requires the active material to be very thin to separate charges before they recombine.
An advanced architecture uses an acceptor molecule with a lower HOMO energy level to drive the exciton splitting via charge transfer. This can be done by placing an acceptor layer between the donor layer and the anode [24], in a planar heterojunction architecture.

Since exciton splitting occurs at the donor-acceptor interface, one may want to increase the size of the interface to increase the exciton splitting probability by forming a continuously phase separated bulk heterojunction [25].

However, the bulk heterojunction suffers from a main drawback: the lack of control on the morphology of the domains. Since the exciton must reach the donor-acceptor interface to split, it is important to ensure that exciton migration to the interface is highly probable within the lifetime of the exciton. Therefore, the average distance between any location in the donor or acceptor domain to the interface must be shorter than the diffusion length of the exciton. Moreover, the donor and acceptor domains must be connected and continuously connected to the cathode and anode, respectively. The optimal structure to achieve this goal is an interdigitated bulk heterojunction with average donor-acceptor domain distance of about the exciton diffusion length which is generally less than $10nm$. This requires an accurate control of the blend morphology that can be achieved by phase segregation using specific solvent mixtures [26, 27], annealing and drying or in a controlled way by using self organized donor-acceptor molecules[28, 29, 30, 31].
Note that the ideal interdigitated bulk heterojunction obtained by self-assembling has not yet proven to be more efficient than the standard bulk heterojunction, and usually obtains less than 2% power conversion efficiencies.

Finally, once the morphology of the active layer is optimal, the solar cell can be further improved by structuration of the top electrode to concentrate the sun light or to actively orient the cell in the direction of sun, or by stacking different active materials in a tandem solar cell to exploit all the solar spectrum. Note that tandem cells needs accurate optmization, not only on the active layer design but also on the sub-cells energetics and thickness.

In this thesis, we focus on the bulk heterojunction solar cells made of a small molecule donor blended with a commonly used acceptor.

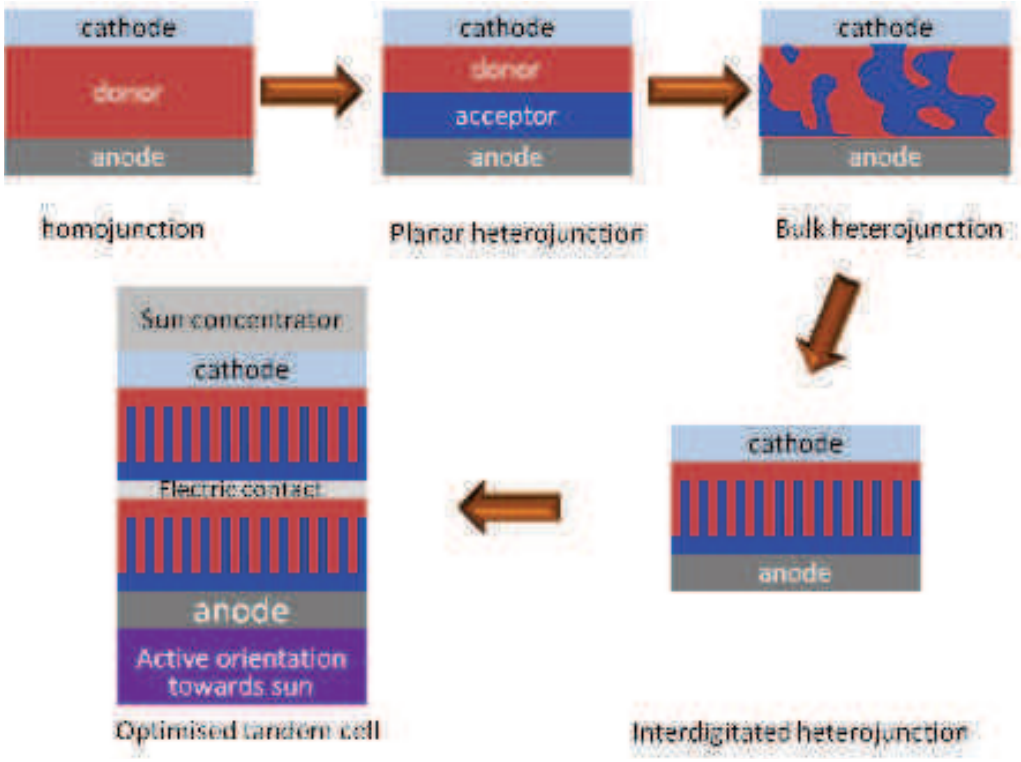

Figure 3.5.: Different architectures for OSC, showing the evolution of the active layer technology to improve the efficiency of OSC. Note that the interdigitated heterojunction is hardly never achieved and usually gives poor solar cell efficiency.

3.4. Principle of heterojunctions

In organic donor acceptor heterojunction, the difference in the HOMO and the LUMO energy levels of the donor and acceptor molecules is used to split the exciton and later collect the resulting separated charges to create an electric current. This is done through a succession of photophysical steps, the yield of which gives the overall efficiency of the solar cell [32].

The primary event is the absorption of a photon by a molecule in the donor domain (the scheme is symetric for an excitation of an acceptor molecule). Excitation of the donor will produce an exciton that may either diffuse to the donor-acceptor interface within its lifetime or de-excites which is a detrimental process for the OSC efficiency.

Once the exciton reaches the donor-acceptor interface, an electron transfer is likely to happen due to the available lower energy states for the electron in the acceptor close enough neighbours. The resulting state consists in a coulombically bound interfacial electron-hole pair, referred as charge transfer (CT) states. These states can either recombine, leading to geminate recombination or overcome the Coulomb interaction and lead to separated charges (charge separated (CS) states).
The free charges can move in their respective domains and reach the collecting electrodes, leading to a current or recombine if they interact with a neighbouring opposite charge close to the interface, which is called non geminate recombination since the charges may originate from different excitons.
These stages are summarised in the scheme in figure 3.6.

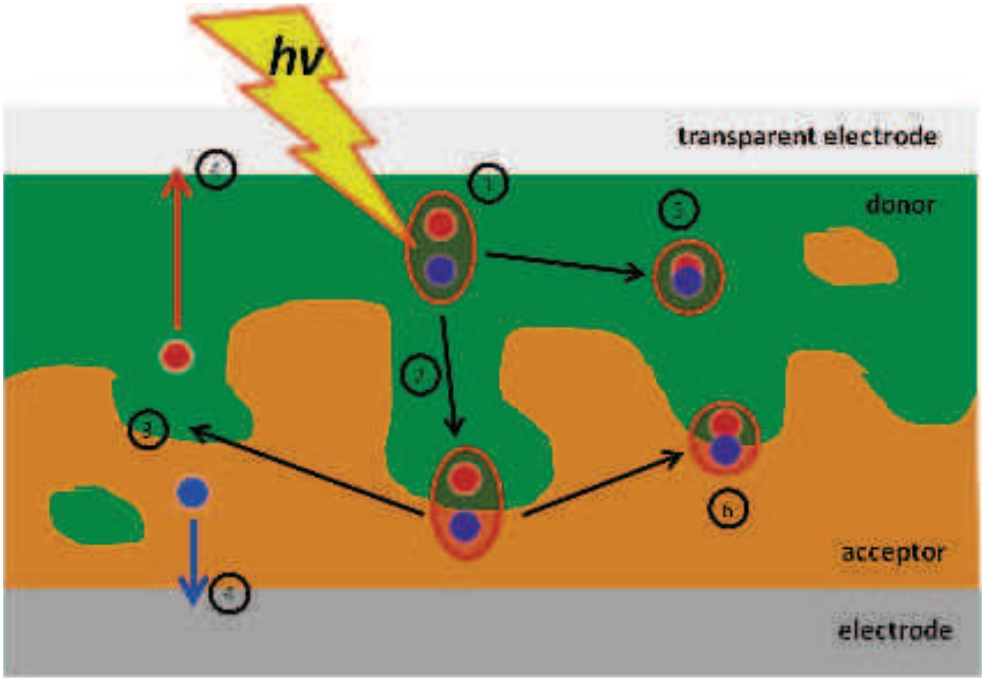

Figure 3.6.: Principle of a bulk heterojunction organic solar cell. (1) exciton generation from an absorbed photon. (2) exciton diffusion to the interface. (3) interfacial CT state separation. (4) free charges diffusion to the electrodes. (5) exciton recombination. (6) CT state geminate recombination.

3.4.1. Exciton Generation

Absorption of a photon in an organic solid state material creates excitons. The lifetime of excitons is determined by the rate of depopulation pathways. The expected loss pathway, favorable to OSC yield is the formation of free charges from charge transfer states, *i.e.* charge transfer to an acceptor which occurs typically on timescales going from less than $100fs$ to some hundreds of picoseconds. However the charge transfer requires the proximity of an acceptor with sufficient overlap with the electron wavefunction. Other processes occuring are internal conversion (radiationless desexcitation, typically picosecond timescale or slower), spontaneous emission (fluorescence, radiative desexcitation, typically nanosecond timescale or slower), intersystem crossing (triplet formation, typically picosecond timescale or slower).
Since the typical timescales needed for charge transfer is shorter or comparable to the other processes, its rate should be higher or comparable, and thus is not the limiting process. However the exciton may be generated in a pure donor domain, thus it is not likely to have an acceptor close by. This would give raise to different excitonic populations. The first one, formed away from the interface which would be quenched by any available quenching pathway but charge transfer. The second one, generated sufficiently close to the interface and quenched by all available depopulation pathways, mainly electron transfer.

Thus, to be efficient for charge generation, the organic material used should have all detrimental pathways slower than the time needed for the exciton to cover the distance to the closest acceptor, which depends on its mobility and on the morphology of the active layer. The splitting of the exciton requires to overcome its binding energy, which is in the order of magnitude of 1eV (0.3 eV is a commonly used value for exciton binding energy).

3.4.2. Charge Transfer States and Geminate Recombination

Charge transfer states are bound electron-hole pairs where each charge is in a different molecule. These states are necessarily located at an in-

terface between donor and acceptor, and are the precursors of separated charges. A charge transfer (CT) state consists in spatially separated charges at the donor-acceptor interface but still interacting through coulombic attraction. The associated binding energy is generally reported to be lower than 1eV. CT states are formed after charge transfer from an exciton, and occurs in the sub 100fs to picosecond timescale. CT states can be formed from excitons by direct electron transfer or *via* energy transfer followed by hole transfer (case of excitons in the acceptor).
The charge transfer from the exciton to the CT state is efficient only if the energy of the latter state is lower than the former. In case the exciton has excess energy, the electron transfer may lead to high energy CT states. The excess energy in CT states may help in avercoming the Coulomb interaction between electron and hole.
CT states are not distinguishable spectroscopically from charge separated (CS) states where the two charges does not interact any more. Charge transfer at the donor-acceptor interface may directly produce free charges, however this phenomenon can be seen as a fast quenching of the CT state population by charge separation. CT states may thus be defined as an interfacial bound electron hole pair, precursor of free charges and formed after charge transfer between donor and acceptor organic molecules.

Marcus theory for charge transfer The charge transfer process has been investigated theoritically by Marcus, which predicts the rate of electron transfer:

$$k_{et} = \frac{2\pi}{\hbar\sqrt{4\pi\lambda k_B T}} V^2 \exp\frac{-(\Delta G^0 + \lambda)^2}{4\lambda k_B T} \tag{3.1}$$

$$V^2 = |\langle \Psi_{reactant}|H|\Psi_{product}\rangle|^2 = V_0^2 \exp(-\beta r) \tag{3.2}$$

where V^2 is the electronic coupling matrix element, V_0^2 being the maximum coupling, β approximates the vanishing wavefunction and r is the intermolecular distance. ΔG^0 is the energy difference between the initial (reactant, *i.e.* exciton) and final (product, *i.e.* CT state) states vibrationnally relaxed and λ is the reorganization energy, meaning the energy necessary to place the product in the reaction coordinates con-

figuration of the vibrationnally relaxed reactant state. The exponential term and the prefactor reflects the overlap of wavefunctions of oscillators sharing the same frequency in the reactant and product state, described classically. This formula is relevant for ambient temperatures but may be replaced by its quantum version for low temperatures, to allow for tunnelling through the energy barrier. Both formula does not account for out of equilibrium charge transfer where the reactant is not vibrationnally relaxed. It may be implemented by considering a distribution of vibrationnal modes in the reactant electronic state and summing over the latter states. In addition, the molecular parameters necessary to estimate the rate of electron transfer are often not directly experimentally accessible, except for ΔG^0.
However the Marcus theory emphasizes on the key parameters for efficient charge transfer: sufficient proximity of molecules for increased interactions and availability of states in the product state.

As said previously, the CT states generated from excitons are the precursors of free charges. To separate electron and hole in CT states, overcoming the Coulomb interaction between both charges is necessary. Since the dielectric constant of organic materials is much lower than in inorganic semiconductors, thus electron and hole are strongly interacting and the Coulombic interaction energy is much higher than thermal energy available in the system. If the charges can not escape each other within the CT state lifetime, it will recombine. This phenomenon is called geminate recombination, since the charge pair recombining were produced by the same exciton.

Onsager model and charge separation Assuming a localized electron-hole pair, where the mobile electron evolves in the potential generated by the hole, Onsager defines a capture radius r_c defining the distance of the electron from the hole at which the electron can escape the potential in a thermally assisted way:

$$r_c = \frac{e^2}{4\pi\epsilon_r\epsilon_0 k_B T} \tag{3.3}$$

In the presence of an external electric field E, the escape probability of an electron at a distance r from the hole can be approximated in the case of low electric fields by:

$$P(r, E) = (1 + \frac{er_c}{2k_BT}E) \exp \frac{-r_c}{r} \tag{3.4}$$

More accurate models suchs as Onsager-Braun including the lifetime of the CT state and even further the heterogeneity of electron-hole distances at donor-acceptor interfaces have also been developped, however, these models requires knowledge on the nanomorphology of the interface that can not be easyly determined experimentally.
This model shows that charge separation is facilitated by a high dielectric constant, which is the case in inorganic semiconductors, by the distance between electron and hole and by electric field. These parameters depend strongly on the morphology of the interface at molecular level.

Charge transfer states Finally, CT states are defined in this report as interfacial states, characterized by an average electron-hole distance corresponding to the capture radius through Coulomb interaction. Escaping the typical Coulomb capture radius corresponds to the formation of free charges. In the case of hot electron transfer from unrelaxed excitons, the residence time in the CT states may be short. On the other hand, thermally assisted charge separation from low energy CT states may occur on longer timescales. This scheme is depicted in figure 3.7 [33, 34, 35].
CT states production and separation/recombination depends on many parameters, such as the materials used and more specificly the energetics and structure of these materials, the nanomorphology of the donor acceptor interface, the excess energy with which they are produced, the influence of electric fields, ... [35, 32]. Note that CT states may also be populated by non geminate recombination.

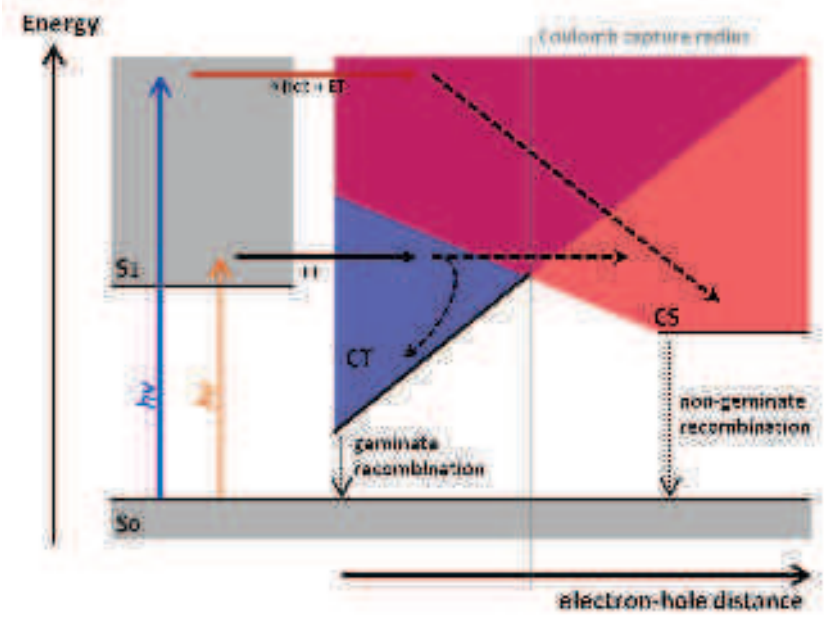

Figure 3.7.: Scheme presenting the energetics of CT states and the corresponding charge separation and charge recombination phenomena, in the case of an electron transfer from excitons with excess energy, and relaxed excitons. The formation of CT states through hot exciton electron transfer is unlikely to end up as a trapped CT state due to the excess of energy. On the other hand, low excess energy may lead to significant free charge generation due to geminate recombination.

3.4.3. Charge Separated States, Non-Geminate Recombination and transport

The splitting of the excitons through CT states produces loosly bound charge carriers, a polaron pair of opposite charges with almost no interaction. These free charges can diffuse in the respective domains and are transported to the electrodes. Since the polarons are charged species, they are accelerated by electric fields, in particular by the built in field due to the difference between the two electrodes wavefunction. As a result, the negative polarons are accelerated to the anode and the positive charges to the cathode (generally ITO).
This transport requires the presence of a continuous domain of the same or lower energy to the electrodes. This requires that all the interfaces are connected directly to the electrodes. Otherwise, the polarons might be trapped in a domain, and would not contribute to the current pro-

duction.

Transport properties depends on the nature of the polarons [36]. Polarons localized within one molecule should be transported through hopping to the next molecules. This can be a favorable phenomenon if adjacent molecules possesses lower energy LUMO levels (in case of negative polaron transport). At some point, the polaron may be trapped in a molecule possessing the lowest local LUMO energy. In this case the transport would be thermally assisted, since the phonons may assist the hopping by providing the polaron the energy necessary to hop to higher energy LUMO molecules. The hopping process is similar to a charge transfer mechanism. Thermally assisted hopping happens in disordered materials where the distribution of LUMO levels is random.

In the case of delocalized polarons, in cristalline domains for instance, the mobility is increased. In addition, in the case of a monocrystal, the transport should be hindered by an increase of the temperature, since it may distort the crystalline lattice and scatter the polarons, much like in the conduction band of silicon. This transport is referred as polaronic transport. On the other hand, molecular mono crystals are not easy to produce by low temperature processing, expected to be used for OSC fabrication. This results in poly crystalline structures. At the interfaces between the different crystal domains, the polarons have to hop to the next crystalline domain.

Transport is limited by the occurence of polaron recombination through interaction with an opposite charge. Since the two charges are not necessarily from the same exciton fission, this recombination is qualified as non-geminate. This recombination may happen when a trapped polaron captures a polaron of opposite charge diffusing in its neighborhood, at interfaces between donor and acceptor domains.

After efficient transport to the elctrodes, the charges may be injected in the conduction band of the electrodes, resulting in the presence of a photocurrent flowing between the electrodes.

3.4.4. Overall charge generation pathway and limitations

The photocurrent generation in a single bulk heterojunction OSC have been developped in the precedent paragraphs. The overall cascade of physical processes is summarised in figure 3.8.

This scheme evidences the different favorable and detrimental physical processes occurig in an OSC. Optimisation of the charge generation should be implemented through reducing the detrimental phenomena yield.

Most of these steps happens in the active layer. As a consequence, the design of the active layer is important. Since chemistry allows to synthetise a wide range of organic molecules with versatile properties, the ressource of active material is almost unlimited. It is therefore necessary to target specificly the physics of a limiting process in order to find a solution through the design of a new molecule, or by modifying a given molecule to improve this step.

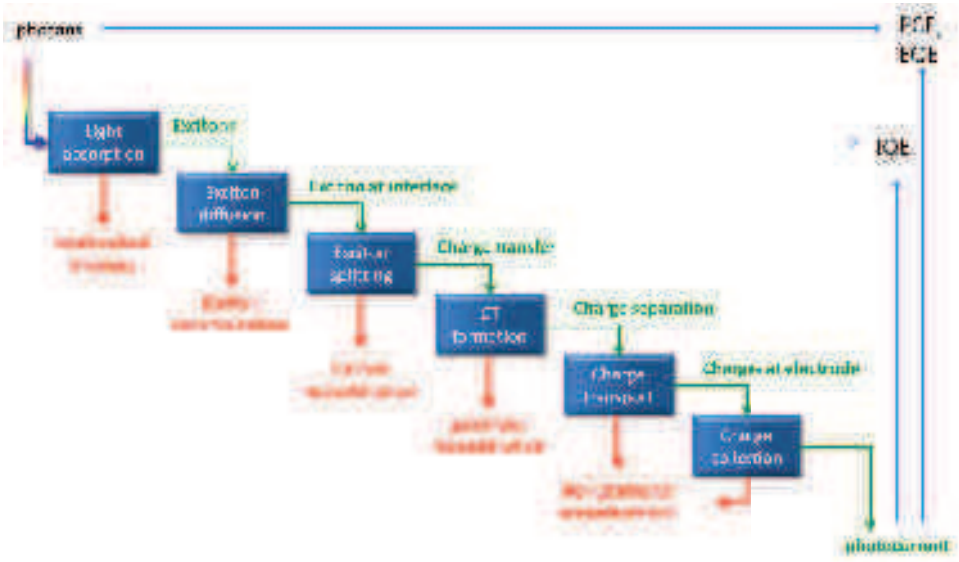

Figure 3.8.: Scheme summarising the different steps leading to the generation of a photocurrent from the sun light photons in an organic solar cell. Red indicated detrimental processes, gree favorable ones.

3.5. Good material properties

Our understanding of charge generation in single bulk heterojunction OSC allows to sketch a few required properties for the active material in oder to ensure good overall efficiency.

The first property an organic material for OPV must have is a broad absorption spectrum overlapping with sun emission spectrum measured on the ground, to absorb a wide range of photons. The absorption spectrum sould extends at the frontier with infrared light photons. This is a trade off between the photons harvesting and the maximum electronic energy one can extract from the photons (HOMO/LUMO levels). An absorption spectrum extending until approximately 800nm is optimal for a single junction cell [37].

A second important parameter is the extinction coefficient of the material. Indeed, the higher the molar absorption coefficient, the thiner can be the active layer for the same absorption. Since organic materials are not efficient conductors, it is important to minimize the path of

charges in these materials without compromising an efficient absorption of photons.

The molecules used must have the correct energetics for its application.The HOMO of the donor and LUMO of the acceptor must allow charge transfer from donor to acceptor and to the electrodes.

The blend of molecules should offer a stable morphology. In particular, the interface between donor and acceptor should be efficient for charge generation, this consists in good phase segregation, large area interface and continuous percolating pathways to the collecting electrodes. In addition, the morphology of the donor and acceptor phase should allow good transport properties, to this end, intermolecular interaction favoring delocalized charge carriers are important.

For large scale technological applications in industry, the active material should possess certain qualities in order to be efficiently produced and processed. It allows to scale up production and make it cost-effective. The organic semiconductors should be soluble in harmless and easy to use solvents. Its synthesis should be simple, environment friendly and yieldy, and use available and cheap raw materials. This allows to fabricate the active material at an affordable price, but also to fulfill one of the marketing imperatives of eco-friendly technology.

3.6. Characterization of efficiency

In order to improve the characteristics of OSC, one should have means to characterize the limiting factors reducing the overall yield of the cell, summarised in figure 3.8. An easy way to characterize the overall yield is to measure the overall efficiency of the cell. This measurement, termed as power conversion efficiency (PCE) is the ratio of the input energy on the output, thus the ratio between the electric energy available at the electrodes divided by the solar energy intercepted by the cell.

The power conversion efficiency of an OSC is limited by the absorption of the active material, since photons that are not absorbed can not be converted. On the other hand, the absorption of the donor material is linked to the difference between the HOMO and LUMO of the donor molecule. The donor HOMO and acceptor LUMO defines the maximum tension at the output of the cell. In the end, the efficiency of a single junction is limited to a little more than 30%, for optical band gaps (or equivalent) between 1 and 1.5eV. This value is predicted by the Shockley-Queisser limit [37].

To have more insight on the limitations of the material, the external quantum efficiency (EQE) can be measured. It corresponds to the number of electrons produced by the cell divided by the number of incident photons of a given energy intercepted. This measure allows to investigate the conversion by the active material regardless of the electronic properties (insensitive to the tension at the cells electrodes). More specific informations about the efficiency of the active layer may be obtained by measuring the internal quantum efficiency (IQE), which is defined by the number of produced electrons divided by the amount of absorbed photons of a given energy. This requires to finely characterize the reflected and transmitted photons. This measurement specificly characterizes the efficiency of the active material, regardless the architecture limitations of the cell. An exemple of such measurements results are presented in figure 3.9.

To characterize the electronic limitations of the cells, the current-voltage characteristic measure can be performed. The latter characteristic allows to define the maximum power point parameter, meaning the operating tension optimal to maximize the energy production. It is usually compared to the maximum available power, defined by the maximum current and tension available in the cell. The maximum tension is obtained in the absence of current through the cell, meaning that the current produced by applying the tension compensates photocurrent generated by the cell. This tension is termed as open circuit voltage V_{oc}. The maximum current is obtained in the short circuit conditions, and

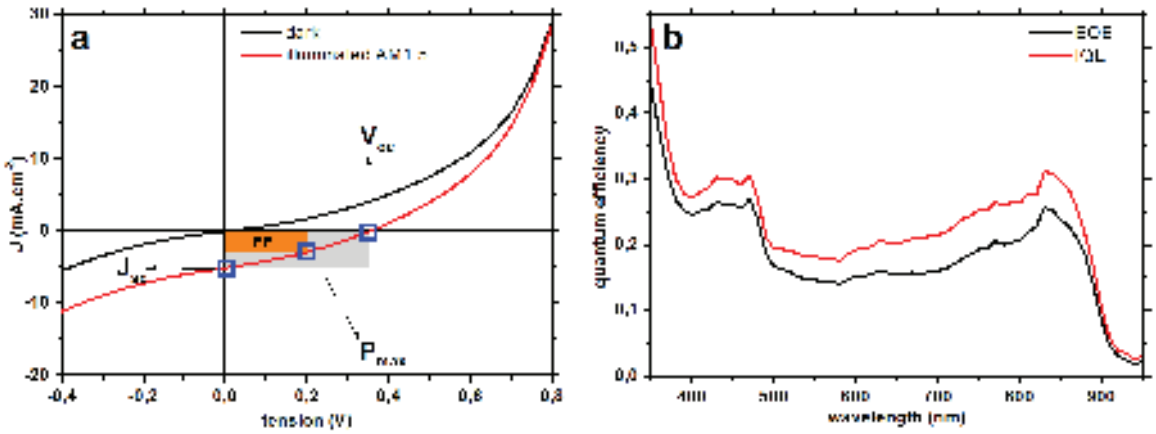

Figure 3.9.: Electronic and quantum efficiency characterizations of a thin film blend of donor and acceptor molecules, on ITO/Pedot:PSS substrate with aluminium top electrode. Panel a shows the electronic characteristics, through a current-tension plot. The maximum power point is evidenced, as well as the short circuit current and open circuit voltage. Panel b shows the EQE and IQE curves for this device. The power conversion efficiency for this device is 0.6% and the fill factor is 32%. The fill factor corresponds to the ratio of the areas of the orange rectangle over the white one.

is referred to as short circuit current J_{sc}. Comparison of the maximum power point conditions with the V_{oc} and J_{sc} product is the fill factor FF, defined as:

$$FF = \frac{P_{max}}{V_{oc} \times J_{sc}}$$

It is a measure of the ideality of the electronic characteristic.These characteristic points are displayed in figure 3.9.

The limitations by specific phenomena may influence differently the characteristic parameters measured on the solar cell. The open circuit voltage depends on the average values of the donor molecule HOMO and acceptor LUMO, but also on the quality of the contacts at the electrode. The CT states energetics may also influence its value. The short circuit current is an indication of the charge generation efficiency and its limitations, such as charge recombination, charge mobility and charge collection at the electrodes. The charge mobility may influence both the V_{oc} and J_{sc}.

The electronic current/voltage and opto-electronic quantum efficiencies measurements are easy to process and gives information about the limiting factors in an OSC, *in situ*. However, many different parameters may influence the characteristic values measured by these techniques, so that it might be difficult to sort out which is the most detrimental of all limitations. These measurements on working solar cells can be completed by investigations of the active material in organic field effect transistors, which allows to measure accurately the charge carriers mobilites for instance. However, the morphology of the active layer, when processed as a FET, might be different, leading to biased results.
In particular, the charge generation processes and the recombination can not be probed directly with these methods since these phenomena occurs in the sub nanosecond timescale.

3.7. Key role of CT states and issues

The CT states are the central states in the photochemical cascade leading to photocurrent production. Indeed, the CT states are directly correlated to the photogeneration of charges as a precursor of it. Excitons are not the relevant species to account for charge photogeneration since the photoluminescence quenching is often not correlated to the charge generation [38, 32]. However, as a relay to charge separated species, the CT state population reflects the exciton quenching by electron transfer, and is depopulated through geminate recombination and charge generation. The CT state population thus lies at the core of charge generation. The evolution of its population is an indicator of the quality of the exciton quenching as well as the yield of free charge generation (or recombination).

Direct and indirect observations of the CT states as well as simulations helps in understanding it, however the conclusions about the physical processes limiting its formation and dissociation are still unclear, and general results may be difficult to obtain due to the diversity of materials used in OSC, resulting in very different scenarios.

In particular, transient spectroscopies have proven to allow the observation of the CT states populations. Even though the ability to describe the physics limiting charge generation relies on systematic studies, transient absorption may be a simple way to check the efficiency of the first steps of the photogeneration, giving direct evidence for losses through poor exciton quenching or excessive CT state recombination.

The main concerns about the physics of CT states are the role of the excess energy in excitons and CT states on charge separation [39, 40] and issues about the role of energetics and morphology at the donor-acceptor interface on CT state dissociation [34, 41, 33].

In this work, we use transient spectroscopies to investigate the photogeneration of charges in a recently synthetised small molecule for OPV[42]. Small molecules have recently been gathering interest due to their better organisation in films [43, 44, 45, 46], in comparison to polymers. Even though the overall efficiency of small molecules is commonly studied by electronic characterization, very few studies of the photophysics of CT states through transient spectroscopies have been performed.
This characterization, through the observation of the CT states dynamics is expected to enlight the nature of the losses lowering the overall efficiency OSC using this donor small molecule. This may help in targeting the major limiting factor in order to improve it.
This work is part of the fundamental physics contribution in the regional european project Interreg IV Rh(e)in Solar. This project involves public and industrial partners in the domains of physics, chemistry and ingeneering from Switzerland, Germany and France.

4. Investigation of the photochemistry of TB2 blended with PCBM

As said previously, CT states lies in the core of the OSC function. The study of CT states in small molecule bulk heterojunction using transient absorption allows to characterize the CT states dynamics and its link with the molecule properties and with the blend nanostructure. As the CT state formation and lifetime is closely linked with the structure and thus with the nature of the used small molecule, it may not always be possible to generalize the observations made with a given set of molecules. We propose here to study a bulk heterojunction made of a dye derivated small molecule donor with a standard acceptor, PCBM ([6,6]-phenyl-C61-butyric acid methyl ester).

To this end, one must characterize both molecules alone in the condensed phase, to determine the photochemistry of excitons. PCBM has been extensively studied [47, 48, 49] because of its wide use as an acceptor, and more specifically in the reference poly-3-hexyl thiophene (P3HT)/PCBM polymer solar cells.
On the other hand, this BODIPY (boron dipyrromethene) derivative donor molecule has not yet been investigated through transient spectroscopies. Transient absorption helps in unrevealing the spectral signatures of excitons in the donor, and transient fluorescence techniques the associated excited state lifetimes. In addition, in order to understand the charge generation process, the charged species associated to the donor molecules are spectrally characterized using spectroelectrochemistry.
Finally, this investigation of pristine films will help in understanding the charge generation in blends.

Bulk heterojunctions of the latter molecules are studied. We pro-

pose here to reduce the problem by studying thin films of blends of the molecules, to avoid experimental issues due to the presence of electrode layers. In particular, the top, non transparent electrode prevents from using standard transmission pump-probe sepctroscopy. In a second time, the active layers cast on substrates similar to the ones used in OSC, to achieve more relevant experimental conditions. This is particularly important as the morphology of the active layer may be influenced by the substrate [50].

Since the characterization is not achieved *in situ*, the effect of electric field due to the polarization of the OSC is absent, as well as the charge transport and collection. Therefore, there should be no electric field assisted CT state dissociation observed. Transport and collection of photogenerated charges occurs in timescales longer than the nanosecond, thus femtosecond transient absorption spectroscopy is not the relevant experiment.
In addition, the situation studied here represents the more unfavorable conditions for charge generation since charge recombination is the only possible phenomenon. However, it allows to characterize this detrimental physical process of recombination specifically.

5. Properties of BODIPY derivative TB2

Among dye derivated organic small molecules, BODIPY derivatives are quite versatile core structures because its optical properties can easily be tailored by targeted substitutions.
The TB2 derivative of BODIPY synthetized by T.Bura showed interesting PCE of 4, 7% blended with PCBM in an ITO/PEDOT:PSS/BODIPY:PCBM/LiF/ OSC structure[42]. Its synthesis from commercial precursors is possible with yields of more than 80% in weight, making this compound a cost effective molecule for OPV.

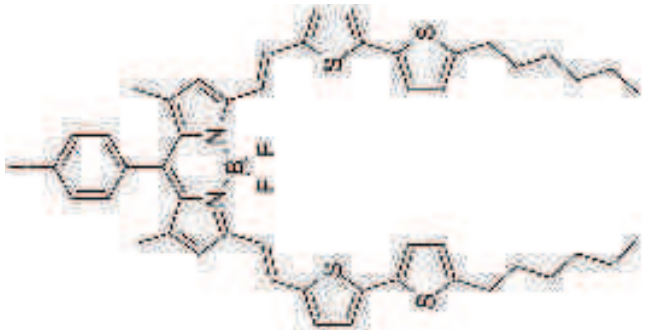

Figure 5.1.: Chemical structure of BODIPY TB2

The conjugated backbone of the molecule includes the BODIPY center and the two bi-thiophene tails, allowing in the end a good absorption in the visible range, making it appropriate for OPV applications. The top phenyl is poorly conjugated due to its orthogonal alignment (represented as planar figure 5.1). In addition, the end of the bi-thiophene units holds solubilizing chains allowing dissolution in chlorinated solvents.
TB2 has a strong molar absorption coefficient of 104000M.cm^{-1} at the absorption maximum, allowing its processing in thin film with high ab-

sorption. Its LUMO level of -3.86eV in comparison with the -4.09eV LUMO of PCBM in solution offers an energy of 0.23eV to drive the exciton splitting.

5.1. Steady state properties

Characterization of steady state absorption and fluorescence were performed on TB2. In addition, spectroelectrochemistry was used to obtain the radical ions spectra of this compound. These characterizations are done on the isolated molecule in solution as well as solid state films, and provides useful spectral characterization of the species expected to contribute to the transient absorption and fluorescence signals. Moreover, films have been studied by electron diffraction and transmission electron microscopy (TEM) to determine the nano-morphology in solid state.

5.1.1. Absorption and fluorescence

Steady state absorption of TB2 is presented in figure 5.2. It consists in two absorption bands with a molar absorption coefficient of $104000 L.mol^{-1}.cm^{-1}$ at the maximum. The main band, peaking approximately at 700nm corresponds to the transition to the first excited state ($S_0 \rightarrow S_1$ transition), and exhibits a pronounced vibrationnal structure as evidenced by the three observable transitions at 720, 660 and 610nm. The second band, located around 450nm corresponds to a transition to a higher lying excited state ($S_0 \rightarrow S_n$ transition) and also exhibits vibronic structure (445 and 380nm).

TB2 produces, in solution (chloroform) the fluorescence spectrum depicted in figure 5.2. The shape of the fluorescence spectrum does not depend on the excitation wavelength, in good agreement with excitation spectra presented in reference[42], which shows similar excitation and absorption profiles. The fluorescence obeys Kasha's rule and stands as a Stokes-shifted mirror image of the $S_0 \rightarrow S_1$ transition band with identical vibrationnal structure (at 760, 840 and 940nm), indicating fast

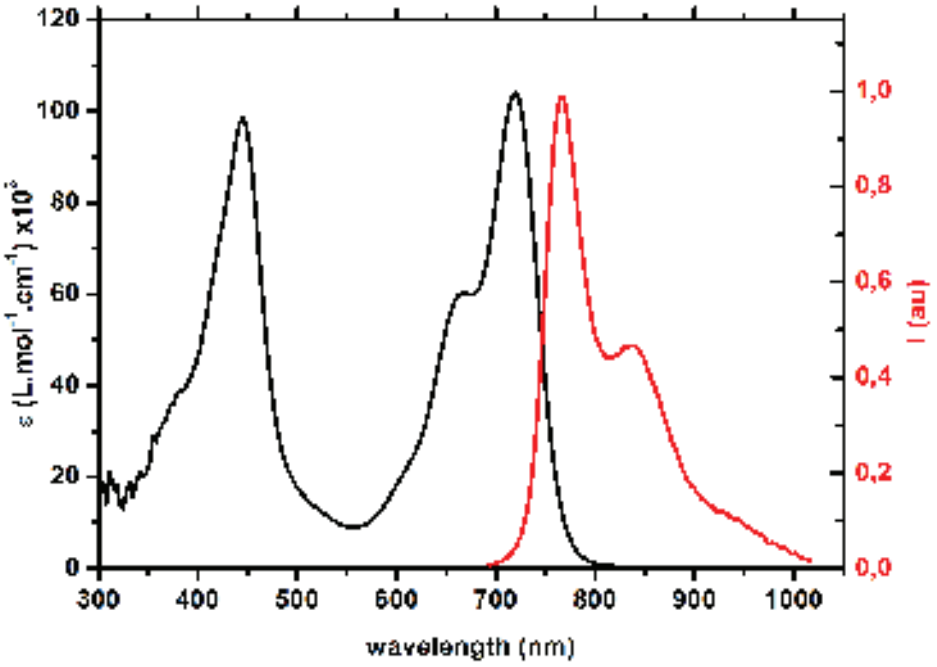

Figure 5.2.: Molar absorption spectrum (black, left scale) and normalized fluorescence spectrum (red, right scale, 600nm excitation) of TB2 in solution in chloroform.

relaxation from the Franck-Condon (FC) region to the vibrationnally relaxed excited state, and thus high radiative rate.

Theoretical determination of the radiative rate of TB2 is possible from the Strickler-Berg relationship[51] using fluorescence and absorption data:

$$k_r = 2.88 * 10^{-9} * n^2 * \frac{\int F(\nu) d\nu}{\int F(\nu) * \nu^{-3} d\nu} * \int \frac{\epsilon(\nu)}{\nu} d\nu \qquad (5.1)$$

Where n is the refractive index of the medium, $F(\nu)$ the fluorescence spectrum as a function of the wavenumber ν and $\epsilon(\nu)$ the molar absorption spectrum. This relation holds on estimating radiative rate within 20% error provided the transition is strongly allowed and that there is no significant change in the conformation of the molecule. For TB2, which has a strong molar absorption, indicative of a strongly allowed transition, this gives a radiative lifetime of 635 ± 130ps.

These properties of high molar extinction coefficient throughout the visible range makes BODIPY TB2 an appropriate absorber for use in thin film OPV cells. Its properties of emission with high radiative rate and small vibrationnal losses suggest the availability of electronic energy for charge generation. However, these properties are determined in solution while OSC are made of solid state molecules. Since solvation plays a critical role in stabilizing the excited states, it may change these properties. It is thus important to characterize the latter for TB2 in thin films.

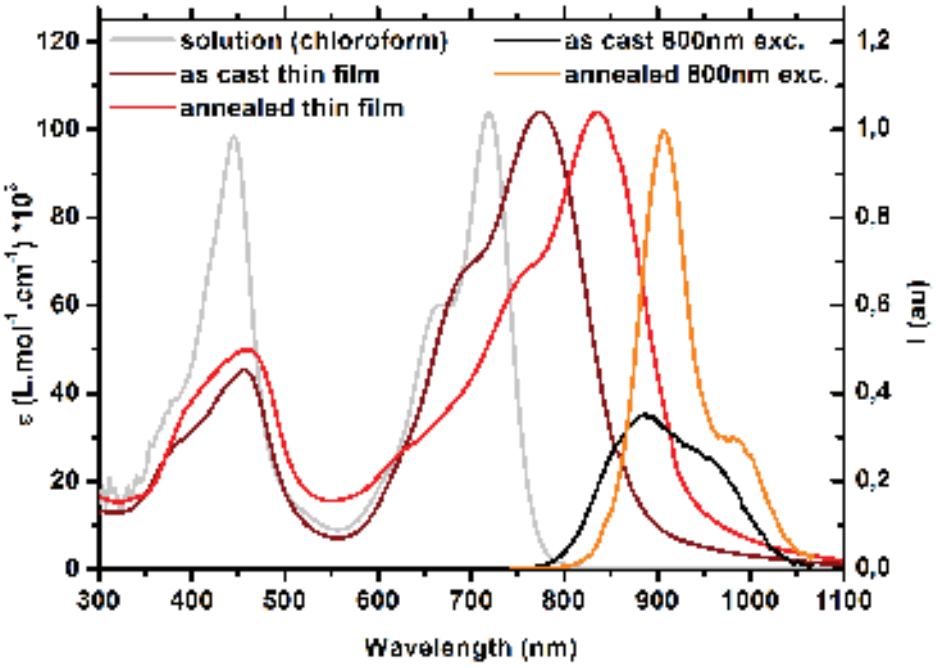

Figure 5.3.: Molar absorption spectrum of TB2 in solution, as cast in film and after 10min annealing at 110^oC (left scale) and fluorescence spectra normalised for the number of absorbed photons of as cast and annealed TB2 films excited at 800nm (right scale).

When used in a film obtained by spin-coating from a chlorobenzene solution at $20mg.ml^{-1}$ mass concentration, the absorption and fluorescence spectra significantly red shifts (absorption maximum at 775nm,

fluorescence maximum at 890nm) and broadens, as shown in figure 5.3. Upon annealing, the main absorption band further red shifts (absorption maximum at 840nm). So does the fluorescence maximum (maximum at 910nm) and it becomes sharper. This further red shift after annealing suggests a packing of the molecule *via* formation of agregates with mainly J character. This is in good agreement with single crystal X-ray diffraction data presented in figure 5.6, showing π-stacking interactions and orientation of the molecules within the crystal.

The absorption bands still contains a pronounced vibrational struture (775, 700 and 620nm for as cast film and 840, 755 and 620nm for annealed film), and so do the fluorescence bands (main band at 890nm and side band at 945nm for as cast film, and main band at 910nm and side band at 980nm for annealed film) even though the sensor sensitivity (corrected for in the emission spectra presented) does not allow efficient detection below 1050nm forbidding the observation of other vibrationnal bands. There is no noticeable change in the fluorescence spectrum upon change in the excitation wavelength.

Note that the fluorescence spectra depicted in figure 5.3 corresponds to the same number of excited molecules and thus indicates a 40% lower quantum yield for the film as cast in comparison with the annealed film (ratio of integrated fluorescence spectra). The red shifted absorption upon annealing also occurs when the films are cast on a glass/ITO/PEDOT:PSS (Poly(3,4-ethylenedioxythiophene) Polystyrene sulfonate) substrate.

In the end, BODIPY TB2 cast in thin film exhibits a strong absorption on large bands of the visible spectrum. Upon annealing, the molecules packs in J-like agregates, as inferred by the red shift in the absorption band. These properties are interesting for harvesting a maximum of visible sunlight.

5.1.2. Morphology

To go further in the characterization of TB2 thin films, they have been characterized by TEM and electron diffraction to investigate the film nanomorphology.
TEM and electron diffraction on TB2 films have been carried out by Laure Biniek, in Martin Brinkmann's team at the *Institut Charles Sadron* as part of the *Interreg IV Rh(e)in Solar* european project.

The TEM images allows to differenciate regions with different electronic density on average over the films thickness. The information is recorded on areas of typical size of tens of microns, with approximately 10nm spatial resolution.
The electron diffraction patterns gives information about the ordering in the films. This experiment probes the ordering across the film thickness and for an area of about $50\mu m^2$.

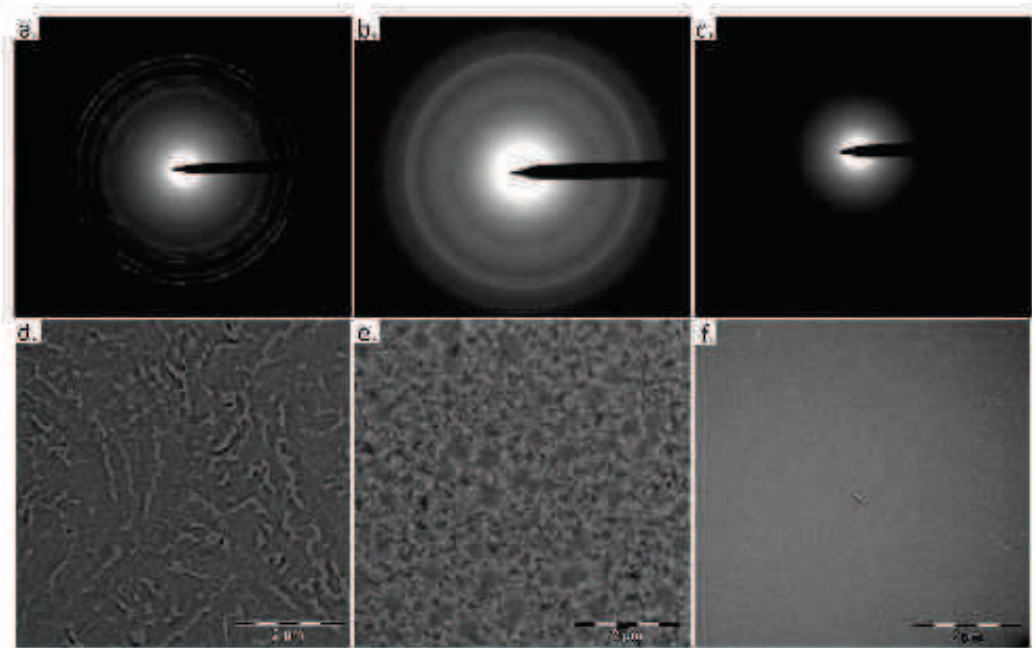

Figure 5.4.: a,b: electron diffraction pattern of annealed TB2 films on quartz and glass/ITO/PEDOT:PSS substrate respectively. c: electron diffraction pattern of TB2 film as cast on quartz substrate. d,e,f: TEM images of the respective TB2 films.

The TEM images and electron diffraction patterns presented in figure 5.4 show that as cast TB2 films are amorphous and exhibit a homogeneous morphology, as evidenced by the diffuse Scherrer ring (panel c) indicating random orientation of the molecules and the featureless homogeneous TEM image (panel f). This statement is also valid for films of TB2 as cast on glass/ITO/PEDOT:PSS substrates (not shown).

The TEM images and the electron diffraction patterns of the annealed films on either quartz or glass/ITO/PEDOT:PSS substrates are presented in the same figure. TEM images shows the presence of hundred nanometer sized crystals in the films (brighter or darker zones in panels d and e). The electron diffraction patterns (shown in panel a and b) exhibit a variety of thin rings and even preferential diffraction directions (diagonal in panel a, figure 5.4).

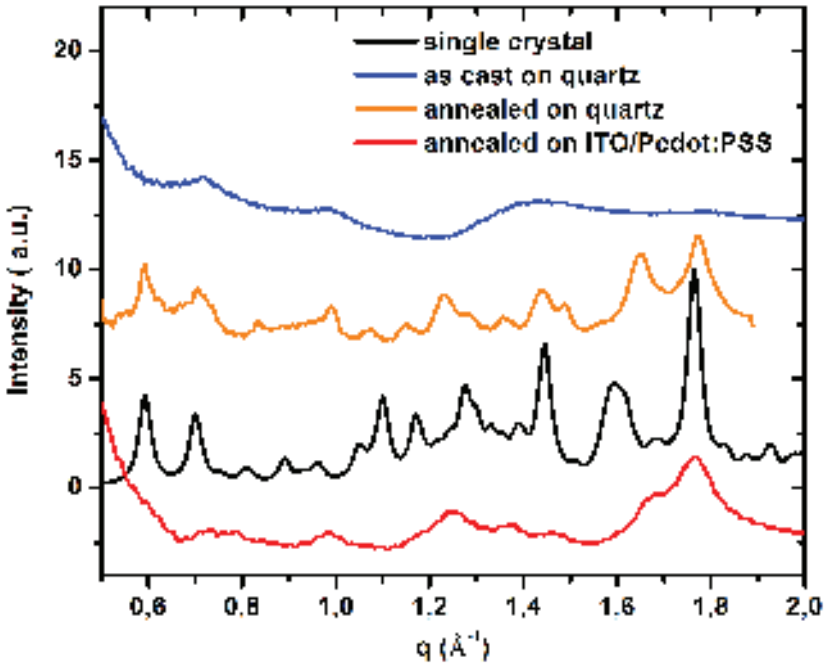

Figure 5.5.: 2D to linear electron diffraction patterns of TB2 films annealed on quartz and ITO/Pedot:PSS and as cast on quartz, together with X-ray diffraction of single TB2 crystals.

The 2D to linear scans extracted from the diffraction patterns of TB2 films as cast, annealed on quartz and annealed on ITO/Pedot:PSS are presented figure 5.5. The single crystal X-ray diffraction from reference [42] is shown for comparison (corresponds to the packing structure displayed in figure 5.6).
The as cast film exhibis hardly no diffraction peaks indicative of an amorphous phase. Upon annealing, diffraction peaks appears indicating the presene of a cristalline phase similar to the one in crystals. Annealing therefore produces cristallisation of TB2.
The annealed film on quartz is polycristalline as indicated by the sharps diffraction peaks similar to the ones obtained by X-ray diffraction. The annealed film on ITO/Pedot:PSS is less crystalline and possesses domains oriented in many directions, as indicated by the larger diffraction peaks.This point out the influence of the nature of the substrate on the film morphology. Indeed, the substrate can favor the overall cristallinity and certain orientations of the molecules due to specific interactions with the first layers of molecules.
The main diffraction peak at 1.77 $\mathring{A}^{-1}$ indicates that the π-stacking direction is parallel to the substrate.
The absence of the group of peaks at $1.6\mathring{A}^{-1}$ in the films, in comparison with the X-ray data as well as the amplification of the peak at $1.65\mathring{A}^{-1}$ indicates preferencial orientation on the substrate, although this orientation can not be determined precisely.

Some additionnal important observations have been made on as cast TB2 films. Indeed after one month of storage under argon atmosphere, in the dark and at ambient temperature, the morphology of the film evolves and tends to adopt a polycrystalline morphology very similar to annealed films. This is interesting since it points out that the aggregated form is the most stable, which makes the aggregated ordered morphology a robust one whereas the as cast films are not stable.

To conclude, as cast films of TB2 have a fine and homogeneous morphology characteristic of an amorphous phase whatever the nature of the substrate. This statement is evidenced by TEM images, electron

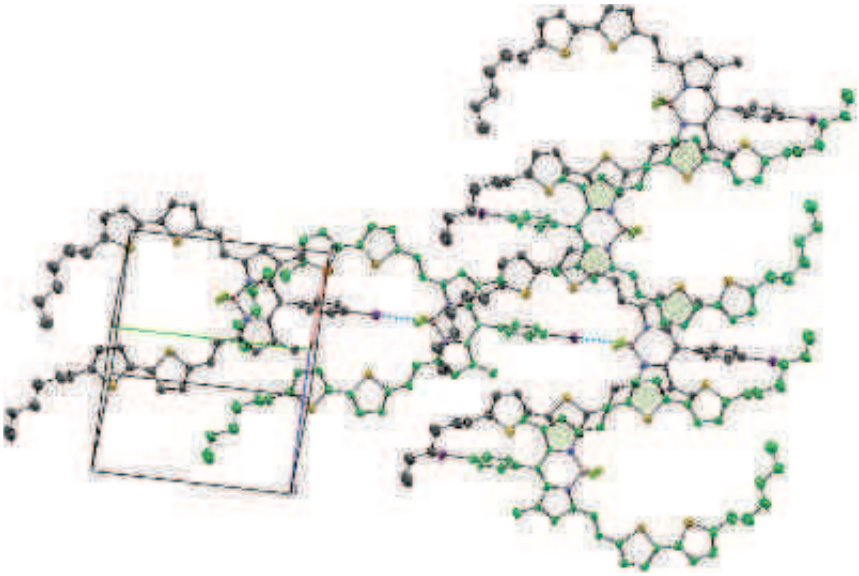

Figure 5.6.: View of the TB2 crystal packing. Dotted lines represents I/F interactions and the green areas indicates π-stacking. The molecules in the same plan share the same color. Reproduced from [42].

diffraction and steady state absorption measurement. This amorphous phase is not stable in the long term and thermal activation triggers aggregation significantly after one month. On the other hand, annealed films exhibit multicrystalline phases with typical domain size in the order of hundreds of nanometers, as evidenced by TEM images and electron diffraction patterns, and also confirmed by steady state absorption spectra showing the characteristic red shift of J-like agregates (see figure 5.3). These observations are in good agreement with single crystal X-ray diffraction indicating in-line arrangement of the TB2 molecules. The degree of order of the annealed samples is influenced by the substrate. These properties are quite interesting because agregation induces strong intermolecular interactions and favors exciton delocalization and transport properties, as well as it broadens the absorption spectrum. Since this morphology is stable, it guarantees the robustness of the thin film electro-optical properties.

5.1.3. Spectroelectrochemistry

As described previously, it is important to have as much spectral information as possible on the expected species involved in a given system when studied with transient absorption spectroscopy. Since in OPV thin films, one expect to create charges, it is important to characterize the spectra of charged species. For this purpose, two main experiments may be used: spectroelectrochemistry or charge modulation spectroscopy. While the latter requires the probed material to be in solid state, spectroelectrochemistry can be processed either in solution or in film.
Spectroelectrochemistry was used to characterize the charged species spectra of TB2 and PCBM. The experiments were run at the *Institut für Polymerchemie* in Stuttgart in S.Ludwigs team with the help of B.Omiecienski. In the first place, the measurement were achieved in solution and then carried out in films.

Principle

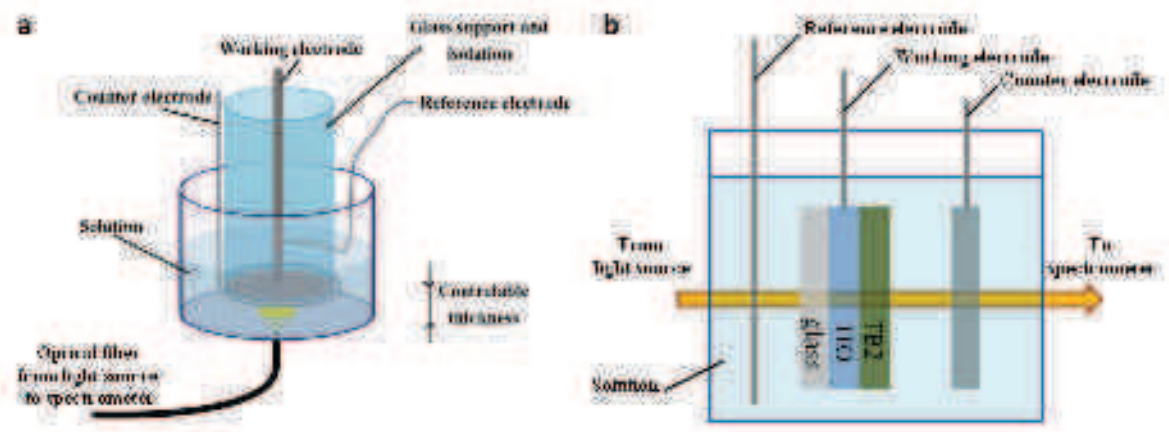

Figure 5.7.: a: Scheme of the spectroelectrochemistry setup for measurement in solution. b: Scheme of the spectroelectrochemistry setup for film measurement

The electronic part of the setup is quite similar in both experiments and consists of a galvanometer measuring the current flowing between the working and the counter electrode while the potential of the working electrode is swept and measured with respect to a reference (Calomel) electrode. In the case of a solution measurement, the working electrode

used has a significant polished planar surface which is used as a mirror for reflecting the white light beam from an optical fiber bundle. The reflected light is guided back in the fiber and analysed by a spectrometer, allowing to measure the absorption spectrum of the species in solution close to the electrode [52]. In the case of a film measurement, the film is deposited on a glass/ITO substrate. The film acts as the working electrode and the redox reaction occurs at the electrolyte/film interface. The absorption is measured through the film in transmission. The electrolyte consists in tetrabutyl ammonium hexafluorophosphate salt at $0.1 mol.L^{-1}$ concentration in a chosen solvent (here dichloromethane DCM for solution experiments). After measuring the cyclovoltammogram of the studied molecule, ferrocene is added in excess and is used to calibrate the potential.

Results

In solution, TB2 shows two reversible oxydation waves (0.38/0.59V and 0.32/0.14V) assigned to the TB2 radical cation and dication, according to previous observations. The corresponding data are displayed in figure 5.8, panels a and b.
Reduction of PCBM leads to two reversible reduction waves (-1.42/-1.81V and -1.34/-0.94V) attributed to PCBM radical anion and dianion and its corresponding spectra are shown in panels c and d.
The molar absorption spectra are scaled to the molar absorption of TB2. This scaling is possible only for TB2 oxydation since the current maxima corresponds to a full ionisation of the TB2 molecules.

The experiments carried out on films of BODIPY TB2 were not successful since the film was systematicly destroyed during experiment, leading to irreversible redox cycles. This is probably due to high solubility of the radical of the molecule in acetonitrile. Water was tested as a solvent because of its high polarity reducing the solubility of the radicals of TB2, but its reduces the spectral window for the absorption measurement since water absorbs in the near infrared (wavelengths >1300nm). However, redox cycles were still not reversible.
A reduction wave is nevertheless obtained (inset in panel b, figure 5.9).

The difference of the absorption spectrum for no bias (0V) from the absorption spectrum measured in the reduction slope for a potential of 0.98V gives the difference spectrum plotted in figure 5.9, panel b. It reflects the depopulation of the ground state population that formed radicals when the potential is increased. Substraction of the groud state absorption from the difference spectrum gives the absorption of the cation and is displayed. Note the difference spectrum like feature in the latter spectrum that may be due to a Stark shift of the groud state absorption due to the electric field present in the film.

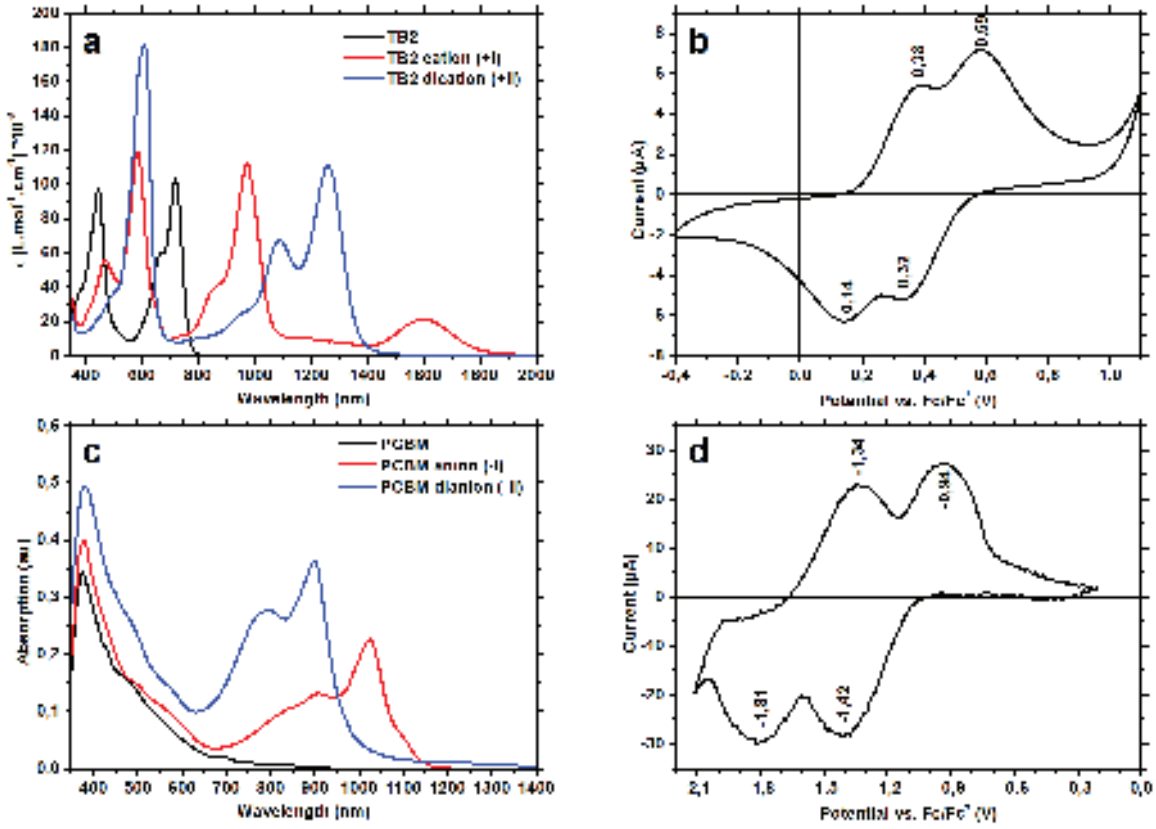

Figure 5.8.: Cyclovoltammograms (right column) as a function of the potential versus ferrocene and spectra (left column) of radicals of TB2 and PCBM in solution in DCM. Oxydation of TB2 (panels a and b): Molar absorption of the neutral, radical cation and radical dication form of TB2. Reduction of PCBM (panels c and d): Absorption of the neutral, radical anion and radical dianion form of PCBM.

Another way to determine the charged species spectra in film is to extrapolate it from solution absorption spectra. Since as cast TB2 in film is amorphous, molecules in the film are randomly oriented as in solution. Going from solution to film is thus merely a change in the properties of the environment. The main observable change is a red shift of absorption bands due mainly to a change in the electrostatic environment (dielectric constant). By shifting in energy the absorption spectra measured in solution, one may approximate the spectra in film. The solvationnal shift applied is assued to be the difference between the energy of the maximum of the main $S_0 \rightarrow S_1$ transition of the neutral TB2 in solution and in film. The obtained spectra are an approximation of the charged species absorption in a film of randomly oriented molecules. As can be seen in figure 5.9 by comparing the shifted steady state absorption spectrum measured in solution with the absorption of the film as cast, the absorption bands of the cation should be larger since no broadening of the vibronic transitions is accounted for in this extrapolation.

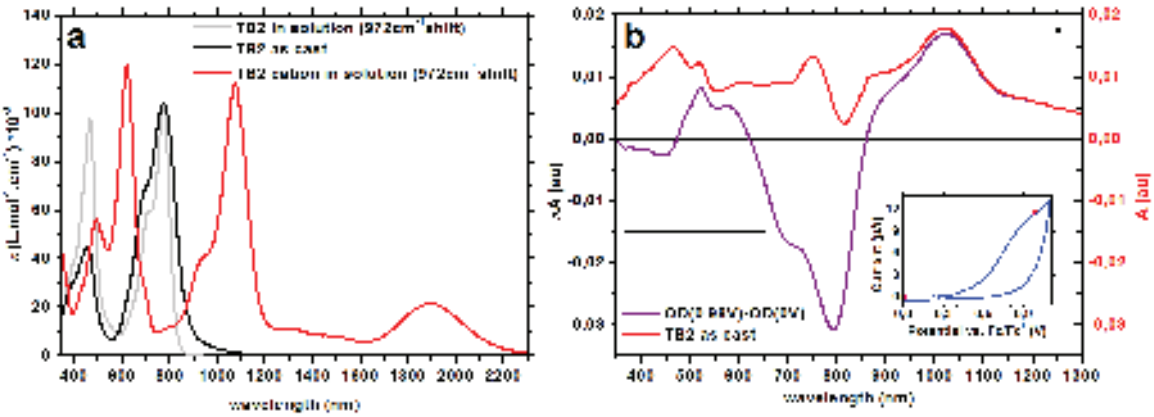

Figure 5.9.: Energy red shifted (972cm^{-1}) molar absorption spectra of TB2 and TB2 cation in solution in panel a. The molar absorption spectrum of TB2 as cast in film is shown to evidence the spectral broadening. Panel b shows the cation minus neutral TB2 difference absorption obtained from spectroelectrochemistry. The inset shows the corresponding points used in the cyclovoltammogram. A temptative substraction of the ground state absorption contribution is also displayed.

The radical cation spectra of TB2 obtained by either methods de-

scribed before shares the same spectral features.The main features of TB2 cations in film are its absorption band in the near infrared with maximum peaking at 1020-1080nm, as well as an other pronounced absorption band located at wavelengths below 600nm. These characteristic features of BODIPY cation are helpful to identify the presence of positive charges located on TB2 in the transient absorption data, since this specie is expected to be formed in the photocurrent generation process in OSC.

5.2. Photochemistry of BODIPY

This part focuses mainly on the photochemistry of the TB2 molecule. This study allows to indentify the excited states of BODIPY as well as its natural depopulation pathways. In a first time, TB2 is studied in solution to obtain the photochemistry of isolated molecules at room temperature. Later, TB2 photochemistry is studied in films, to observe the photochemistry of the molecule in similar conditions than in an OSC. This allows to see the influence of the intermolecular interactions evidence by steady state absorption and fluorescence measurements. This allows to obtain the excited state spectra in film as well as to identify new excited state depopulation pathways due to intermolecular interactions.

5.2.1. Isolated in solution

TB2 is soluble in a variety of chlorinated solvents. To study its photochemistry as an isolated molecule, TB2 is dissolved in chloroform. Solutions of TB2 with OD of approximately 0.3 at the absorption maximum through 1mm are circulated in a flow cell with a peristaltic pump and appropriate solvent resistant tubings. The excitation was at 600nm in the $S_0 \rightarrow S_1$ absorption band, with an intensity of approximately 100μW, in a regime of linear response. The pump and probe beams are linearly polarized, and the pump-probe polarization angle is of magic angle to

cancel any contribution from the rotationnal motion of the molecules in solution. Note that the transient fluorescence signal is measured in a direction orthogonal to the pump beam, through an analyser oriented at magic angle with respect to the pump polarization.
The combination of pump-probe and streak camera measurements allows to decifer the transient spectra and understand the photochemistry of this compound.

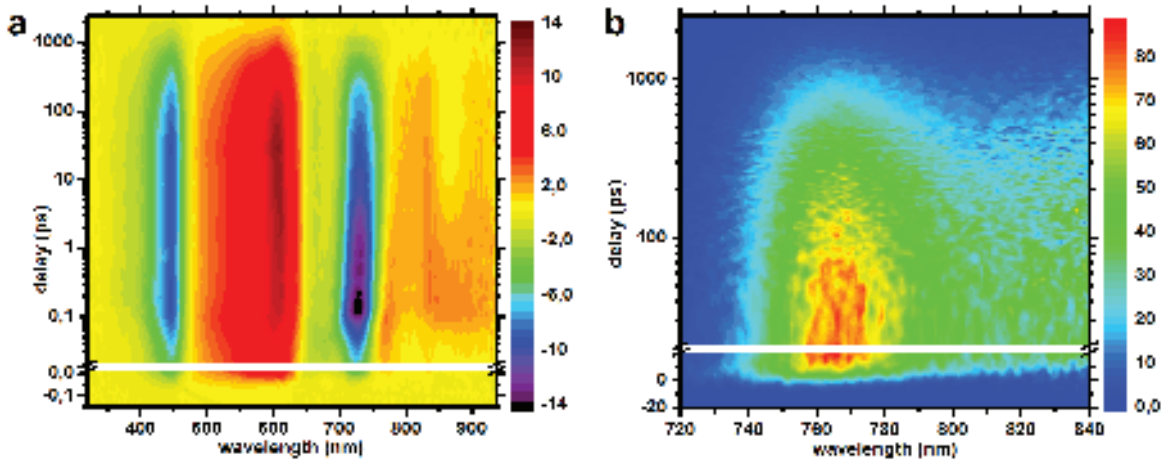

Figure 5.10.: Transient absorption (left) and fluorescence (right) data of TB2 excited at 600nm.

After data processing described in section 2.3, the TA and TF maps shown in figure 5.10 are obtained. The TF data shows two vibronic bands peaking at 770 and 840nm in good agreement with the structured steady state fluorescence spectrum. The fluorescence signal decays in less than a nanosecond, indicating a long lived excited state.The TA data shows mainly the formation after excitation of an excited state characterized by an induced absorption peaking at 605nm with weaker contributions in the 800-950nm range along with a ground state bleaching of the $S_0 \rightarrow S_1$ and $S_0 \rightarrow S_2$ absorption bands peaking at respectively 450 and 730nm. The main contributions decay within the nanosecond timescale.

The transient fluorescence experiment probes exclusively the excited state of the TB2 molecule. Spectral cuts of the TF data are presented

in figure 5.11, panel b. The first hundred picoseconds are characterized by slight spectral shifts of the main emission band at 760nm. In the same timescale, the relative amplitudes of the 760nm and 830nm emission bands changes. On longer timescales, the fluorescence decays bi exponentially with 200 and 800ps time constants (kinetic trace in figure 5.12 panel b). The overall decay occurs in 660ps (sum of the two decays weighted by their relative amplitudes).
The excited state of TB2 in solution is thus characterized by vibrational relaxations in the first hundred picoseconds. The excited state population decays in 660ps.

The transient absorption data probes all the species possessing a transition dipole moment in the spectral range. The transient spectra are presented in the panel a of figure 5.11. The difference spectra contains the characteristic negative contributions from ground state bleaching at the location of the $S_0 \rightarrow S_1$ and $S_0 \rightarrow S_2$ absorption bands at 450 and 720nm, indicating the depopulation of the groud state. A negative stimulated emission (SE) contribution is expected in the 740 to 1000nm region, as it corresponds to the region of steady state fluorescence and that fluorescence emission occurs on the probed timescales. It is probably overlapping with the induced absorption of the corresponding excited state. An induced absorption due to the excited state is dominating in the 500 to 650nm region, together with weaker induced absorption signals in the 780 to 950nm region. These features are characteristic of BODIPY derivatives [53, 54], and indeed suggests an overlap of the SE signal with ESA in the infrared region.
The evolution of the difference spectra shows spectral shifts in the 550-900nm region in the first picoseconds, indicating vibrational relaxation of the excited state of TB2. These relaxations are observed in the ESA and SE dominated kinetics presented in figure 5.12 and appears as growth/decays in the first 10ps. Note the presence of a hundred femtosecond decay of the latter kinetics attributed to the relaxation from the Franck-Condon region. Later, the excited state population decays mono exponentially with no evidence for photoproducts, since the ground state bleaching decays in the same way and shows no remaining bleach for long

delays within the present signal to noise ratio. The excited state decay occurs in 790±18ps (average of the time constants fitted for the decay of the kinetics plotted in figure 5.12).

There is a discrepancy between the mono-exponential deay of the excited state population measured by TA in comparison with the bi-exponential decay on the case of TF. Note that the longer lifetime fitted in TF data of 800ps is in good agreement with the lifetime obtained by TA of 790ps, in regard with the time resolution of the TF experiment (25ps in this time range). The 200ps time constant, observed only in the transient fluorescence experiment is attributed to anisotropy effects, in regard with the 90^o detection of the fluorescence signal. Indeed, in this configuration, the magic angle between the pump and the analyser in the detection arm does not allow the complete correction of the rotationnal motion contribution.

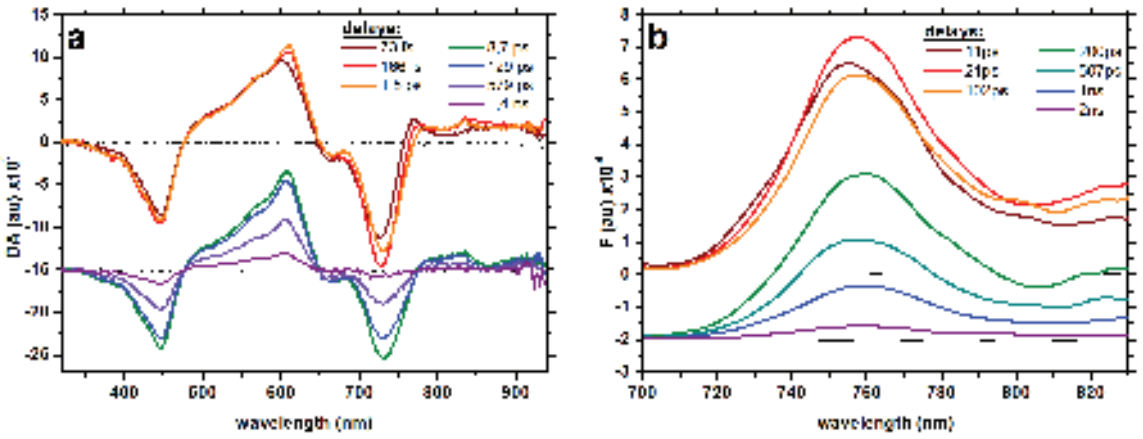

Figure 5.11.: TA difference spectra (a) and TF spectra (b) of TB2 in chloroform excited at 600nm for different time delays after excitation. Delays are indicated on the graphs.

Global analysis of the TA and TF data is performed and is summarized in the plots in figure 5.14. The three singular kinetic traces (two in the case of TF data) obtained by SVD and necessary to reproduce accurately the data set are kept and fitted optimally with four time con-

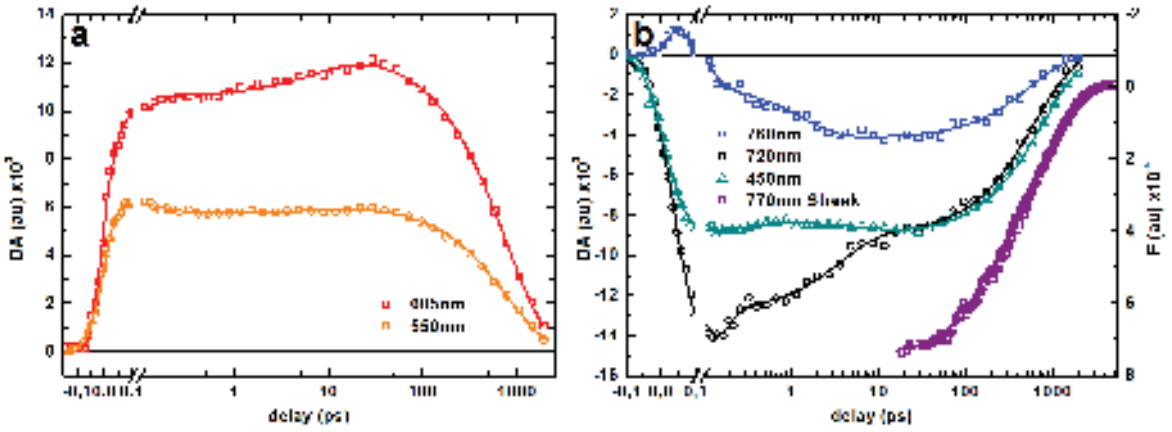

Figure 5.12.: Transient kinetics of TB2 in chloroform. The transients in panel a reflects mainly the ESA. Panel b displays the kinetics of SE and GSB, together with a transient fluorescence kinetic for coparison. The raw kinetics traces are plotted together with multi exponential fits (lines).

stants (three for TF data) of 30fs (within the 48fs fitted IRF), 100fs, 6ps and 740ps (2ps —within the 10ps time resolution—, 150ps and 780ps for TF data).
The DADS corresponding to the sub IRF lifetime in TA data is attributed to coherent artifact contributions from the molecule (Raman scattering, ...) and imperfect chirp correction. Its amplitude is irrelevant since the kinetic is within the IRF and thus unresolved (the same holds for the sub IRF 2ps DAS from TF data).
The 740ps DADS and the 780ps DAS (panels b and d) corresponds to the decay of the relaxed excited state characterized by the ESA, GSB and SE spectral features.
The 100fs DADS is attributed to the vibrational relaxation of the excited state out of the Franck-Condon region. The 6ps DADS and 2ps DAS corresponds to the vibrational relaxation of the excited state (panels a and c).

The combination of TF and TA experiments shows that the photochemistry of TB2 in solution is dominated by the excited state dynamics. The absence of photoproduct indicates that the relaxation of the excited state occurs through radiative desexcitation and internal conversion.

The radiative lifetime of TB2 has been estimated from the Strickler Berg equation in section 5.1.1 to be 635±120ps which is significantly lower than the 740-780ps lifetime of the excited state estimated from the global fit of TF and TA data. This points out the limitations of the Strickler Berg method. This might be due to the 6ps vibrational relaxation of the excited state that may correspond to a significant change in the TB2 geometry, violating the hypothesis for the use of the latter equation.
The long fluorescence lifetime of TB2 indicates low internal conversion rate and thus a high quantum yield. This is suprising on the view of the 7.5% fluorescence quantum yield reported for this moelcule (see supplementary information of reference [42]). However, the measurements presented here are carried out in a different solvent, which may explain this apparent discrepancy.

Figure 5.13.: Reaction scheme describing TB2 photochemistry in solution in chloroform upon 600nm excitation. Dotted arrows indicates vibrationnal relaxations, plain arrows electronic transitions.

The photochemistry of isolated TB2 in chloroform is summarised in figure 5.13. The long fluorescence lifetime of TB2 indicates that the excitation photon energy is converted into electronic energy available during 740-780ps.

5.2.2. In film as cast

When cast in film, the photochemistry of TB2 is expected to change since the steady state properties described in section 5.1.1 are changed. The intermolecular interactions may drastically change the excited state dynamics of this compound. In this part, excitation pulses are 800nm, 40fs pulses from the amplified system, to excite TB2 in the $S_0 \rightarrow S_1$ transition for the transient absorption measurement. The excitation density

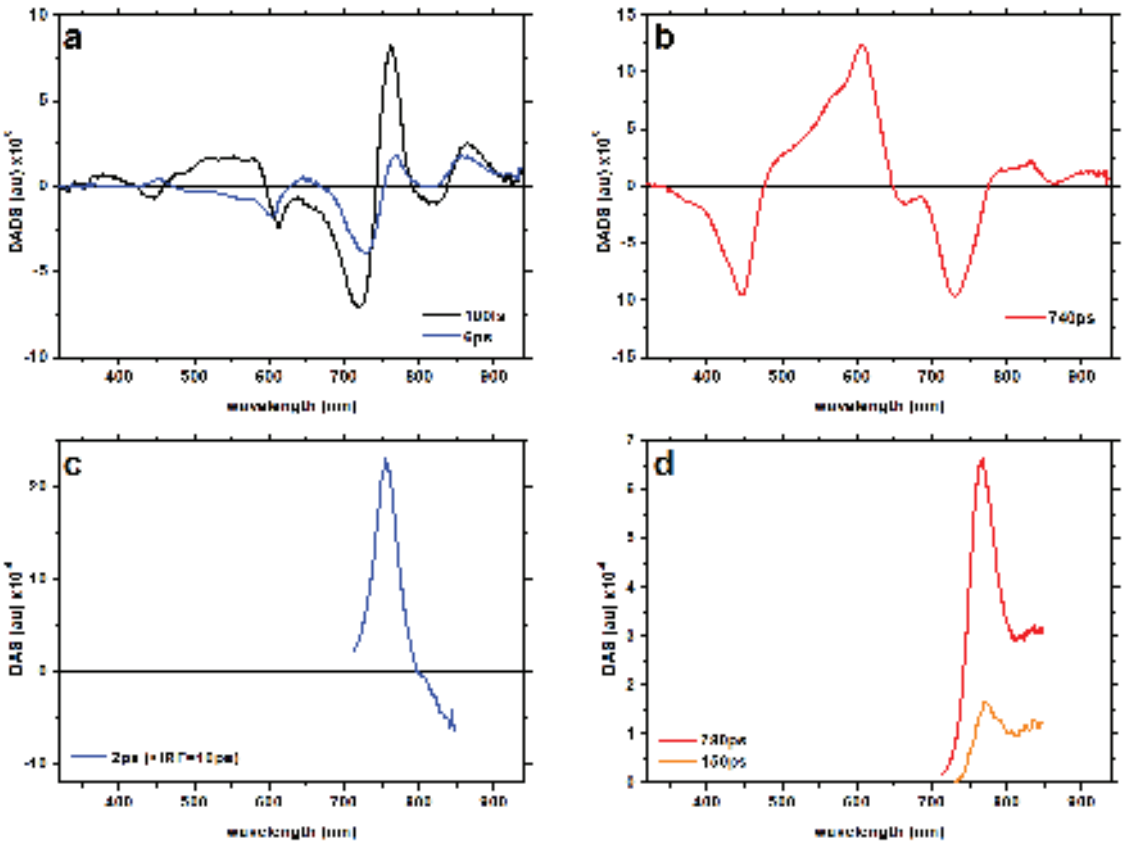

Figure 5.14.: Global fitting of TA (a and b) and TF (c and d) data. The sub IRF DADS associated to 27fs is not shown. The time constants associated with the DAS and DADS are displayed on the graphs. Panels a and c corresponds to vibrational relaxation of the excited state and panels b and d to the relaxed excited state population.

is about $25\mu J.cm^{-2}$, which is a trade off between linear response upon excitation and signal to noise ratio and lead to the excitation of about 2.5% of the molecules in the film within the pump path. Transient fluorescence measurements are performed with 750nm, 120fs pulses from an OPA pumped by a Tangerine laser source, in similar excitation conditions. The time resolved fluorescence signal is recorded at the edge of the cutoff wavelength of the streak camera and is thus spectrally deformed, but the temporal information is still relevant.

The TA and TF data maps shown in figure 5.15. At first sight, the time

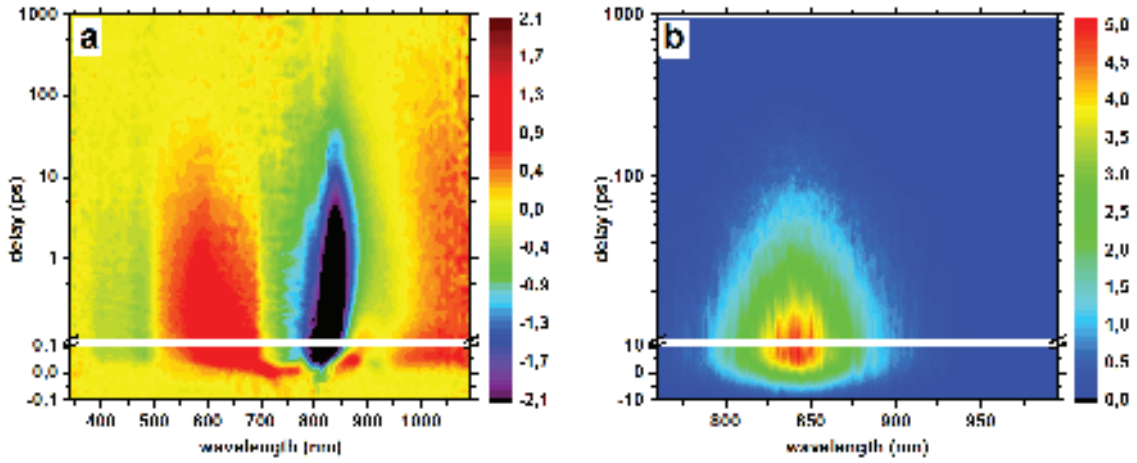

Figure 5.15.: Transient absorption (a) and fluorescence (b) data of BODIPY TB2 in film as cast excited at 800nm and 750nm respectively.

resolved difference spectra evolves in the first hundred femtoseconds to form a photoinduced excited state absorption dominating around 610nm and 1050nm and decays in a tens of picoseconds. The time resolved fluorescence spectra shows no major spectral evolution and consists in an emission band peaking at 840nm and decaying on the same timescales.

The transient fluorescence data shows no evidence for spectral evolution. As mensioned before, the temporal evolution is the main information to be exctracted from this data. The spectrally integrated transient fluorescence signal is presented in figure 5.17, panel d. It is fitted by a bi-exponential decay with time constants of 14 and 80ps. The DAS corresponding to the global analysis of the TF data using the first singular kinetic fitted with two time constants are presented in panel d of figure 5.18.

Transient absorption data are presented as selected difference spectra for some time delays in figure 5.16. The early time delays are presented in panel a and shows the initial formation of an induced absorption band extending from 600 to the near infrared and overlapping with SE and GSB present in this spectral region (see absorption and fluorescence spectra in figure 5.3). This gives raise, in the first hundred femtoseconds, to

two positive absorption bands centered at 710 and 900nm, broadening in the short waveength direction so as to form two large positive absorption bands in the 520-710nm and 950-1100nm regions. This spectral evolution in the first hundred femtoseconds is attributed to vibrational relaxation of the excited states in the film.
Later, as shown in panel b, the two absorption bands reduces together with the GSB bands at 475 and 750nm, an the stimulated emission in the 825-1100nm region. Note that the positive absorption band in the 950-1100nm region decay slower than the 520-710nm one. There is no signature of photoproduct formation through new absorptions or long lived GSB. The spectral changes on the picosecond timescale is thus attributed to vibrational relaxation of the excited states together with its recombination via fluorescence and internal conversion. Note that the absence of spectral resolution in the streak camera experiment does not allow to cross observe this picosecond vibrational relaxation.

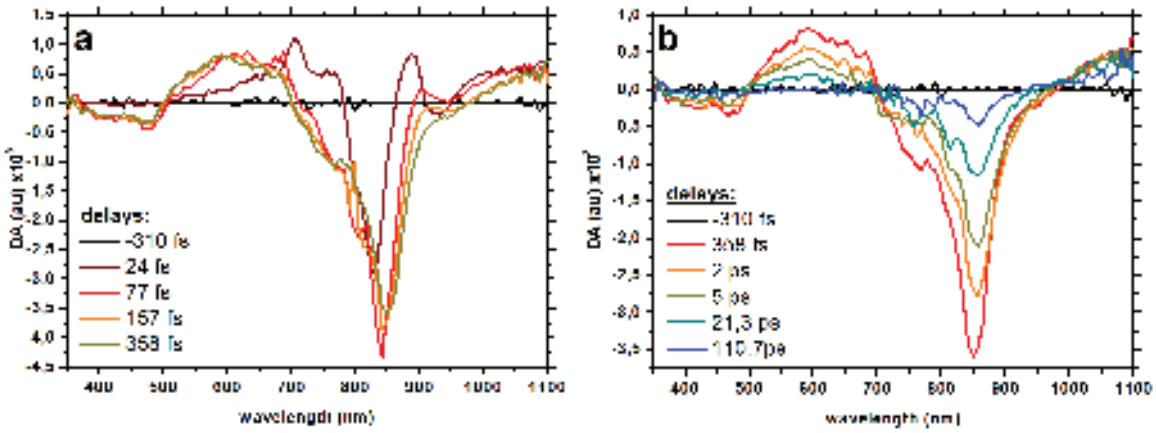

Figure 5.16.: Transient absorption spectra at different delays for TB2 film as cast excited at 800nm showing the hundred femtosecond timescale evolutions on the left and the longer delays on the right. The delays are indicated on the graphs.

The figure 5.17 shows the kinetic evolution of the transient absorption data. Panel a shows the spectral shift mensioned before appearing as a 60fs raise time in the buildbup of the ESA positive absorption for shorter wavelengths. The later decay is similar with 1.5ps and 30ps from the

local fits. The temporal evolution of the near infrared absorption band is presented in panel b. The kinetic traces shows a rapid 60fs evolution followed by a >100ps decay. The blue kinetics shows the competition between ESA and SE due to the vibrational relaxation in the first hundred femtoseconds. Negative contributions from the SE are present in the blue and orange curves and corresponds to decays of about 30ps. The SE dominated kinetics shows the same evolution but are dominated by the negative SE contributions (panel d). The evolution of SE in in good agreement with the transient fluorescence kinetic trace presented in the same panel. Note the lower time resolution of the latter experiment (approximately 6ps IRF). The GSB dominated kinetics presented in panel c shows the evolution of the depopulated ground state. The kinetics traces are fitted with 4 time constants of 60fs, 1.5ps, 50ps and >100ps.

Global analysis of the TA data requires six time constants (10fs, 90fs, 780fs, 4ps, 45ps and 760ps) to fit the four main kinetics necessary to reproduce accurately the data. The same analysis on transient fluorescence data is achieved using the first main singular kinetics (from SVD) and three time constants. The obtained DADS and DAS are displayed in figure 5.18. The 800 to 850nm spectral region is removed during the DADS calculation because of low signal to noise ratio in this region for long time delays. Indeed, the fundamental 800nm beam used to generate white probe light is usually spatially filtered, but the beam pointing change at long delays prevents optimal correction.
The DADS corresponding to a time constant of 10fs models the coherent artifact and chirp correction error and is disregarded.

The TF DAS are presented in figure 5.18, panel d, and corresponds to the two decay times of 14ps and 80ps, indicating the depopulation of excited states on this time scale. The overall decay of the fluorescence signal is 33ps (weighted sum of the decays with their respective amplitudes) and matches the 45ps timescale obtained by global fitting of the TA data (panel c). There is no evidence for unresolved fluorescence signal (figure 5.17, panel d). This indicates that the changes in

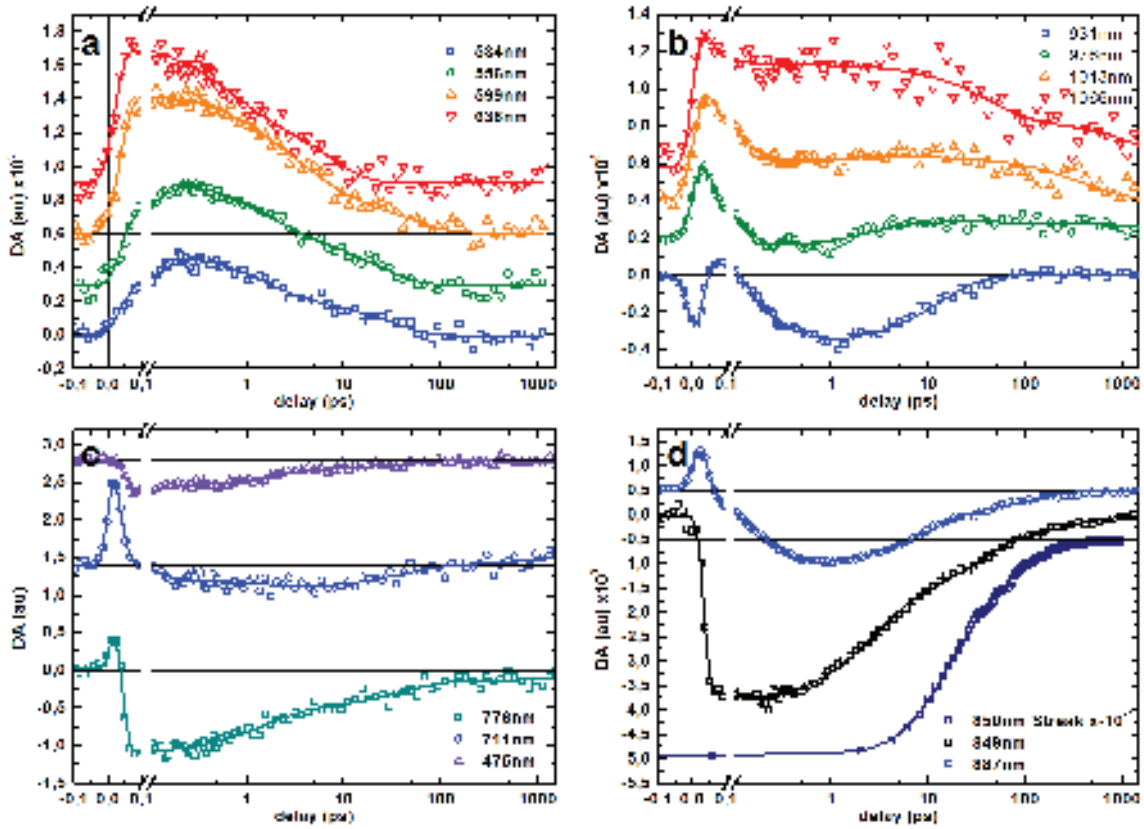

Figure 5.17.: Transient absorption and fluorescence kinetics of pristine TB2 films as cast on ITO/PEDOT:PSS substrates. The ESA dominated kinetics showing the broadening of the excited state absorption are presented in panel a and the near infrared induced absorption band with SE contributions in panel b. SE dominated kinetics are presented in panel d together the spectrally integrated streak camera kinetic. In panel c are displayed GSB dominated kinetics. Wavelengths are indicated on the graphs, thick lines are multi exponential fits of the data.

the fluorescence signal are not important within the first 6ps. This is surprising as the 4ps DADS is related to a reduction in the excited state population, as evidenced from the kinetic traces and the GSB recovery on these timescales.
The shorter timescales DADS of 90fs and 760ps (panel a and b) are GSB conservative and are attributed to the spectral shift and broadening of the excited state absorption band, indicating vibrational relaxation of the latter states. This relaxation may be related to the localization of the TB2 excitation, which typically occurs on this timescale [55].
The 760ps DADS (panel c) is non emissive (absence of >100ps decay in the TF signal) and the presence of GSB in this DADS indicates that the depopulation of this state repopulates the ground state. The positive contributions of this DADS are very similar to the 4ps and 45ps DADS, although the near infrared absorption band has a slightly higher intensity, which may indicate the absence of SE band overlapping. This DADS is attributed to the recombination of dark excited states, in the absence of clear evidence on the formation of these states that would allow to consider it as a photoproduct.

These observations allow to propose a reaction scheme describing the photoreaction in TB2 as cast films. After absorption of the exciting 800nm photon, delocalized excitons are created in the material [56, 57]. The difference spectra as well as the kinetic traces shows that the exciton absorption is broadening, on the timescale of 100fs and 780fs. The first decay is attributed to exciton localization, while the second one could indicate either the localization of more delocalized excitons, or the vibrational relaxation of localized excitons, or to localized excitons diffusion to neighboring molecules of lower energy excited state. Later at the picosecond timescale, three classes of excitons are decaying. In the absence of evidence for the conversion of one form to the other, the three excitonic populations are represented as parallel populations, decaying via internal conversion and spontaneous emission to the ground state. These excitons classes are spotted thanks to its fluorescence lifetime and its similar excited state absorption. The longer lived excitonic class is dark and decays exclusively through internal conversion.

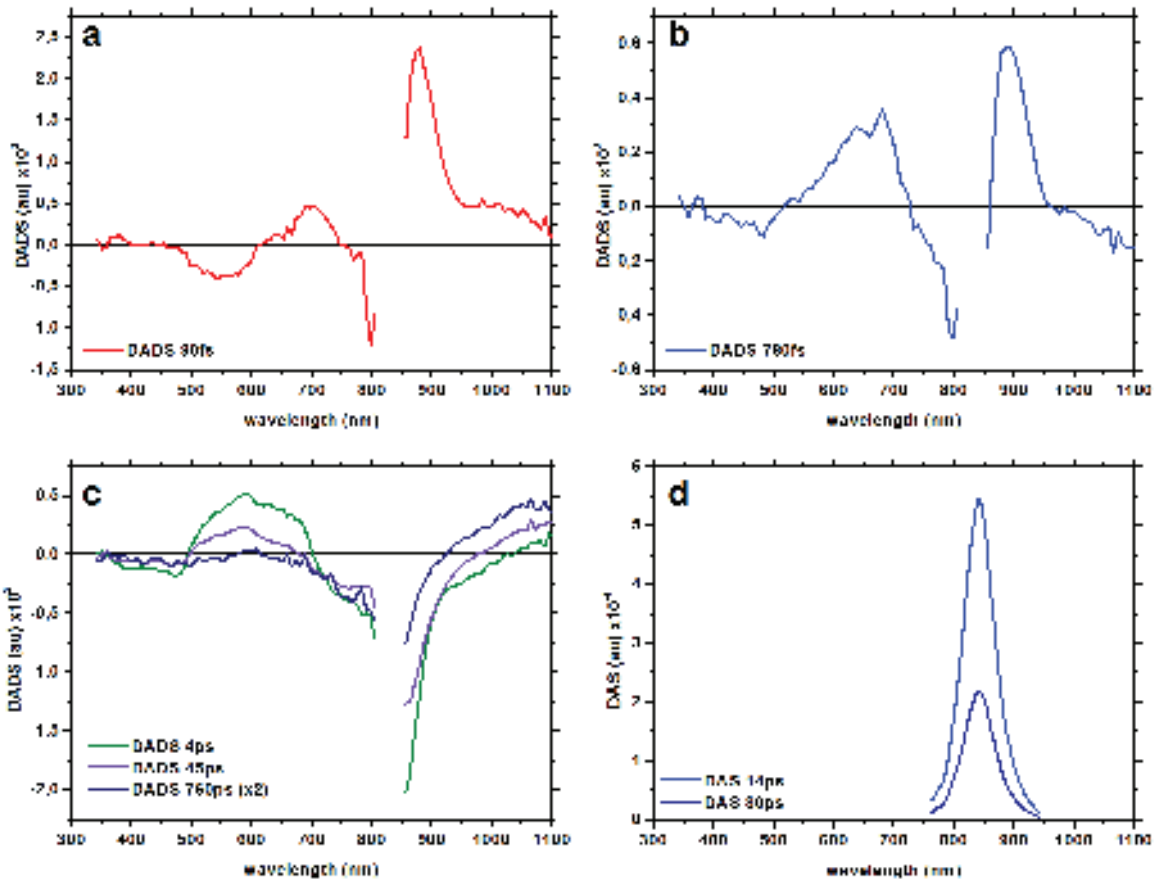

Figure 5.18.: DADS and DAS of neat BODIPY TB2 films as cast on ITO/PEDOT:PSS excited at 800nm and 750nm respectively. Early times DADS are displayed on top and the picosecond decays measured by transient absorption (left) and fluorescence (right) are shown on bottom panels. The decays are indicated on the graphs. Note that the sphape of the DAS does not represent the fluorescence spectrum due to the cutoff of the streak tube sensitivity. The 800 to 850nm spectral region of DADS is absent due to low signal to noise ration in this region.

The as cast TB2 films are mainly amorphous, which is not a favorable situation for strong intermolecular coupling. The transient absorption and fluorescence data does not show direct evidence of intermolecular interactions such as exciton migration or hopping. The three classes of excitons should represent different quenching mechanisms but also different molecular classes since the induced absorption is different. There is no evidence of a difference in the fluorescence spectrum since the streak camera sensitivity limitations in the near infrared does not allow to have enough signal in the wavelengths longer than 900nm to make such conclusions. These different exciton classes can be due to specific conformations of the BODIPY molecules in the amorphous blend, or at the interfaces.
The proposed reaction scheme summarising the observations is presented in figure 5.19.

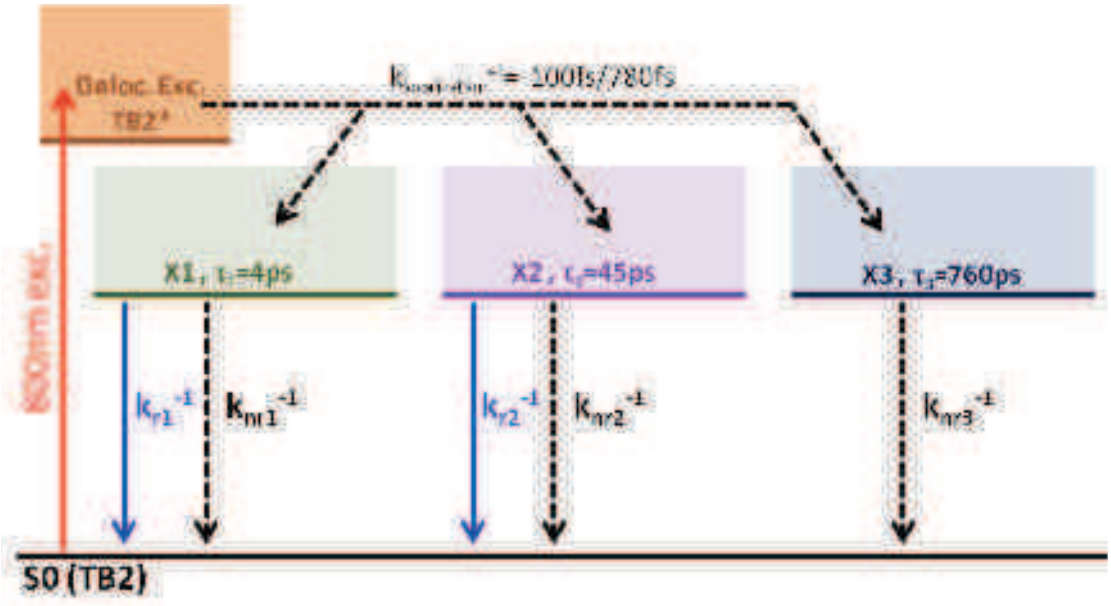

Figure 5.19.: Reaction scheme for BODIPY TB2 in film as cast excited at 800nm. Solid arrows represents radiative transitions and dashed ones non radiative ones. Lifetimes of states are indicated.

5.2.3. In annealed films

The annealed TB2 films contains J-like aggregate, thus its excited states are expected to be different than the solution and as cast film ones. These intermolecular interactions may influence the nature and kinetics of the photo generated excited states. The pristine TB2 annealed films are studied by TA and TF experiments. The TF technique used for this film is the optically time gated fluorescence using a fluorescence up conversion configuration.

The processed TA and TF data presented as 2D graphs show at first glance a different behaviour from the as cast films. Note that in most of the difference absorption spectra presented here, the low amplitude difference absorption region below 710nm is multiplied by a factor of 10. The first hundred femtoseconds exhibit changes in the difference absorption spectra that leads to a weak induced absorption between 500 and 700nm and a pronounced negative signal with four bands at 750, 850,950 and 1030nm. This signal decays in the first tens of picoseconds to form a quasi static long time difference spectrum with two positive features peaking at 720 and 810nm and a negative one at 875nm. The transient fluorescence mainly shows the picosecond decay of the fluorescence since the spectral region probed is spectrally thin due to phase matching conditions of the up conversion, and does not allow to evidence spectral shifts.

The spectrally averaged transient fluorescence signal is presented in figure 5.22, panel c. This fluorescence decay is fitted with three exponential decays presented in table 5.1. This indicates three different excitonic populations evolving on different timescales. The overall decay is 3.7ps (sum of decay time weighted by their amplitudes in the fit) which is 10 times smaller than the overall fluorescence decay of the as cast film (33ps). The 70% higher fuorescence signal of the annealed TB2 film is in apparent contradiction with the average fluorescence lifetimes. However, this might be explained by the presence of agregates. Indeed, upon agregation, the oscillator strength of the transition is increased, leading to higher radiative rates.

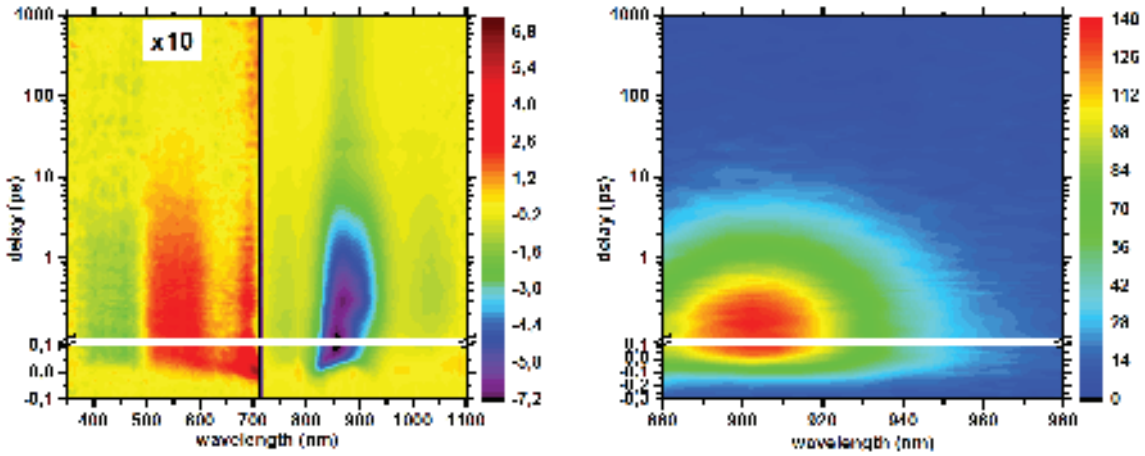

Figure 5.20.: TA and TF data maps of TB2 in film annealed excited at 800nm. Note that the TA dataare multiplied by 10 for wavelengths inferior to 710nm.

The spectral evolution of the TA signals is presented in figure 5.21. The initial excited state absorption appear as two positive features peaking at 700 and 875nm (panel a) decaying to form a larger positive signal in the 500-700nm region together with an intense SE signal in the 900-1100nm region. The two characteristic emission bands observed in the steady state fluorescence spectrum are observed in the SE signal at 900nm and 1030nm. The negative contributions from the GSB of the $S_0 \rightarrow S_1$ and $S_0 \rightarrow S_2$ transitions are present around 850nm and 450nm respectively. The transient absorption signal decays on the picosecond timescale (panel b) to form a long lived difference spectrum with two positive features at 700 and 820nm an a negative signal at 870m. This difference spectrum remains almost constant until the 5ns (maximum delay probed by the TA experiment).

The early evolution of the induced absorption evidences a sub 100fs relaxation of the initially excited state, as evidenced by the ESA kinetics plotted in figure 5.22, panel a (red and orange curves). The raise of the 535nm trace corresponds to the decay of the short lived (<100fs decay, see table 5.1) positive signal of the 710nm, and is attributed to the broadening of the initial excited state absorption. This early evolution

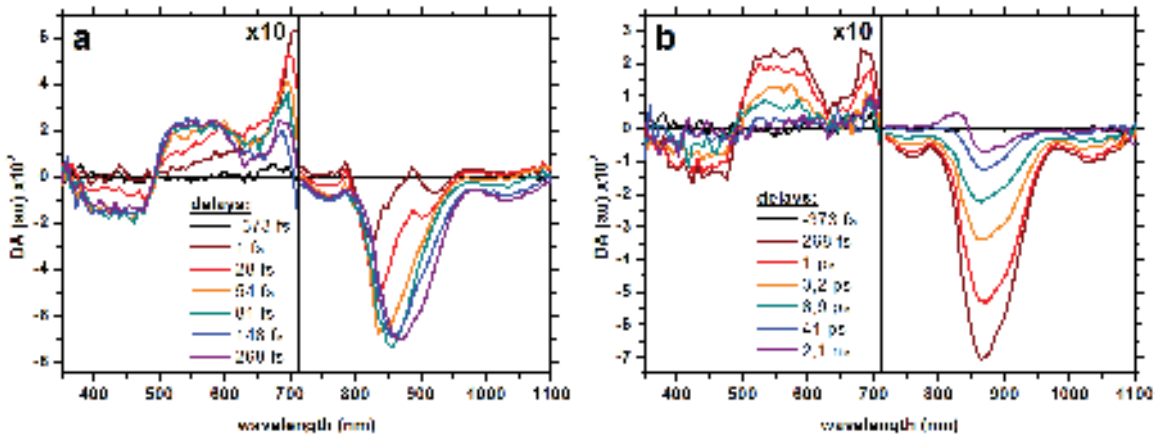

Figure 5.21.: Selected TA spectra measured on BODIPY TB2 neat film annealed on ITO/PEDOT:PSS for delays indicated on the graphs. Early times difference spectra on the left and longer times on the right.

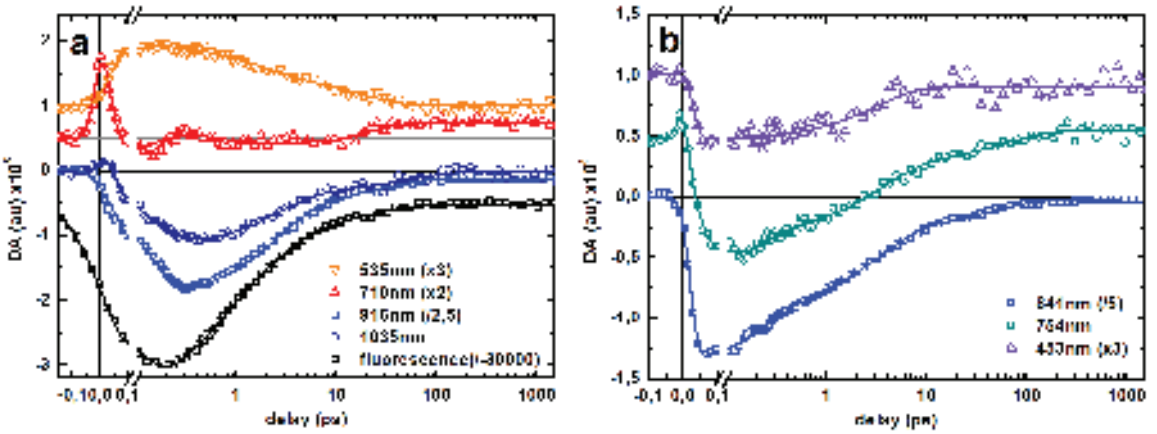

Figure 5.22.: Transient absorption kinetics of pristine TB2 films annealed on ITO/PEDOT:PSS at different wavelengths. ESA and SE dominated kinetics are presented in panel a, together with the TF kinetic trace obtained by fluorescence up-conversion. Panel b shows GSB dominated kinetic traces. Raw data are displayed as scatter plots and multi exponential fits in thick lines of the corresponding color.

GSB 841nm	ESA 535nm	SE 916nm	TF 900nm	Global Fit TA
-	40fs (-20)	80fs (+185)	-	0.1ps
0.2ps (29)	-	-	0.6ps (49)	0.5ps
3.2ps (38)	1.6ps (50)	2.5ps (78)	2.9ps (39)	3.4ps
39ps (15)	18ps (50)	29ps (20)	25ps (12)	45ps
>5ns (18)	-	>5ns (5)	-	>5ns

Table 5.1.: Overview of different kinetic fits. Decays are indicated along with relative amplitudes in purcent in parenthesis. The amplitudes indicated with a sign corresponds to a decay associated with an opposite sign with regard to the other decays. Their amplitudes are normalized to the absolute value of the sum of the other amplitudes.

of the initially excited state is also evidenced in the SE traces at 916 and 1035nm, as well as in the GSB trace at 754nm (panel b) showing an initial raise of the signals in the first hundred femtoseconds. In addition, the DADS obtained by global fitting and associated with this timescale (130fs DADS, figure 5.24, panel b) presents two positive bands peaking at 910 and 1030nm, characteristic of the fluorescence of TB2, and indicating and increase in the stimulated emission signal. There is no sign of TB2 GSB which indicates that the excited TB2 population is unchanged on this timescale. This increase in the TB2 SE with conservation of the excitonic population is in very good agreement with the relaxation of high energy "dark" excitons to the lower energy emissive excitons in J-aggregates. Note that this rise of fluorescence is of the same order of magnitude than the IRF of the TF experiment. As a consequence, its observation in the TF kinetic trace is hindered.
The picosecond evolution of the 535nm trace is similar to the GSB, SE and TF traces presented, with a bi-exponential decay (table 5.1). Note the presence of a long lived difference absorption signal for the 916 and 713nm traces, indicating the presence of a long lived species (apprearing as >5ns delays in table 5.1).

The formation of the long lived species can be evidenced by the 710nm trace (red trace, panel a, figure 5.22), as a rise in approximately 25ps. This increase in absorption is concomitant with the longer decay of the ESA, SE and TF signals, indicating the formation of this long lived species from the photogenerated excitons. The long time difference spec-

trum is presented in figure 5.23, and matches well the derivative of the steady state absorption of the annealed TB2 film for the $S_0 \rightarrow S_1$ absorption band around 800nm. This is characteristic of an electroabsorption signal caused by a Stark shift of the absorption bands of the molecules. This effect is due to the presence of an electric field that can be induced by the presence of charges significantly separated [33]. As the molecules in the blend are agregating, these charge separated states are likely to be polarons [58]. Therefore, we attribute this long lived signature to the presence of polarons, formed on the picosecond timescale. The comparison of the DADS and the difference absorption in panel a shows that the EA signal is competing with GSB in the 600 to 850m region. The timescale of formation of the polarons is further verified by the analysis of kinetic traces measured at extrema of the polaron signature (figure 5.23, panel b). The 720 and 880nm traces corresponds to a positive and negative long time signal and exhibits an approximately 25ps rise and fall, respectively, of the TA signal. It is interesting to remark that a similar trend is observed around 250fs. The 25ps decay of the excitonic population selectively probed by transient fluorescence is therefore attributed to the formation of polarons.

The 2.9ps decay of the excitons measured by TF is found in the GSB, ESA and SE evolution (see table 5.1), but there is no evidence for the formation of a photoproduct on this timescale. This decay of the excitonic population is thus attributed to the recombination of excitons.
The shortest exciton lifetime of 0.6ps is hardly found in the excited state kinetics (SE and ESA) measured by TA, neither in the GSB. However this timescale apprears in the global analysis (decays reported in table 5.1 and DADS in figure 5.24), and the associated DADS presents typical positive ESA and negative SE signatures, indicating the decrease of the excitonic population. The features around 700 ad 820nm (blue curve, figure 5.24, panel a) are similar to the polaron signature at long times but appears as decaying. This is concomitant with the short time features spotted in the kinetics in figure 5.23, panel b. This could be the signature of early charge separation, however, these sub picosecond kinetics are hardly fitted by the typical sum of decaying exponential functions.

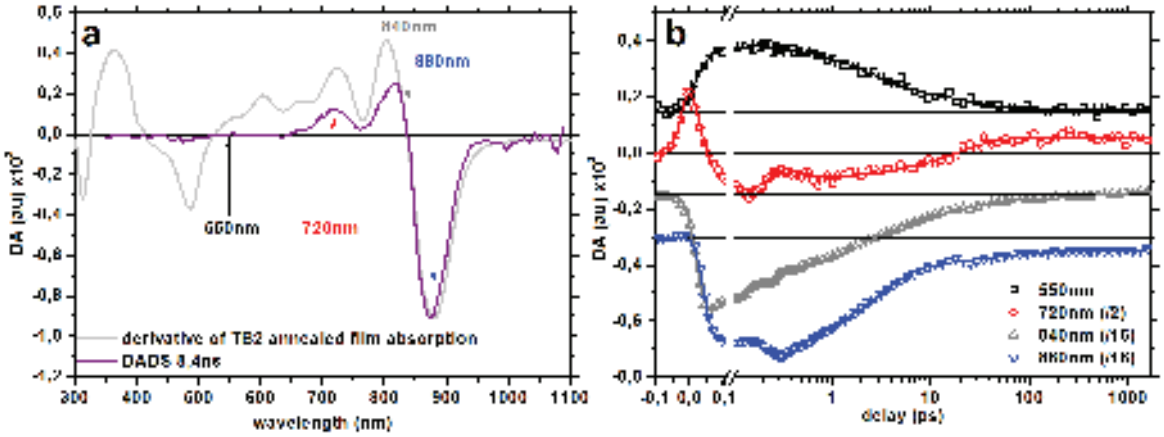

Figure 5.23.: Evidence for polaron formation in the TB2 film on ITO/PEDOT:PSS annealed excited at 800nm. Panel a shows the long time difference spectrum (>5ns DADS) together with the first derivative of the pristine TB2 film annealed absorption. Panel b shows kinetic traces at wavelengths showing maximum, minimum or null difference spectrum in the long time difference spectrum.

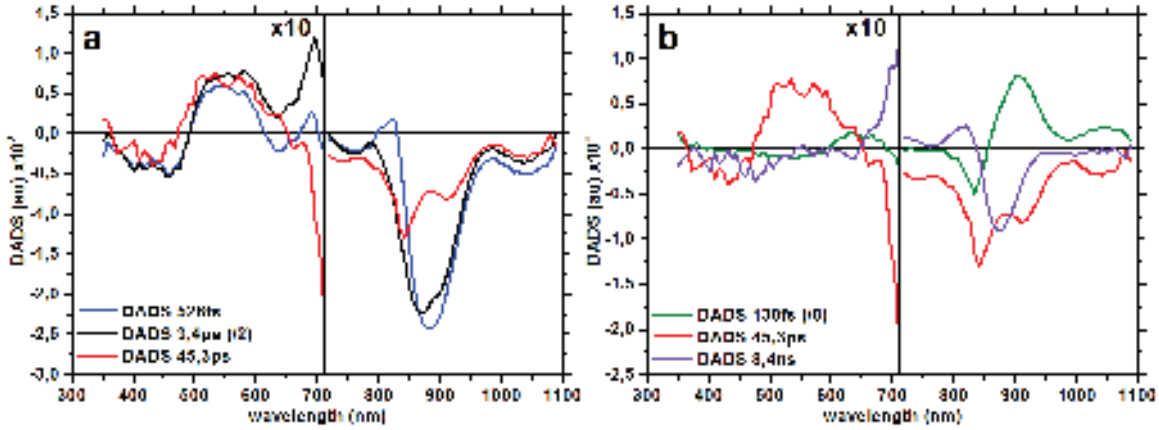

Figure 5.24.: DADS of BODIPY TB2 in film annealed excited at 800nm. On the left are displayed the DADS associated to the decay of the excitonic population. The inset enlarges the visible region. On the right, DADS associated with polaron formation. Note that the <710nm wavelength region is magnified by a factor of 10. See legend on graphs.

This signal could also be due to oscillations indicative of a coherent phenomenon occuring at early times. This feature is not an artifact specific to this data set since it is found in different runs on different substrates. As it reflects a strong depopulation of the excitonic population (50% of the amplitude decays with the 0.6ps time constant in the TF signal), we attribute this time constant to early charge separation, but it may also include contributions from exciton-exciton anihilation as well.

Finally, on view of the TF and TA data, we can sketch the reaction scheme describing the photophysics of annealed pristine TB2 film. The reaction scheme is presented in in figure 5.25. Upon photon absorption, excitons are created in TB2. The excitonic population in TB2 J-like agregates relaxes into the lowest fluorescent state. This leads to three distinct excitonic populations. The first one (X1) decays in 0.6ps, and may correspond to excitons generated close to interfaces between cristalline domains. The decay of this population is attributed to the early separation of charges at such interfaces, as ultrafast charge generation has been oberved in similar systems [56, 57]. The longer 2.9ps lived class of excitons (X2) recombines, and are attributed to excitons diffusing and reaching defects or trap states leading to their recombination. The 25ps lived excitonic population (X3) is depopulated with the buildup of an electroabsorption signal attributed to charge separation into polarons (Pol), by analogy with a very similar system reported in literature [33, 58]. These excitons are thought to reach interfaces between different agregates favorable to charge generation. Note that the observation of charge separation is indirect, and that there is no evidence for induced absorption from electron or hole polarons within the spectral range investigated here. Experimental development in order to probe infrared wavelengths is currently developped in the lab in order to investigate the expected polaronic transitions present in this spectral region [59]. As it may allow to probe polaronic transitions, it would allow to have strong evidence for the early formation of polarons proposed before.
The polarons formed are long lived (>5ns) and in absence of evidence for radiative recombination, it is thought to recombine via internal conver-

sion. It is not surprising to observe charge separation in pristine donor films [60], but since TB2 is known to be ambipolar, with similar electron and hole mobilities [42], it may be an efficient material used alone as an active layer for solar cells.

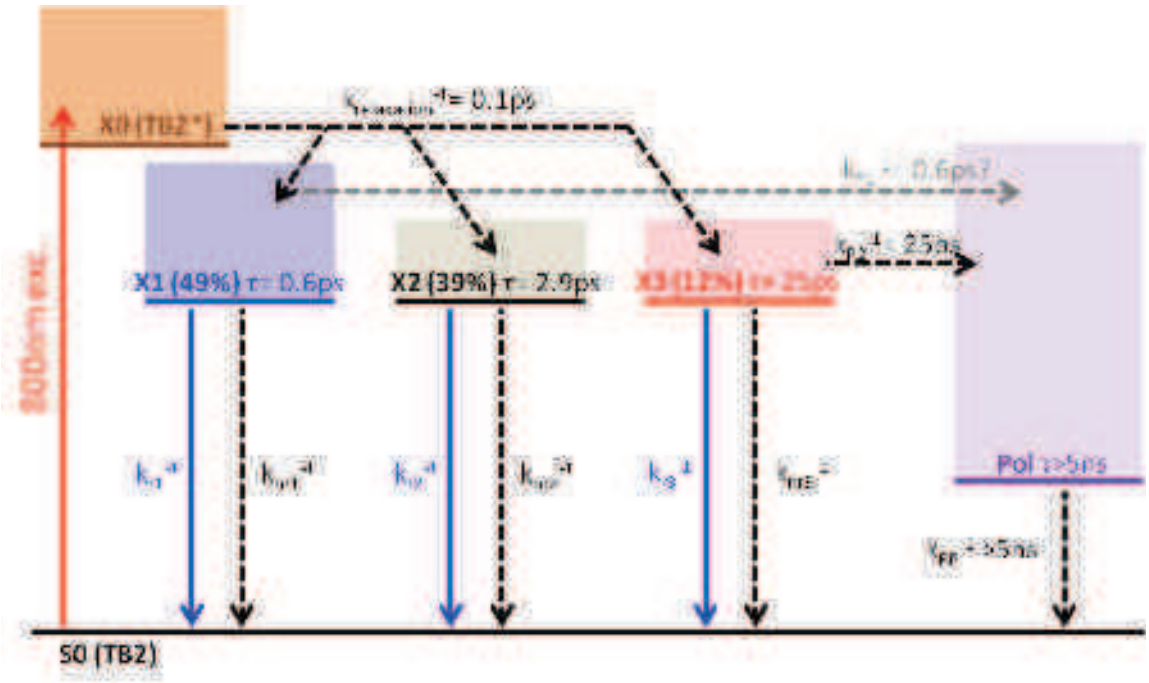

Figure 5.25.: Reaction scheme for annealed pristine TB2 in film excited at 800nm. Solid arrows represents radiative transitions and dashed ones non radiative ones. Grey arrows and rates corresponds to possible phenomena with poor experimental evidence.

6. Charge generation in blends

TB2 is used in organic solar cells as a donor molecule in association with PCBM. Even though polarons can be generated directly by excitation of neat TB2 films annealed, efficient solar cells require the presence of an acceptor to split the excitons into free charges.
This part focuses on thin films of TB2 blended with PCBM with different morphologies obtained by annealing the films to promote aggregation of TB2. The poor absorption of PCBM in the red part of the visible spectrum allows to selectively excite the BODIPY moieties in the blends, and thus to characterize charge generation from the excited donor.
The previous part allowed to characterize the excitons generated in BODIPY TB2 and their relaxation pathways. The following part focuses on deciphering the photochemistry of blends since charge generation via exciton splitting with PCBM is a process in competition with the natural lifetime of the excitons.

6.1. PCBM as a standard acceptor

PCBM is a commonly used acceptor and electron conducting organic material, based on a C60 fullerene grafted with a solubilizing chain. The PCBM structure is presented as an inset in figure 6.1, panel a.
The absorption of PCBM in films is characterized by a sharp absorption band at 340nm, on top of Soret band, and a large and weak absorption band centered around 550nm and extending from 450 to 700nm. This absorption is characteristic of the C60 fullerene molecule [61, 49, 62]. The absorption spectrum of PCBM on fused silica presented in panel a of figure 6.1 is in good agreement with the typical C60 absorption. The weak tail extending to wavelengths >700nm is probably due to scattering. On the other hand, the as cast and annealed PCBM film on ITO/Pedot:PSS

are significantly different. After correction for the sub-layers absorption, two large and weak absorption bands are present centered at 700 and 1100nm. According to the very similar fluorescence properties of the films on either substrates (panel b) these absorption bands are likely to be optical artifacts due to the superposition of dielectric layers, but one can not exclude the presence of interfacial states between PEDOT:PSS and PCBM.
The fluorescence spectrum of PCBM is very similar whatever the substrate and the annealing conditions and consists in a large absorption band extending from 700nm to the near infrared with pronounced vibrationnal structure. The main emission peak is at 730nm and the two smaller ones peaks at 805 and 910nm. Going from fused silica to ITO/PEDOT:PSS changes the relative amplitudes of the emission peaks. Finally, the PCBM absorption can be spotted thanks to the characteristic narrow absorption band peaking at 340nm and present in all the films. The fluorescence spectrum of PCBM is characterized and can be used to evidence the excitation of PCBM by steady state fluorescence spectroscopy.

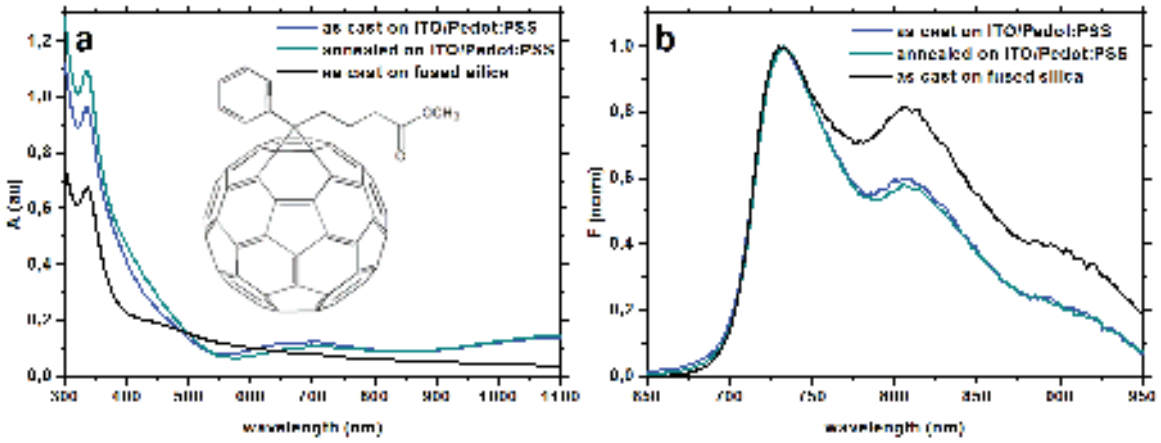

Figure 6.1.: Steady state absorption (a) and fluorescence excited at 340nm (b) of different PCBM films. Fluorescence spectra are corrected for detector response and normalized. PCBM chemical structure appears as an inset in panel a.

6.2. Blends and morphology

Two series of BODIPY:PCBM blends on either fused silica or glass/-ITO/PEDOT:PSS substrates have been obtained by spin coating from 18.2mg.mL^{-1} solutions in chlorobenzene on the respective substrates. Annealing is performed on a hot plate during 10min. The film absorption is measured after processing. The absorption spectra of the films on ITO/PEDOT:PSS and fused silica are presented in figure 6.2 and 6.3 respectively.
The spectra contain the known contributions from BODIPY TB2 $S_0 \rightarrow S_1$ and $S_0 \rightarrow S_2$ absorption bands at approximately 450 and 800nm. The TB2 concentration is kept constant for the samples cast on the same substrate. The increased PCBM weight ratio is very similar to an increse of the PCBM concentration since TB2 and PCBM shares very similar molar weight (900 and 910g.mol^{-1} respectively). The PCBM contribution to the absorption spectra consists in the very specific narrow absorption peak at 340nm together with weak and broad absorption in the 400-700nm range.

Figure 6.2, panel a shows the effect of annealing on a 1:0.5 weight ratio blend on ITO/PEDOT:PSS. Upon annealing, the absorption of amorphous TB2 peaking at 775nm is reduced and the absorption band peaking at 840nmn characteristic of the TB2 J-like agregate increases as well as a long tail extending to the near infrared. The absorption is also enhanced around 600nm, and a small broadening of the 450nm absorption band in the short wavelength direction is observed. This observation allows to infer that the main effect of annealing is to form agregates of TB2.

The panel b shows the effect of PCBM loading on annealed blends. For the 1:0.5 blend, as stated before, the TB2 contribution fits the absorption of aggregated TB2. While increasing the PCBM fraction, the characteristic absorption of PCBM at 340nm and the short wavelength edge of the spectra increases, indicating a higher PCBM concentration. In addition, the characteristic red shifted absorption band of the TB2 ag-

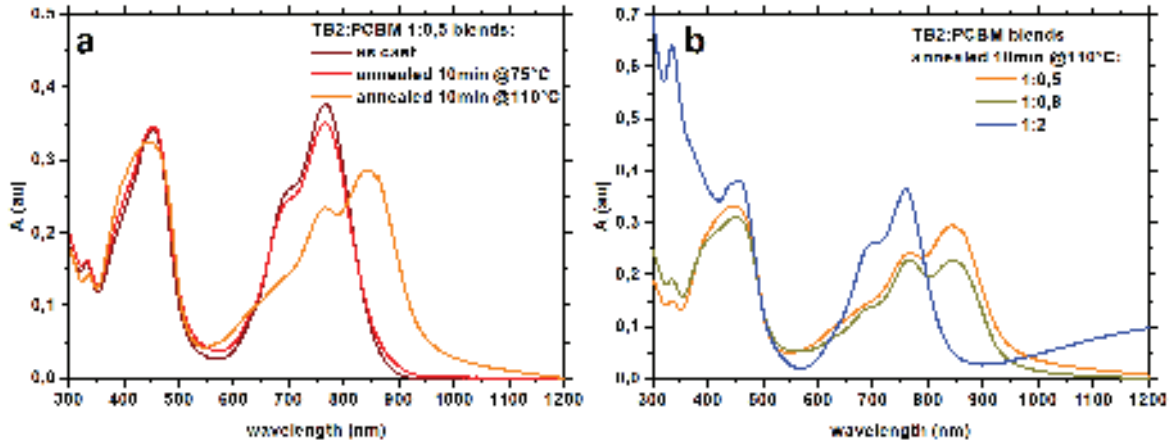

Figure 6.2.: Steady state absorption of different TB2:PCBM blends in films deposited on glass/ITO/PEDOT:PSS substrates. All blends share the same BODIPY TB2 content. Panel a shows the effect of annealing conditions on the absorption of the 1:0.5 blends. Panel b shows the evolution of the absorbance of the annealed films as a function of the PCBM loading.

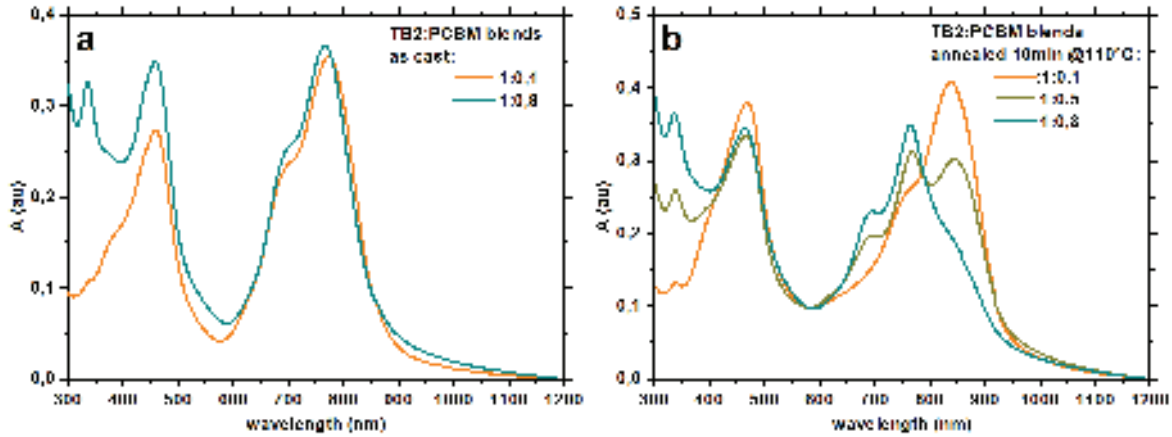

Figure 6.3.: Steady state absorption of different BODIPY:PCBM blends in films deposited on fused silica substrates. The panels a and b displays the evolution of the absorbance of as cast and annealed blends (respectively) as a function of the PCBM loading.

gregate is reduced for the 1:0.8 blend, and disappears for the 1:2 weight ratio blend. In the latter absorption spectrum, the TB2 $S_0 \rightarrow S_1$ contribution is intermediate between the as cast absorption and the absorption in chloroform. This blue shift may be explained by the change in the average dielectric constant due to the drastic increase of PCBM concentration.Note the formation of a new large absorption band in the near infrared peaking at 1200nm or more in 1:2 weight ratio blends (as observed for neat PCBM films) that may be due to interfacial states of PCBM with the PEDOT:PSS layer or to the presence of CT transitions accessible from the ground state due to the many BODIPY/PCBM interfaces.

As a conclusion, annealing the films triggers the aggregation of TB2. On the other hand, increasing the PCBM fraction hinders the aggregation of TB2. As the as cast and annealed PCBM films shows very similar absorption, one can not access to information about PCBM aggregation using steady state absorption.

The figure 6.4 shows linear plots of radial electron diffraction intensity intergrated in the angular direction from the 2D diffraction patterns (not shown) together with TEM images of TB2:PCBM blends on fused silica. The diffraction patterns of as cast films are diffuse as indicated by the weak modulation of intensity and the absence of distinct peaks (black, red and cyan curves in panel a), indicating poor organisation in the film. Upon annealing, thin peaks appear in the 1:0.1 and 1:0.8 blends, attributed to better organisation of TB2 (note the $1\mathring{A}^{-1}$ peak as in the diffraction pattern of annealed TB2, grey curve), whereas the 1:0.8 ratio blend shows contributions of the PCBM (large peak around $1.4\mathring{A}^{-1}$). Increasing the PCBM fraction changes the relative intensities of the different diffraction peaks characteristic of TB2. This shows that the crystallization of TB2 is different, but still present.
Note that quantification of the crystallinity of one or the other molecule in the films is made difficult by the similar crystalline parameters of both molecules. Indeed, TB2 is triclinic with an inclination of the lattice close to 90^o [42], which makes it similar to the PCBM monoclinic structure

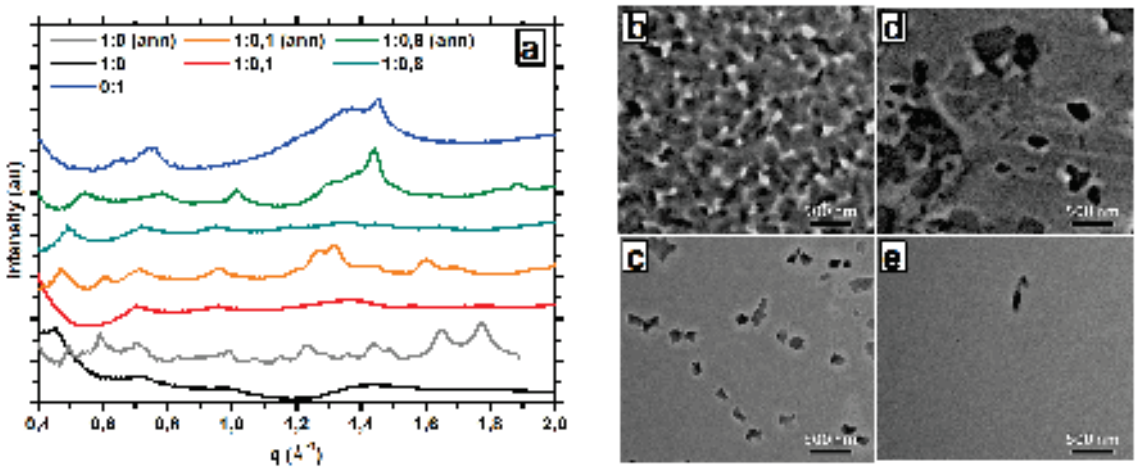

Figure 6.4.: Linear plots of electron diffraction signal for different blends on fused silica (a). TEM images of 1:0.1 TB2:PCBM blends as cast and annealed films (c and b) and images of 1:0.8 blends annealed and as cast (d and e).

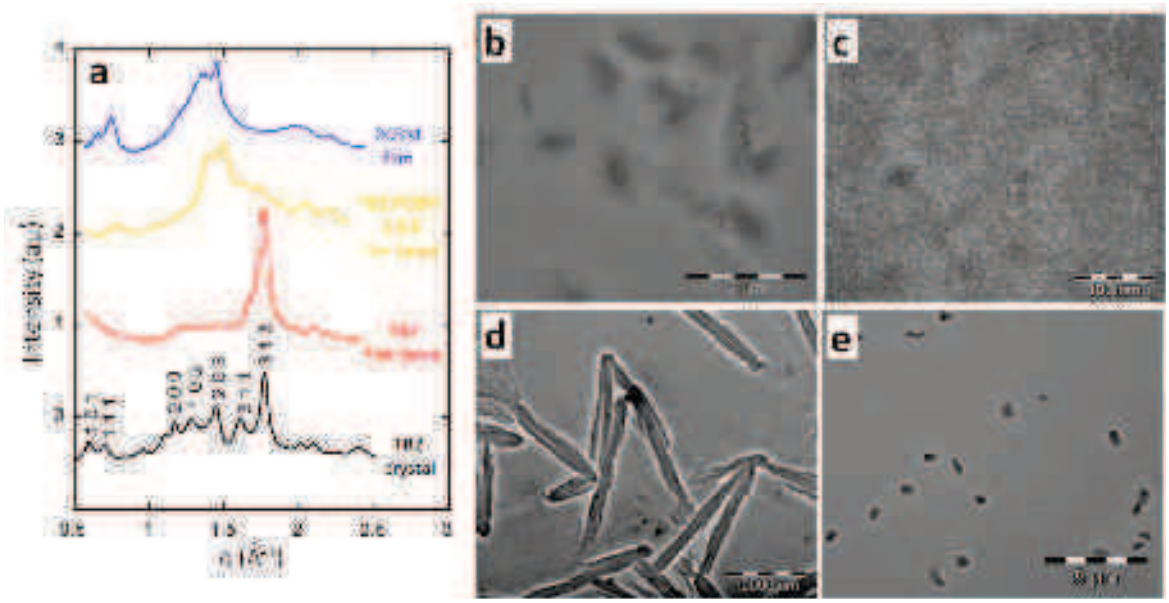

Figure 6.5.: Linear plots of electron diffraction signal of different fims on ITO/PEDOT:PSS, and the X-ray single crystal pattern marked with the crystal orientations (a). TEM images of the 1:0.5 blend on ITO/PEDOT:PSS annealed and as cast (b and c) as well as annealed 1:0.8 and 1:2 weight ratio blends (d and e).

[63]. In addition, both share the same lattice parameters (a and b from PCBM similar to c and d from TB2).
TEM images show mainly homogeneous as cast films (panels c and e), and some clusters attributed to TB2 for the 1:0.1 blend (darker zones in panel c). The annealed 1:0.1 ratio blend shows a very similar TEM image as the neat TB2 annealed film on fused silica, whereas the 1:0.8 blend exhibits large clusters, attributed to TB2 (darker zones in panel d) by analogy with the 1:0.1 film although it could also be PCBM clusters.

Figure 6.5 shows in panel a the comparison of radial distributions of electron diffraction intensity of blends cast on ITO/PEDOT:PSS with single molecule films annealed, and the X-ray single crystal diffraction pattern. It shows the presence, in the blend, of characteristic signatures of both molecules. For the same reasons than quoted previoulsy, the similar lattice constants of both molecules do not allow to clearly disentangle the relative contributions of each molecule. As a consequence, one can not exclude the formation of co-crystals of both molecules. The presence of a small amplitude peak located at 1.8 $\mathring{A}^{-1}$ indicates the presence of TB2 molecules oriented parallel to the substrate (L.Biniek, private communication).
Panels b and c presents the TEM images of 1:0.5 blends annealed and as cast. Much like on fused silica (figure 6.4, panels d and e), annealing leads from an homogeneous film (c) to a more heterogeneous one (b). This may indicate the formation of agregates, since aggregation upon annealing is evidenced by absorption.
The TEM images shows interesting phase segregation in the 1:0.5, 1:0.8 and 1:2 blends (panels b, d and e), as indicated by the contrasted zones. Note the presence of crystal like dark features in the TEM image of the 1:0.8 and 1:2 blends, whereas there is no evidence for the presence of agregates from the absorption spectrum of the latter film.

Despite the above relatively complex information content, the diffraction patterns are qualitatively in good agreement with the steady state absorption spectra, in terms of the TB2 crystalinity and its dependance on annealing. Highest TB2 crystal order is obtained from annealed films

of pristine TB2. For these annealed films, increasing the PCBM fraction modifies the crystalisation of TB2, in line with the absorption spectra indicating a reduction of the (J-like) aggregation of TB2.
The TEM and electron diffraction measurements were meant to get more quantitative information about the nano-morphology of the films, however a more precise analysis of the TEM images and electron diffraction patterns does not allow to conclude on that point so far. Indeed, area selection electron diffraction have been used on the darker sites evidenced by TEM to determine its constitution, however the similar lattice parameters of the two molecules hinders access to quantitative information about the presence and size of segregated domains of the latter molecues. This might be achieved using electron spectroscopic imaging techniques such as electron energy loss spectroscopy, that allows to have element-specific contrast by selectively probing the characteristic iodine or fluor atoms of TB2.
So far, the agregation of TB2 is qualitatively highlighted in a much "cheaper" way using steady state absorption. However, the distribution of agregates in the bulk can not be investigated. It can not be decided wether these darker zones corresponds to pure TB2 or PCBM phases using the present experiments.

To conclude on blend morphology, annealing allows TB2 to form J-like agregates. Increasing the PCBM content in the blends hinders the agregation of TB2. The organization of the films depends on the substrate used. These observations show that accurate control of the acceptor content and the morphology of the film separately is impossible since both parameters are correlated. It also shows the influence that the substrate may have on the film organisation.

6.3. Evidence for charge transfer by steady state spectroscopy

Charge transfer is the expected phenomenon to split the excitons generated through the excitation of TB2 in the blends. Since charge transfer

leads to a depopulation of the excitonic population, and that the charge transfer states are not expected to recombine radiatively at the same wavelengths of emission, an efficient charge transfert may quench drastically the excitons fluorescence.

Steady state measurements are performed on the films described previously, with different substrates and annealing conditions. The TB2 fluorescence for as cast and aggregated TB2 have been characterized and described previously and consists in spectra mirror image of the $S_0 \rightarrow S_1$ absorbtion bands, and spans in the 850 to 1000nm region. These two spectra are used as a reference in figures 6.6 and 6.7. The fluorescence spectra are corrected for the sensor response and the number of absorbed photons (division by $1 - 10^{-OD(\lambda_{ex})}$), so that the fluorescence intensity can directly be compared on the graphs.

The fluorescence of the blends processed on fused silica are presented in figure 6.6, panel a for as cast films and panel b for annealed films. The fluorescence spectra of the as cast blends (panel a) matches the shape of the neat TB2 as cast film, and the fluorescence signal drastically drops with increasing the PCBM fraction. The same statement is valid for the annealed blends (panel b) except that there is a slower quenching with increasing the PCBM fraction. The sharper emission spectrum of annealed TB2 allows to evidence a slight red shift of the fluorescence spectrum with increasing the PCBM fraction. There is no sign of contributions from amorphous (as cast) TB2 for high PCBM loadings, even though TB2 agregation is hindered, indicating that the fluorescence is mainly emitted from the aggregates.

When processed on ITO/PEDOT:PSS, the annealed blends shows mainly the same evolution (figure 6.7, panel a). Surprisingly, the 1:0.8 TB2:PCBM blend shows a higher fluorescence than the lower PCBM content 1:0.5 one. This is not the case for the same fims cast on fused silica. In regard with the micrometer sized phases observed in the TEM images (figure 6.5, panel d), this could indicate that the large clusters are pure TB2 crystals, leading to unefficient exciton diffusion to PCBM rich

regions. The panel b shows the evolution of the fluorescence with the annealing conditions for the 1:0.5 blend. Importantly, the main effect of annealing is to unquench the fluorescence.

The efficient quenching observed for as cast blends can be explained by the morphology of these blends. The electron diffraction patterns indeed shows that these blends are homogeneous and that there is no evidence for crystallisation of one or the other molecule. Thus, with such an homogeneous mix, the TB2 excitons are more likely to be located close to a PCBM molecule. This situation favors both resonant energy transfer and electron transfer, which are expected to quench the excitonic population. On the other hand, annealed blends are less efficiently quenched and the TEM images idicates the presence of clusters and the electron diffraction patterns indicates the ordering of PCBM and TB2. In addition, the absorption spectra indicates the presence of TB2 aggregates. In this case, the exciton is more likely to be created in TB2 aggregates, far from the PCBM and must diffuse prior to be quenched, which increases the probability of relaxation via radiative emission.

The fluorescence quenching of TB2, after selective excitation of TB2 and upon addition of PCBM corresponds to new TB2 exciton relaxation pathways induced by PCBM. The expected phenomenon is exciton splitting via formation of charge transfer states, expected to happen via either direct charge (electron) transfer from BODIPY excitons to PCBM, or by energy transfer from BODIPY excitons to PCBM, followed by hole transfer. However, the latter phenomenon is unlikely to happen since the rate of energy transfer from a donor to an acceptor depends on the overlap integral of the fluorescence spectrum of the donor with the absorption spectrum of the acceptor. Thus, despite the fluorescence of TB2 is expected to have a high molar emission coefficient, the absorption of PCBM in the 800 to near infrared range is very weak ($< 50 M^{-1}.cm^{-1}$), leading to a poor overlap integral. The LUMO levels of TB2 and PCBM have been measured (in solution [42]), and are favorable to a charge transfer. In addition, there is no evidence for PCBM fluorescence in the present measurements, indicating that the excited state of PCBM is not likely to be involved, however the latter may be rapidly quenched by an

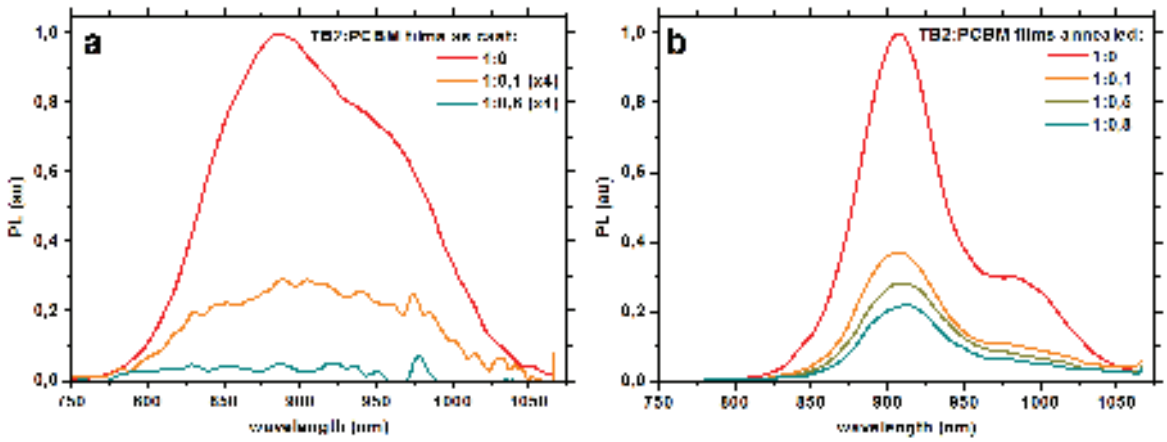

Figure 6.6.: Steady state fluorescence of TB2:PCBM blends on fused silica. As cast blends are displayed on panel a, annealed ones on panel b. Data are corrected for sensor response and for the number of absorbed photons.

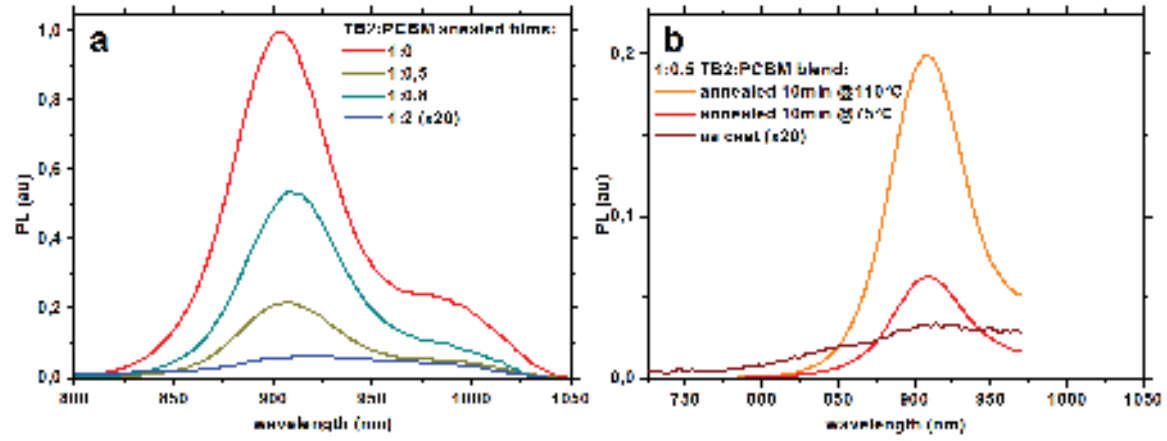

Figure 6.7.: Steady state fluorescence of BODIPY:PCBM blendson ITO/PEDOT:PSS. The influence of the PCBM content is presented on panel a and the effect of annealing on the 1:0.5 blend in panel b. Data are corrected for sensor response and for the number of absorbed photons.

ultrafast hole transfer. Therefore, even though a resonance energy transfer can not be completely excluded (in particular in intimately mixed blends where the intermolecular distances between donor and acceptor may be sufficiently short to overcome the bad spectral overlap between donor flurorecence and acceptor absorbance), the overall phenomenon responsible for the exciton quenching is charge transfer to PCBM, and most likely dominated by electron transfer.

In summary, the combination of electron diffraction, TEM, absorption and fluorescence spectra allows to infer an efficient charge transfer responsible of TB2 excitons quenching in BODIPY:PCBM blends. The quenching is very efficient in as cast films on either substrates due to an homogeneous mixing of PCBM with TB2 molecules, reducing the average distance between excited TB2s and the nearest PCBMs. On the other hand, in annealed films, the fluorescence quenching is less efficient. This is explained by important phase segregation leading to increased average distance between donor and acceptor molecules. Even though the exciton delocalization might be improved due to agregation of TB2, exciton quenching turns out to be limited by the diffusion of excitons to the closest PCBMs. This points out the importance of the blend morphology on the formation of charge transfer states. However, it is important to note that even though the quenching is very efficient in as cast films, the absence of significant clustering of PCBM and agregation of BODIPY may drastically reduce the mobility of holes and electrons respectively.

6.4. Investigation of blends photochemistry

As shown before, a set of films of TB2:PCBM blends have been produced, on two different substrates and with different annealing conditions. These blends presents different morphologies and leads to different fluorescence quenching in comparison with the neat TB2 films. The fluorescence quenching indicates the transfer of the TB2 excitons energy, attributed to electron transfer to PCBM, leading to the formation of CT

states.

Even though the quenching of excitons is an indication of the formation of CT states, it does not give information on the efficiency of the CT state separation into free charge carriers [38]. The very different degrees of fluorescence quenching within the blends presented here suggests indeed a variety of different CT state production efficiency. In particular, the 1:0.5 blend annealed gives the best PCE when used in OSC while it exhibits a lower fluorescence quenching than other blends. Investigation of the yield of free charge generation requires thus to probe the CT state populations and their kinetics, possibly evidencing the formation of free charges.

As indicated by the strong fluorescence quenching in the as cast films, the CT state formation is expected to occur in the sub nanosecond timescale, and its separation into free charge usually occurs on the picosecond or sub-picosecond timescale [32]. This requires the use of ultrafast transient spectroscopies to resolve such kinetics. In particular, transient absorption spectroscopy has been extensively used to investigate the CT states in organic materials for photovoltaics [64, 34, 32, 65].

In this part, we aim at providing direct spectroscopic evidence for the formation of CT states in the blends, and the dynamics and yield of their possible separation into free charge carriers. The different blends with different PCBM contents and morphologies allows to investigate the role of both parameters on charge generation. In particular, the record efficiency 1:0.5 bend [42] is investigated with three different degrees of TB2 aggregation, which will provide indications on the role of morphology on charge generation.

6.4.1. Ultrafast charge transfer in as cast blend

The 1:0.5 TB2:PCBM weight ratio blend as cast on a glass/ITO /Pedot:PSS substrate gives an homogeneous film with no evidence of ordering by π-stacking forming agregates (see figure 6.2 panel a and 6.5, panel

c). For this blend, the fluorescence is quenched by more than 99% (figure 6.7, panel b), indicating a very efficient electronic relaxation of excitons. One can selectively excite the TB2 molecules in the blends with 800nm photons. The same excitation density is used for this films than for the neat TB2 film as cast. The transient absorption data resulting is presented in figure 6.8.

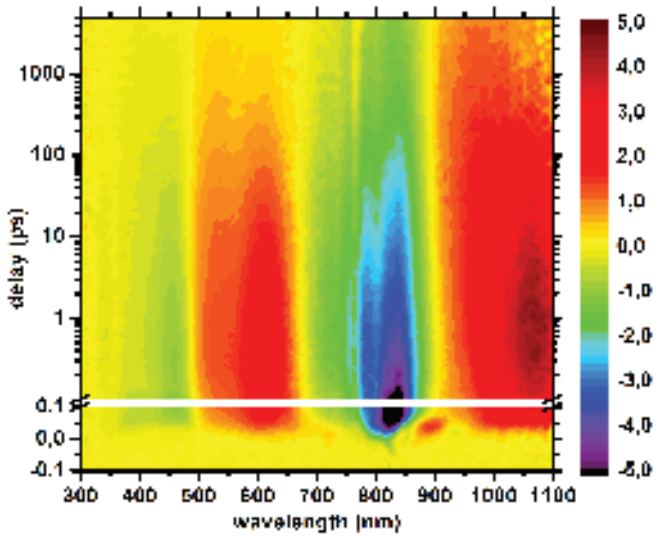

Figure 6.8.: Transient absorption data map of TB2:PCBM blend 1:0.5 weight ratio as cast on ITO/PEDOT:PSS excited at 800nm.

The corresponding transient spectra are presented in figure 6.9. In the first femtoseconds (panel a), the difference spectra matches the early difference spectra measured in pristine TB2 film as cast (figure 6.10). The characteristic induced absorption bands peaking at 710 and 875nm indicates the presence of hot delocalized excitons. This induced absorption competes with the two negative contributions from the GSB of TB2 around 450 and 750nm. This transient absorption rapidly reduces in the sub hundred femtosecond regime together with the buildup of two absorption bands maximum around 610 and 1050nm and possessing a shoulder on the short wavelength side. These features are found only for the blend (see panel b of figure 6.10). Note the presence of the characteristic PCBM GSB as a narrow negative contribution around 340nm,

indicating the depopulation of PCBM ground state.
On the picosecond timescale (panel b of figure 6.9), the photoproduct absorption bands decay in approximately 100ps, together with the PCBM and TB2 GSB signal, to form two broad positive bands in the 520-650nm and 920-1100nm regions. These positive absorptions evolves together with the negative features characteristic of TB2 GSB, and decays on the nanosecond timescale, beyond the maximum delays probed by the present experiment.

The transient absorption kinetics measured at different characteristic wavelengths allows to characterize the time evolution of the different absorption bands. These kinetics are presented in figure 6.11.The 896nm trace kinetic is representative of the short lived photoinduced absorption band observed around 900nm (panel b). It then displays negative contributions from the GSB and SE in the 0.1 to 1ps time range, and later positive signal from the absorption of the long lived species. This initial ESA decays within the first 100fs, and is associated with a decay of the GSB at 808nm (panel a) and the buildup of the positive absorption bands at 529,609 947 and 1052nm. The associated stimulated emission may contribute to the rise of the 947nm kinetic trace.
The DADS associated to the femtosecond time constants (panel a of figure 6.12) indicates the reduction of the early ESA signal in 80fs, and the formation of absorption bands around 550 and 1050nm. The 590fs DADS exhibits a broader absorption reducing around 650nm, very similar to the 780fs DADS obtained from the global analysis of the pristine TB2 as cast film (figure 5.18, panel b). These two DADS are thus attributed to the depopulation of the initial delocalized excitations in TB2 and to some relaxing excited states. These DADS shows the formation of absorptions (negative features) around 550 and 1050nm that matches well the picosecond lived absorptions. The presence of a sharp positive feature centered around 340nm, characteristic of PCBM absorption, indicates the depopulation of the ground state PCBM. The rapid quenching of the TB2 excited state is thus attributed to an energy or charge transfer to the PCBM molecules, with two time constants of 80 and 590fs.
This hundred femtosecond lived ESA (the average lifetime of ESA from

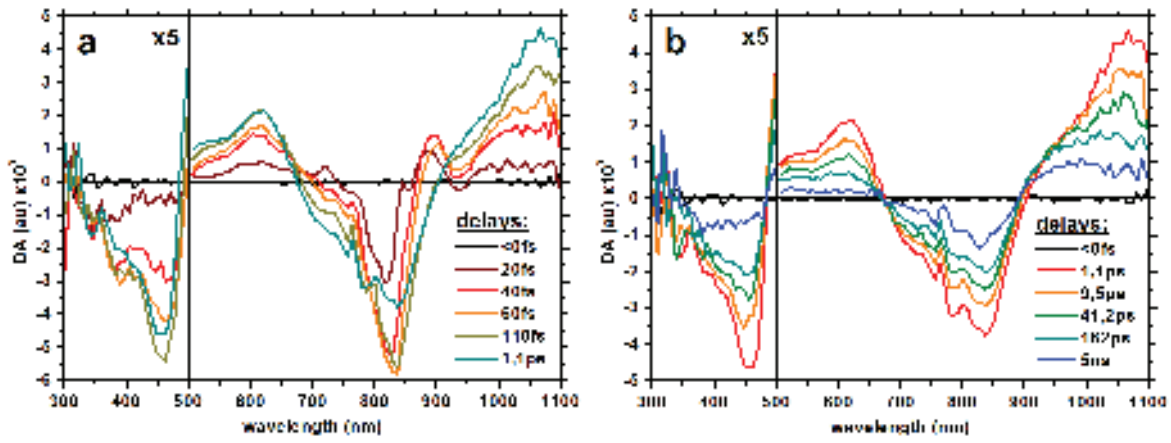

Figure 6.9.: Selected transient absorption spectra of the 1:0.5 TB2:PCBM weight ratio blend as cast on ITO/PEDOT:PSS, showing the buildup of the photoinduced absorption of excited states on the sub picosecond timescale in panel a and the decay of the photoinduced absorption on longer timescales in panel b. The time delays are indicated on the graph. The data is magnified by a factor of 5 on the left part of the graphs.

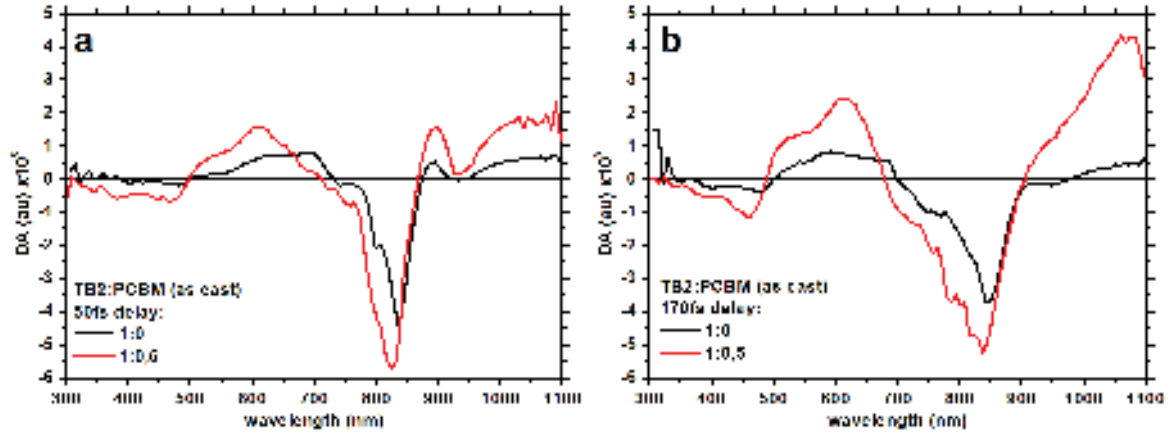

Figure 6.10.: Comparison of the early delays difference absorption signals of neat TB2 and 1:0.5 blend as cast on ITO/PEDOT:PSS. Panel a shows the 50fs delays and exhibits very similar difference absorption spectra. Panel b shows 170fs delays for both films and evidences different species produced from the early excitonic population decay.

the DADS is τ_{blend} =170fs) is in good agreement with the strong fluorescence quenching observed for this blend. The neat TB2 film average fluorescence lifetime measured by the streak camera is τ_{TB2} =33ps, leading to a ratio of lifetimes $\frac{\tau_{blend}}{\tau_{TB2}} = 0.5\%$ while the steady state fluorescence quenching is of about 99% ($\frac{I_{blend}}{I_{TB2}} = 0.9\%$, where I denotes the integrated fluorescence spectrum measured in the same conditions and corrected for the number of absorbed photons).

The picosecond evolution occurs on three different timescales (8.5ps, 165ps and 8.7ns from the global fit). This evolution is characterized by the reduction of the GSB of TB2 and PCBM (771nm trace338nm traces in panel a of figure 6.11) and a decrease of the long lived photoproduct absorption bands (529, 609, 947 and 1052nm traces, panel b). The associated DADS are presented in panel b of figure 6.12, and shows the reduction of the previously quoted signals. The 8.5ps and 165ps DADS are very similar and are thus attributed to the same phenomenon while the 8.7ps is qualitatively different, and corresponds to a different phenomenon. These DADS matches well the calculated and measured difference absorption spectra of TB2 cations in film (figure 5.9). These DADS are thus attributed to TB2 cations, resulting from the TB2 exciton splitting through interaction with PCBM. As the TB2 cations absorption appears with negative contributions from TB2 GSB in the DADS, the corresponding DADS are attributed to the recombination of TB2 cations.
The presence of TB2 cations requires the presence of excess electrons in the films, which are most likely present as PCBM anions. Indeed, the TB2 cation containing DADS shows the presence of PCBM GSB. Even though PCBM anions are known to possess an absorption band around 1050nm (overlapping with the TB2 cations absorption), the higher energy absorption bands are large and featureless (see PCBM anion spectrum in solution in figure 5.8, panel c). As a consequence of the low molar absorption of PCBM, these features are not likely to be identified due to the much higher molar absorption coefficient of TB2 ($\epsilon_{PCBM}(\lambda_{max})$=4900M.cm^{-1} [66] while $\epsilon_{TB2}(\lambda_{max})$=104000M.cm^{-1} [42] in solution). Finally, the long lived absorptions are attributed to CT and CS states formed in the blend.

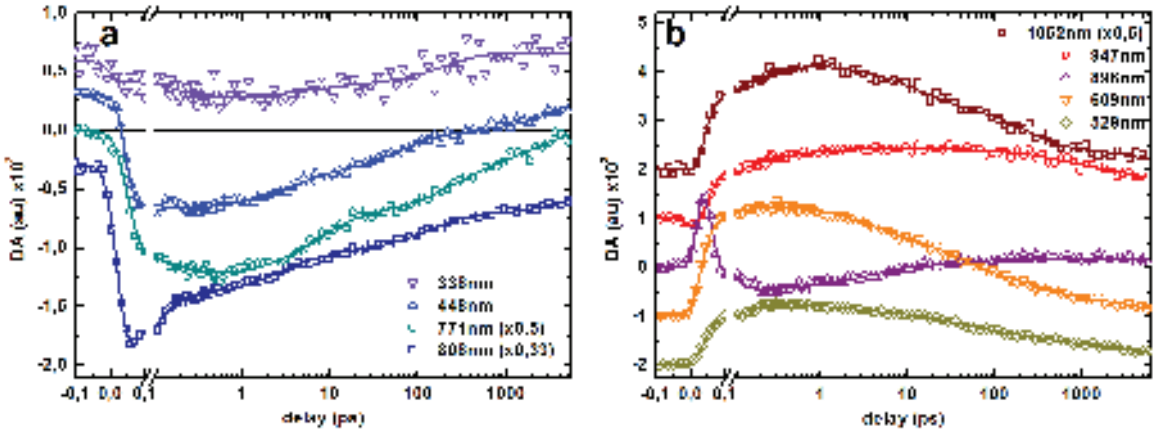

Figure 6.11.: Selected kinetics of the 1:0.5 TB2:PCBM weight ratio blend as cast on ITO/Pedot:PSS, showing BODIPY and PCBM GSB dominated kinetics in panel a and ESA and charged species absorption dominated kinetics in panel b. The measured data are displayed as symbols and the multi exponential decay fits as lines of the respective color.

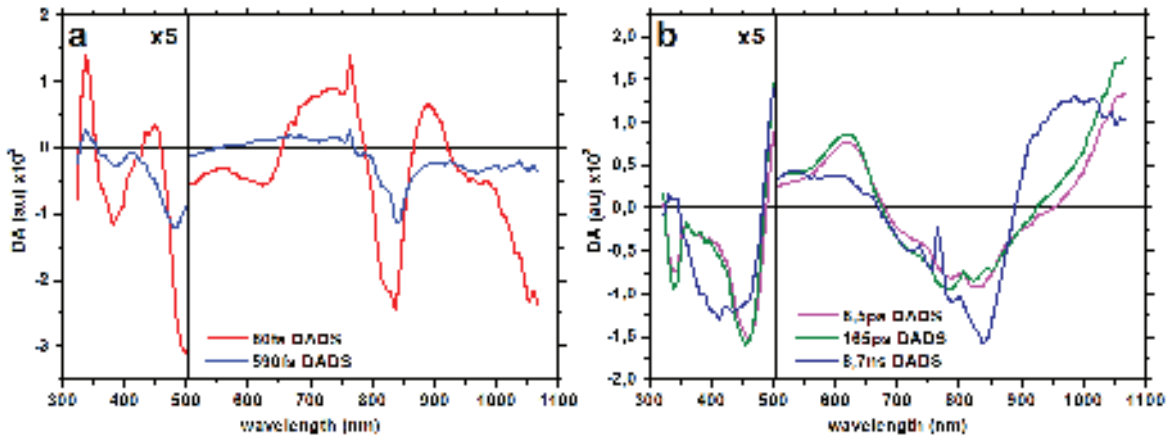

Figure 6.12.: DADS from the global analysis of 1:0.5 weight ratio blend of BODIPY TB2 and PCBM excited at 800nm. The DADS corresponding to excitons are diplayed in panel a, and those associated to charged species are in panel b. The 10fs sub IRF DADS associated to coherent artifacts and errors in chirp correction is not presented. See legend on the graphs.

While the 165ps and 8.7ns DADS corresponds well with the decay of GSB and charge absorption decay (figure 6.11), the evolution of the 950nm kinetic trace shows a rise on the 1-10ps time range (red trace in panel b). Since this wavelength corresponds to the maximum of the 8.7ns DADS (figure 6.12, panel b), this DADS is thus associated with the formation of the nanosecond lived difference absorption. In addition, the 8.5ps and 165ps DADS share very similar difference absorption spectra, and the differences between both in the 600nm and 1000nm region matches well the difference absorption of the 8.7ns DADS. This difference represents 1/4 of the 8.7ns DADS, indicating that the 8.5ps DADS contributes to the formation of 1/4 of the 8.7ns lived species population. The 8.5ps DADS is thus attributed to the formation of the long lived species, and to recombination, as indicated by the presence of negative TB2 GSB features. On the other hand, the 165ps and 8.7ns DADS are attributed to recombination only.

Surprisingly, the 8.7ns DADS does not show evidence for PCBM GSB, suggesting that the associated species is only due to TB2 cations. We can not exclude that the PCBM GSB contributions are present but within the typical noise level, however, since TB2 is ambipolar [42], it could be possible that this long lived charges be TB2 anions and cations signature. This DADS being very similar to the difference absorption mesured in spectroelectrochemistry on films, it is attributed to free charges recombination. Indeed, it is the signature in absorption of the charge carriers participating to the current in the film in the spectroelectrochemistry experiment. Since the latter experiment is performed on neat TB2 films, this may support the hypothesis of ambipolar transport of free charges in TB2. As a consequence, the 8.5ps and 165ps DADS are attributed to interfacial CT states since it presents characteristic features of TB2 cations and PCBM GSB, and contributes to the formation of the long lived CS states. The 8.7ns lifetime of this species is thus attributed to non-geminate recombination, while the 165ps DADS is attributed to geminate recombination. The 8.5ps decay is accordingly attributed to both geminate recombination and charge separation.

Note that even though 1/4 of the CS states population is generated by charge separation of CT states, there is no sign for the formation of the remaining part on the picosecond timescale. It is therefore attributed to the initial quenching of the TB2 excitons in the first femtoseconds, in view of the initial rise in the 950nm kinetic trace of the panel b of figure 6.11. It is not possible to evidence which of the 80fs and 590fs decay of the TB2 excitons mainly forms the CS states, but the DADS suggests that the CT states are mainly populated by the 80fs decay (figure 6.12, panel a).

The photochemistry of this blend is summarized in figure 6.13. The 1:0.5 blend as cast is mainly characterized by the very efficient TB2 exciton quenching by CT and CS state formation in 80fs and 590fs. The two timescales for the exciton quenching might be due to the distribution of TB2-PCBM distances in the blend. The 80fs quenching occurs on similar timescales that the exciton relaxation. This early quenching is expected from the finely intermixed amorphous blend, and is responsible of the very low steady state fluorescence emission of the blend. This close mixing of both molecules may allow for resonant energy transfer from TB2 excitons to PCBM molecules. However, several observations makes resonant energy transfer unlikely to explain the present charge generation. First, there is no indication of TB2 GSB increase that would indicate a hole transfer from PCBM to TB2 in order to produce the TB2 cation, nor increase of the TB2 excited state population. Second, there is no sign of PCBM fluorescence in the steady state fluorescence experiments. Finally, the LUMO energies of TB2 and PCBM are suitable for electron transfer, as a consequence the latter phenomenon is assumed.
The excitonic quenching through electron transfer leads to the formation of interfacial CT states and to free charges (CS states). For this blend, the charge generation yield (CT and CS states) is about 100%. Two populations of CT states are produced. The first one is 8.5ps lived and undergoes charge separation and geminate recombination, and contributes to the formation of 1/4 of the final CS state population. The other CT state population only recombines in 165ps. This indicates that the longer lived CT states are stabilized but can not separate, wether

the shorter lived CT states either recombines or separates, much like the Onsager model picture. The CS states seems to involve only TB2, which is known to be ambipolar.
Assuming similar molar absorption coefficients for the CT and CS states absorption at their maximum in the 1000nm region, only 30% of the generated charges leads to free charges through CS states, leading to an overall 30% yield for free charge generation. This yield would be further reduced by the transport and collection efficiencies. On the other hand, the built in field due to the presence of a top electrode may participate to the separation of CT states, increasing the initial free charge generation yield. The nanosecond lifetime of the CS states generated suggests important non geminate recombination, which is detrimental to charge transport.

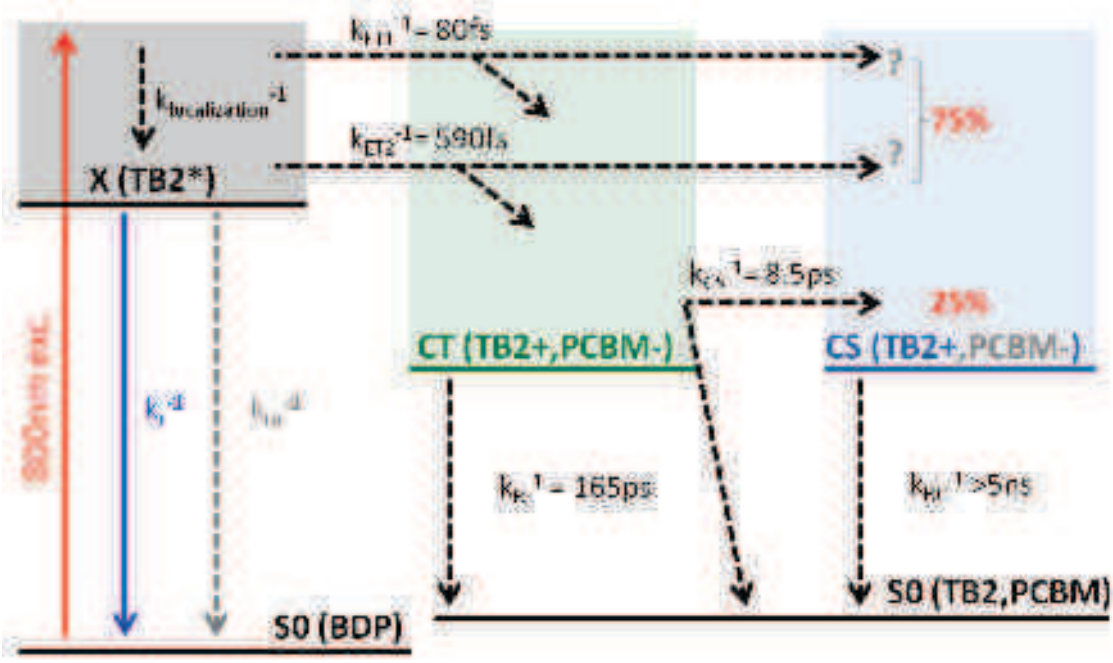

Figure 6.13.: Reaction scheme summarising the photophysics of the 1:0.5 weight ratio blend of BODIPY TB2: PCBM as cast on ITO/Pedot:PSS substrate. Radiative transitions are indicated as plain arrows, non radiative ones in dashed arrows. Grey indicates possible phenomenon that are not observed. The purcentages in red indicates the contributions of the different processes to the formation of CS states.

6.4.2. Ultrafast polaron formation in record efficiency blend

The record efficiency blend is the 1:0.5 weight ratio blend of BODIPY TB2 with PCBM annealed. Annealing influences the films properties and may increase the power convertion efficiency. Indeed, annealing triggers the formation of J-like aggregates of TB2 through π-stacking and iodide-fluor interaction, leading to the delocalization of excitons and the red shift of TB2 absorption may change the fraction of the solar spectrum absorbed. The important intermolecular interactions in agregates contributes to the 2D delocalization of polarons and may increase the transport properties [36]. In addition, aggregates may also slightly change the electronic gap of the donor material and as a conequence, change the open circuit voltage. Finally, it has been shown for P3HT that annealing increases the yield of free charge generation [65].

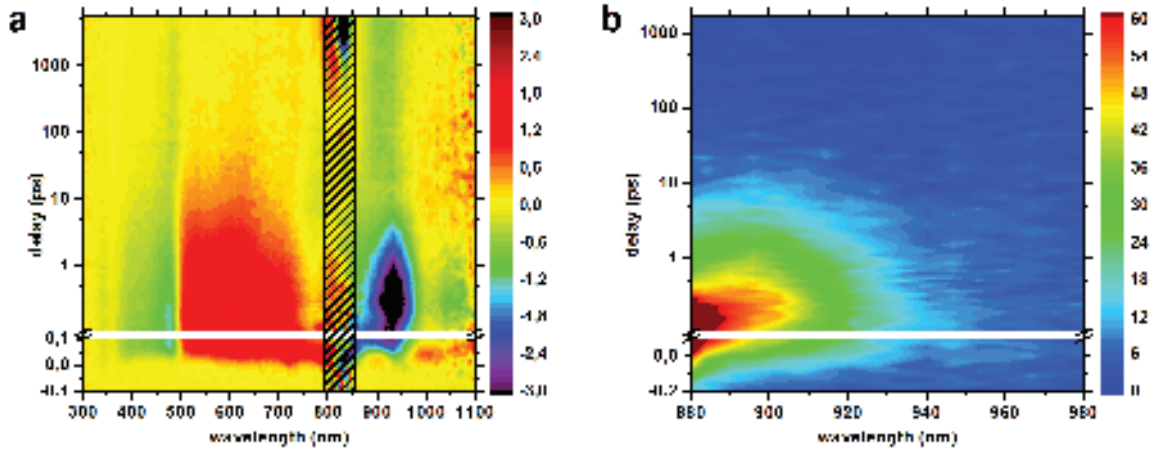

Figure 6.14.: Transient absorption data map of BODIPY:PCBM blend 1:0.5 weight ratio cast on ITO/PEDOT:PSS annealed excited at 800nm (a) and transient fluorescence up conversion data of the same blend under the same excitation conditions (b).

To investigate the effect of annealing on the 1:0.5 weight ratio blend, and understand the phenomena underlying the good overall properties of this blend, we performed ultrafast spectroscopy on blends processed in a similar way than the published record one [42]. The blend is casted on a glass/ITO/Pedot:PSS substrate and annealed at 110^{o}C for 10min.

To allow transient absorption and fluorescence measurement in transmission, no top electrode was evaporated on the device, and the active layer thickness is reduced to a maximum OD of about 0.3. Data are recorded upon 800nm excitation selectively exciting BODIPY molecules in the blend. Both transient absorption and fluorescence spectroscopies were used to characterize this sample. The transient fluorescence measurement used is the optically gated up conversion of the fluorescence. Figure 6.14 gives an overview of the data collected. The transient absorption data map (panel a) shows typical BODIPY GSB signal at 450nm and around 800nm along with a photoinduced absorption ranging from 500 to 750nm and signs of stimulated emission between 850 and 1100nm, in the 0.1 to 1ps time range. The pump region from approximately 750 to 850nm is disregarded due to high scattering of the pump photons by this film drastically decreasing the signal to noise ratio. The transient fluorescence measurement does not allow to fully spectrally resolve the fluorescence spectrum (panel b). It allows nevertheless to characterize the time evolution of the main fluorescence band.

The transient fluorescence kinetic trace is displayed in panel d of figure 6.16. The kinetic trace is fitted with three exponential decays of 60fs, 1.9ps and 16ps. Note that the shorter decay is below the typical time resolution of the experiment (150fs). This represents three excitonic population, labeled as X1, X2 and X3 respectively. The overall decay of the excitonic population is 2.2ps. Comparison with the average decay of the excitonic population of the neat TB2 fim annealed of 3.7ps gives a fluorescence quenching of 60%, while the steady state fluorescence quenching (see figure 6.7, panel a) is calculated to be 22%. This can be explained by the sub IRF decay, which results in a bad estimation of the amplitude associated with the latter decay and resulting in a biased value for the overall decay (calculated as the sum of the decays weighted by their amplitudes and normalized to the sum of the amplitudes). Note that the sub 100fs decay preserving the unresolved fluorescence intensity and giving the correct fluorescence quenching would be a 15fs decay.

The spectral evolution of the TA data are presented in figure 6.15.

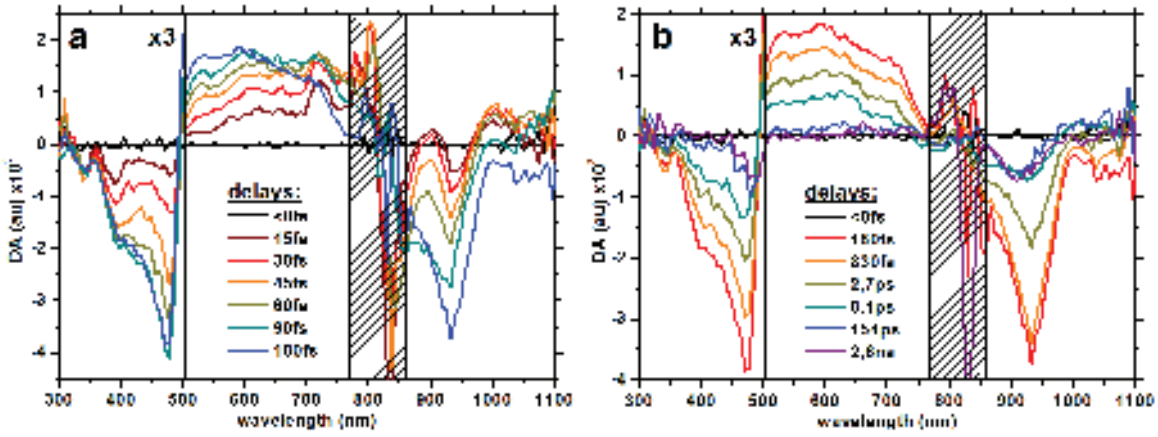

Figure 6.15.: Transient difference absorption spectra measured at different delays for the 1:0.5 weight ratio blend annealed on ITO/PEDOT:PSS. Delays are indicated on the graphs. In panel a is presented the spectral evolution for short time delays, and panel b longer time delays. Stripes hide the spectral regions with low signal to noise ratio due to pump photons scattering.

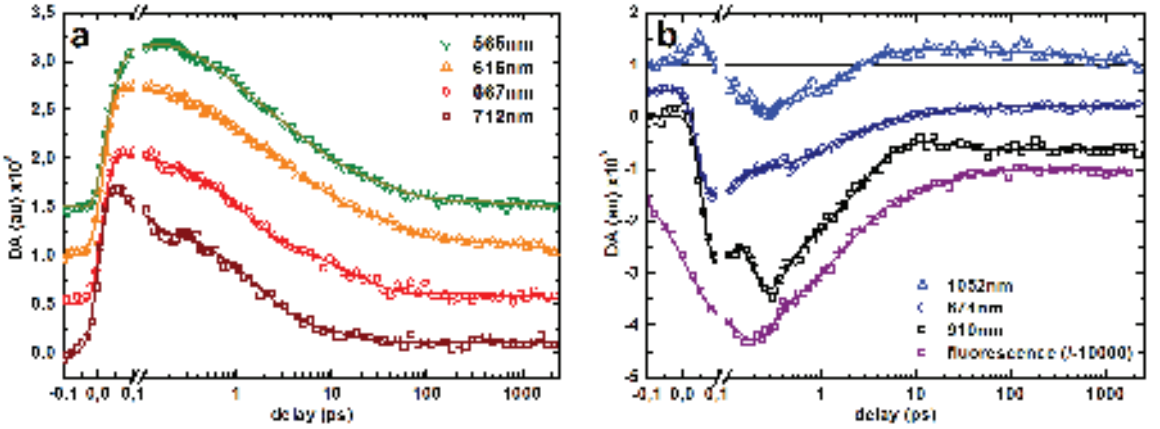

Figure 6.16.: Transient absorption kinetics of the 1:0.5 weight ratio blend annealed on ITO/PEDOT:PSS. Panel a mainly shows the evolution of the ESA. Panel b focuses on SE dominated kinetics along with the fluorescence up conversion signal integrated between 910 and 940nm. The thick lines are multi-exponential fits of the different kinetics.

On the short delays timescale (panel a), the two characteristic positive features peaking at 720 and 900nm and characteristic of TB2 excitons (see the early signatures in panel a of figure 5.21 for the neat TB2 film annealed) are present, together with the negative TB2 SE bands around 920 and 1035nm. The TB2 excitons relaxation to the emissive state in 80fs (see DADS in panel a of figure 6.18 leads to the formation of the induced absorption band extending from 500 to 800nm, much like the early kinetics of the neat TB2 film. This evolution is supported by the hundred femtosecond decay of the kinetic trace probed at 712nm (TB2 "dark" excitons), and the raise of the 565nm trace in panel a of figure 6.16.

However, this absorption band is very different from the relaxed TB2 excitons transient absorption signal found in neat TB2. The decay of this absorption occurs bi-exponentially with time constants of 1.5 and 15ps (global fit) together with the SE signals and the TF trace (panel b). The DADS associated with these decays are presented in figure 6.18, panel a. This absorption band evolving with the TB2 SE on the very same timescale than the TF signal is therefore attributed to TB2 X2 and X3 excitons. Surprisingly, these two populations have very different signatures than in the neat TB2 film. This is very likely to be an effect of PCBM since the DADS as well as the early evolution of the difference spectra shows the characteristic GSB band of PCBM at 340nm, although the latter molecule is not excited by the 800nm pump pulses. This indicates an interaction of these TB2 excitons with the PCBM molecules. This may be the indication of co-crystalline domains (possibly due to the shared lattice parameters of T2 and PCBM) an would require further investigation of the blend morphology. This could also be due to Wannier-like excitons, perturbating the ground state of neigboring PCBM molecules in the vicinity of donor-acceptor interfaces.

After the relaxation of these excitonic populations, a long lived difference absorption signal is formed, very similar to the electroabsorption signal attributed to polarons in neat TB2. This long time spectrum is analysed in a similar way than in the neat TB2 case and compared to

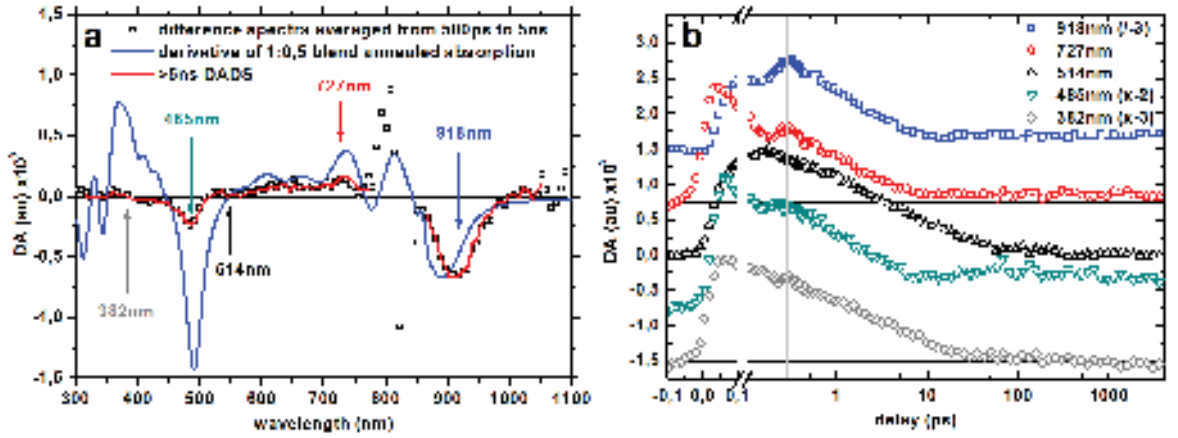

Figure 6.17.: Polarons signature and its hundred femtosecond formation in annealed 1:0.5 weight ratio blend of BODIPY:PCBM on ITO/PEDOT:PSS substrate. On the right, scaled kinetics at characteristic wavelengths of the polaron spectrum (positive, negative and null signal). See legends on the graphs.

the first derivative of the film absorption spectrum in figure 6.17, panel a. The long time spectra and the associated DADS matches well the derivative of the absorption spectrum of the blend and is thus indeed attributed to an electroabsorption signal due to the presence of polarons in TB2. Note that similarly to the case of the as cast film, the very low molar extinction of PCBM hinders the observation of signatures of GSB or any other signal that may indicate the presence of negative polarons in PCBM. The kinetics at the extrema of the long lived signal, presented in panel b, exhibits a rise time in the approximately 10ps regime, and an other rise around 250fs, much like in neat TB2. The 10ps rise occurs in the same timescale than the X3 population decay, and the associated 15ps DADS (panel a, figure 6.18) indeed shows a positive band centered on 900nm, matching well the negative band of the polaronic signal (see DADS >5ns in panel b). The polaron population is thus formed from the X3 population.

The 1052nm kinetic trace in panel b of figure 6.16 shows a small positive absorption in the 5-500ps range, that is shorter lived than the polaron signature (see the tail of the 918nm trace in figure 6.17, panel

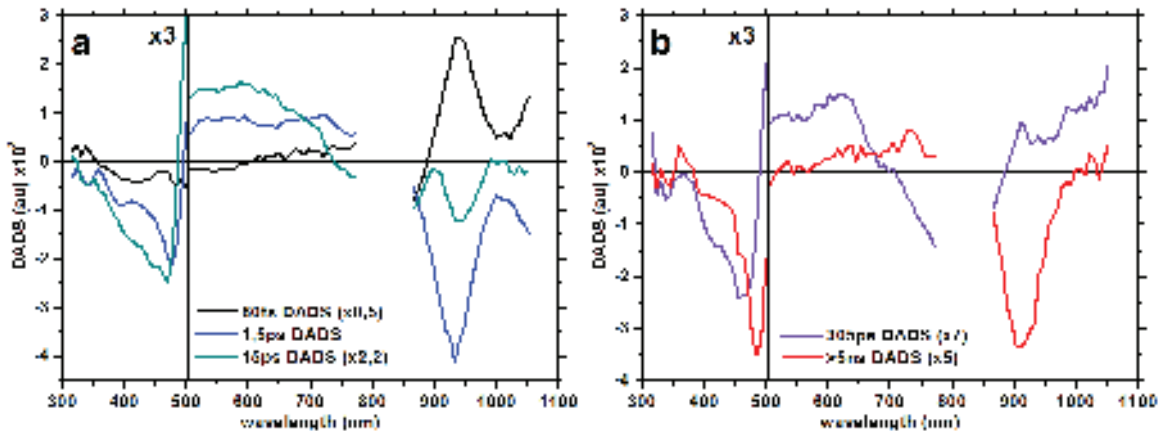

Figure 6.18.: DADS from the global fitting of transient absorption data. On the left are displayed the DADS associated with the exciton population decay, and on the right the DADS associated with long lived photoproduct species.

b). This small signature indicates the presence of an other photoproduct than the polarons. This photoproduct is associated with the 308ps DADS, presented in figure 6.18, panel b and possessing a positive signature in this region. This small amplitude DADS is very similar to the CT state signature found in the 1:0.5 blend as cast (figure 6.12, panel b). This DADS is thus attributed to the recombination of interfacial CT states. The positive feature in the 900-950nm region while the similar DADS for the as cast blend is almost flat and close to zero may indicate the formation of polarons from these CT states. Note the small amplitude of this CT state signal (magnification by 7 in the graph), indiating a small population of CT states.
There is no signature for the formation of these CT states, but according to the ultrafast formation of the latter species in the as cast blend, they might be formed in the first hundre femtoseconds However the weak amplitude of this signal does not allow to assess its formation timescale. These CT states may be formed by the X1 and/or X2 TB2 excitonic populations.

The X1 and X2 populations decay should be associated with the production of CT states or polarons. Comparison with the lifetime of the excitonic population in neat TB2 films shows that the lifetimes of the

three excitonic populations are reduced (0.6, 2.9 and 25ps for the neat film and 0.06, 1.9 and 16ps for the blend). In particular, X1 lifetime is drastically reduced. This indicates a quenching phenomenon induced by PCBM. Since the product signatures includes CT and polarons, this quenching must be associated with charge generation. A global analysis (see annexe A.3) using only the delays superior to 0.15ps, and therefore avoiding the critical short delays timescales (and its kinetics that can not be well fitted with a sum of exponential decays) indicates a decay of about 80fs, the associated DADS is very similar to the one presented here, except that it exhibits a positive narrow feature around 490nm very similar to the negative signal induced by polarons (figure 6.17, panel a). This indicates that this timescale is associated both to the relaxation of the initial dark exciton population X0 into the bright excitonic populations and the polaron formation. In addition, the absence of TB2 GSB signature in the associated DADS suggests the absence of recombination on this timescales.
There is no clear indication of CT state formation neither in the kinetic traces not in the DADS. These states might be formed from any of the excitonic populations.

These observations are summarized in figure 6.19. Comparing with the as cast blend, it is important to note that the exciton quenching is much less efficient in the case of the annealed film. Indeed, in the as cast film, most of the excitonic population is quenched within the first hundred femtoseconds while the annealed film present picosecond lived excitons. It also explains the less efficient fluorescence quenching. A second important remark is that the nature of the free charge carrier is different in both blends. Indeed, while the long lived species in the as ast film are localized into CS states with typical absorption in the visible, the annealed blend produces polarons that are more delocalized and that display hardly any absorption band in the investigated spectral range. In addition, the free charge carriers seems to be longer lived in the case of the annealed blend since the polaron signature hardly decays within the 5ns delay.
CT states are produced in both annealed and as cast blends, but the

amount of CT states produced in the former blend is smaller, so that it hardly appears in the TA signal of the annealed blend. This indicates that the formation of TB2 aggregates through annealing decreases the CT state formation, and points out the influence of morphology on charge generation by preventing the formation of bound interfacial states.

The 1:0.5 blend annealed photochemistry, when compared with the neat TB2 film annealed, shows that the presence of PCBM facilitates the formation of free charges, as indicated by the faster kinetics of the X1 and X3 populations. As a consequence, the yield of polaron formation is expected to be higher. However, the absence of polaronic transition in the probed spectral window does not allow to compare the amount of polarons formed. Indeed, the electroabsorption signal depends on the concentration of charges but also on their spatial distribution and on the dielectric constant. The last two parameters are unknown an the latter is probably change by the presence of PCBM in the blend. The excitonic population can not be used neither to estimate the number of exciton quenched by charge transfer. Indeed, the DADS associated with their decay presents GSB signatures indicating that part of them recombine. Finally the GSB can not be used since the initial and final amplitude of GSB is unknown due to the overlapping contributions of other species.

To conclude, the efficiency of the TB2:PCBM 1:0.5 weight ratio blend is limited initially by the X2 and X3 excitonic population that is not completely quenched by charge transfer to PCBM. It represents 13 to 37% of the overall excitonic population (assessing a 15fs or 60fs decay of the X1 population, respectively). Finally, some CT states are formed and recombine, which contributes in reducing the yield of charge generation. As a consequence, the maximum free charge generation yield is of 63 to 87%, which is much higher than the 26% internal quantum efficiency measured on a device using the same active layer (see annexe A.5). This indicates that the main limitation is not the charge generation but later processes such as charge transport and collection. Nevertheless, the initial charge generation processes are not optimal, and could

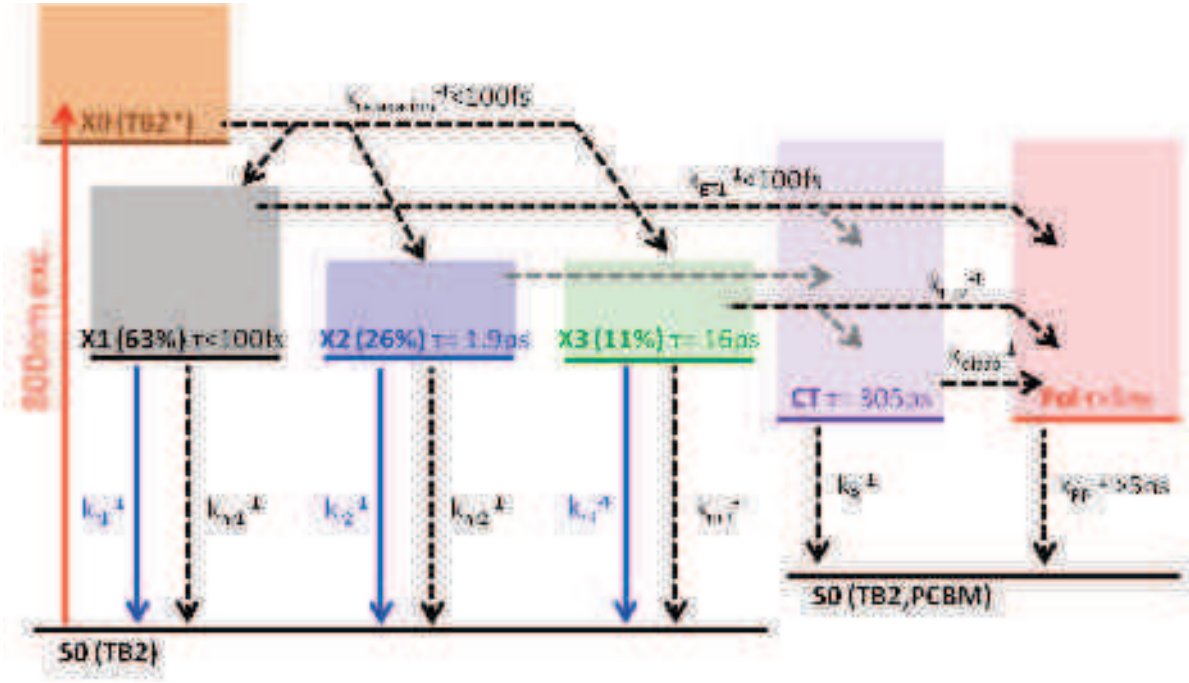

Figure 6.19.: Reaction scheme of 1:0.5 weight ratio BODIPY:PCBM blend annealed on ITO/PEDOT:PSS substrate and excited at 800nm. Lifetimes of electronic states are indicated, and the known rate constants of the different processes are displayed aside the arrows for radiative transitions and the dashed arrows for non radiative transitions. The possibe but not observed phenomena are displayed in grey. The repartition of the excitonic population in the different relaxed states is indicated in purcent in parenthesis. For a 15fs decay of the X1 population, the distribution is changed into 87, 9 and 4% for X1,X2 and X3 respectively.

participate to increasing the overall efficiency. In addition, it points out the importance of the morphology on the charge generation process as well as on the nature of the free charge carriers.

6.4.3. Influence of morphology on charge generation

To study the influence of the blend morphology on the photophysics of the films, three blends with a 1:0.5 weight ratio mixture of BODIPY and PCBM have been prepared on ITO/Pedot:PSS with different annealing conditions. This PCBM loading permits the formation of TB2 agregates

upon annealing. The degree of BODIPY agregation can be seen in the steady state absorption spectra through the increase of the red shifted absorption characteristic of the TB2 J-like aggregate (figure 6.20, panel a). Two films were annealed for10 min at 75 and 110 ^oC, leading to a different amount of agregated BODIPYs, and are compared with the as cast blend.

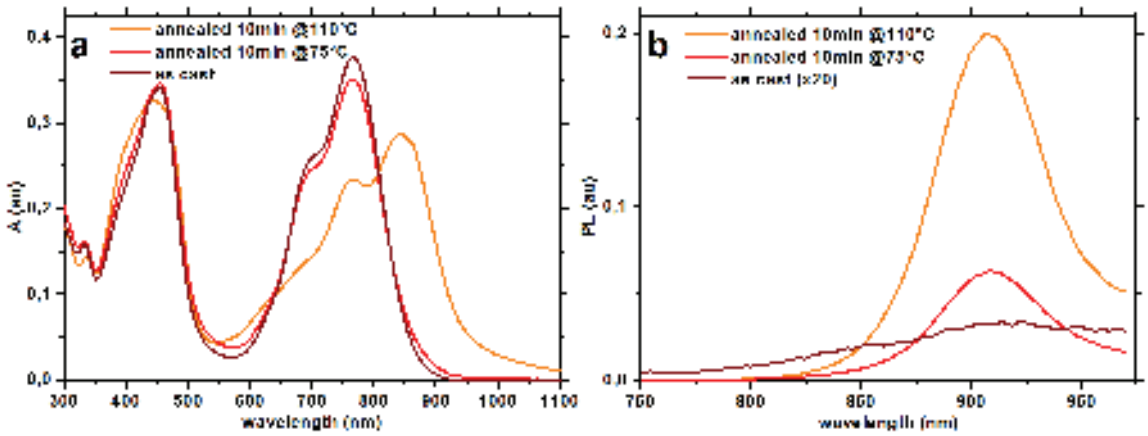

Figure 6.20.: Absorption (panel a) and photoluminescence (panel b) of the 1:0.5 blends on ITO/PEDOT:PSS for different annealing conditions.

The blend annealed at 75^oC shows similar global behaviour than the as cast one. This is expected from the similar absorption spectra of both films. Selected difference spectra are presented in figure 6.21, and shows the similarity with the as cast blend. The difference absorption spectra are normalised for the same number of absorbed photons. As a consequence, we can observe a reduction in the CT species absorption peaking at 610 and 1050nm when annealing (panel b). The longer lived CS absorption is also reduced. This indicates that the latter species are less populated when the TB2 molecules in the blend starts aggregating. However there is no obvious spectral signature of polaron formation. Note that given the very low concentration of aggregated TB2 (see the low amplitude J-like aggregate band in the absorption spectrum of the 75^oC annealed film), and the small amplitude of the electroabsorption signal characteristic from polarons, the latter species, in present, can

hardly be detected.

The fluorescence spectrum of the 75^oC annealed film is less quenched than in the as cast film, as shown in figure 6.20, panel b. In addition, the fluorescence spectrum is very similar to the one of aggregated TB2. This signal coud be used to identify the presence of TB2 excitons in aggregated TB2. The kinetic traces at 950nm of the three blends is presented in figure 6.22, panel a. This wavelength is characteristic of the fluorescence of the TB2 aggregates, and contains also GSB contributions from TB2. It also contains positive contributions from the long lived CS states. Comparison of the kinetic traces at this wavelengths shows a reduced difference absorption signal going from the as cast to the 75^oC annealed film, in the 0.1-10ps range. The difference of the as cast and 75^oC annealed film kinetic traces is presented in panel b, and is superimposed with the 110^oC annealed film kinetic trace. Both traces are very similar and are therefore attributed to aggregated TB2. The amplitude of the difference signal is 7 fold lower than the 110^oC annealed film, which is not in good agreement with the approximately 60% quenching of the steady state fluorescence spectra. This may be due to a later aggregation of TB2 since the fluorescence measurement has been carried out after the TA experiment. Nevertheless it indicates the presence of excitons in the TB2 aggregates. This also suggests that there might be a small amount of polarons formed in the TB2 aggregates.

In the presence of TB2 aggregates, the excitons formed in the bulk but are only partially quenched by the sub 100fs charge transfer, and by the later charge transfer on the picosecond timescale. On the other hand, in the amorphous TB2 phase, most of the excitonic undergoes charge transfer to PCBM which results mainly in a sub 100fs excitonic lifetime. The intermediate 75^oC annealed film presents a small amount of TB2 aggregates and presents TA signatures of both the amorphous and aggregated phases.

After charge transfer, charged species are formed in both cases but the nature of the charge carriers is different. Indeed in the case of TB2

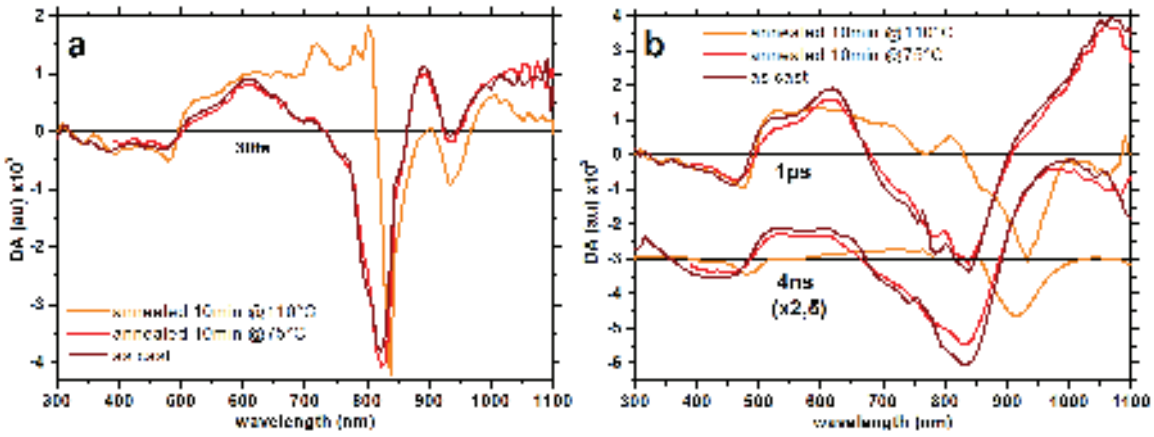

Figure 6.21.: Spectral evolution of the TA signals of the 1:0.5 blends on ITO/PEDOT:PSS for different annealing conditions. Panel a presents the early delays while panel b shows the longer timescales. Delays apprear on the graphs, the 4ns difference absorption spectra are multiplied by 2.5. The difference absrption spectra are normalized to the number of absorbed photons.

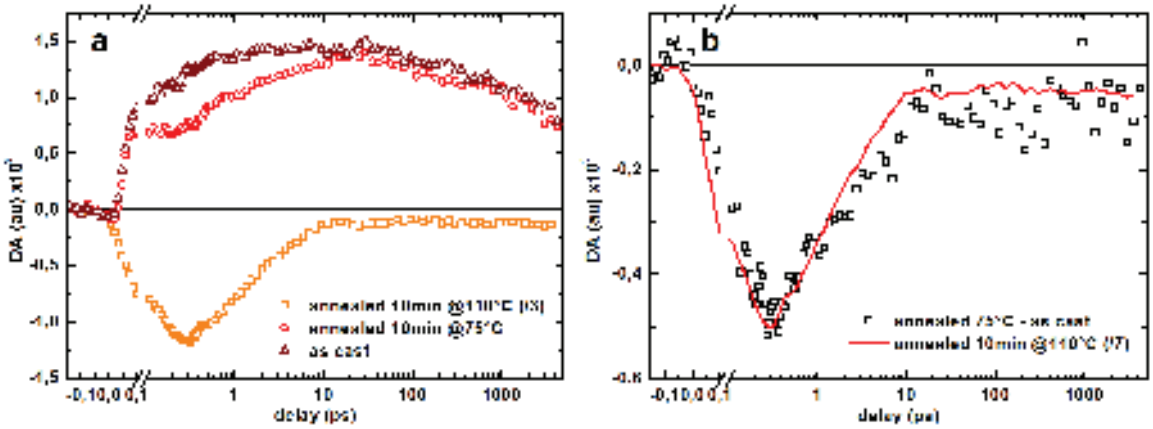

Figure 6.22.: Transient absorption kinetics measured at 950nm (panel a and b respectively) for 1:0.5 blends of BODIPY and PCBM on ITO/PEDOT:PSS for different annealing conditions. The kinetics are normalized to the number of absorbed photons. Panel a compares the kinetics for the different ennealing conditions. Panel b shows the difference of the kinetic traces of the blend annealed at 75°C and the as cast blend. This difference is compared with the kinetic trace of the blend annealed at higher temperature.

agregates, mainly polarons are formed whereas in the absence of agregates, bound CT and localized CS states are mainly formed (see DADS in figure 6.12, panel b). This aggregated form allows the formation of delocalized charge carriers. These polarons have a delocalized electronic wavefunction extending over several molecules. On the other hand, the as cast films are dominated by CT states, that are bound at donor-acceptor interfaces, and to CS states, that can be viewed as less bound pairs of charges.

The present annealing conditions of the intermediate blend does not allow to evidence the presence of polarons. To go further in the study of the morphology impact on charge generation and evidence polaron formation, a higher TB2 aggregate concentration film should be studied. Fore instance a 110^{o}C annealing for 5min should allow the formation of more TB2 aggregates. In addition, broadband transient fluorescence measurements should allow to have indications about the nature and lifetimes of the excitonic populations in the amorphous and aggregated TB2 domains. Indeed, the fluorescence spectrum of the amorphous TB2 is broader than the aggregated TB2 one, and should allow to disantangle both signatures. In addition, the opto-electronic properties of such blends as an active layer in an OSC could be characterized to observe the effect of the nature of the charge carriers on the transport and collection properties.

To conclude, it appears that annealing affects the charge generation through the formation of TB2 aggregates. The TB2 aggregates have a very different photochemistry than the amorphous TB2, leading to the formation of different free charge carriers. The exciton quenching is much more efficient in amorphous TB2, but leads to the formation of bound CT states that recombines and therefore do not participate to the free charge generation. On the other hand, aggregated TB2 leads mainly to the formation of polarons. These delocalized charge carriers are expected to have better mobilities in the blend, and their longer lifetime in comparison with the CS states in amorphous TB2 indicates a less efficient charge recombination, which is less detrimental to charge trans-

port. The incomplete quenching of excitons in aggregated TB2 should thus be compensated by a more efficient free charge carrier generation, as expamplified by the absence of bound CT states recombining (165ps lived CT states in the amorphous blend).

6.4.4. Influence of PCBM loading on charge generation in blends with amorphous TB2

In the work of T.Bura and coworkers [42], a set of different TB2:PCBM weight ratios were tested in OSC. Changing the PCBM concentration has an impact on the power conversion efficiency. Surprisingly, cells with very low PCBM content gave honorable PCE (3.6% for a 1:0.2 TB2:PCBM weight ratio blend). It is thus important to understand the effect of the PCBM loading on the initial photophysics of the active layer.

Now that the photochemistry of charge generation in as cast 1:0.5 weight ratio blend is understood, we can use it as a reference system for charge generation in blends containing amorphous TB2. The steady state absorption spectra in figure 6.6 and 6.7 indicates that the 1:0.1 blend as cast on fused silica, the 1:2 blend annealed on ITO/PEDOT:PSS do not present significant contribution from the absorption of the J-like aggregate band of TB2. Their photochemistry indeed presents signatures of amorphous CT and CS states, very similar to the reference 1:0.5 as cast blend on ITO/PEDOT:PSS (see the TA maps in annex A.4).

Global analysis of the two films is performed. The time constants are summarised in table 6.1 (an additionnal 10fs time constant is used for the global fits but is not displayed) and some DADS are presented in figure 6.23, with the results obtained for the 1:0.5 blend as a comparison. Note that the 1:2 blend requires one less time constant to fit the singular kinetics. The time constants found by blobal fitting are very similar to the ones of the reference blend. The main difference between the blends lies in the sub picosecond regime, as shown by the kinetics traces in panel b of figure 6.23. Given the similarity of the time constants, of the

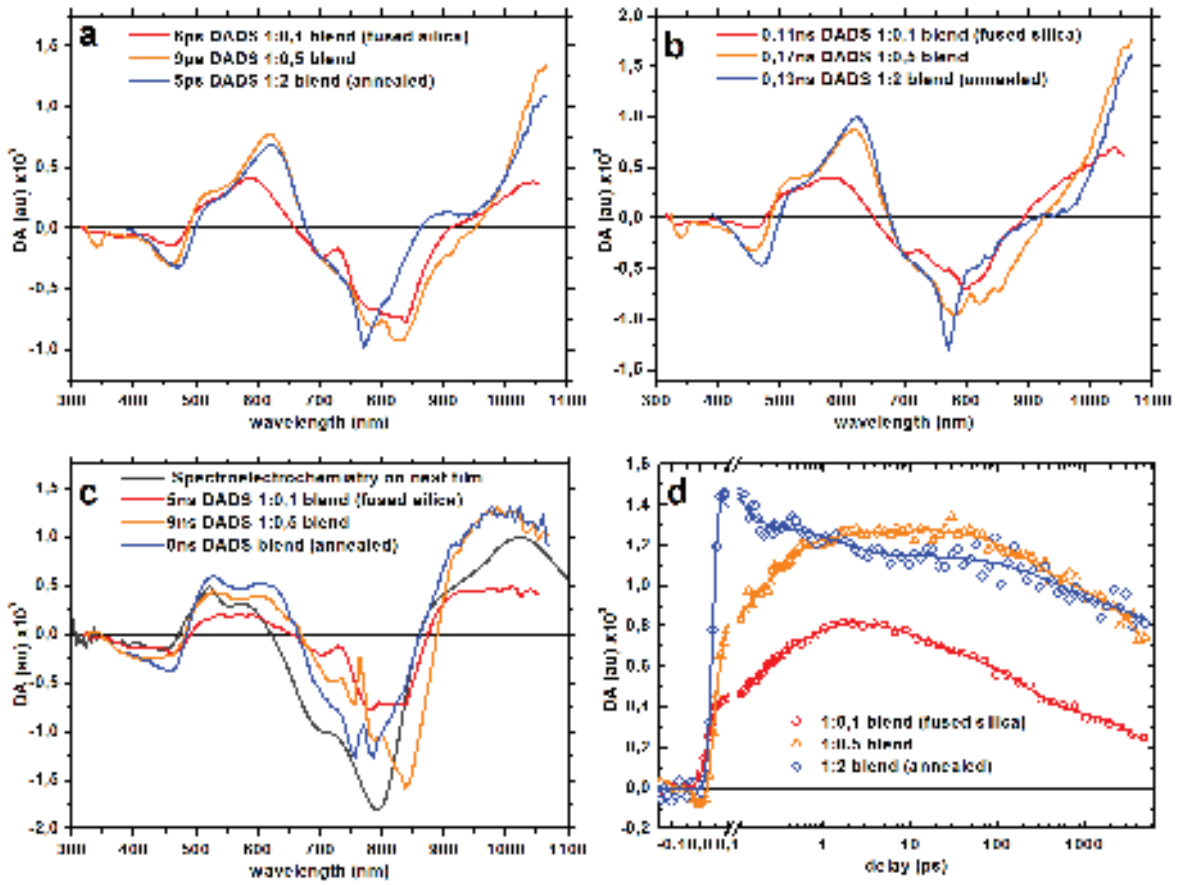

Figure 6.23.: DADS of CT and CS recombination for different BODIPY:PCBM blends containing amorphous TB2. Panel a shouws th DADS associated with the charge separation of CT into CS states. The DADS associated with the recombination of bound CT states are in panel b, and the DADS associated with the non-geminate recombination of CS states are in panel c. Note that around 800nm, the pump photons gives raise to artifacts and balanced signal to noise ratio. Panel d shows the kinetic traces of the difference absorption measured at 950nm, where the CS state absorption is maximum. In all the figures presented, the signal is corrected to correspond to the same amount of absorbed photons. See legend for details, by default, blends are cast on ITO/PEDOT:PSS.

DADS and of the time constants, the photochemistry of these blends is discussed on the basis of the 1:0.5 blend (as cast) reaction scheme (see figure 6.13). The shorter time constants in table 6.1 are attributed to the excitonic populations. Note that only the shorter lived population is present in the 1:2 blend. The longer time constants are attributed to the two CT states populations (CT1 contributes to the formation of CS states, CT2 is essentially recombination), and to the recombination of CS states, accordingly to the model system.

There is no striking difference in the lifetime of the CT and CS states when increasing the PCBM weight ratio. However, the lifetime of the excitonic populations is significantly reduced when the PCBM concentration increases. In particular, in the 1:2 blend, the X2 population of relaxed excitons is absent, indicating a more efficient quenching of the excitonic population. This is in line with the absence of detectable transient fluorescence signal for this blend (not shown). The important concentration of PCBM, which represents almost two PCBM molecules for one TB2 , may significantly increase the charge transfer process probability by offering a higher density of states for the electron (Fermi golden rule).

PCBM ratio	τ_{X1} (fs)	τ_{X2} (ps)	τ_{CT1} (ps)	τ_{CT2} (ns)	τ_{CS} (ns)
0.1**	100	0.7	6 (0.4)	0.11 (0.75)	5 (0.5)
0.5	80	0.6	8.5 (1.3)	0.17 (1.75)	9 (1.25)
2*	70	-	5 (1.1)	0.13 (1.6)	8 (1.25)

Table 6.1.: Summary of time constants fitted by global analysis of the transient absorption data. The amplitudes associated with the lifetimes appears in parenthesis. The maximum of the DADS in the infrared region is used to determine the amplitudes. * annealed film. ** fused silica substrate.

The efficiency of charge generation can be estimated using the amplitude of the CS states difference absorption signal from the global analysis. In the absence of collecting electrodes, the only fate of these free charge carriers is to recombine. The associated DADS are presented in panel c of figure 6.23, and corresponds to the same amount of absorbed photons. The differences in the shape of these DADS comes from

the different TB2 GSB contribution, specially in the case of the 1:0.2 blend. The difference in the average dielectric constant due to the different PCBM fraction may also play a role. In the 900-1100nm region, the negative contribution from the TB2 GSB is very low, and reflects mainly the absorption of the CS states. The latter graphs shows that the concentration of CS states is higher (and almost equal) for the 1:2 blend and the reference blend, while it is 2.5 times lower for the 1:0.1 blend (using the amplitude at 950nm). This shows that the 1:0.1 blend is less efficient in free charge generation, which may be explained by a lower CS state generation at early times, as indicated by the lower overall amplitude of the 950nm kinetic trace shown in panel d. Surprisingly, event though the exciton quenching is much more efficient in the 1:2 blend than in the reference one, the final concentration of CS states is similar, and so are the amplitudes of the CT recombination DADS, excluding the formation of bound CT states. This may result from a negative contribution (GSB) of the large absorption transition present in this wavelength range in the absorption spectrum of the 1:2 blend (figure 6.2, panel b), lowering the DADS spectrum in this range.

In summary, in amorphous blends, the increase of the PCBM fraction in the blend increases the free charge generation yield. For high PCBM fraction (2 for 1 TB2), a significantly faster charge transfer occurs, and is attributed to the higher probability of electron transfer due to the higher density of acceptor sites. There is no clear evidence for an increased CT state dissociation, as pointed out by studies on similar systems [67]. However, even though the charge transfer efficiency is nearly 100% for the 1:2 blend, the same blend used in OPV cells gives only 1% PCE [42], indiacting that the efficiency of charge transfer is not sufficient to achieve a good active material. In this case the high PCBM loading results in the absence of aggregated TB2, and therefore results in amorphous TB2, which has been shown to bear different free charge carriers, with higher recombination rate. The low relative TB2 content may also significantly lower the average hole mobility [42], resulting in poor hole transport [67]. The effect of PCBM loading on annealed films is also an important issue as the increase of PCBM leads to a lower contentration of TB2

agregates.

7. Conclusion

Using transient absorption and fluorescence spectroscopies, we investigated TB2, a novel small molecule for use as donor in OSCs. The systematic study of different blends of the latter molecule with PCBM as an acceptor allowed to understand the processes of charge generation occuring in the record efficiency 1:0.5 annealed blend.

The study of TB2 in solution and in film allowed to evidence the influence of intermolecular interactions on the photochemistry of TB2. We showed that the excitation of TB2 in solution, in an as cast or annealed in film leads to different excited state species, and their decay occurs throug different processes. In particular, the excitons generated in the films have a shorter lifetime and leads to the formation of polarons. These observations are rationalised with the morphology of the two films, characterized by steady state absorption and electron diffraction, and showing the presence of J-like aggregates of TB2 when annealed. The initial excitation is delocalized in the films over a few TB2 molecules but relaxation leads to the formation of either localized, Frenkel like excitons in amorphous TB2, while in aggregated TB2, the excitons remain delocalized as inferred from the transient spectro-temporal properties. This leads to different relaxation paths or photochemistry of excitons. In particular, aggregated TB2 leads to the formation of polarons while amorphous TB2 excitons mainly recombine.

Different blends of TB2 with PCBM were produced, with varying PCBM contentration and annealing conditions. The blends were characterized by steady state absorption and fluorescence, as well as with TEM and electron diffraction. These different techniques provide evidence for as cast films being mainly amorphous and that the aggrega-

tion of TB2 is reduced when the PCBM fraction in the blend is increased (annealed films). In addition, it was shown that the nature of the substrate changes the blend morphology. As a consequence, the different films studied presents various morphologies. The steady state fluorescence measurements permitted to evidence and quantify the quenching of the TB2 exciton fluorescence, through the presence of PCBM with increasing concentration.

The investigation of TB2 blended with PCBM in a 1:0.5 weight ratio, with different annealing conditions showed that TB2 undergoes charge transfer with PCBM efficiently, and that the charge generation process strongly depends on the aggregation of TB2. In particular, the nature of the free charge carriers is very different. We obtained indirect evidence for polaron formation in the annealed blend, while the as cast blend showed mainly the signatures of localized bound CT states and CS states. In both cases, the charge generation occurs on two timescales [56]. First, a sub picosecond charge transfer produces mainly free carriers, and on a later picosecond timescale, free carriers are produced from excitons in the case of the annealed blend, and from CT states in the case of an as cast blend. The sub picosecond exciton dissociation occursbefore thermal relaxation and localization are completed.

The systematic study of the blends with different PCBM content showed that the morphology of the blends has a strong influence on the photochemistry. In the case of as cast blends, presenting amorphous morphology, the increase of PCBM fraction continuously increases the exciton quenching. This is explained by the higher density of acceptor states for the donor exciton. The free charge generation increases with the PCBM content.

The analysis of these blends suggests that the record efficiency blend possesses a specific morphology allowing for an optimal phase segregation between donor and acceptor domains. From the exciton quenching, the quantumu efficiency of free charge generation is estimated to be at least 63%. This efficiency is limited by the non radiative recombination

of excitons on the picosecond timescale and by recombination of CT states that only partially contribute [35] to the formation of polarons. The former explains the incomplete fluorescence quenching observed for this blend.

While the localised CS states found in amorphous blends possess an absorption in the probed wavelength range, only indirect indications for polarons in annealed blends is provided through an electroabsorption signal. The quantification of final polaron concentration in annealed blends, in order to determine the charge generation yield, would require a direct observation of the polarons through an absorption band. Such a polaron absorption band should be located in the infrared and would require the detection of near-infrared photons in the pump-probe experiment. Such a detection system is under development in the lab.

The present accessible wavelength range going from 300 to 1100nm presents the advantage of monitoring most of the GSB and excited state features. In particular, it allows to observe the PCBM GSB which is of prime interest to justify the presence of CT states. It also points out issues about the nature of the long lived CS states since they do not present the signature of PCBM, suggesting that TB2 bear both free holes and electrons. Further investigation is needed to understand the nature of the long lived charge carriers, and this question may also be adressed in the case of polarons in aggregated TB2.

This systematic study of BODIPY:PCBM blends shows that the record efficiency of the 1:0.5 blend annealed can be improved since unquenched excitons are observed undergoing non-radiative recombination as in pristine TB2 films. This indicates that a portion of the excitonic population does not participate in the formation of charges and thus limits the internal quantum efficiency from the start. In addition, bound CT states are produced in this blend and are likely to recombine, however they seem to contribute at least partly to polaron formation. Comparison of the estimated free charge generation yield with the internal quantum efficiency measured on the same blend shows that the transport and col-

lection of free charges significantly limits the efficiency of OSC using this blend as an active layer.

In terms of an outlook, the as cast blends are an interesting basis for the investigation of the effect of an applied bias on the OSCs on the charge generation [68] since these blends shows an important concentration of bound CT states that an induced electric field may help to separate, as expected from the Onsager model.
Additional investigation of the annealed blends is needed, in paticular the detection of the polaronic transitions in TB2 aggregates could provide useful information on the amount of photogenerated charges as well as to have direct information about the timescale of formation of these free carriers.
The role of the excitation wavelength is also an interesting issue, in particular the blends photochemistry upon excitation of the acceptor molecule in the UV and the role of the reulting excess energy on the charge generation process.
A supplementary issue of interest is the observation of exciton diffusion, which can be studied using TF anisotropy measurements.
Further morphology characterization should be interesting to better understand the film organisation at the donor-acceptor domain size in the case of annealed films. The presented TEM and electron diffraction patterns are only qualitative determinations of the film morphology, and an improved characterization would be interesting in the view of reducing the amount of unquenched excitons by a better morphology control.

Part III.

Anabaena Sensory Rhodopsin: an ultrafast natural photoswich

8. Photoisomerization in Retinal Proteins

8.1. Motivations

Retinal proteins are found in many reigns of life, from mammals to archea. These proteins are light-sensitive, and use visible light as energy to serve many physiological purposes, such as photon sensors, ion pumps and channels [69]. Retinal proteins are thus a versatile basis for solar energy conversion. No less than four retinal proteins are present in the archea *halobacterium salinarium* [70], with the ion pumps bacteriorhodopsin (bR) and halorhodopsin (hR), pumping protons and chloride respectively, and the two sensory rhodopsins responsible of the bacteria phototaxis (SRI and SRII).
These various applications results from the protein optimization for a given application thanks to natural selection.

One may want to take advantage of these available biological systems to avoid the long ingeneering of sythetic systems for the same purpose, from scratch. For instance, studying efficient photoisomerizing retinal proteins, and understanding the key parameters of this effect inspired the synthesis of artificial photoswitching molecules[71, 72]. This may have important applications in the design of efficient molecular motors[73] or nano-manipulators[74, 75].
On the other hand, one may want to improve the yield of the relevant phenomena occuring in the photochemistry of these proteins, in order to directly use the proteins as tools in biophysical research. Retinal proteins can be used for fluorescence microscopy applications [76], to create light controlled action potentials for fundamental neurobiology applications [77] or measure action potentials [78, 79].

For all these reasons, the understanding of retinal proteins photochemistry, and its link with the protein structure and composition, may help in developping new micro and nano applications triggered by light.

8.2. Retinal Proteins

The retinal proteins are a family of transmembrane proteins composed of a 7-helix amino acid structure, referred to as the opsin. The proteins are expressed by living forms across cell membranes. The retinal proteins possesses a retinal chromophore bound to a lysine residue, through a protonated Schiff base (see figure 8.1).
The protonated Schiff base retinal (PSBR) is the solar energy receptor. Its main absorption band is located in the visible range with a maximum molar absorption coefficient up to $50000 M.cm^{-1}$, located between 400 and 650nm[80], depending on the opsin. This makes PSBR a rather efficient visible light absorber.
The photochemistry of retinal proteins is a consequence of the PSBR photochemistry, which primarily converts the photonic energy into vibrationnal energy in the first picoseconds. The latter excess energy is transferred to the opsin to accomplish the biological function on longer timescales of micro- to miliseconds.

One may resume the PSBR photochemistry by the scheme presented in figure 8.2. This simple scheme accounts for the observed photochemistry of PSBR. Excitation of the ground state of the PSBR with visible light leads to the formation of an excited state in the Franck Condon region. Relaxation of the excited state leads to the formation of the relaxed excited state, that might be in a reactive geometry. The reactive geometry excited state may lead through a conformation change to the ground state of the PSBR in either product form accessible (ground state of the initial form or any produt form). The non reactive excited state configurations, if populated (note that the reactive/non reactive geometries might already be present in the ground state, but in the ab-

Figure 8.1.: JSmol view of the *Anabaena* Sensory Rhodopsin (ASR) structure (exported from RCSB protein data bank, protein code: 1XIO). Amino acids forming the opsin are labeled with different colors. This representation evidences the 7 helix structure typial of retinal proteins. The PSBR is the grey structure inside the protein structure.

sence of evidence for that phenomenon, and for sake of simplicity, it is not represented).
Dedicated terminology for this scheme is being employed, naming the different steps of the PSBR photoreaction. The relaxed excited state is referred as the "I" intermediate, and usually exhibits fluorescence. The newly formed, vibrationnally hot products are termed "J" intermediates, and leads to the relaxed product form, called "K" form. Later products due to interactions with the protein in retinal proteins have been neamed the same way (see figure 8.4).

Figure 8.2.: Reaction scheme describing PSBR photochemistry. S_0 and S_1 indicates the ground and excited state respectively, FC denotes the Franck Condon geometry, R the reactive geometry, nR the non reactive one and P the product(s) geometry.

8.2.1. Examples of retinal proteins: rhodopsin and bacteriorhodopsin

The reactant and product geometries of the PSBR can vary a lot, since possibly any isomeric form could be synthetized and put in solution, and may lead to a variety of products. However, the reactant conformation of PSBR in opsins is reduced, in general to not more than two ground state conformations, the relative concentration of which depends on illumination (light adaptation , see below). The most striking retinal protein is the rhodopsin (Rh). This protein is responsible of vision in vertebrates. The first step of vision is the isomerization of the PSBR from a *11-cis* to a *all-trans* form in 200fs[81]. This ultrafast isomerization is accompanied with a quantum efficiency of 64-67%[82], making it the most efficient isomerization observed yet. In addition, this isomerization happens in a coherent way[83] (Notion further described in section 8.4). However, Rh is not photostable, and a lot of progress has been made in decifering the photochemistry of protein-bound PSBR by the study of the bR protein, which is much more resistant and still possesses a high isomerization quantum yield. Thus bR is used as a benchmark system in order to investigate retinal isomerization thanks to its good photoresistance, even though its efficient *all-trans* to *13-cis* isomerization is not based on the same PSBR conformational change.

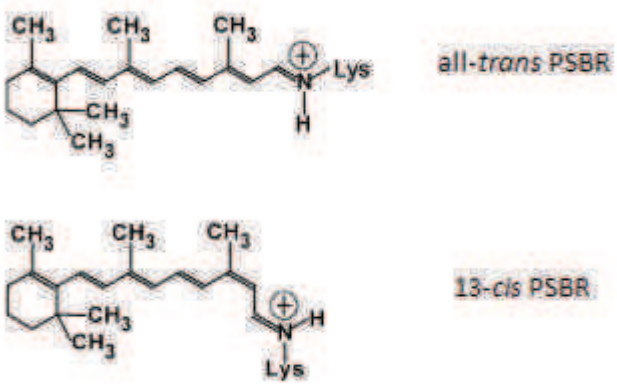

Figure 8.3.: The two PSBR isomers found in bR, ASR and many other retinal proteins.

Bacteriorhodopsin, in ambient illumination conditions, starts its photochemistry by the isomerization of a *all-trans,15-anti* retinal isomer to a *13-cis, 15-anti* form (see figure 8.3). This initiates a photocycle, depicted in figure 8.4, that makes use of the sun light to pump protons across the protein. The isomerization of retinal allows the translocation of protons through a set of intermediate protein/retinal conformations. This succession of states results in a migration of the proton from the inner to the outer region of the cells (L $\rightarrow$ M transition , figure 8.4) [84]. The cycle ends up with a new proton loaded for transport and the PSBR in the *all-trans* form (N $\rightarrow$ O transition).
When left in the dark, an even mixture of *all-trans* and *13-cis* is formed by thermal relaxation of the *all-trans,15-anti* form to the more stable *13-cis,15syn* form[85]. When put in visible light again, the excited *13-cis, 15-syn* PSBR converts into the *all-trans, 15-anti* form, this photoreaction is termed as light adaptation. The light adapted functionnal bR is essentially in the *all-trans, 15-anti* form.
As a consequence, it is not possible to observe pure *13-cis* PSBR samples of bR. Observation of the *13-cis* PSBR photochemistry requires to substract the contributions from the *all-trans* PSBR [86].

The PSBR photochemistry in bR happens on the sub picosecond timescale and has been extensively studied by transient spectroscopies. After excitation by visible light, the *all-trans* PSBR is promoted in the first excited state. After sub 100fs spectral shifts due to the relaxation from the Franck Condon region, the isomerization happens in approximately 500fs, which is the lifetime of the "I" intermediate, in good agreement with the low fluorescence quantum yield of 2.5×10^{-4}[87]. This observation is also evidenced from transient fluorescence measurements[88, 89]. The bR "I" intermediate has proven to be a quasi-stationnary state on the excited state potential, with a molecular configuration different than the ground state one, but still "almost planar" [89, 90, 91], and a reactive intermediate in the photocycle[92, 93]. Finally, the hot "J" intermediate, with *13-cis* PSBR, vibrationally relaxes in 3-5ps, as evidenced from the blue shift of its characteristic absorption in transient absorption measurements, to form the nanosecond lived "K"

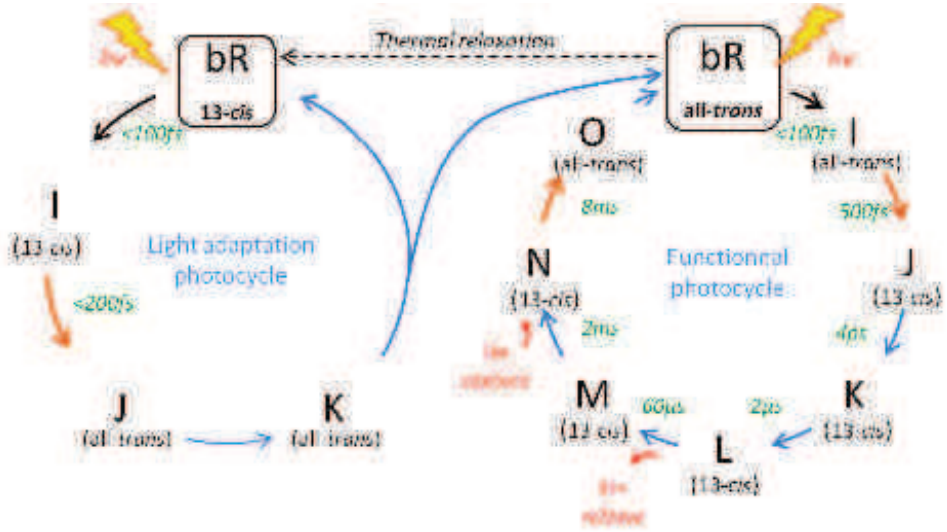

Figure 8.4.: Photocycle of bacteriorhodopsin. Orange arrows indicates isomerization, red arrows functionnal steps and bue arrows relaxations. The right hand cycle is the functionnal one, the left one traduces the light adaptation of bR. Caracteristic time of the different evolutions are indicated in green.

intermediate.
The *all-trans* PSBR in bR is thus fast and efficient (isomerization quantum yield >0.6[69]). Note that the photochemistry of the *13-cis* PSBR in bR is even faster (<200fs excited state lifetime)[86].

8.2.2. Role of the opsin protein

The amino acid composition of the protein surrounding the PSBR not only changes the biological function of the retinal protein, but also modifies the PSBR photochemistry dynamics.
The different opsins of retinal proteins favors a stable ground state isomer (*e.g. all-trans* PSBR for bR, hR, SRI, SRII, proteorhodopsin, channelrhodopsin, ...). However, differences in the electronic energy levels, leading to a modification of the $\S_0 \rightarrow S_1$ transitions are evidenced by the change in the maximum absorption of the PSBR in the different environments[80, 94], pointing out the role of electrostatic interactions beween the chromophore and the amino acids located in its vicinity in the ground state.

In addition, the opsin restricts the outcome of the reaction to single isomers (*13-cis* PSBR for the previous proteins) and generally increases significantly the yield (isomerization quantum yield >0.5). Moreover, the isomerization occurs on sub picosecond timescales. As a comparison, the *all-trans* PSBR in solution has excited state lifetimes of a few picoseconds [69] and forms more than one photoproduct isomer with poor yields (<0.5) [95].
The protein suppresses non-reactive internal relaxation channels [96] and some reactive channels, hereby optimizing the yield of a specific photoproduct formation.

This selectivity, efficiency and speed of PSBR isomerization when attached to the protein are explained by the interaction with the neighboring amino acids located in the close vicinity of the retinal chromophore. These close amino acids form the *binding pocket*, and represents a very heterogeneous environment as a comparison with a solubilization in a given solvent. Indeed the amino acids of the binding pocket are localized sites with specific properties (hydrophobicity, polarity, acidity, hydrogen bonding, . . .) while the solvent molecules share the same properties with only an heterogeneity of orientations.

The nature of the protein-PSBR interactions leading to the specific photochemitry of PSBR in retinal proteins have been extensively investigated [97]. More specifically, targeted changes of the local properties of the binding pocket through mutations of the amino acids [97, 94] or through change in the pH [98] were studied. This allowed evidencing that the presence of a counter ion in the vicinity of the chromophore is necessary to have a fast excited state lifetime [95]. Theoretical calculations explains the effect of the counterion on leveling energy barriers in the excited state [99]. However, counterions are also present in PSBR in solution, and form an ion pair with the protonated Schiff base. The shorter reaction times observed in proteins are rather attributed to steric interactions exerted by the protein on the PSBR [100], but this question is still not fully settled.

The origin of selectivity of product formation is not clear but it is suggested that steric hindrances exerted by the binding pocket on the chromophore may avoid couplings to specific vibrationnal modes driving other possible isomerization channels. It would finally result in the impossibility to explore all the possible configurations in the excited state because of energy barriers.

The efficiency of isomerization has long been linked to the isomerization speed in view of the Landau-Zener theory for avoided crossings (between the excited and ground states), however it is now thought to depend on the topology of the excited state potential energy surface, and to the populated configurations in the excited state before isomerization. The higher quantum efficiency observed for protein-bound PSBR would thus be a simple consequence of its shorter excited state lifetime. However, the concept of a conical intersection and the perception of isomerization as a consequence of a wavepacket propagation across such intersection has led to new insight recently (see below).

8.3. Isomerization and Conical intersections

A detailed understanding of the photoisomerization kinetics rely on a precise description of the potential energy surfaces (PES) of both the excited and ground states as a function of the molecular coordinates that are relevant in driving or assisting the reaction.

In the model system of bR, the isomerization is commonly described by a two state / two mode model, which is supported by theoritical calculations[101]. This description of the PSBR photochemistry, schematically represented in figure 8.5 holds for many retinal proteins.

After excitation, the Franck-Condon region is populated in the excited state of the reactant conformer. In a first time, the relaxation of the C=C stretch vibrations leads to a rapid relaxation in approximately

50fs, due to a change in the bond order change of the π-conjugated system. Indeed, the isomerizing bond acquires a single bond character to allow the rotation. On longer timescales, the torsional modes around the isomerizing bond activates. In addition, these vibrationnal modes are associated with the translocation of the positive charge initially located close to the Schiff base, to the head of the chromophore [102]. In other words, significant charge translocation occurs due to the bond alternation, but more globally on the PSBR conjugated backbone in form of a large 30D dipole moment change [103, 104].

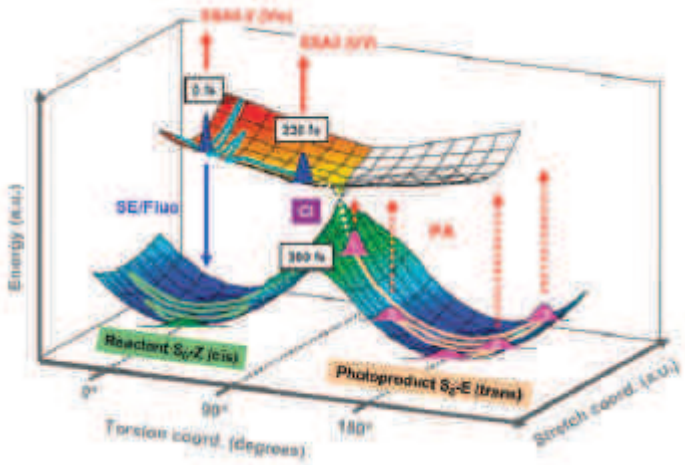

Figure 8.5.: Two state / two modes model describing the photochemistry of the *cis* form of a synthetic biomimetic photoswitch (ZW-NAIP) [72]. The conical intersection is the branching point between the excited state potential energy surface (up surface) and the ground state energy surface (bottom surface). This specific molecules have been synthetized so that their potential energy surface (PES) mimic the one of Rh. The presence of wavepackets in the excited and ground state are hinted on by oscillations and non exponential kinetics observed in transient absorption measurements.

The conical intersection, which is the crossing point between the excited and ground states is a consequence of the degeneracy of the latter states, possessing the same energy in the vicinity of the 90^o angle of torsion[103].
Historically, before the mid-90s the commonly established theoretical description relied on the Landau-Zener treatment in an adiabatic picture [105]. This model and its application to PSBR isomerization [106] estab-

lish a link between the probability of producing the product state with the steepness of the potential energy surfaces of the excited and ground state along the reaction coordinates (described by their slopes s_1 and s_2, respectively), the nuclear speed at the conical intersection (v) and the interaction between the two states (V_{12}), see equation (8.1).

$$p_{1\to 2} = \exp\left(\frac{-4\pi^2 V_{1\to 2}^2}{hv|s_1 - s_2|}\right) \tag{8.1}$$

This description of an avoided crossing between S0 and S1 for a close-to-90^o twisted dihedral angle configuration is nowadays replaced by the non-adiabatic transition state theory, involving a real crossing of the energy level, *i.e.* the above conical intersection (CI). Nevertheless, an intuitive interpretation of the LZ model persists and suggest that for a given topology of the CI, the speed of the isomerization, in other terms the speed of a hypothetic wavepacket in the vicinity of the 90^o degeneracy, inevitably controls the efficiency of the isomerization. The work of Mathies and Shank [107, 108, 109] is consistent with this. However, there is accumulating evidence today that this relation does not hold [110, 111, 112].

8.4. Issues about isomerization kinetics and yield

The concept of a coherent photoisomerization reaction was introduced by the early experiments of Mathies and Shank on Rh who observed oscillatory modulations of the transient absorption kinetics of the *all-trans* photoproduct *after* isomerization [83]. Similar observations have been recently reported for biomimetic photoswitches [110, 113, 72]. In these cases, the S_1 PES is barrierless and the excited state lifetime shorter than the period for torsional motion around the isomerizing double bond. This leads to a situation where all molecules undergo the torsional or out-of-plane motion in a synchronized fashion: coherent vibrational motion, in contrast to stochastic rate equations with an average reaction rate. In most condensed phase systems, the phase of these vibrational modes may be lost through interactions with the phonon bath surrounding the

studied system. During the coherence time, however, the phase of the vibrationnal modes is maintained, and the wavepacket may surive after the passage of the CI in the ground state PES through mode couplings, preserving the phase relation resulting in a wavepacket in the product and/or reactant state, as depicted by the trajectories of the wavepackets in figure 8.5.

It now appears that the propagation of the wavepacket across the CI is the critical step that determines the isomerization yield, which in turn is guided by the landscape of the PES in the vicinity of the CI (the CI topology) and by the degree of mixing of the S_0 and S_1 wavefunctions. However, there is no rational design rule that allows to predict the effect of a chemical substitution of PSBR or similar families of photoswitches on their quantum yield.

Many investigations have been carried out in order to modify and understand the topology of the PES of the PSBR excited state and of the CI. These investigations are performed on PSBR and its variants in solution [95] as well as on PSBR in different opsins [114].
The relationship between the isomerization speed and yield is still not clear and the role of the coherence in the isomerization process (coherence requires anyway a fast isomerization) in order to achieve high quantum yields, like Rh not proven.

An additional complication comes from the fact that femtosecond transient spectroscopies have access to the dynamics of the excited and product states only for configuration that are sufficiently populated and feature sufficient $S_i \rightarrow S_n$ transition dipole moment. Indeed, even though the excited state wavepacket progressing toward the CI is expected to lead to dynamic spectral shifts, as observed in Rh and biomimetic photoswitches [115, 109, 72], the direct observation of the wavepacket in the vicinity of the CI is hindered by its very short lifetime in these range of large torsional angles as well as the strongly reduced transition dipole moment [116, 117]. Optical spectroscopy is thus incapable of providing direct insight into the excited or ground state wavelacket at the CI.

It is still possible to have insights on the CI through quantum chemistry calculations. Simulations of PSBR in solution and in proteins allow to have more information on the role of the different parameters (electrostatics of the binding pocket, solvent effects, pH, steric hindrance, ...) on the topology of the PES of the excited state and of the CI. But since simulations rely on drastic simplifications to obtain models that can be simulated at affordable cost in time, the experiments are important to validate the models.

Yet, the influence of the external parameters on the topology of the PES and of the CI, specially the influence of the opsin on it, is still unclear and needs further investigation to fully understand the conical intersections and the isomerization process.

9. Anabaena Sensory Rhodpsin

A new retinal protein was discovered in the freshwater cyanobacteria *Anabaena Nostoc*. It is thought to serve the biologic function of light sensor through a chemical interaction with a transducer coded in the same region of the bacteria's genetic code [118, 119].

ASR stands out among other retinal proteins as it affords PSBR in two isomeric forms (*all-trans,15anti* and *13-cis, 15syn*) in ambient light conditions. In dark adapted conditions, the *all-trans isomer* is found in >95% of the proteins. Interestingly, it was recently found that the photochemistry of both isomers is significantly different since the *all-trans, 15-anti* (referred as *all-trnas* hereafter) form isomerizes in approximately 750fs while the *13-cis, 15-syn* (*13-cis*) one is much faster with a shorter than 150fs isomerization [112] at pH 7. The *13-cis* excited state lifetime is very sensitive on the pH value [98]. Moreover, the isomerization quantum yield of both isomers have been measured by steady state measurements to be 0.24 and 0.36 for the *13-cis* and *all-trans* forms respectively [120]. Interestingly, in ASR, the faster isomerization speed gives the lower quantum yield. As the two forms are host in the same protein, it may represent an interesting system to investigate the role of the retinal structural properties on the isomerization.

These experimental observations can be compared with quantum mechanics/ molecular mechanics (QM/MM) calculations predicting the presence of a barrier in the excited state potential energy surface along the reaction coordinates that may explain the difference in excited states lifetimes [121]. However, such quantum chemistry simulations does not provide information about the isomerization quantum yield [122].

The photochemistry of both PSBR isomers in ASR can be observed with a sufficient time resolution using femtosecond time resolved spectroscopies. However, the investigation of PSBR by TA spectroscopy suffers from the overlapping contributions of both isomers. Deciphering the isomer specific kinetics is thus necessary to investigate each isomer photochemistry.

The purpose of this study of retinal in ASR is to investigate both the isomerization dynamics and isomerization quantum yields of the two forms of the PSBR in very similar experimental conditions.

9.1. Photoswiching of ASR

As already mensioned, ASR can accomodate PSBR in the *13-cis, 15syn* or *all-trans, 15anti* forms. Each isomer can interconvert to the other one after absorption of a photon. This results in two interconnected photocycles [123] presented in figure 9.1.

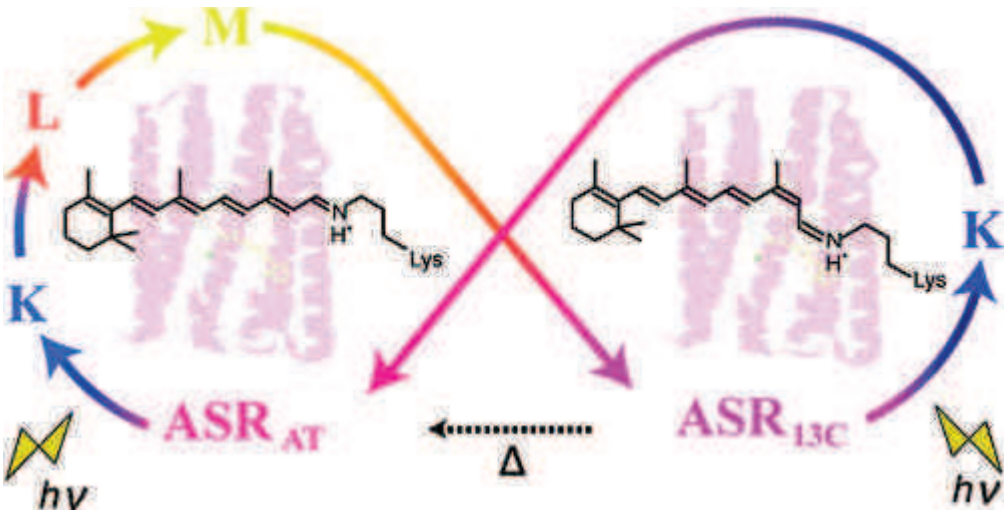

Figure 9.1.: Scheme of the photocycle of ASR. Reproduced from reference [70].

The first steps of ASR photoreaction, starting from either isomer, is very similar to bR. The main difference is that the K intermediate of

one isomer leads to the formation of the other one.
The *13-cis* form of retinal possessing a higher energy than the *all-trans* one, the former can thermally relax towards the other form with a time constant on the order of a day at ambient temperatures.

As a consequence, any sample of ASR in the light adaptated conditions is a steady state mixture of *all-trans* and *13-cis* retinal. The relative isomer ratio is determined by the photostationnary equilibrium reached under the illumination conditions. Indeed, each retinal isomer possesses a different absorption spectrum, therefore illumination at the maximum absorption of the one isomer will increase the concentration of the other isomer. On the other hand, without photon absorption, the *all-trans* form will be produced by thermal relaxation. In the end, one can control the isomeric content of an ASR solution by selecting the illumination conditions used.
For instance, when left in the dark for one day (dark adapted ASR sample, DA ASR), the ASR sample is essentially composed of *all-trans* ASR (more than 95%) while constant illumination with orange light (orange adapted ASR sample, OA ASR) will promote *13-cis* isomeric form to more than 60% . This can be observed by the change in the steady state absorption spectrum of the sample presented in figure 9.2.

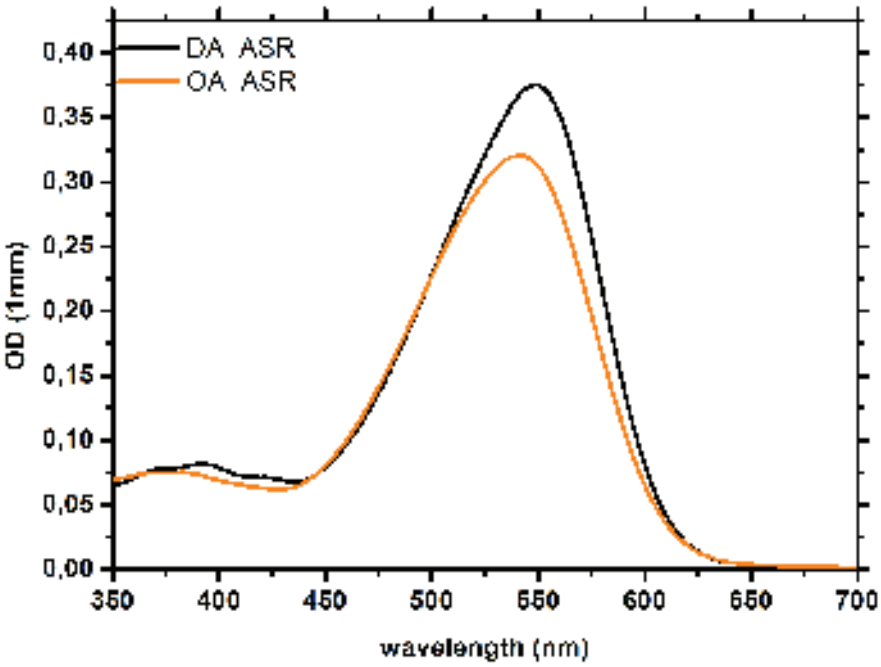

Figure 9.2.: Absorption spectra of the same ASR sample dark adapted and orange adapted.

10. Determination of the isomeric content as a function of the light adaptation conditions

10.1. Determination of the isomeric content in the ground state using HPLC

When illuminated in the linear regime of absorption, the number of *13-cis* PSBR converted from *13-cis* to *all-trans* ASR can be expressed as:

$$N_{13C\rightarrow AT} = N_{phot} \times (1 - 10^{-\epsilon_{13C} c_{13C} l}) \times \phi_{13C\rightarrow AT} \tag{10.1}$$

Where N_{phot} is the number of incident photons, ϵ is the molar absorption coefficient, c the concentration, l the optical path length and $\phi_{13C\rightarrow AT}$ the quantum yield for the *13-cis* to *all-trans* isomerization.
In the case of a photostationnary equilibrium, this equation set for each isomer must be equal(neglecting the thermal conversion of *13-cis* to *all-trans*). This leads in the approximation of a small absorbance, with x defining the fraction of *13-cis* isomer in the total amount of ASR:

$$x = \frac{\epsilon_{AT}\phi_{AT\rightarrow 13C}}{\epsilon_{13C}\phi_{13C\rightarrow AT} + \epsilon_{AT}\phi_{AT\rightarrow 13C}} \tag{10.2}$$

Where ϵ is the molar absorption coefficient at the main wavelength of the illumination light spectrum, and ϕ the quantum yield of interconversion for each isomer. Using this equation and the molar absorption spectrum of each isomers, one may conclude that it should be possible to accumulate as much as 72% of the *13-cis* isomer using orange light. While the ASR sample left in the dark will accumulate the *all-trans* isomer to almost 100% due to the dominant process of thermal conversion in the abscence of light. Such a *13-cis* isomer accumulation is important

conditions	*all-trans* content	*13-cis* content
DA	95.7 ±0.5	4.3 ±0.5
BA	45.3 ±0.3	54.7 ±0.3
OA	35.5 ±1.0	64.5 ±1.0

Table 10.1.: Determination of the isomer fractions using HPLC for different light adaptation conditions. DA: dark adapted sample, the sample is left in the dark at ambient temperature for more than 12h. OA and BA: orange and blue adapted samples, which are set in a photostable equilibrium using respectively a 590nm and 490nm LED. The uncertainity indicated refers to the standard deviation calculated using a set of 3 different experiments for the same stabilization conditions.

to measure the photochemistry of the latter isomer using transient absorption spectroscopy.

The retinal isomeric content in such proteins can be determined by several means, such as proton nuclear magnetic resonance (NMR) or high precision liquid phase chromatography (HPLC) on chromophores chemically detached from the opsin. We used the second method with the help of our Korean partner Kwan Hwan Jung in Seoul. ASR samples from our Japanese partner Hideki Kandori were prepared using the reported protocol [119]. The samples were either dark adapted or light adapted. In the present work, dark adaptation is performed by storing the ASR solution in the dark, at ambient temperature for at least 12h. Light adaptations are obtained by exposing the ASR solutions, contained in plastic microtubes to the light of LEDs with central wavelengths of 490nm (blue adapted, BA) and 590nm (orange adapted, OA). The light flux of the LEDs is about 10mW during at least 10min, and the concentration of ASR usually corresponds to an OD of 0.3 through 1mm. The chromophore extraction and HPLC were performed using standard procedures [124], and repeated to reduce the experimental errors. The results are presented in table 10.1.

The so determined isomeric content is in good agreement with previously determined isomeric content for the DA and light adapted (LA) forms [125]. The error bar on the determined isomeric content shows that

the light stabilization is reproducible. Our light stabilization technique allows thus to produce samples with precisely known isomeric fraction, in a reproducible way. Note that the ASR solutions are solubilized in a buffer solution of pH 7.5, and fresh samples were used for all the reported experiments to prevent from change in the *13-cis* PSBR ASR content [98].

This determination of the isomeric content of samples allows to calculate, in a consistent way, the steady state absorption spectra of the *13-cis* and *all-trans* retinal ASR. Using the absorption spectra of one sample with at least two light adaptation conditions with significantly different known isomeric content , one can calculate the absorption spectra of the pure isomeric forms:

$$\begin{pmatrix} A_{13C} & A_{AT} \end{pmatrix} = \begin{pmatrix} A_{LA_1} & \dots & A_{LA_n} \end{pmatrix} \times \begin{pmatrix} x_{LA_1}^{13C} & \dots & x_{LA_n}^{13C} \\ 1 - x_{LA_1}^{13C} & \dots & 1 - x_{LA_n}^{13C} \end{pmatrix}^{-1} \tag{10.3}$$

Where $x_{LA_x}^{13C}$ is the *13-cis* ASR content for a given light adaptation, and A is the absorption spectrum. This matrix calculation is performed using Matlab.
Then, knowing the solution concentration or using the known value of the *all-trans* ASR molar absorption [120], one obtains the pure isomer molar absorption spectra presented in figure 10.1

We are thus capable of producing samples with accurately known and reproduceable isomeric content, which allows to perform spectroscopic analysis of our samples in very similar conditions allowing to disantangle each isomer contribution in the experiments.

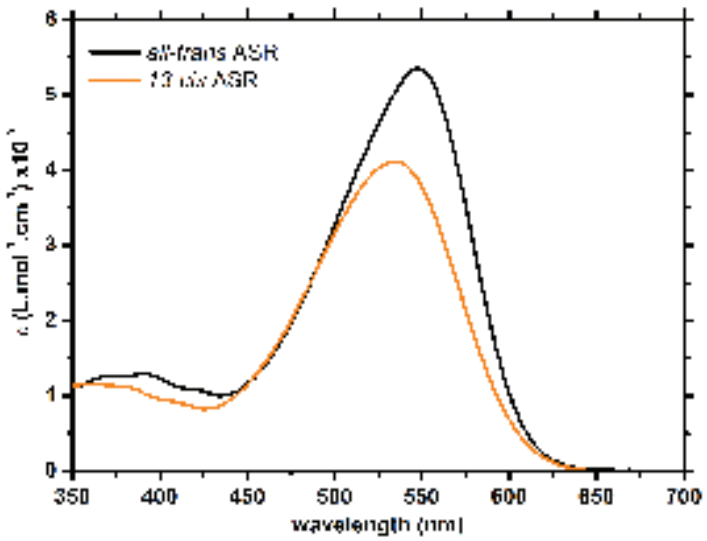

Figure 10.1.: Molar absorption spectra of the *all-trans* (black line) and *13-cis* (orange line) retinal ASR. Calculated using a sample with three different light adaptations (DA, BA, OA).

10.2. Calculation of the isomeric content in the excited state and of the pure isomer photochemistry.

We saw previously that the PSBR isomeric fraction in the ASR samples can be varied using different light adaptation conditions. The separation of pure PSBR contributions in the fluorescence spectrum of ASR samples or from the transient absorption data requires to estimate the contributions of the PSBR isomers in the excited state.

The photochemistry of an ASR sample is composted of the two parallel photoreactions of the *13-cis* and *all-trans* PSBR. Provided that the photochemistry is triggered by a single pulse excitation, the two photoreations are not conneted, and the *all-trans* and *13-cis* PSBR ASR photoproducts does not participate to the reaction. The transient absorption and the steady state fluorescence experiments may fulfill the conditions if the flow of sample is fast enough in the spectroscopy cell, to avoid re-excitation of the excited volume of the sample. Both experiments were carried out in these conditions.

Another important prerequisite for the observation of the photochemistry of ASR is to excite the relaxed ground state form of the protein. Indeed, the overall cycle of retinal proteins may last as long as some miliseconds (*e.g.* bR [84]), so that the relaxed from of both the PSBR and the protein is only effective on this timescale. The typical time for the solution to travel in the opaque tubings from and to the sample reservoir is on this order of magnitude in our experimental conditions. In addition, a significant volume of sample stays in the microtube containing the sample so that the excited sample is diluted significantly (the excitation volume is typically on the order of hundred of picoliters, while the sample volume in the reservoir is 300-500 microliters). Note that less than 10% of the sample in the excitation volume is actually excited.

The latter remark points out the question of the light stabilization during the experiment. Indeed, the conversion triggered by the photochemical measurement should not change the photostationnary equilibrium obtained by light stabilization. The excitation beam used in the experiment corresponds to an average power of some hundred microwatts while the stabilizing light power from the LED is more than ten watts. This ensures that the sample is well stabilized.

The total number of initially excited molecules depends, in a linear regime of excitation, on the absorption spectrum of the molecule $A(\lambda)$, the excitation energy E, the Avogadro number N_A and the excitation wavelength λ_{ex}, through equation 10.4:

$$N^* = \frac{E\lambda_{ex}}{hcN_A}(1 - 10^{-A(\lambda_{ex})}) \tag{10.4}$$

The contribution of each PSBR isomer in the number of initially excited molecules depends on the probability to excite the one or the other isomer. This probability depends on the cross section of each isomer, which is proportionnal to the molar absorption coefficient ϵ, and on the relative number of the same isomeric form in the ground state (*e.g.* x_{13C} for *13-cis* PSBR). After normalization over the two PSBR isomers, and multiplication by the total number of initially excited molecules, one

obtains the relative number of *13-cis* PSBR excited, from equation 10.5:

$$n^*_{13C} = N^* \times \frac{x_{13C}\epsilon_{13C}(\lambda_{ex})}{x_{13C}\epsilon_{13C}(\lambda_{ex}) + (1 - x_{13C})\epsilon_{AT}(\lambda_{ex})} \tag{10.5}$$

Note that equation 10.4 and 10.5 may be ponderated by the spectrum of the excitation beam, when the latter is larger than the typical spectral variations of the absorption or molar absorption spectra. In the present case, the difference in the results is negligible. The results are shown in table 10.2 for different light stabilizations and a 560nm excitation.

	DA ASR	BA ASR	OA ASR
x^*_{AT} (%)	99	56	46
x^*_{13C} (%)	1	44	54

Table 10.2.: ASR retinal isomer fraction in the excited state for different light adaptation conditions, calculated after equation 10.5

The excited state isomer contributions determined with equation 10.5 allow to calculate the pure isomer contributions in fluorescence or transient absorption experiments. Two experiments using the same sample and experimental conditions, but with two different light stabilization conditions should be used (in this work, mostly DA and OA ASR). In this case, the only varying parameter is the absorbance of the sample at the excitation wavelength, leading to a different number of excited molecules N^*. The data sets are corrected for the number of excited molecules, by dividing the data sets by $1 - 10^{-A_{LA}}$, where A_{LA} represents the absorbance of the sample for a given light adaptation (the pre-factor in equation 10.4 is shared). Then, the pure PSBR isomer contributions can be extracted using equation 10.3, with: $x^{13C}_{LA} = x^*_{13C}$ for the corresponding light stabilization condition and A the fluorescence spectrum or the transient absorption map corrected for the number of excited molecules.

This caculation of the pure PSBR isomer contributions relies on the proportionnality of the fluorescence and transient absorption signals with the initially created excited state population. This is checked experimentally by making sure that the response is linear with the excitation. It

suggests that the populations created in the photochemistry of ASR are proportionnal to the initial population of excited states. This requires the chemical reaction starting from the reactant excited state to be of first order kinetics. Under these assumptions, the transient absorption signals for one PSBR isomer can be written:

$$\Delta A(t,\lambda) = N^* \frac{l}{V} \sum_{i=species} \epsilon_i(\lambda) U_i(t) \tag{10.6}$$

Where $U_i(t)$ is the temporal profile of the population evolution of the corresponding species of molar absorption spectrum $\epsilon_i(\lambda)$. Note that populations can be negative (case of ground state bleaching). The fluorescence measurement can be seen as a particular case of this equation where the difference absorption is replaced by the fluorescence signal and the temporal evolution is integrated.

Note that in this work, mainly DA and OA ASR samples are used to determine the pure PSBR isomer contributions. As a result, the contribution of *all-trans* PSBR ASR and *13-cis* PSBR ASR on the combination of the two measurements is very different. The *13-cis* PSBR in ASR accounts for only 28% of the overall data. This leads to a greater incertainty on the values calculated for pure *13-cis* PSBR in ASR as well as a lower signal to noise ratio.

As a consequence, it is possible to decipher the photochemistry of ASR samples, and obtain the contributions of each PSBR isomer, knowing the ground state isomer fraction and the excitation wavelength and by measuring the same sample under two different light stabilization conditions.

11. Photoisomerization dynamics

The steady state measurements on ASR illustrate our ability to efficiently control the isomer content of the measured samples and to measure for the first time the fluorescence spectrum and quantum yield for both isomers of the retinal chromophore.
The same isomer stabilization technique is used for the transient absorption measurements. The latter experiments allows to characterize the photochemistry of ASR with sub picosecond time resolution in the very same conditions than the steady state characterizations, in particular those of the HPLC experiment allowing to characterize the isomeric content of the samples.
The purpose of these experiments for different isomeric contents is to separate the photochemistry of each isomer of the chromophore in ASR, and finally use the so determined excited state lifetimes in combination with previously determined fluorescence quantum yields in the same experimental conditions to determined the radiative rate of both PSBR excited state in ASR.

11.1. Photochemistry of ASR

The photochemistry of ASR is studied using transient absorption spectroscopy with detection from the near UV to the near infrared. The excitation wavelength from a TOPAS is tuned from 535nm to 580nm to investigate the influence of excess energy on the photochemistry. These experiments have a time resolution of around 45fs (FWHM on the SRS signal measured in the solvent with approximately 15fs accuracy). The experiments are performed on samples with different light adaptation conditions to vary the contributions of the two retinal isomers in ASR.

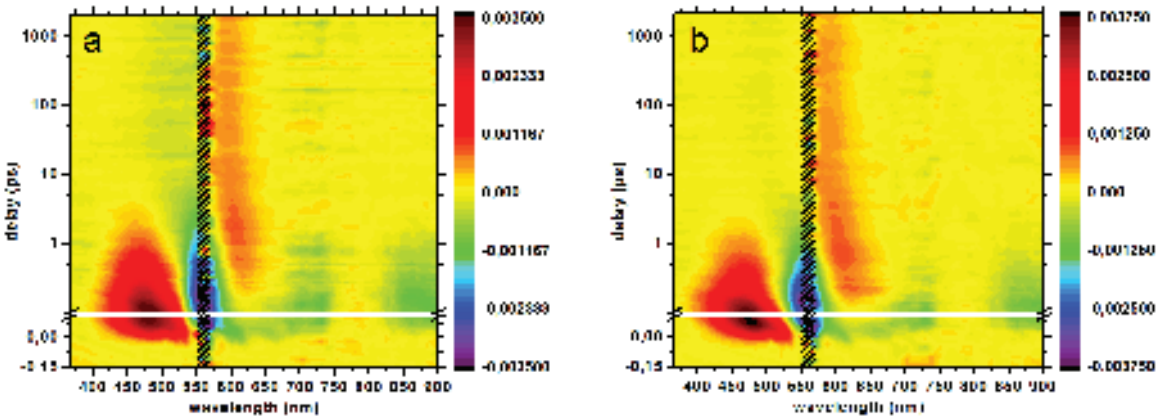

Figure 11.1.: Overview of the transient absorption data of DA (a) and OA (b) ASR excited at 560nm. The spectral region centered on the excitation wavelength is disregarded due to low signal to noise ratio in this region.

If not mentioned, excitation wavelength is 560nm.

With a low excess energy excitation at 560nm, the photochemistry of OA and DA ASR shows the same general trends. Both shares the same features as bR. Figure 11.1 presents an overview of the data as 2D maps. The difference absorption spectra presented in figure 11.2 (top panels) shows that after excitation at zero delays, the excited state of the PSBR dominates as a positive feature located in the 350-550nm region. The *13-cis* containing OA ASR (b) exhibits a more important blue shift of the ESA. The associated stimulated emission band spanning from 650 to 900nm and the corresponding GSB band is centered around 560nm. The negative ground state bleaching is attenuated due to the positive contributions of the other species. An induced absorption band can be spotted between 750 and 825nm, since it splits the stimulated emission band into two parts. Its contribution evolves along with the SE and the main ESA band, leading to the conclusion that this induced absorption band is a signature of the same excited state.
At longer timescales (bottom panels), the ESA and SE decays while the "J" photoproduct is formed and appears as a positive band in the 600-650nm region for the DA ASR (panel c) and 600-675nm for the OA ASR (panel d). The photoproduct absorption band blue shifts on the

picosecond timescale, indicating the vibrational relaxation to the relaxed K form. This blue shift is more important in the OA ASR case. There is no sizeable change in the difference absorption signal after ten picoseconds.

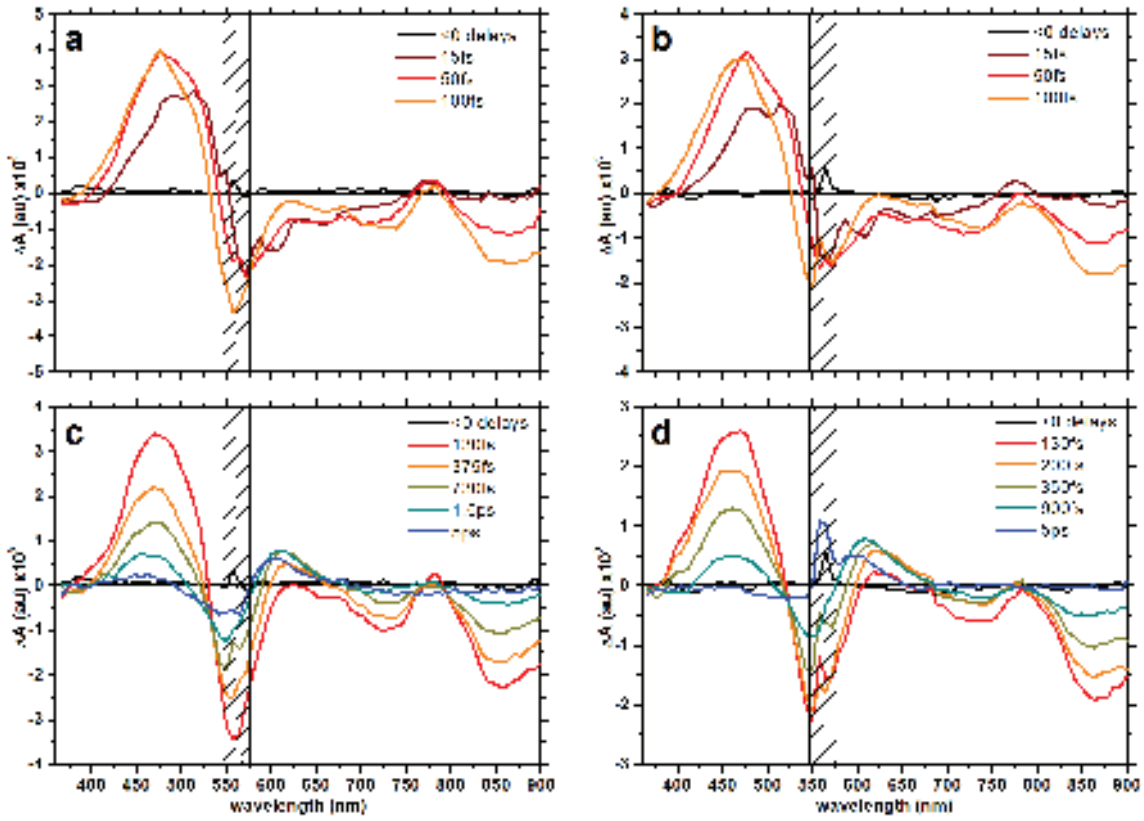

Figure 11.2.: Short time delays spectral evolution of DA and OA ASR (a and b, respectively). Spectral evolution for longer times for DA and OA ASR (c and d, respectively). The pump wavelength region is disregarded due to low signal to noise ratio. Delays are indicated on the graphs.

As shown before, the four main contributions of ESA, GSB, photoproduct and SE are significantly overlapping in the 350-700nm region, giving rise to small amplitude features were one or the other contribution dominates. The only spectral region with almost pure contribution is the near infrared region for wavelengths superior to 825nm, where the stimulated emission dominates and the 775-800nm excited state absorption band becomes negligible. This spectral region gives the temporal

evolution of the excited state population alone.

11.2. Determination of the pure *13-cis* transient absorption information

Using the well characterized isomeric composition of the OA and DA samples, and the experimental conditions, the isomer-specific time resolved data can be calculated (see section 10.2). The corresponding maps are presented in figure 11.3. The *13-cis* data in panel b are significantly noisier than the *all-trans* ones presented in panel (a) due to the ≈25% overall *13-cis* contribution in the combination of the two datasets.

These pure isomer data evidences the very short excited state lifetime of the *13-cis* through the short lived ESA and SE bands respectively blue and red shifting in the 450nm and 700-900nm regions, in panel b of figure 11.3. The photoproduct absorption is centered around 610nm and has a larger positive contribution than for the *all-trans* PSBR. The positive absorption around 450nm between 150 and 500fs could be a contribution from the photoproduct absorption (see absorption spectra in figure 12.1, panel a).

The *all-trans* difference absorption excited state features are much longer lived (panel a). The ESA bands at 475 and 775nm together with the large SE band spanning from 650 to 900nm slowly decays an are still sizeable at 1.2ps delays. The photoproduct absorption band grows slowly around 625nm and overlaps with the SE.

These calculated isomer specific data shows that the photochemistry of the two retinal isomers is significantly different dynamically and spectrally. Qualitatively, the present data are in good agreement with previously published ones [122].

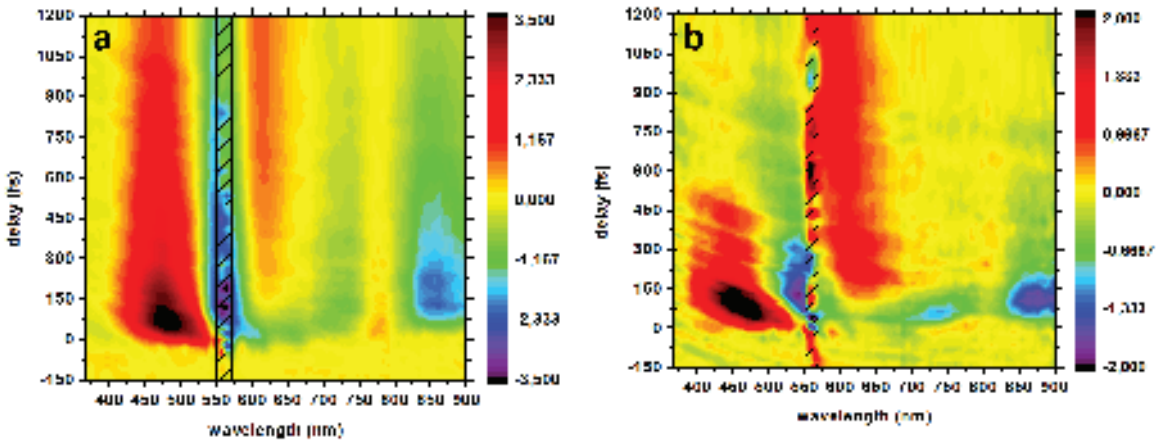

Figure 11.3.: Overview of the transient absorption data of *all-trans* (a) and *13-cis* (b) ASR excited at 560nm. The spectral region centered on the excitation wavelength is disregarded due to low signal to noise ratio in this region. These pure isomer TA maps are obtained by the procedure described in chapter 14.

11.3. Excited state lifetime

The kinetics of stimulated emission are displayed in the panel a of figure 11.4 for a data set with better signal to noise ratio where the focus is made on the short time scales. The data are used to characterize the excited state lifetime of both PSBR isomers in ASR. The kinetic traces of SE at 875nm are used since they are free from other species contributions.

decay	amplitude (%)			
(fs)	DA ASR	OA ASR	*all-trans* ASR	*13-cis* ASR
100	0	53	0	89
770	100	47	100	11

Table 11.1.: Values obtained by global fitting of OA and DA ASR SE traces together, and by global fitting of *all-trans* and *13-cis* SE traces together. Since the time constants found in the two cases are similar, they appear here shared. The values for the amplitues are normalized to the sum of the (negative) amplitudes.

Globally fitting the SE kinetics measured at 875nm for both DA and

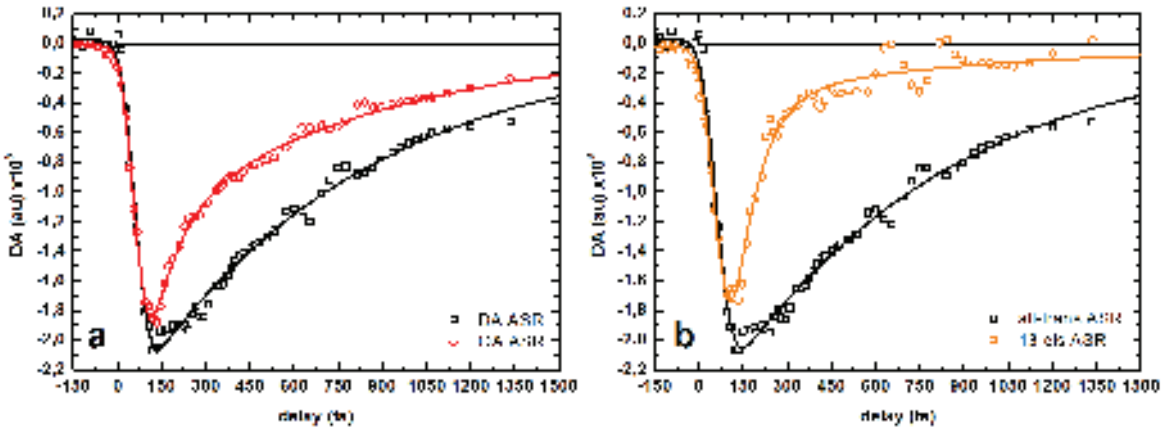

Figure 11.4.: Kinetic traces measured at 875nm for DA and OA ASR excited at 560nm in panel a. Pure *all-trans* and *13-cis* ASR kinetics calculated from the DA and OA ASR data in panel b. The symbols are measured data and the thick lines of the respective color is the bi exponential global fit mensioned in the text. See legend.

OA ASR requires two time constants, as well as for globally fitting both pure isomer kinetics calculated. The time constants found in both cases are identical given the experimental time resolution, and equals 100 and 770fs. The amplitudes in the fits are shown in table 11.1.They show that the DA ASR kinetic trace is dominated by the 770fs time constant, as well as the *all-trans* ASR kinetic. On the other hand, the OA ASR shows a balanced repartition of the amplitudes on both time constants, which is also in good agreement with its isomeric content (see table 10.2). The *13-cis* ASR kinetic is dominated by the 100fs time constant. The 11% contribution fitted is regarded as negligible regarding the similar amplitude noise level for this data set (representing $\approx$ 5% of the maximum signal), and may be explained by the uncertainty on the calculation of the excited state isomer fraction, which is estimated to be 5-10% .These observations shows that each of the two time decay is characteristic of the corresponding retinal isomer.

Finally, the *13-cis* retinal ASR is the fastest isomer with an excited state lifetime of 100fs, whereas the *all-trans* retinal ASR is longer lived with a 770fs excited state lifetime.

This determination of the excited state lifetime of both PSBR isomers in ASR indicates that in our experimental conditions, the *13-cis* PSBR has a shorter lifetime than accounted for in the calculation of the average radiative rate in [126], and the *all-trans* PSBR a larger one. These new values, measured in the same experimental conditions significantly changes the figure 5 of the latter paper, and indicating that the *13-cis* isomers in both proteins have a higher average radiative rate than the *all-trans* ones (see section 14.2).

11.4. Isomerization and photoproduct

The isomerization speed is of interest here since the relationship between isomerization speed and efficiency is one of the main problematics in isomerizing molecules.
The excited state lifetime is an indication of the isomerization speed since the latter state is depopulated during isomerization. If isomerization yield is significant, specially when the isomerization is the dominant phenomenon. However, in the case of significant alternative pathways to the ground state such as internal conversion or radiative decay, the estimation is biased.

The formation of the K photoproduct state of ASR is shown in figure 11.5, by kinetic traces monitored for wavelengths >600nm. In this spectral region, both K, SE, and small GSB contributions are present. The raise of the positive K state absorption signal is faster in the case of OA ASR, in panel b. However, it is unclear wether this rapid raise is a consequence of the isomerization speed or the influence of negative contribution from the fast red shifting stimulated emission signal.

Globally fitting these kinetics requires two additional decays than the ones found for the near infrared stimulated emission signal. The supplementary time constants are 4.5ps and a >>1ns one. By analogy with other retinal proteins, these two time constants are respectively

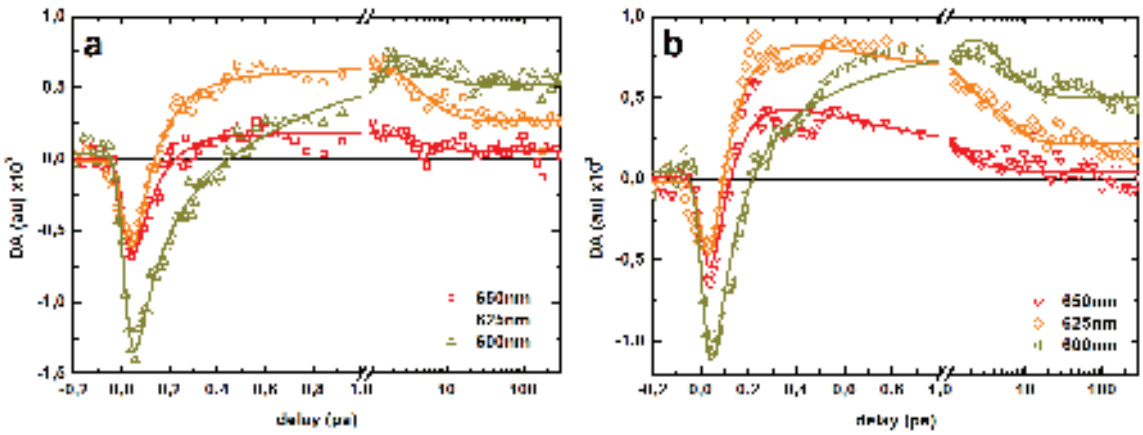

Figure 11.5.: Selected kinetics showing the formation of the photoproduct K for DA (panel a) and OA (panel b) ASR excited at 560nm. Symbols represents raw data and the thick line of corresponding color is a global fit of the DA and OA kinetics shown with four time constants of 100fs, 770fs, 4.5ps and infinite.

attributed to the thermalization of the "J" photoproduct leading to the formation of the long lived "K" intermediate. This thermal relaxation gives rise to the blue shift of the photoproduct absorption bands (figure 11.2, panels c and d). The "K" state is long lived in comparison with the time span of our measurement, leading to a stationary long time difference spectrum for delays superior to 10ps (see long delays in figure 11.1). This long time difference spectrum is discussed in section 12.1.

The kinetics presented here contain contributions from GSB and SE, evidenced by the negative signal for delays inferior to 500fs. The isomerization time is thus deduced from the excited state lifetime assuming that the entire excited state population leads to the conical intersection as in the case of bR [93]. The excited state lifetimes of 100 and 770fs for *13-cis* and *all-trans* PSBR in ASR deduced from the pure SE signals are thus used to define the isomerization time.

The isomerization of the *all-trans* PSBR ASR is thus very similar to the *all-trans* PSBR in bR [86]. On the other hand, the *13-cis* PSBR isomerization in ASR occurs in 100fs and is similar to the *11-cis* PSBR

in Rh [109, 81]. Note that the OA ASR photoproduct kinetics in figure 11.5 presents non exponential behavior in the 0.1-0.8ps range (panel b) whereas the DA ASR does not (panel c). These oscillations in the signal again reminds of the *11-cis* PSBR in Rh [83] and may indicate a vibrationnal coherence rapidly damped in the probed populations. This issue is further discussed in the following section.

11.5. Vibrational coherences and isomerization of *13-cis* retinal in ASR

The excited state absorption of both retinal isomers in ASR shows a significant blue shift in the first hundred femtoseconds. This is the indication of a vibrational relaxation in the excited state [110]. This spectral shift, already evidenced in the spectral evolution (figure 11.2) showing a shift of the absorption maximum of the ESA, can be spotted in the kinetics presented in figure 11.6 by a wavelength dependant rise and decay (more pronounced in the case of *13-cis* in panel b) of the TA signals. It is associated to a 30fs time constant after the fitting of *all-trans* kinetics of figure 11.6. The 100fs excited state lifetime of *13-cis* retinal ASR is very close to the characteristic time of relaxation from the Franck-Condon region to the vibrationally relaxed excited state, and only three times longer than the estimated vibrationnal relaxation time in pure *all-trans* data.
In the case of *13-cis* retinal ASR, theoretical calculations [121] predicts a barrierless decay of the excited state population to the conical intersection. This is in good agreement with the present excited state kinetics, and suggests that the excited state of the *13-cis* retinal in ASR funnels to the conical intersection through a vibrationally coherent motion in the excited state, as the excited state lifetime is shorter than the characteristic low frequency modes period of torsion.

The oscillations are extracted from the data by globally fitting the OA ASR transient absorption data with a sum of exponential decays, with 0.1, 0.77, 4.5ps decays and an infinite decay corresponding to the

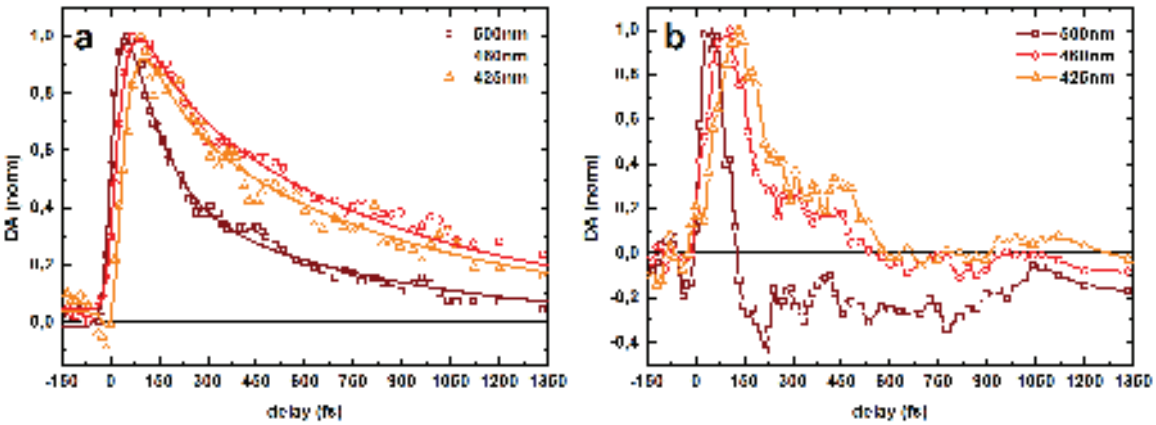

Figure 11.6.: Selected kinetics normalized to the maximum of the signal showing the excited state blue shift in *all-trans* (panel a) and *13-cis* (panel b) retinal ASR excited at 560nm. The *all-trans* retinal ASR raw data appears as symbols and the thick lines are three exponential fits with time constants of 30fs, 100fs and 770fs. The *13-cis* raw kinetics displayed are not fitted.

long time difference spectrum. The residuals of this global fit contain the unfitted low frequency oscillatory signal [114, 112, 127, 72, 128, 83]. Such residuals are presented in figure 11.7 for selected probe wavelengths. Note that in our case, Fourier transform analysis of the residuals is meaningless due to the non uniform time sampling and the strong damping of the oscillations.

The latter kinetics exhibit pronounced oscillatory behavior, with amplitudes significantly higher than the typical noise level. Figure 11.7 shows at 200 fs a signal enhancement at 600-650 nm and reduction at 460-530nm and an opposite behavior at 420-450 fs. The first pattern is repeated though smeared out temporally at 700-800 fs. At 1.0-1.2 ps a weak signal increase is observed for all wavelength. This behavior is interpreted as the manifestation of one cycle of oscillation with a 0.5-0.6 ps period. The temporal broadening may indicate the presence of two oscillatory frequencies. These ground state oscillations are observed at the blue and red edges of the ground state absorption spectrum, as expected, since these transition energies correspond to the locations of the turning point of the wavepacket in the ground state potential. The

damping time was not determined precisely, given the limited S/N ratio, but it is on the same order of magnitude as the period itself. Damping is most probably imposed by vibrational relaxation in the ground state, since the intramolecular vibrationnal relaxation [110] and the phonon bath due to the protein surrounding the chromophore may dissipate the energy of the vibrational modes and thus destroys the coherence of the wavepacket.

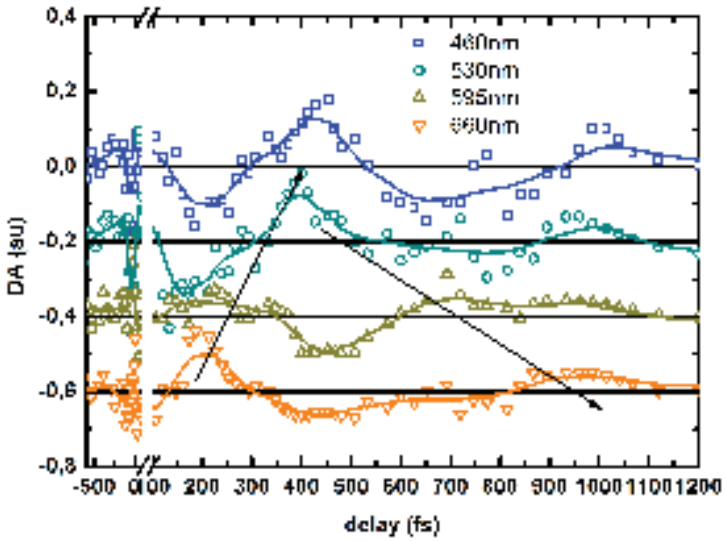

Figure 11.7.: Residuals of the fit of the OA ASR data with a sum of exponential decays, showing unfitted oscillatory contributions. The phase of the oscillations are evidenced in the residuals for chosen probe wavelengths indicated on the graph. The thick lines are smoothed curves to guide the eye. The black arrows indicates the phase shift.

Together with the oscillatory photoproduct kinetics presented in figure 11.5 and 11.6 panel b, these observations are very similar to the photochemistry of Rh measured by transient absorption spectroscopy [81]. In the case of Rh, this behavior has been attributed to a vibrationnal coherence triggered by the femtosecond excitation, preserved after the crossing of the conial intersection.

In summary, the TA data show non exponential kinetics for the *13-cis*

PSBR that indicate a wavepacket-like propagation on the excited state. This wavepacket rapidly funnels in the conical intersection in the absence of energy barrier, and is responsible for the short excited state lifetime of this isomer. There are indications that coherence of the wavepacket may be conserved through the crossing of the conical intersection, and the wavepacket propagates in either the reactant or the photoproduct state, or both. However, the coherence is rapidly lost in approximately 1ps through intramolecular relaxation or energy dissipation in the phonon bath of the protein. As a consequence, all the excited population is in the ground state of either isomer after the CI crossing. Further experiments with a higher signal to noise ratio are necessary to investigate these low amplitude modulations.

12. Isomerization quantum yield

The photochemistry of retinal is driven by the fate of the chromophore at the conical intersection. We showed until now that the photochemistry of *all-trans* and *13-cis* retinal ASR differs in their excited state since the first one is depopulated statistically and the other one through a coherent vibrational motion.

The isomerization quantum yield of both retinal isomers in ASR have been characterized by Kandori *et al.* [120] and shows that the *all-trans* isomer is more efficient than the other isomer with an isomerization quantum yield of 38% versus 26% for the other one. Interestingly, the shortest lived excited state gives the lowest yield, which is contrary to the supposed relation between quantum yield and reaction speed proposed from Rh [83, 108, 109].

We propose here to estimate the relative isomerization quantum yields of both isomers, in the very same conditions as the excited state lifetime measurement, from the transient absorption measurement. Indeed, the long time stationnary difference spectrum observed in transient absorption is due to the isomerized chromophore contributions, and can be used to estimate the amount of isomerized chromophores. Moreover, the "K minus ground state" difference absorption of the two retinal isomers is significantly different and allows to estimate the contribution of each one in the long time difference spectra.

12.1. Long time difference spectrum

The long time difference spectra are characterized by an induced absorption band around 600nm due to the "K" form of the retinal in ASR, and a negative contribution due to the ground state bleaching at 500nm. For a given light stabilization conditions, this long time difference spectrum $\Delta A(\lambda)$ can be expressed as a function of the difference in the molar absorption $\epsilon(\lambda)$ of the "K" state and the ground state of each retinal isomer and the fraction n_{AT} (for *all-trans* retinal) of excited isomers N^* , and the isomerization quantum yields $\Phi_{C\to T}$ (for the *13-cis* to *all-trans* isomerization):

$$\Delta A(\lambda) = \frac{l}{V}\times N^*\times\{[\epsilon_{K_{AT}}(\lambda)-\epsilon_{AT}(\lambda)]n_{AT}\Phi_{T\to C}+[\epsilon_{K_{13C}}(\lambda)-\epsilon_{13C}(\lambda)](1-n_{AT})\Phi_{C\to T}\} \tag{12.1}$$

Knowing the "K minus ground state" difference spectra of both isomers and the isomer fraction in the excited state, one may fit the long time delay difference spectra for a given light stabilization conditions by a linear combination:

$$\Delta A(\lambda) = \alpha n_{AT}[\epsilon_{K_{AT}}(\lambda)-\epsilon_{AT}(\lambda)]+\beta(1-n_{AT})[\epsilon_{K_{13C}}(\lambda)-\epsilon_{13C}(\lambda)] \tag{12.2}$$

Finally, the ratio of the coefficients used in the linear combination simplifies with the path length l, volume V and excitation density N^* factor and gives the ratio of the isomerization quantum yields:

$$\frac{\Phi_{T\to C}}{\Phi_{C\to T}}$$

This ratio can be calculated for different experiments and light adaptations in order to reduce the incertainty on its value.

12.2. Calculation of the "K" species absorption spectrum at room temperature

The "K minus ground state" difference spectra may be obtained by the difference in the absorption spectra of each species for the same concentration. However, so far, no "K" species spectrum have been determined

except at low temperatures (130K) [123]. The K and steady state absorption spectra of both isomers are available for this low temperature.

The procedure is described in annex B.1, and permits to obtain the "K" species molar absorption spectrum for both PSBR isomers at room temperature and finally the "K minus ground state" molar absorption differences can be calculated for both isomers. These spectra are displayed in figure 12.1. These difference spectra reproduce well the shape of the long time difference spectra, with a characteristic positive "K" ASR contribution peaking at 600nm and the negative ground state bleaching contributionin the 450-550nm range. The *13-cis* "K minus ground state" absorption is very singular since the GSB contribution is dominated by the "K" species absorption. Both spectra are in good agreement with the pure isomer long time difference spectra calculated from experiments and presented in panel a of figure 12.2.

The so determined "K minus ground state" ASR difference absorption spectra at room temperature for both retinal isomers can be used to estimate the relative isomerization quantum yield of the two retinal isomers in ASR.

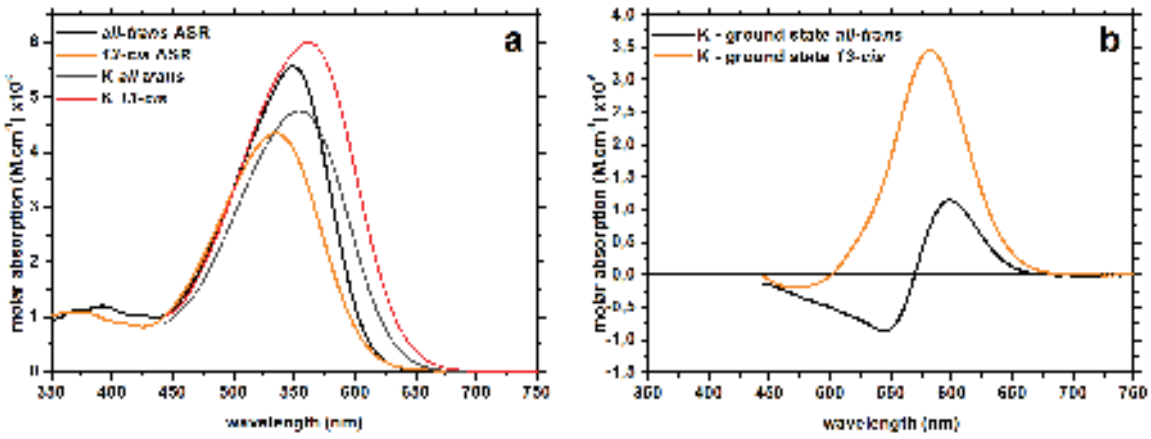

Figure 12.1.: Molar absorption spectra at 273K of ground state and K state for both retinal isomers in ASR in panel a. The K spectra are calculated using the procedure descibed in the text. Panel b shows the K minus ground state molar absorption spectra for both retinal isomers in ASR.

12.3. Relative ASR retinal isomer isomerization quantum yield

The isomer specific"K minus ground state" ASR difference spectra calculated in the previous section are used in a linear combination to fit the long time difference spectra of OA, DA and BA ASR samples. This fit with equation 12.2 gives the ratio of the isomerization quantum yields.

After correction for the different effective excitation densities, transient absorption data measured in the same conditions on the same samples but for different light adaptation conditions are fitted with a linear combination of the *all-trans* and *13-cis* "K minus gound state" ASR difference absorption spectra multiplied by the corresponding fraction in the excited state, just like equation 12.2. First, the DA ASR difference spectrum is fitted with the *all-trans* "K minus ground state" difference spectrum, assuming that the 3% *13-cis* ASR contribution is neglectable. This first step gives the value of α (cf equation 12.2). The second step is to fit the different light adapted measurements to fit the β parameter. An example of fitting is displayed in figure 12.2. This method allows to take into account the DA ASR measurement without

adding incertainty on the quantum yield ratio because of the large incertainty on the β coefficient due to the negligible *13-cis* retinal isomer contribution.

This procedure is repeated for three different data sets allowing to obtain four different realisations of the isomerization quantum yield ratio. The average value obtained for the isomerization quantum yield ratio is:

$$\frac{\Phi_{T\to C}}{\Phi_{C\to T}} = 2.3 \pm 0.3$$

The corresponding value obtained using the absolute quantum yields determined in ref [120] and the coresponding error bar is 1.6±0.5. The value obtained here is larger than the latter one.

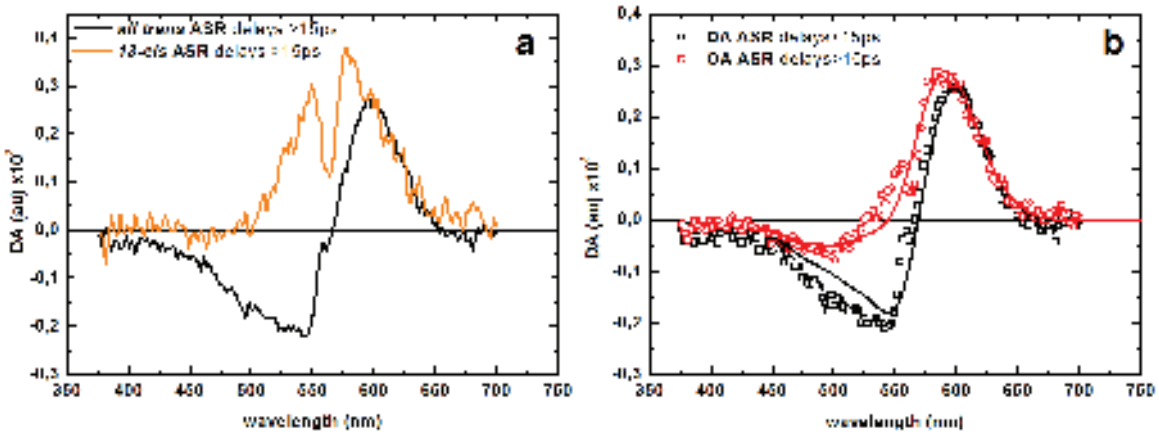

Figure 12.2.: Panel a shows the pure isomer long time difference spectra, averaged for delays superior to 15ps, for the same excitation density. Panel b shows the averaged (for delays >15ps) long time difference spectrum of OA and DA ASR samples measured by transient absorption spectroscopy with 560nm excitation and corrected for the different excitation density. The thick lines of respective colors is a linear combination of the *all-trans* and *13-cis* "K minus ground state" difference spectra fitting at best the raw data. Note the decreased signal to noise ratio around the excitation wavelength in both graphs.

The experimental conditions were well controlled in a temptative way to determine the absolute isomerization quantum yield for each isomer.

Indeed, if the concentration of excited molecules is known, and the optical path length, a complete modeling of the long time difference spectrum with the isomerization quantum yield as a parameter can be performed (using equation 12.1), within the limit of accuracy for the density of excited molecules N^*. In order to limit errors on this side, the pump spot size was measured with a beam profiler precisely at the sample position, as well as the pump power. The sample absorption is precisely known, and so are the optical path length and the sample concentration. Using equation 10.4, with E the energy per pulse gives the number of excited molecules. The excitation volume is the cylinder which base is the surface defined by beam intensity FWHM, and length the optical path. The ratio of the number of excited molecules N^* on excitation volume V gives the concentration of excited molecules with a relative uncertainty of about 10-20%.
With this method, the absolute isomerization quantum yields obtained are significantly lower than the ones determined by Kandori. Indeed, it gives an isomerization quantum yield of 16%±5 for the *all-trans* retinal isomer and 7%±2 for the *13-cis* retinal isomer in ASR. Since these values are extraordinarily low for protein-bound PSBR, which usually show quantum yields in the 50% range, we prefer to rest on the discussion of the ratio of these values since it eliminates the possible influence of systematic errors (pump intensity and profile). We note however that the long-time difference spectra were reproduced very reliably in amplitude and shape in two separate experiments on two different protein samples from K. Jung and H. Kandori's labs.

In summary, we determined the relative isomerization quantum yield of both retinal isomers in ASR, in good agreement with literature results using different methods. Our estimate of the relative quantum yields suggests a larger difference between the absolute isomerization quantum yields of the two retinal isomers. This relative isomerization quantum yield is estimated in the very same conditions that the excited state lifetime observation, and found to be 2.3±0.3 for the *all-trans* over *13-cis* retinal in ASR isomerization quantum yield ratio.

13. Isomerization speed and coherence versus quantum yield

The understanding of the key parameters ruling the efficiency of isomerization is of prime interest to create efficient artificial photoswitches. In particular, in the absence of means to directly observe the conical intersection through absorption or emission in the visible, the correlation between the excited state lifetime and the isomerization quantum yield have been studied, giving raise to opposite results [110, 129, 108]. It has recently been shown that there is an anti-correlation between excited state lifetime and isomerization quantum yield for PSBR in solution [95] and that the intuitive Landau-Zener picture does not apply to PSBR [111]. Unpublished reports on biomimetic photoswitches (M.Gueye and J.Léonard) indicates that these two quantities may not be correlated at all.
Coherent isomerizations requires a fast excited state lifetime in order to preserve the coherence generated in the excited state from damping via intramolecular processes. These coherent processes are thought to play a role in the isomerization quantum yield [108].

PSBR in ASR, as a result of the present experiments and also reported ones [112], is another example underscroing that isomerization quantum yield and excited state lifetime are unrelated quantities. Both quantities are determined by separate regions of the PESS (and probably results from different parameters of the PSBR molecule), respectively the conical intersection and the vicinity of the Franck-Condon region.

In addition, ASR is a new example showing that a barrierless excited state potential, featuring a 100fs excited state lifetime and indications for a wavepacket assisted isomerization reaction can be relatively ineffi-

cient with a quantum yield in the 10-20% range only.

The excited state lifetime and thus the speed of isomerization, as well as the coherent wavepacket propagation observed are likely to depend on the shape of the potential energy surface of the ground and excited states involved, as well as on the topology of the conical intersection [95]. The complexity of these hypersurfaces and the impossibility to explore them at will experimentally with standard transient spectroscopies makes it difficult to evidence specific schemes yielding to efficient isomerization. Exploring the potential energy surfaces is possible through quantum chemistry simulations but this requires an accurate descritpion of the studied molecues which is time consuming. The chemical design of molecules with specific potential energy surfaces topologies together with isomerization quantum yield characterization might be the simplest way yet to design efficient photoswiches [95]. Combination of systematic experimental (transient absorption) and theoretical (QM/MM simulation and PES calculations) investigations of PSBR in different environments is the key to succeed in this way, the latter possibly allowing to explore all the parameters of the PSBR photoreaction, and the former allowing to validate the models through a restricted observation of it.

14. Fluorescence quantum yield

Since it is possible to perform experiments in very similar conditions and to disantangle the contributions of each isomer of PSBR in ASR, we can study by steady state measurements the excited state properties of both.

Steady state fluorescence measurement is a well suited measurement to characterize the excited state of molecules. However, in the case of retinal proteins, the fluorescence signal is weak and thus requires special care for a precise and quantitative measurement since the excited state lifetime is sub picosecond for both isomeric forms of PSBR in bR and ASR [86]. This leads to fluorescence quantum efficiencies in the range of 10^{-4} as in the case of *all-trans* bR with a quantum yield of 2.5×10^{-4} [87].
We aim for a comparative study of the fluorescence quantum yields of both all-trans and 13-cis forms of ARS and bR via steady-state fluorescence spectroscopy. This requires in principle the use of a well-characterized similarly low quantum yield standard and the measurement of the complete emission spectra. However the detection of such fluorescence spectra is challenging since the emission occurs at wavelengths larger than 650nm and to a large extent even above 1000nm where common Si-based CCD are notoriously less sensitive and noisy.

In a recent letter, we reported the measurement of the fluorescence spectra of the "I" fluorescent state of ASR for both PSBR isomeric forms [126]. The paper is included in this manuscript is the following pages.

14.1. Steady state emission of the fluorescent intermediate of ASR as a function of light adaptation conditions

Chemical Physics Letters 587 (2013) 75–80

Contents lists available at ScienceDirect

Chemical Physics Letters

journal homepage: www.elsevier.com/locate/cplett

Steady state emission of the fluorescent intermediate of Anabaena Sensory Rhodopsin as a function of light adaptation conditions

A. Cheminal [a], J. Léonard [a], S.Y. Kim [c], K.-H. Jung [c], H. Kandori [b], S. Haacke [a,*]

[a] Institut de Physique et Chimie des Matériaux de Strasbourg, Labex NIE, UMR 7504 Université de Strasbourg – CNRS, 67034 Strasbourg, France
[b] Department of Frontier Materials, Nagoya Institute of Technology, Showa-ku, Nagoya 466-8555, Japan
[c] Department of Life Science, Institute of Biological Interfaces, Sogang University, Shinsu-Dong 1, Mapo-Gu, Seoul 121-742, South Korea

ARTICLE INFO

Article history:
Received 2 July 2013
In final form 17 September 2013
Available online 27 September 2013

ABSTRACT

Steady-state fluorescence measurements of the first excited state of the anabaena sensory rhodopsin (ASR), and Bacteriorhodopsin are reported for different light stabilization conditions, including the dark-adapted state. We determine the fluorescence spectra of both all-trans (AT), and 13-*cis* (13C) protonated Schiff base of retinal, and compare the effect of the proteins. Referenced against the fluorescence quantum yield of AT-bR (2.5×10^{-4}) we find for AT-ASR, 13C-ASR, and 13C-bR the values of 3.3×10^{-4}, 0.8×10^{-4}, and 1.7×10^{-4}, respectively. Using reported excited state lifetimes, the radiative rates are deduced, and their differences discussed on the basis of a configuration-dependent oscillator strength.

1. Introduction

Retinal proteins can be regarded as molecular photo-sensors, with biological functions encompassing vision, microbial photosynthesis or photo-taxis. As such they offer remarkable photophysical and mutation-dependent properties such as relatively high extinction coefficients for both one- and two-photon absorption and photo-chromic contrast that lend them interesting potential for engineering as new efficient fluorescent proteins. Very promising results in this direction were recently achieved by using the Proteorhodopsin optical proton sensor [1] and Archaerhodopsin 3 (Arch) from *Halorubrum sodomense* [2]. In the same context, although rather based on absorption properties, channel rhodopsin and its mutants form now a relatively well-established molecular system affording spectrally tunable absorption properties for various application schemes in optogenetics [3]. Those retinal proteins are based on the same scheme: a 7-helix amino-acid structure anchored in the bacteria membrane holding a retinal chromophore in a *binding pocket* via a protonated Schiff base.

Yet the main drawbacks of retinal proteins is their poor quantum yield of fluorescence, as compared to the green fluorescent protein (GFP) and its variants, but locked retinal proteins have already shown a large increase of the fluorescence lifetime [4–8]. One of the most stimulating issues in the study of retinal proteins is understanding the molecular dynamics, involving both the chromophore vibrational modes and the protein response, that govern the isomerization reaction and fluorescence is a precursor of it [9–19]. For bR, it was indeed shown that emission occurs from a short-lived but quasi-stationary state, with only slight twisting, if any, around the C_{13}=C_{14} double bond [11]. Unlike the wavepacket excited state reaction of rhodopsin [20,21] and recently synthetized rhodopsin-mimicking photo-switches [22], the S_1 population accumulates in that fluorescent state [10], with the main portion of it proceeding along the isomerization coordinate within ≈0.5 ps.

In this context, ASR is a very interesting retinal protein as it is reported to afford two stable isomers forms of the retinal chromophore (protonated Schiff base of retinal, PSBR) in ambient conditions, each of which having its own photocycle, and its own isomerization quantum yield [23]. Since the isomer content is illumination dependent [24], wild-type ASR could be a starting point for designing genetically encodable photoswiches for fluorescence imaging applications.

The non-radiative excited state decay rates of retinal proteins are in the 10^{12}–10^{13} s^{-1} range, causing the very weak fluorescence quantum yield ($<5 \times 10^{-4}$). As the PSBR undergoes vibrational cooling at similar rates, the fluorescence spectra are excitation-wavelength dependent, which was referred to as a violation of Kasha's rule [25–27]. This, in addition to the illumination condition-dependence of the trans/*cis* composition in ASR, sets severe constraints for the recording of meaningful time-averaged fluorescence spectra.

We propose here to study the fluorescent state, or *I* intermediate, of ASR in different light-adaptation conditions, and under excitation with a sufficiently low excess energy, in order to determine the fluorescence spectrum of this intermediate for the first time. We compare it with the well-characterized bR with the aim of deepening our understanding of the isomer-dependent photophysics of these two proteins [17]. Unlike most recent work that explored very broadly the relation between electrostatic properties

* Corresponding author.
E-mail addresses: haacke@unistra.fr, stefan.haacke@ipcms.unistra.fr (S. Haacke).

0009-2614/$ - see front matter © 2013 Elsevier B.V. All rights reserved.
http://dx.doi.org/10.1016/j.cplett.2013.09.044

of the retinal binding pocket and the protein's spectral properties [28–30], controlling the *cis*/trans composition in one, and the same protein environment allows to single out the effect of PSBR conformation.

2. Experimental details

The samples are aqueous solutions or suspensions of ASR solubilized in buffer (200 mM NaCl, 25 mM Tris–HCl, 0.05% DDM, pH 7.0), and prepared according to the reported protocol [24,31], and wild type bR from strain S6 buffered at pH = 7.0 [32]. Samples were characterized by VIS absorption giving OD at the light-adaptation independent isosbestic points of 0.22 at 497 nm for ASR, and 0.33 at 530 nm for bR through 1 mm path length, thus concentrations of respectively 143, and 81 μM according to the molar extinction coefficients determined by Kandori [33] (see Figures S1–2 in SI).

Orange-light adapted (OA) and blue-light adapted (BA) ASR are obtained using, respectively an orange (590 nm) and a blue (490 nm) LED, shining through the transparent sample container for more than 15 min, with high enough intensity (>10 mW average power) so as to stabilize the PSBR isomer content in ASR. Light adapted bR (LA-bR) was obtained by exposure to the orange LED for more than 1 h. Absorption spectra were recorded on a Perkin–Elmer Lambda 900 spectrophotometer through a 1 mm path length cuvette, and with recording times (<1 min) much shorter than the time scale of dark adaptation. The so-determined extinction coefficients were calibrated against the well-known peak value of LA-bR at 568 nm [34]. Fluorescence spectra were recorded under stable light-adaptation through constant illumination of the sample container. The fluorescence signal was constant under these conditions.

We left the sample in the dark over more than 12 h at room temperature to obtain the dark-adpated (DA) state (the time constant for DA is about 4 h at 50 °C) for both bR, and ASR. The fluorescence excitation was low enough to maintain the samples in the DA state during 10 min. We collected 10 emission spectra from this DA state until the fluorescence intensity fell by 3% (see SI, Figure S8).

The PSBR isomer content in each stabilization condition was obtained via high performance liquid chromatography (HPLC) using the reported protocol [35] for ASR. The molar compositions of the PSBR isomers were calculated from the peak areas in the HPLC chromatograms. The relative content of AT PSBR is 0.96, 0.45, and 0.36 for DA, blue-light adapted and orange-light adapted, respectively, as reported in Table 1. These values are the average of three independent light-adaptation HPLC experiments that showed very high reproducibility for the isomer content. The illumination dose was high enough to rapidly obtain the same steady-state light-adaptation conditions, as for the fluorescence experiments. The values for DA and OA are in excellent agreement with [36], but we note that lower AT concentrations (15–20%) were reported for red-light illumination (>560 nm) [23]. The origin of these discrepancies is not clear, but it might be due to different light-adaptation rates, the protein coming from different strains or differences in the protein extraction and solubilization procedure. Anyway, in light of the high reproducibility of the HPLC experiments and a very good agreement of the calculated extinction coefficient spectra of both ASR isomers (Figure 4) with literature [37], the above values appear to be a solid basis for the present isomer-specific analysis of the fluorescence spectra.

Table 1
Sample isomer content determined by HPLC for ASR (this Letter) and bR (from Ref. [38]).

Isomer content (%)	DA ASR	BA ASR	OA ASR	DA bR	LA bR
AT	0.96	0.45	0.36	0.4	0.97
13C	0.04	0.55	0.64	0.6	0.03

For bR, the AT PSBR content is assumed to be 40% in DA bR, and 97% in LA bR, according to reported values [38]. The AT PSBR content of the five different forms of bR and ASR investigated are summarized in Table 1.

The static fluorescence setup consists in a plasma lamp-generated unpolarized white light source, spectrally filtered by a monochromator and focused in the sample through a telescope. This excitation beam passes through a CG435 Schott glass filter to prevent excitation by spurious UV from the second order of diffraction. The sample flows from a tank (1.5 mL vial) to a 0.2 mm path length flow cell via a peristaltic pump. The flow cell is placed at a 45° with respect to the incident beam, such that reflections propagate in the direction opposite to the detection. A nitrogen cooled CCD (−120 °C) mounted on a monochromator (3 nm resolution) detects the signal. The cooled multichannel detector affords lower dark count signals and allows for longer integration times than in a conventional PMT fluorometer. Moreover, the sensitivity is better in the near infrared, necessary for the measurement of a weak fluorescence in the VIS–NIR region. Excitation, if not specified later, is at 540 nm with 10.8 μW thus approximately 1 mW.cm^{-2}. In the detection arm, a Semrock 544 nm dielectric cutoff filter prevents scattered excitation photons from entering the detection monochromator. Detection is carried out in the 580–1000 nm window. The setup described here is isolated from parasitic light sources allowing detection of the fluorescence signal with the lowest possible background (<20 counts for 30 s integration time). The spectral response of the system, including CCD, monochromator and filter, is characterized, and corrected for.

Fluorescence measurements consist in measuring the sample and its buffer in the very same conditions. Signals due to the solvent and the electronic background can thus be directly subtracted.

In the buffer, one dominant peak is present and matches the Stokes shifted Raman scattering of the excitation beam on the O–H stretching modes of water, expected at 660 nm. Although the background is directly subtracted from the data, the Raman peak has to be weighted before subtraction, due to absorption by the sample.

Pure isomer absorption spectra are calculated from the isomer ratio determined for the respective light stabilization conditions, and emission spectra are deduced from the contribution to the fluorescence of each isomer calculated from the absorption at the excitation wavelength and the isomer ratio (Table 1).

3. Experimental results

First characterization was carried out on bR, as a reference for setup optimization. The set-up neatly produced bR's characteristic broad fluorescence spectrum (Figure 1), corrected for the detector's spectral response), extending from 600 nm to the NIR, with a maximum located around 730–740 nm [27,39]. The flowing speed is high enough to prevent re-excitation of photocycle intermediates, as indicated by the linearity of the integrated fluorescence signal and the absence of any detectable spectral changes upon increase of excitation intensity (SI, Figures S3–4). The detected fluorescence is thus due to the I_{460} fluorescent intermediate of bR only. The same excitation conditions were used for ASR, leading to identical behavior (SI, Figures S5–7). Dark Adapted bR (DA-bR) is slightly red-shifted with respect to the LA form and shows a ≈30% reduction of the fluorescence signal with comparison to LA-bR indicating a lower quantum yield of the 13C PSBR. The DA-bR spectrum agrees well in shape and intensity with the one reported in [39].

A. Cheminal et al. / Chemical Physics Letters 587 (2013) 75–80

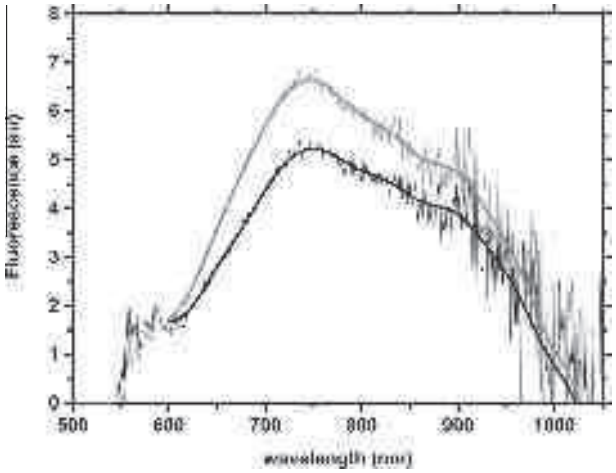

Figure 1. Corrected fluorescence spectra of light adapted bR (grey) and dark adapted bR (dark grey) with smoothed curves to guide the eye, note the Raman band of the protein and membrane between 550 and 600 nm.

Figure 2 depicts the fluorescence spectra of dark-, orange-, and blue-adapted ASR solutions, corrected for the detector's sensitivity. They exhibit qualitatively the same shape as bR, but are shifted towards the blue with a maximum located at 700–710 nm, and a peculiar shoulder around 650 nm. We note that, due to the limited detector sensitivity in the near-IR, both the bR and ASR spectra lack a near-IR tail that is expected to extend up to 1400 nm, when compared with recently reported profiles of stimulated emission [17].

A 50% reduction of the signal is observed from DA- to OA-ASR. With an increased concentration of 13-*cis* PSBR (DA → BA → OA), the spectra shift to shorter wavelengths by 5 nm (SI, Figure S9), but these changes are small compared to the spectral width. As one could have anticipated from the relatively weak shifts of the absorption spectra of DA- and LA-ASR, these isomer-dependent changes are much smaller than those observed for azo-benzene and photo-switchable fluorescent proteins. Figure 3 shows the effect of alternating light-adaptations obtained by sequences of orange and blue adaptations of the sample. The transition between the two stable states is completed in a few minutes, as attested by reproducible levels of spectrally integrated intensities (less than 3% error bar, see SI, Figure S8). This shows an excellent reproducibility of the isomer content under the given illumination conditions, and the stability of the used setup.

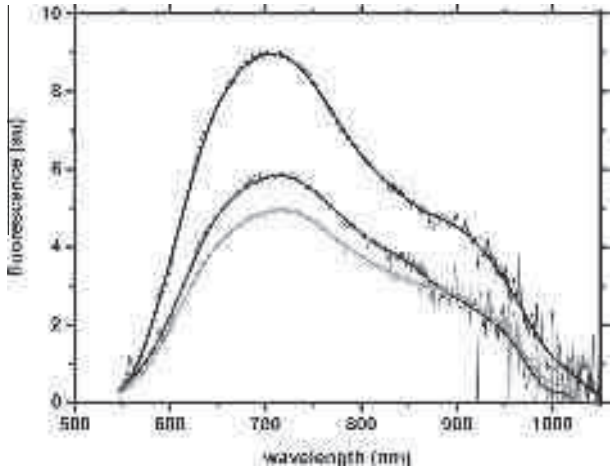

Figure 2. Corrected fluorescence spectra at of OA ASR (grey), BA ASR (dark grey) and DA ASR (black) with smoothed curves to guide the eye.

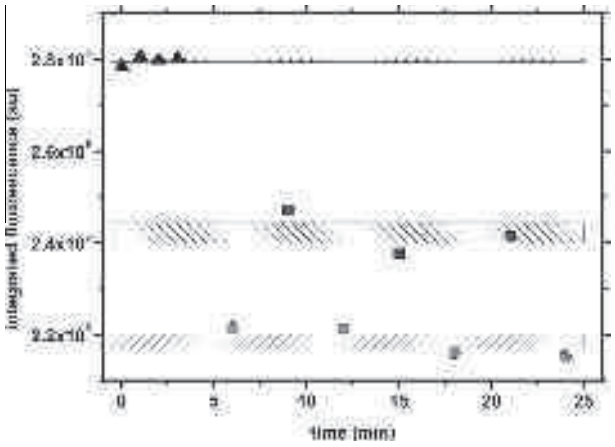

Figure 3. Successive measurements of spectrally integrated ASR fluorescence excited at 495 nm through different light adaptations DA: Dark Adapted, black triangles; OA: Orange Adapted, grey circles; BA: Blue Adapted, dark grey squares. Rectangles of corresponding colors are centered on the mean value and their thickness refers to the standard deviation. Note that the relative error is <3%.

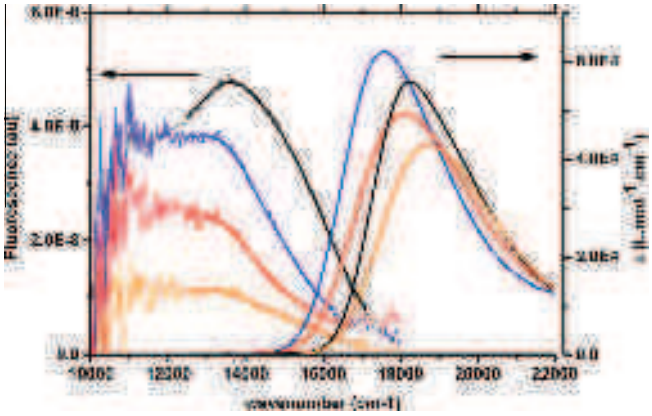

Figure 4. Calculated fluorescence and extinction coefficients spectra of all-trans retinal ASR (black), 13-*cis* retinal ASR (orange), all-trans retinal bR (blue) and 13-*cis* retinal bR (red). Fluorescence spectra are smoothed to guide the eye. The spectral shape below 11,500 cm^{-1} is noisy and undetermined due to the low detector sensitivity. Fluorescence spectra are normalized by the excitation probability. Relative amplitudes thus reflect the fluorescence quantum yield.

The relative intensity drop between DA-ASR and OA-ASR is notably larger than in bR, i.e., when decreasing the amount of AT PSBR through dark-adaptation of bR (Figures 1 and 2), although the isomer content is almost the same in OA-ASR and in DA-bR (Table 1). This suggests directly that the ratio of the isomer fluorescence quantum yields (Φ(AT-bR)/Φ(13C-bR)) is smaller in bR than in ASR, as will be shown below.

The isomer-specific fluorescence spectra $F_{iso}(\lambda)$ (Figure S11) are obtained from the DA and LA spectra of Figures 1 and 2 by accounting for the LA-dependent isomer content (Table 1). Figure 4 plots these spectra as a function of photon energy $F_{iso}(\nu)$ on a linear scale. We use the well-known relation $F(\nu) = AF(\lambda)\frac{1}{\nu^2}$, with A being an arbitrary but fixed scaling factor for that conversion. This conversion procedure amplifies the signal intensity and the noise for $\lambda > 850$ nm. The data are therefore deemed to be reliable for $E > 11{,}500\ cm^{-1}$ only.

The fluorescence quantum yield Φ of the different protein-embedded isomers can be approximated by $F_{iso}(\nu)$ integrated over the limited spectral range of Figure 4, which immediately suggests

the following order: Φ(AT-ASR) > Φ(AT-bR) > Φ(13C-bR) > Φ(13C-ASR). When the noiseless high-energy portion of the $F_{iso}(v)$ is compared with relevant ext. coefficient of the PSBR species, the absence of the mirror image relation is obvious (Figure 4), as already reported for AT-bR [27]. This is also highlighted in Figure S12, where both the fluorescence profile and the absorption spectra are normalized to unity. Interestingly, the 13C fluorescence spectra are distinctively more red-shifted from the absorption maximum than the AT isomers (Figure S12). Also the relatively large high-energy tails of the 13C spectra require a quantitative explanation, on the basis of high-level quantum chemistry calculations [40–42].

For a determination of the isomer-specific Φs, we use $\Phi_{ref} = 2.5 \times 10^{-4}$ of LA-bR as a reference value,[39] according to the relation:

$$\Phi = \Phi_{ref} \frac{n^2 I(1 - 10^{-OD_{ref}})}{n_{ref}^2 I_{ref}(1 - 10^{-OD})} \quad (1)$$

Here n is the refractive index of the solvent, I and I_{ref} the spectrally integrated fluorescence signals and OD and OD_{ref} the optical density at the excitation wavelength. Since our data are limited to the short wavelength (<1000 nm) range, we used the recently published near-IR spectra of the stimulated emission of LA-bR and DA-ASR [43] to extend the fluorescence spectra for the four different isomer species until 1400 nm (cf. Figure S14). This procedure is described in detail in the Supplementary information. We assume the same profile for DA-ASR and LA-ASR, since their similarity was shown experimentally [36]. It turns out that this long-wavelength tail bears not more than 15% of the total intensity, and this irrespective of the protein and isomer content.

For Rhodamine B (Rh B) measured in the same conditions and referenced against LA-bR, we find $\Phi = 0.88$ in good agreement with literature values [44], providing confidence in the procedure and an error bar <10%. Results are reported in Table 2: AT-ASR shows the highest quantum yield of 3.3×10^{-4}, followed by AT-bR, 13C-bR (1.7×10^{-4}), and the lowest being 13C-ASR (0.8×10^{-4}). Note that the value of the 13C-bR quantum yield of 1.7×10^{-4} is higher than the 0.7–1.2 $\times 10^{-4}$ value found by Kouyama et al. [39]. Since our fluorescence spectra are in very good agreement with [39], in particular with respect to the DA-induced intensity drop, the difference in Φ(13C-bR) may be explained by a different hypothesis on the excited state isomer ratio.

At first sight, a quantitative agreement is found between the quantum yields and the excited state lifetimes τ_X recently determined for both isomers in ASR and bR by pump–probe spectroscopy: 13C isomers have a 3 (bR) or ≈5 times (ASR) smaller τ_X than AT. This suggests that the protein-embedded isomers share the same radiative rate k_r. However, we will show in the following that the 13C PSBRs have a 60% higher k_r than the ATs.

4. Discussion

The present letter is, to our knowledge, the first reported characterization of the fluorescence spectrum of the "I" fluorescent states of the ground state of AT-*15-anti* and 13C-*15-syn* PSBRs in ASR and of 13C-*15-syn* in bR. The well-characterized LA-bR fluorescence spectrum of the I_{460} fluorescent state is reproduced and used as a reference. Excitation at 540 nm allows exciting the PSBR with low excess energy, guaranteeing that only S_0 and S_1 are involved in the fluorescence process. In addition, bR's fluorescence spectra superimpose for excitation wavelengths superior to 540 nm, suggesting that emission occurs from a vibrationally relaxed fluorescent state [27], in line with theoretical predictions according to which high-frequency modes relax on a 100–200 fs time scale, i.e., slightly faster than bR's excited state lifetime of 500 fs [10].

AT PSBR offer the largest quantum yields, and ASR enhances the difference in the quantum yield of the PSBR isomers. For a further analysis the fluorescence quantum yields, it is interesting to compare them with the excited state lifetimes of the PSBR isomers in both proteins, recently investigated with best time resolution by the Ruhman team and others (Table 2). A Strickler–Berg analysis has proven to fail in estimating the radiative rate constant for retinal proteins [25]. Indeed, as we show in Figure 4, the fluorescence spectra are not mirror images of the absorption spectra, indicating important structural evolution between the Franck–Condon state and the quasi-stationnary fluorescent I state, as already reported for AT-bR. As pointed out in [45], C=C bond length alternation and dihedral angle twist dominate the excited state structural relaxation on the way to the conical intersection.

A simple linear relation holds between the fluorescence quantum yield and the average lifetime:

$$\Phi = k_r \times \tau_{fluo} \quad (2)$$

This linearity is tested in Figure 5 and allows for an estimation of k_r for the different PSBR conformations and protein environments. k_r is an average value over the different dihedral angles and conformations that define the fluorescent state (see below). It is interesting to see that, within the experimental accuracy, three of the four samples lie on a straight line corresponding to $k_r = 4.5 \times 10^8\ s^{-1}$. 13C-bR shows a higher quantum yield, indicating an almost twice as large radiative rate (red line).

Since these conclusions depend of course on the literature values used for τ_{fluo}, it is necessary to comment on their uncertainty (Table 2) expressed by the relatively large error bars in Figure 5. Values for the bi-exponential decay times, 0.45–0.5 and 5–10 ps

Table 2
Calculated fluorescence quantum yields for pure AT and 13C retinal in bR and ASR. Quantum yields are calculated versus LA bR. Rhodamine B (Rh B) measured in the same conditions gives quantum yield of 0.88 in good agreement with quantum yields found in literature [44], providing a qualitative additional reference. τ represents the excited state lifetimes, determined by TA spectroscopy (ASR) and fluorescence up-conversion and Kerr gating (bR).

	bR LA	bR AT	bR 13C	ASR AT	ASR 13C
Φ ($\times 10^4$)	2.5 [39]	2.5	1.7	3.3	0.8
τ (ps)	0.5 [27,46,47]	0.5/5 [47]	0.15 [17]	0.75/4 [17]	0.15 [17]

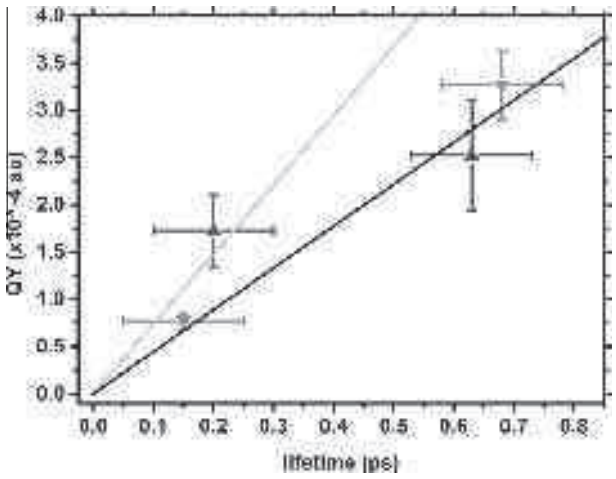

Figure 5. Fluorescence quantum yield of ASR (grey, triangle down) and bR (dark grey, triangle up) for each isomer in function of the fluorescence lifetime (see Table 2). Linear fits of 13C retinal points (light grey, coefficient $a = k_r = (1.4\ ns)^{-1}$) and AT retinal points (black, coefficient $a = k_r = (2.2\ ns)^{-1}$) are plotted. Quantum yield error bars account for the relative uncertainties on the integrated fluorescence (0.05) and reference quantum yield (0.1) and lifetime error bars account for fitting uncertainty for AT retinal (100 fs) and time resolution for 13C lifetimes (100 fs).

of AT in bR are consistently reported in literature, with a non-specified amplitude for the latter. We assumed a 5% amplitude for the slower decay time of AT-bR, consistent with [26,46], yielding the 0.63 ps average value, and the error bar accounts for some scatter in the literature data. The situation is similar for AT-ASR. However, the average value is slightly higher (0.75 ps), irrespective of whether the reported mono- or double exponential fit values are used [43].

However, the short-lived 13C-PSBR fluorescence lifetimes are hardly ever completely resolved, even with highest time resolutions. For reported time resolved fluorescence and absorption spectroscopy on 13C containing retinal proteins, the shortest time constants fitted (often quoted between 100 and 200 fs) are close to the time resolution of 90 fs [36]. The lower boundary of the error bars accounts for that. In addition, the 13C excited state decay traces reported in [17] indicate a small amplitude long-lived tail decaying on a <1 ps time scale. It is not clear whether this is a remainder of the 13C/AT decomposition procedure, but we have nevertheless included it through the higher boundary of the error bars for the 13C values of τ_{fluo}.

Therefore, on the grounds of the presently available data, 13C-bR seems to have a higher radiative rate than the three other PSBR/protein conformations of this Letter. 13C-ASR, with its relatively large error bars for τ_{fluo} could also belong to the steeper line with $k_r = 7.0 \times 10^8\ s^{-1}$. It has been shown by quantum chemistry calculations for bovine rhodopsin [40,41], and in rhodopsin-mimicking photoswitches that the S_1–S_0 transition dipole moment or oscillator strength reach a maximum and decreases as a function of the increasing isomerizing C_{13}=C_{14} dihedral angle on the path to the conical intersection. Hence, the configurations of the excited state fluorescent window, populated during the excited state lifetime, and not the Franck–Condon geometry determine the average radiative rate k_r. Calculating k_r with the Strickler–Berg relation from the integral of the extinction coefficients translates into relative oscillator strengths *in the Franck–Condon regions* and yields $k_{rFC}(AT-bR) = 1.15 \times k_{rFC}(13C-bR)$ and $k_{rFC}(AT-bR) = 1.08 \times k_{rFC}(AT-ASR)$, in clear contradiction to the above findings for k_r (Figure 5).

Recent QM/MM calculations [42] give some hints for explaining the different average radiative rates, as they indicate a significant difference between the excited state potential energy surface (PES) of 13C, and AT-ASR. While the former is barrierless, AT-ASR was found to have an activation barrier, trapping PSBR during the >0.5 ps fluorescence lifetime in a local energy minimum with a larger dihedral angle. The situation for AT-bR is very similar. The short ≈150 fs lifetime of the 13C isomers suggests that the emission stems from the PES close to the Franck–Condon zone, i.e., with little C_{13}=C_{14} torsion. This would lead to a higher oscillator strength for the $S_1 \rightarrow S_0$ transition for 13C PSBRs, and explain the present observations.

5. Conclusion

We report the first steady state fluorescence measurement of the *I* intermediate in the photocycles of Anabaena Sensory Rhodopsin (ASR) for both PSBR isomers as well as for 13C-*15syn* PSBR in bR, and compare it to the known AT-bR fluorescence.

Different light adaptation conditions and characterization of the isomer content allowed calculation of the pure isomers fluorescence spectra as well as the fluorescence quantum yield with respect to AT-bR and in good agreement with RhB reference measured in the same conditions.

The fluorescence quantum yields of AT-, 13C-ASR and 13C-bR are respectively of 3.3×10^{-4}, 0.8×10^{-4} and 1.7×10^{-4}, compared to the 2.5×10^{-4} of AT-bR. Photo-switching of ASR merely does not change its emission spectrum, but the increase in quantum yield is an interesting observation. Within the error bars, the AT PSBRs display the same radiative rate of $4.5 \times 10^8\ s^{-1}$.

For 13C-PSBR on the other hand, the quantum yields are consistent with a higher value of $k_r = 7.0 \times 10^8\ s^{-1}$, however some uncertainty exists as to the existence of slower excited state components in the 13C isomers. Nevertheless, the recently predicted dependence of the PSBR transition dipole moment as a function of C_{13}=C_{14} twisting angle qualitatively explains this increase of k_r. Further work is needed to determine the PSBR configurations in the respective fluorescent states for the two protein environments, in order to confront it with the theoretical predictions made for rhodopsin and AT-bR. A quantitative understanding could indicate routes to modify ASR in view of an enhanced contrast of AT vs 13C fluorescence yields, thereby providing a new photo-switchable far-red emitting fluorescent protein.

Acknowledgments

We thank M. Gallart, D. Cianfarani, and M. Ziegler for their kind help with the fluorescence setup. Insightful discussions with M. Olivucci contributed to the interpretation of the data. Financial support came from the ANR Grant MolNanoMat (2011-INTB-1012-01).

Appendix A. Supplementary data

Supplementary data associated with this article can be found, in the online version, at http://dx.doi.org/10.1016/j.cplett.2013.09.044.

References

[1] J.M. Kralj, D.R. Hochbaum, A.D. Douglass, A.E. Cohen, Science 333 (2011) 345.
[2] J.M. Kralj, A.D. Douglass, D.R. Hochbaum, D. Maclaurin, A.E. Cohen, Nat. Methods 9 (2012) 90.
[3] P. Schoenenberger, Y.-P.Z. Schärer, T.G. Oertner, Exp. Physiol. 96 (2011) 34.
[4] H. Kandori et al., Biochemistry 28 (1989) 6460.
[5] T. Ye et al., Chem. Phys. Lett. 314 (1999) 429.
[6] S. Haacke, S. Vinzani, S. Schenkl, M. Chergui, ChemPhysChem 2 (2001) 310.
[7] H. Kandori et al., Chem. Phys. Lett. 334 (2001) 271.
[8] S. Gozem et al., J. Chem. Theory Comput. 8 (2012) 4069.
[9] M.C. Nuss, W. Zinth, W. Kaiser, E. Kölling, D. Oesterhelt, Chem. Phys. Lett. 117 (1985) 1.
[10] R. González-Luque et al., Proc. Natl. Acad. Sci. 97 (2000) 9379.
[11] S. Ruhman, B. Hou, N. Friedman, M. Ottolenghi, M. Sheves, J. Am. Chem. Soc. 124 (2002) 8854.
[12] P. Kukura, D.W. McCamant, S. Yoon, D.B. Wandschneider, R.A. Mathies, Science 310 (2005) 1006.
[13] S. Schenkl, F. van Mourik, G. van der Zwan, S. Haacke, M. Chergui, Science 309 (2005) 917.
[14] A. Strambi, P.B. Coto, L.M. Frutos, N. Ferré, M. Olivucci, J. Am. Chem. Soc. 130 (2008) 3382.
[15] J. Léonard et al., Proc. Natl. Acad. Sci. 106 (2009) 7718.
[16] I. Schapiro et al., J. Am. Chem. Soc. 133 (2011) 3354.
[17] A. Wand, N. Friedman, M. Sheves, S. Ruhman, J. Phys. Chem. B 116 (2012) 10444.
[18] R. Diller, in: M. Braun, P. Gilch, W. Zinth (Eds.), Ultrashort Laser Pulses in Biology and Medicine, Springer Berlin Heidelberg, 2008, pp. 243–277.
[19] J. Briand, J. Léonard, S. Haacke, J. Opt. 12 (2010) 084004.
[20] Q. Wang, R. Schoenlein, L. Peteanu, R. Mathies, C. Shank, Science 266 (1994) 422.
[21] R. Schoenlein, L. Peteanu, R. Mathies, C. Shank, Science 254 (1991) 412.
[22] J. Briand et al., Phys. Chem. Chem. Phys. 12 (2010) 3178.
[23] O.A. Sineshchekov, V.D. Trivedi, J. Sasaki, J.L. Spudich, J. Biol. Chem. 280 (2005) 14663.
[24] K.-H. Jung, V.D. Trivedi, J.L. Spudich, Mol. Microbiol. 47 (2003) 1513.
[25] G.G. Kochendoerfer, R.A. Mathies, J. Phys. Chem. 100 (1996) 14526.
[26] S. Haacke, S. Schenkl, S. Vinzani, M. Chergui, Biopolymers 67 (2002) 306.
[27] S. Schenkl et al., Phys. Chem. Chem. Phys. 4 (2002) 5020.
[28] L. Song, M.A. El-Sayed, J.K. Lanyi, Science 261 (1993) 891.
[29] W. Wang et al., Science 338 (2012) 1340.
[30] F. Melaccio, N. Ferre, M. Olivucci, Phys. Chem. Chem. Phys. 14 (2012) 12485.
[31] A.R. Choi, S.Y. Kim, S.R. Yoon, K. Bae, K. Jung, J. Microbiol. Biotechnol. 17 (2007) 138.

[32] D. Oesterhelt, W. Stoeckenius, in: L.P. Sidney Fleischer (Ed.), Methods in Enzymology, Academic Press, 1974, pp. 667–678 [31].
[33] Y. Wada, A. Kawanabe, Y. Furutani, H. Kandori, H. Ohtani, Chem. Phys. Lett. 453 (2008) 105.
[34] R.H. Lozier, R.A. Bogomolni, W. Stoekenius, Biophys J. 15 (1975) 955–962.
[35] K. Shimono, Y. Ikeura, Y. Sudo, M. Iwamoto, N. Kamo, Biomembranes 1515 (2001) 92.
[36] A. Wand et al., J. Am. Chem. Soc. 133 (2011) 20922.
[37] A. Kawanabe, Y. Furutani, K.-H. Jung, H. Kandori, J. Am. Chem. Soc. 129 (2007) 8644.
[38] P. Scherrer, M.K. Mathew, W. Sperling, W. Stoeckenius, Biochemistry 28 (1989) 829.
[39] T. Kouyama, K. Kinosita, A. Ikegami, Biophys. J. 47 (1985) 43.
[40] E.N. Laricheva et al., J. Chem. Theory Comput. 8 (2012) 2559.
[41] L.M. Frutos, T. Andruniów, F. Santoro, N. Ferré, M. Olivucci, Proc. Natl. Acad. Sci. 104 (2007) 7764.
[42] A. Strambi, B. Durbeej, N. Ferré, M. Olivucci, Proc. Natl. Acad. Sci. 107 (2010) 21322.
[43] A. Wand, B. Loevsky, N. Friedman, M. Sheves, S. Ruhman, J. Phys. Chem. B 117 (2012) 4670.
[44] G. Weber, F.W.J. Teale, Trans. Faraday Soc. 53 (1957) 646.
[45] P. Altoè, A. Cembran, M. Olivucci, M. Garavelli, Proc. Natl. Acad. Sci. 107 (2010) 20172.
[46] M. Du, G.R. Fleming, Biophys. Chem. 48 (1993) 101.
[47] B. Schmidt et al., Bioenergetics 1706 (2005) 165.

14.2. Further discussion

With the use of the bR [87] fluorescence as a reference, measured in the same experimental conditions to calibrate our fluorescence quantum yield measurement, we obtained the values displayed in table 14.1.

	bR *all-trans*	bR *13-cis*	ASR *all-trans*	ASR *13-cis*
Φ	2.5×10^{-4}	1.7×10^{-4}	3.3×10^{-4}	0.8×10^{-4}

Table 14.1.: Determination of the fluorescence quantum yields of retinal isomers in bR and ASR and of RhB dye calculated using the fluorescence quantum yield of bR *all-trans* as a reference.

The measurement of the ASR fluorescence quantum yield allows to discuss the radiative rate of both PSBRs in ASR [126]. It is interesting to redo the radiative rate calculation using the transient absorption data presented in chapter 11 instead of literature ones, since this experiment is performed with identical light stabilization conditions. The radiative rate can be estimated either from the Strickler Berg equation 5.1 or from the relation between the fluorescence quantum yield Φ and the excited state lifetime τ_{fluo}:

$$\Phi = k_r \times \tau_{fluo} \tag{14.1}$$

While the radiative rate calculated using equation 14.1 is valid within the accuracy of the experimentally determined Φ and τ_{fluo}, the Strickler-Berg formula should not be relevant for PSBR isomerization reactions. As indicated by the absence of the mirror image relation between absorption and emission spectra (in particular for the *13-cis* PSBR proteins, see figure 4 in the paper), the transition from the Franck-Condon zone to the quasi stationnary fluorescent state I involves in bR and ASR a significant conformational change. The latter is responsible for a reduction of the transition dipole moment, as predicted theoretically for Rh [116]. Since the Strickler-Berg relation assumes the same electronic transition dipole moment for the $S_1 \rightarrow S_0$ transition than for the initial $S_0 \rightarrow S_1$ transition, the radiative rate calculated with equation 5.1 is thus the radiative rate in the vicinity of the Franck-Condon region and is noted k_r^{FC}.

On the other hand, the radiative rate calculated with equation 14.1 reflects the effective radiative rate due to the conformation-dependent transition dipole moment averaged over the excited state lifetime. It is thus the average radiative rate over the configurations on the excited state potential energy surface explored within the excited state lifetime, and this rate is noted $k_r^{average}$.

The so determined radiative rates are presented in table 14.2. Note that the use of the consistent transient absorption data to estimate the excited state lifetime leads to an increase in the estimation of the *13-cis* PSBR radiative rate to approximately $8{\times}10^{-8}\mathrm{s}^{-1}$, while the one of the *all-trans* PSBR stays close to $4{\times}10^{-8}\mathrm{s}^{-1}$, in comparison with the previously determined rates. This makes the two PSBR isomers very similar whatever the opsin environment, while it was not clear wether the *13-cis* PSBR ASR shared the same radiative rate in figure 5 of subsection 14.1.

	bR *all-trans*	bR *13-cis*	ASR *all-trans*	ASR *13-cis*
$k_r^{FC}(\times 10^8 s^{-1})$	1.2	1.1	1.2	0.9
$k_r^{average}(\times 10^8 s^{-1})$	4	8.3	4.3	7.6

Table 14.2.: Determination of the radiative rate in the Franck-Condon region and of the average radiative rate over the excited state reaction coordinates for both retinal isomers in ASR and bR.

The transition dipole moment of the $S_1 \rightarrow S_0$ transition in PSBR was shown to evolve during the excited state lifetime, passing by a maximum value and dropping when approaching the conical intersection [116, 117]. This is linked to the rotation of the isomerizing bound and the change in the bond length alternation, as simulated by QM/MM calculations[103]. These simulations are in good agreement with our observation of an increase of the radiative rate, evidenced by a lower radiative rate in the Franck-Condon region than on average during the excited state lifetime..

15. Conclusion

This work on ASR has been performed in collaboration with Corean and Japanese partners (K.H. Jung, Sogang university, Seoul, and H.Kandori, Nagoya Institute of Technology, Nagoya) providing us the ASR sampes and the HPLC characterization. Even though partially redundant with already published results, this work presents a more comprehensive investigation of the photophysical properties of both PSBR isomers in ASR in time resolved and steady state experiments performed at room temperature, with fresh samples and small variations in pH, and most importantly, under well controlled and identical light adaptation conditions.

We characterized the isomer content of the ASR samples independently by HPLC thereby establishing an easy and reproduceable protocol for stabilizing the isomer content under steady state background illumination by a few mW LED. This allowed to prepare samples with accurately known isomer content and to single out isomer specific properties, such as absorption, fluorescence and transient absorption. Most importantly, it enabled to make a clear link between the ultrasfast photochemistry of the PSBR in ASR measured with transient spectroscopies together with the measurement of the isomerization quantum yield by steady state experiments.

The transient absorption experiments confirmed the shorter excited state lifetime of the *13-cis* PSBR in comparison with the *all-trans* one. We showed that the *13-cis* isomer excited state decays in 100fs and exhibits non exponential kinetics characteristic of a wavepacket in the excited state. We obtained evidence for weak and rapidly damped low frequency oscillations in the ground state, suggesting the partial preserva-

tion of the wavepacket coherence after the CI. These specific excited state dynamics confirm the barrierless PES of this PSBR from the Franck-Condon region, as predicted by QM/MM simulations.
On the other hand, the *all-trans* ASR decays mono-exponentially in 770nm. The rate-equation like photochemistry of this isomer is in agreement with the presence of a barrier, leading to a stochastic isomerization process.

We estimated the room temperature molar absorption spectrum of the "K" intermediate, as an extrapolation from the published 130K spectra for both PSBR isomers. This species is the relaxed form of retinal obtained after isomerization. The analysis of the stationnary "K minus ground state" difference absorption spectra at delays >10ps, allowed us to determine the isomerization quantum yield directly from the femtosecond transient absorption measurement data, as the first event right after the thermalization and structural relaxation of the isomerization photoproduct. The relative isomerization quantum yield determined by this technique is ($\frac{\Phi_{T\to C}}{\Phi_{C\to T}} = 2.3 \pm 0.3$) and indicates that the *13-cis* isomer, even though much faster decaying from the excited state, has a significantly lower quantum yield than its *all-trans* counterpart. Within the limited accuracy of our method, we obtain values for the absolute quantum yields. For both isomers, the values found are lower than the ones published by Kandori [120], in particular for the *all-trans* isomerization, even for the upper boundary value (≈20%).
Nevertheless, our results confirm that ASR is very special among retinal proteins since the isomerization quantum yields for these two functional processes are much lower than almost all the retinal proteins investigates to the date. It also points out ASR as a novel example where the isomerization quantum yield and excited lifetime show opposite trends.

What could be the reason for these relatively low isomerization quantum yields, in terms of benefit for the evolution-selected biological function ? With this retinal protein, natural selection allowed to produce an opsin which uses the interconversion of two PSBR isomers to achieve a biological function. Surprisingly, the initial steps of these photoreac-

tions, starting with the isomerization of the PSBR, are achieved with a relatively low quantum yield in comparison to the general trend in retinal proteins, showing usually >50% isomerization quantum yields for functional processes. This may result from a trade-off in the binding pocket design in order to achieve both isomerizations in a balanced way.

Last, but not least we determined the low fluorescence quantum yields of $3.3 \pm 0.4 \times 10^{-4}$ and $0.8 \pm 0.1 \times 10^{-4}$ for *all -trans* and *13-cis* retinal in ASR respectively. The ensuing radiative rates are not the same for both isomers. We discuss this observation in terms of the structural evolution of the both forms of the PSBR in the excited states. This provides indications for a decrease of the radiative rate (and thus of the oscillator strength) when going from the Franck-Condon region to the CI. Further studies are needed to substantiate this finding experimentally.

We pointed out that the understanding of the parameters driving the isomerization quantum yield of PSBR in proteins can not rely simply on lifietime measurements, as the one used in the present work based on UV-VIS spectroscopy, which samples only those regions where the transition dispole moments are high enough. Ideally, one would like to be able to determine the shape of the PES of the PSBR excited state from the Franck-Condon region all the way to the conical intersection, and thereafter. The typical ultrafast pump-probe experiment is limited to achieve this purpose since it only allows to explore a small portion of the PES. One approach to explore the PES further could rely on multi-pulse experiments, such as (ultrafast) pump-push probe experiments with a visible pump and an infrared one. This could allow to inject energy into vibrational modes of the excited state with the infrared pulse and may allow to explore the PES. One may also want to excite vibrational modes in the ground state with an infrared pulse and later promote the PSBR in the excited state with the visible pump to start the reaction from a different Franck-Condon region with different coordinates. This would allow to access new regions of the excited state PES, and may evidence the role of the protein in driving the isomerization.
The investigation of both isomers of the PSBR with a new TA setup

with 7fs time resolution is scheduled and will help to have more insight on the excited state of the PSBR, and further characterize the coherence of the *13-cs* PSBR. In particular, pump-dump-probe experiments with the same setup could provide further information on the evolution of the PSBR excited state of both PSBR isomers, and invetigate the origin of the excited state barrier and its role on the isomerization process. The study of mutants of the protein where the amino acids of the binding pocket are changed, using TA, may help in understanding the role of the binding pocket on the very special photochemistry of this protein.

Part IV.

General Conclusion

To conclude, transient absorption techniques is a powerful tool to investigate the ultrafast processes of energy conversion. Transient absorption allows to follow with sub picosecond resolution the different species involved in the photochemistry of the studied materials through their optical transitions. However, this technique suffers from the overlap of the different contributions hardening the understanding of the reactions. Its combination with transient fluorescence measurements allows to single out the excited state contributions. Nevertheless, it may not be sufficient for complicated systems such as active layer for OPV where both the donor and acceptor molecules contributes and forms new species, such as charged species. In this case, combination of transient absorption and fluorescence with other spectroscopic techniques is essential. In particular, in the case of photovoltaics, the spectroelectrochemistry allows to characterize the charged species absorption and to distinguish these signatures in the difference absorption spectra obtained by TA.

However, the TA has its limits, and the observation of the species involved in the photochemistry studied requires that they possess characteristic features that allow to identify tem, and that they possess a sufficient absorption in the probed spectral window (case of PCBM anions and polarons in TB2 aggregates). In addition, the classic TA experiments does not allow to access to spatial information in the samples. In particular, in the case of active layer for photovoltaics, the morphology plays an important role, although the characteristic size of the probed region only allows to have a global information. In this case, the morphological information needs to be investigated with other techniques such as TEM or electron diffraction, to obtain useful information on the morphology.

This thesis was made possible by the fruitful collaborations with Nicolas Leclerc and Raymond Ziessel (TB2 synthesis, ICPEES), Thomas Heiser (film preparation and electronic characterization, ICUBE) and Laure Biniek and Martin Brinkmann (electron diffraction, ICS) within the Rhin Solar european project, Beatrice Omiecienski in Sabine Ludwigs (spectroelectrochemistry, IPOC) within the Molnanomat project,

Kwan Hwang Yung (ASR samples and HPLC measurements, Institute of Biological Interfaces) and Hideki Kandori (ASR samples, Nagoya Institute of technology).

List of Figures

List of Tables

Part V.

Annexes

A. BODIPY:PCBM blends photochemistry

A.1. film preparation

The fims studied here have been prepared by spin coating solutions of pure TB2 or blends with PCBM from chlorobenzene solutions with a concentration of TB2 of 18.2mg.mL^{-1}. After deposition of a droplet of solution on the substrate (either 1inch side ITO coated glass with PEDOT:SS or directly in approximately 1inch side fused silica microscope pates), the spinnig is set in a first time to 2000rpm for 2min, with a 600rpm.s^{-1} acceleration, and later for 1min at 2500rpm with the same acceleration. It generally allowed to produce homogeneous samples (in the center of the substrate) except in certain cases where there are indication for the presence of precipitated molecules inducing rings, as shows in figure A.1.
The transient absorption measurements were carried out in homogeneous regions.

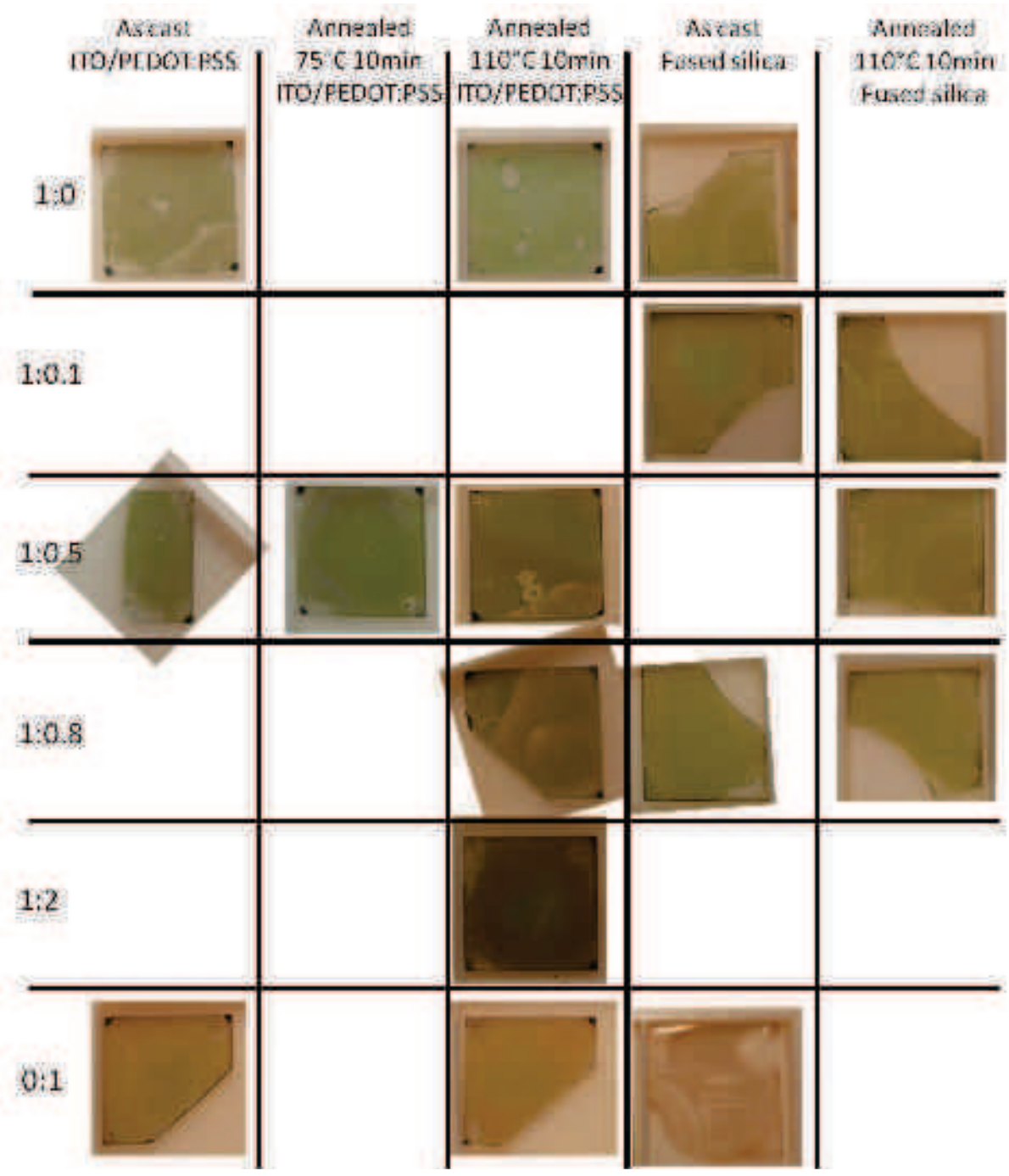

Figure A.1.: Pictures of the different films produced and used in this study.

A.2. Exciton-exciton anihilation

The figures A.2 and A.3 shows the effect of the excitation density on the excited state kinetic of TB2 in as cast and annealed films. The intensity indicated corresponds to the pump intensity. The pump spot has a diameter of 75μm, which results in an average excitation density of 60μW.cm^{-2} for a 40μW pump.

When increasing the pump intensity, the signal is longer lived. Multi-exponential fits of the decays indicate that the >10ps part of the signal decay with essentially the same time constant in all cases (25ps and 1.7ns for the as cast TB2 and 27ps and a >5ns decay for the annealed TB2 film), whereas at shorter delays, the decays are shorter (1.3ps, 2.1ps and 2.1ps with a 0.13fs rise for the as cast film, reducing the intensity and 0.37/3ps, 0.78/2.9ps and 0.9/6.5ps for the anealed TB2 fim, going fro 120 to 40 μW). The amplitudes associated with the decay are changed at all timescales. In particular, in the case of the as cast TB2 film, the signal shows a rise in the sub picosecond regime wereas for higher excitation densities the signal mainly decay on this timescale.

This change in the sub picosecond kinetics is attributed to exciton-exciton anihilation [32] due to the high density od excitons generated by the pump pulse. The data presented in the main text corresponds to a 40μW excitation, which is a trade off between signal to noise ratio and low excitation density.
At this pump fluence, we expect these phenomena to be reduced but we can not exclude that it is absent. Going to lower fluences leads to a dramatic decrease in the signal to noise ratio detrimental to the detection of the short amplitude long lived transient absorption signals. The same fluence was used for the TA and TF measurements in the blends. In this case, the charge generation is expected to dominate the exciton-exciton anihilation process [130].

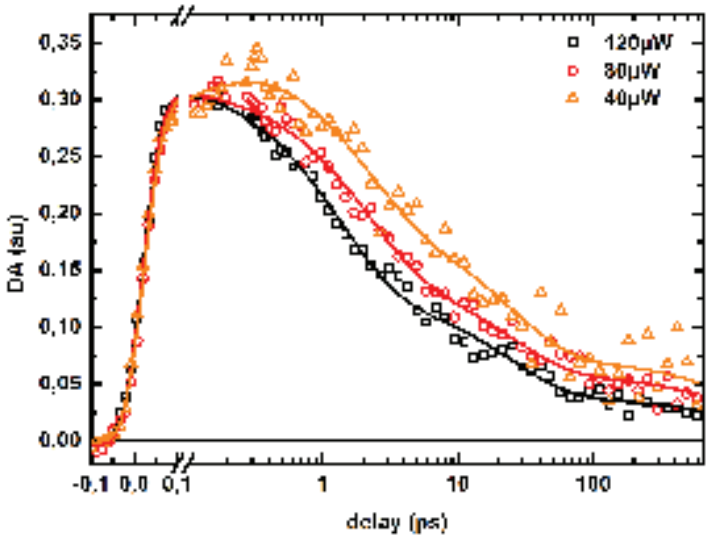

Figure A.2.: Set of ESA kinetic traces of a TB2 film as cast on ITO/PEDOT:PSS as a function of the excitation density. Each kinetic trace is an average of the ESA signal in the 515-590nm range. The 120, 80 and 40μW traces are divided by 3,2 and 1 respectively to match the amplitude of the signal with the excitation intensity.

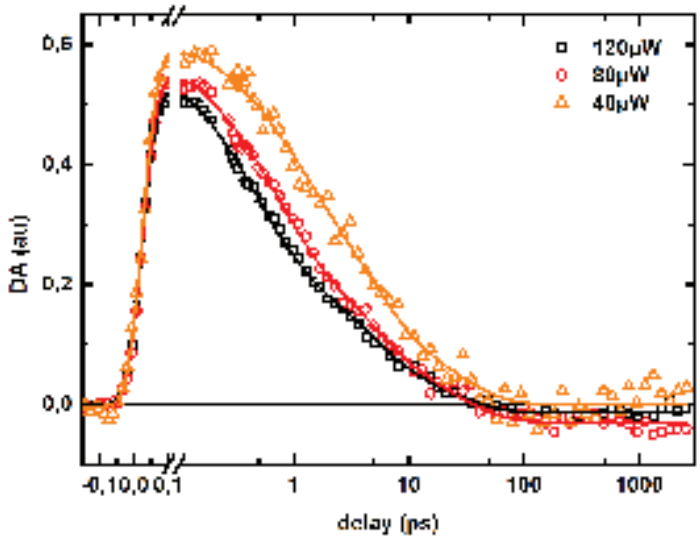

Figure A.3.: Set of ESA kinetic traces of an annealed TB2 film on ITO/PEDOT:PSS as a function of the excitation density. Each kinetic trace is an average of the ESA signal in the 515-590nm range. The 120, 80 and 40μW traces are divided by 3,2 and 1 respectively to match the amplitude of the signal with the excitation intensity.

A.3. Global analysis of the 1:0.5 blend annealed

The kinetic traces from the TA data of the 1:0.5 blend annealed shows signatures at early times that can hadly be fitted by a sum of exponentials. A classic global analysis is performed on the data set but the early singular kinetics are not fitted correctly (see the top two graphs on the right in figure A.4). The associated early times DADS are likely to not represent the initial processes with high fidelity.

To have a better insight on the early kinetics, the TA data between -100 and 160fs are disregarded and the analysis is performed on this reduced data set. The singular kinetics at short delays are much well fitted (see the top two graphs on the left side of figure A.4). The DADS corresponding to the picosecond or longer delays are similar, but the sub picosecond ones are changed. First, the 10fs DADS associated to coherent artifact is absent in the truncated analysis, however a new 0.35ps DADS is fitted. An approximately 70fs DADS is found in both cases but the DADS associated is different. The one obtained using the truncated data shows the characteristic signature around 500nm of the raise in the electroabsorption signal associated to polarons, which indicates an early free charge generation in this blend Note the presence of the characteristic signature of the TB2 SE, which may indicate that the relaxation of the TB2 excitons occrus on this timescale. The 0.35ps DADS contains the signature of the TB2 GSB around 450nm, which indicates exciton recombination on this timescale. This may indicate that there is still some exciton-exciton anihilation in the blends or that there is recombination pathways at short time delays.

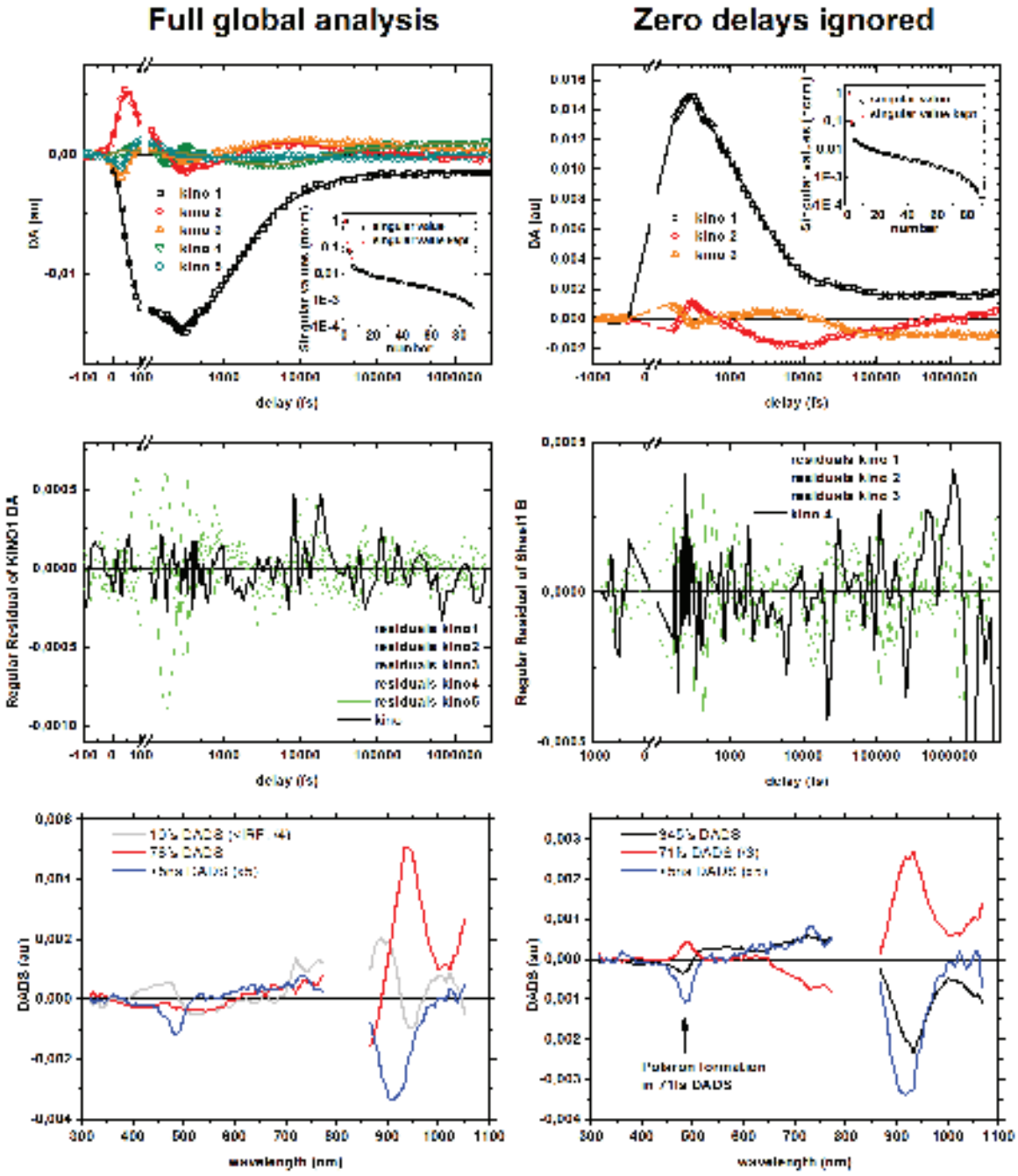

Figure A.4.: Comparison of the early DADS using two different global analysis on the TA data of the 1:0.5 blend anealed. The left column shows the analysis using the whole TA data and in the left panel the vicinity of the zero delays are disregarded. The intermediates panels shows the comparison of the residuals of the fit with the first discarded singular kinetic from the SVD.

A.4. Transient absorption maps of films with amorphous TB2

Figure A.5 shows the TA maps of the blends studied containing amorphous TB2 with various PCBM contents. It shows that the blends are characterized by the TB2 cation signature with absorption maximums at 600nm and 1050nm, while the neat TB2 films shows excited state dynamics as a comparison.

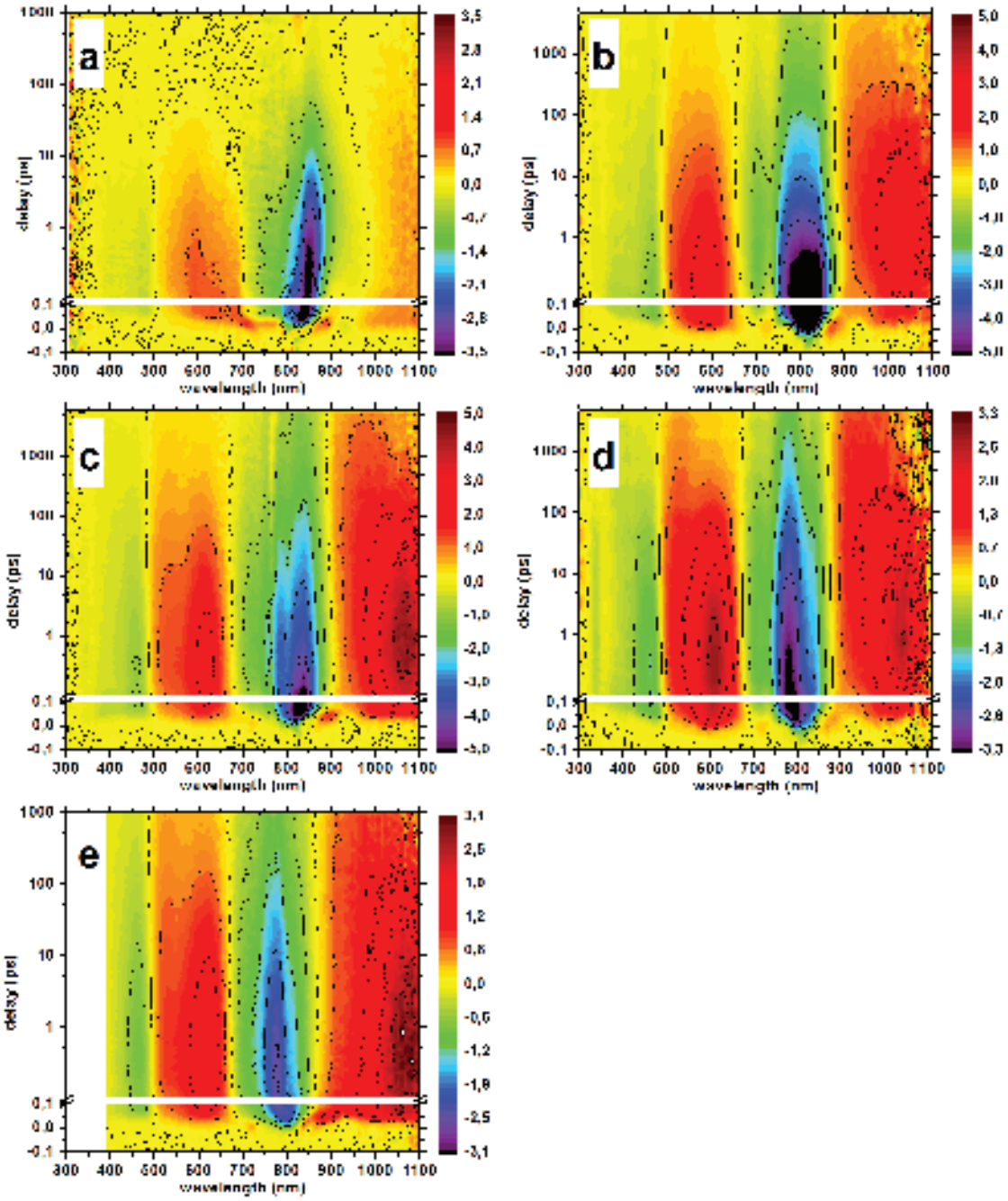

Figure A.5.: Comparison of the TA maps of blends containing amorphous TB2. The maps are not corrected for the number of absorbed photons. Panel a to e displays respectively the 1:0, 1:0.1 (fused silica), 1:0.5, 1:0.8 (fused silica) and 1:2 TB2:PCBM blends. Cast on ITO/PEDOT:PSS if not mensioned.

A.5. Electronic characterization

OSC have been prepared using fims produced in the same conditions than the transient spectroscopy investigation. The best cells out of a set of 8 cells of each have been selected for measuring the internal quantum efficiency. These measures are presented in figure A.6. The corresponding PCE was 0.6, 0.7 and 0.4% for the 1:0.5, 1:0.8 and 1:2 TB2:PCBM blends respectively.
The PCE values are significantly lower than the reported ones, which might be explaines by a thiner active layer (EQE lowered) and the use of aluminium alone for the top electrode instead of aluminium and lithium flouride, which may drastically reduce the charge collection.

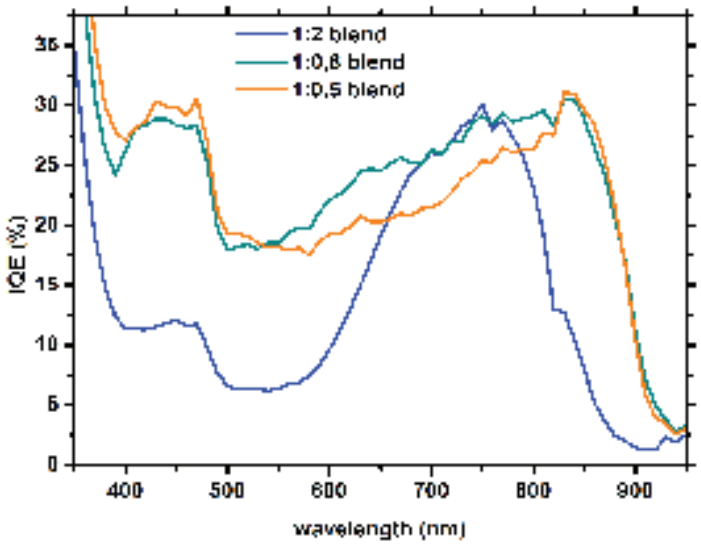

Figure A.6.: Internal quantum efficiency of different TB2:PCBM blends on ITO/PEDOT:PSS annealed 10min at 110^o. Measurement performed at the ICube laboratory by N.Leclerc.

B. Anabaena sensory Rhodopsin

B.1. Details of the calculation of the "K" species absorption spectrum at room temperature

To obtain the "K" species absorption spectra at ambient temperature, we suppose that the change in the absorption spectrum when going from 130K to 273K occurs mainly through a change in the inhomogeneous broadening of the vibronic transitions, induced by the change in the amino acid structure surrounding the chromophore with temperature, and a shift in energy of the latter transitions for the same reasons. These changes are characterized on the steady state species since its spectra are known for both temperature conditions.
The first step is the fitting of the $S_0 \rightarrow S_1$ chromophore absorption band by a sum of equally spaced gaussian functions sharing the same broadening. This should represent the inhomogeneous broadening of the vibrationnal levels of the $S_0 \rightarrow S_1$ absorption band. The energy spacing of the gaussians would represent the dominant vibrationnal modes. The fitting of the steady state and K state of both retinal isomers in ASR are presented in figure B.1.

The fits of the 130K steady state absorption are then used with the same amplitude and spacing for the vibrationnal levels, but with an energy shift and a different broadening of the gaussians to fit the shape of the 273K steady state molar absorption spectra. The resulting parameters are the spectral shift of the absorption band $\Delta\nu_0$, the broadening of the vibrationnal lines shapes $\delta\omega$ and the proportionnality coefficient α scaling the fitted absorption profile as a molar absorption. The parameters fitted are displayed in table B.1 and the fits are exposed in figure B.1, panels a and b.

	ν_0 (cm^{-1})	ν (cm^{-1})	ω (cm^{-1})	$\Delta\nu_0$ (cm^{-1})	$\delta\omega$ (cm^{-1})
all-trans ASR	17652	877	548	39	126
13-cis ASR	17857	1258	445	185	105
$K_{all\text{-}trans}$ ASR	17327	1105	690	-	-
$K_{13\text{-}cis}$ ASR	16219	836	714	-	-

Table B.1.: Parameters used to fit the 130K absorption spectra. ν_0 indicates the energy of the first vibrationnal line shape, ν is the spacing bitween vibrationnal levels, ω is the broadening parameter of the gaussians. The last two columns presents the shift and broadening parameters used to fit the 273K molar absorption spectra using the same parameters and model emplyed to fit the 130K steady state absorption spectra.

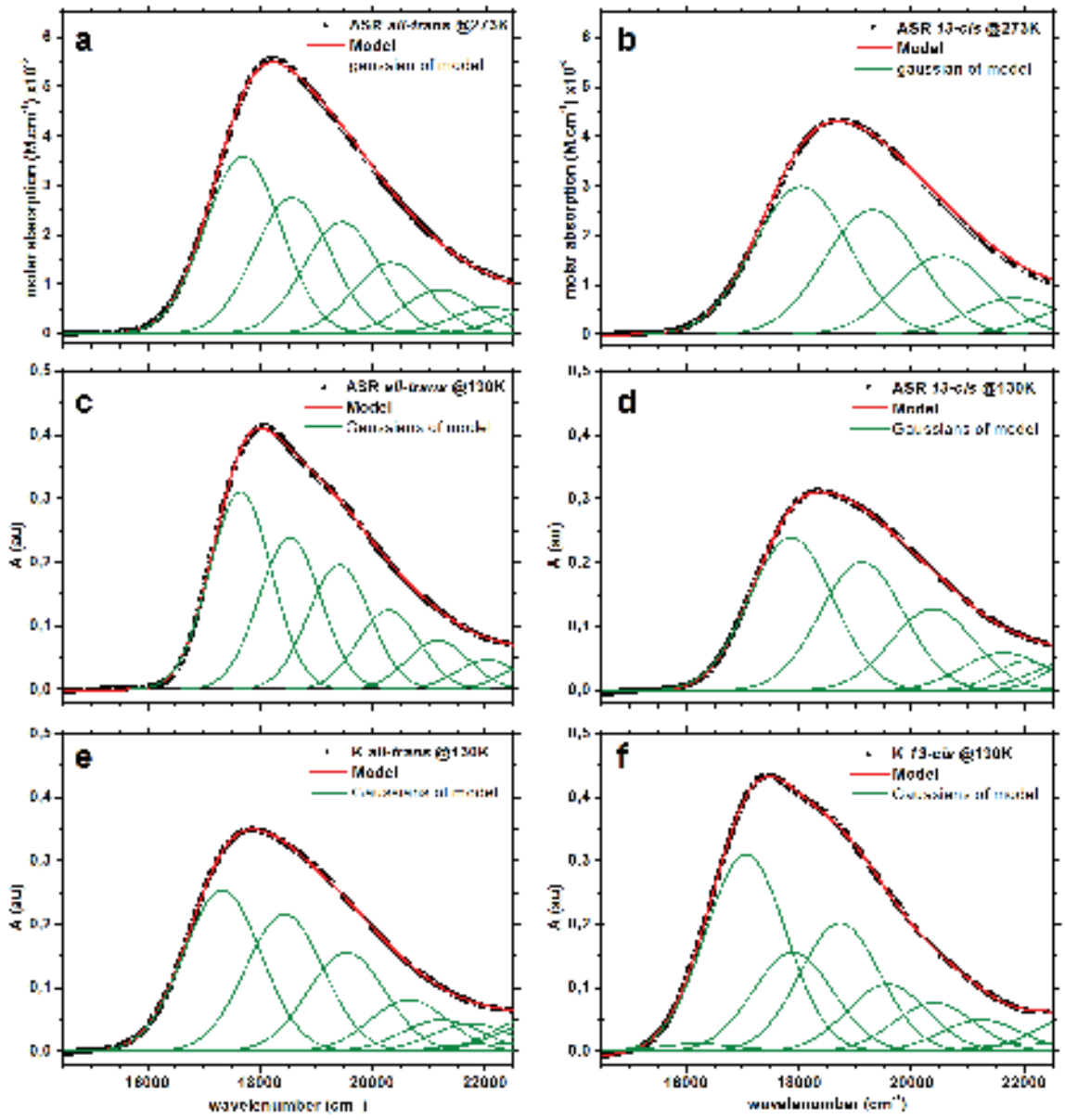

Figure B.1.: Fit of the 273K ground state molar absorption spectra for both PSBR isomers in ASR (a and b).130K absorption spectra of the ground state (c and d) and K state (e and f) absorption spectra of both PSBR isomers in ASR. The symbols represents raw data, the thick red line the fit and the thin green curves shows the gaussian curves modeling the vibronic levels with inhomogeneous broadening.

B.2. Influence of excitation wavelength

The isomerization of ASR have been proven not to depend on the excitation wavelength in the 488 to 594nm range [120]. We tested this behaviour by proceeding to transient absorption measurements for different pump wavelengths, to see the influence of the excess energy on the photophysics. The pump wavelengths used are 400nm, 535nm, 560nm and 580nm, and the samples were measured in two different light adapted states to deduce the pure isomer contributions. The excitation conditions are shown in figure B.2.

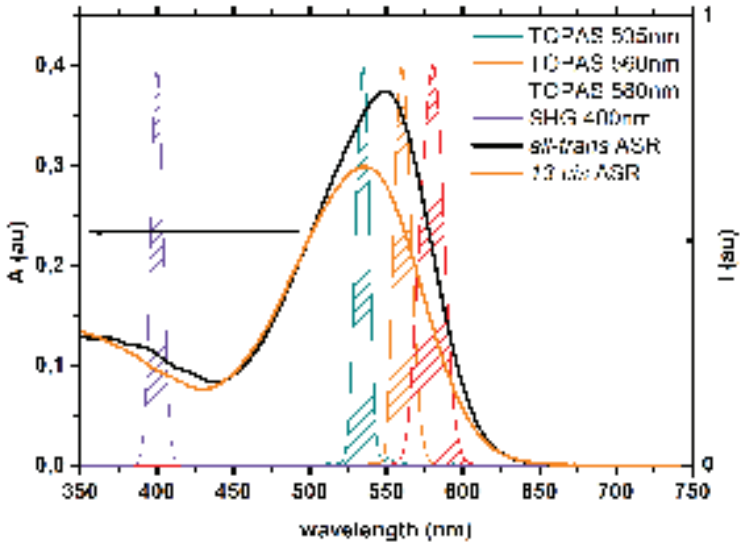

Figure B.2.: Spectra of the different pump beams used, along with the absorption spectra of both retinal isomers in ASR. The source used to obtain the pump beams are indicated. See legend for details.

Except in the case of the 400nm excitation, changing the excitation wavelength has no sizeable influence on the photophysics of both retinal isomers in ASR, within our experimental sensitivity, as exemplified by ESA kinetics comparison in figure B.3. The ultrafast relaxation of the ESA in the first hundred femtoseconds is very similar, and the longer time kinetic evolution are similar. The low frequency oscillations on the 150fs to 1.2ps timescale seems to have a different phase but the signal

to noise ratio on these data sets does not allow to characterize them precisely. The 400nm excitation data presents different evolution in the vicinity of zero delays, due to the lower time resolution, and the longer times evolution shows a evolution on a longer timescale. For the latter experiment, a <100fs lived broad induced absorption spanning from 600 to 750nm is present (figure B.4). This induced absorption may either be the signature of a $S_0 \rightarrow S_n$ excitation for this higher energy excitation, or to a $S_1 \rightarrow S_n$ transition accessible in the Franck-Condon region. The relaxation of this excited state qualitatively leads to the same excited state populated by excitation at lower photon energy, but its lifetime is longer. This may indicate that the relaxation of this higher energy state populates S_1 in different reaction coordinates.

In conclusion, the excess energy has no sizeable effect on the excited state kinetics of both retinal isomers in ASR within our experimental resolution, for a $S_0 \rightarrow S_1$ excitation. Excitation to higher energy states with higher photon energy leads to the population of the same excited state but its kinetics is different. In particular, the *all-trans* PSBR does not show slower kinetics with the 580nm excitation, as one may expect from the barrier on the excited state.

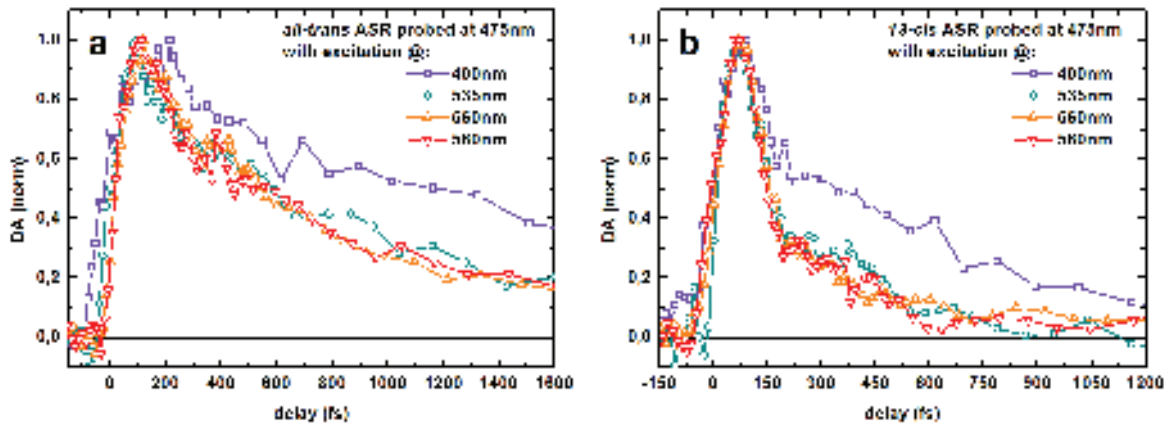

Figure B.3.: Panel a shows the normalised kinetics of the *all-trans* retinal in ASR probed at 475nm in the ESA for different excitation wavelengths. Panel b shows the same kinetics for the *13-cis* retinal ASR. Note that the time resolution for the 400nm excitation is worse than for the other experiments.

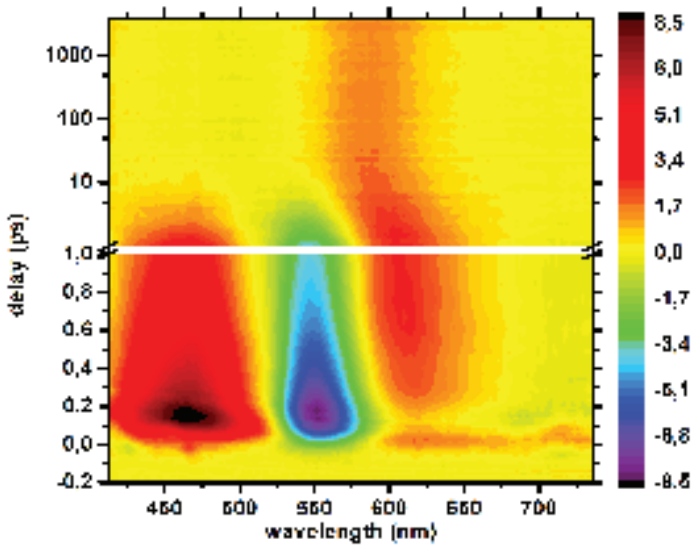

Figure B.4.: Transient absorption map of OA ASR excited with 400nm pulses.

Bibliography

[1] E. Riedle, M. Beutter, S. Lochbrunner, J. Piel, S. Schenkl, S. Spörlein, and W. Zinth. Generation of 10 to 50 fs pulses tunable through all of the visible and the nir. *Applied Physics B*, 71(3):457–465, 2000.

[2] Robert Huber, Helmut Satzger, Wolfgang Zinth, and Josef Wachtveitl. Noncollinear optical parametric amplifiers with output parameters improved by the application of a white light continuum generated in caf2. *Optics Communications*, 194(4–6):443 – 448, 2001.

[3] Q.Z. Wang, P.P. Ho, and R.R. Alfano. Supercontinuum generation in condensed matter. In RobertR. Alfano, editor, *The Supercontinuum Laser Source*, pages 33–90. Springer New York, 2006.

[4] Y.R. Shen and Guo-Zhen Yang. Theory of self-phase modulation and spectral broadening. In RobertR. Alfano, editor, *The Supercontinuum Laser Source*, pages 1–32. Springer New York, 2006.

[5] M. Bradler, P. Baum, and E. Riedle. Femtosecond continuum generation in bulk laser host materials with sub-μj pump pulses. *Applied Physics B*, 97(3):561–574, 2009.

[6] Julien Nillon, Olivier Crégut, Christian Bressler, and Stefan Haacke. 2 mhz tunable non collinear optical parametric amplifiers with pulse durations down to 6 fs. In Kaoru Yamanouchi, Steven Cundiff, Regina de Vivie-Riedle, Makoto Kuwata-Gonokami, and Louis DiMauro, editors, *Ultrafast Phenomena XIX*, volume 162 of *Springer Proceedings in Physics*, pages 761–765. Springer International Publishing, 2015.

[7] A. L. Dobryakov, S. A. Kovalenko, A. Weigel, J. L. Pérez-Lustres, J. Lange, A. Müller, and N. P. Ernsting. Femtosecond pump/supercontinuum-probe spectroscopy: Optimized setup and

signal analysis for single-shot spectral referencing. *Review of Scientific Instruments*, 81(11):–, 2010.

[8] Thomas Gelot, Patricia Tourón-Touceda, Olivier Crégut, Jérémie Léonard, and Stefan Haacke. Ultrafast site-specific fluorescence quenching of 2-aminopurine in a dna hairpin studied by femtosecond down-conversion. *The Journal of Physical Chemistry A*, 116(11):2819–2825, 2012. PMID: 22289047.

[9] J. Shah. Ultrafast luminescence spectroscopy using sum frequency generation. *Quantum Electronics, IEEE Journal of*, 24(2):276–288, Feb 1988.

[10] X.-X. Zhang, C. Würth, L. Zhao, U. Resch-Genger, N. P. Ernsting, and M. Sajadi. Femtosecond broadband fluorescence upconversion spectroscopy: Improved setup and photometric correction. *Review of Scientific Instruments*, 82(6):–, 2011.

[11] Lijuan Zhao, J. Luis Perez Lustres, Vadim Farztdinov, and Nikolaus P. Ernsting. Femtosecond fluorescence spectroscopy by upconversion with tilted gate pulses. *Phys. Chem. Chem. Phys.*, 7:1716–1725, 2005.

[12] Gerald Auböck, Cristina Consani, Roberto Monni, Andrea Cannizzo, Frank van Mourik, and Majed Chergui. Femtosecond pump/supercontinuum-probe setup with 20 khz repetition rate. *Review of Scientific Instruments*, 83(9):–, 2012.

[13] C. Ruckebusch, M. Sliwa, P. Pernot, A. de Juan, and R. Tauler. Comprehensive data analysis of femtosecond transient absorption spectra: A review. *Journal of Photochemistry and Photobiology C: Photochemistry Reviews*, 13(1):1 – 27, 2012.

[14] S. A. Kovalenko, A. L. Dobryakov, J. Ruthmann, and N. P. Ernsting. Femtosecond spectroscopy of condensed phases with chirped supercontinuum probing. *Phys. Rev. A*, 59:2369–2384, Mar 1999.

[15] International Energy Agency. *Key World Energy STATISTICS*, 2013.

[16] Shahriar Shafiee and Erkan Topal. When will fossil fuel reserves be diminished? *Energy Policy*, 37:181–189, 2009.

[17] Albert Einstein. Uber einen die erzeugung und verwandlung

des lichtes betreffenden heuristichen gesichtspunkt. *Annalen der Physik*, 17:132–148, 1905. [in German].

[18] Laju Bu, Xiaoyang Guo, Bo Yu, Yao Qu, Zhiyuan Xie, Donghang Yan, Yanhou Geng, and Fosong Wang. Monodisperse cooligomer approach toward nanostructured films with alternating donor-acceptor lamellae. *Journal of the American Chemical Society*, 131(37):13242–13243, 2009. PMID: 19754184.

[19] Shoji Miyanishi, Yue Zhang, Keisuke Tajima, and Kazuhito Hashimoto. Fullerene attached all-semiconducting diblock copolymers for stable single-component polymer solar cells. *Chem. Commun.*, 46:6723–6725, 2010.

[20] M. Kasha, H. R. Rawls, and M. Ashraf El-Bayoumi. The exciton model in molecular spectroscopy. *Pure and Applied Chemistry*, 11:371–392, January 1965.

[21] Martin Pope and Charles E Swenberg. *Electronic processes in organic crystals and polymers*, volume 74. Oxford University Press New York, 1999.

[22] T. Holstein. Studies of polaron motion: Part ii. the "small" polaron. *Annals of Physics*, 8(3):343 – 389, 1959.

[23] T Holstein. Studies of polaron motion: Part i. the molecular-crystal model. *Annals of Physics*, 8(3):325 – 342, 1959.

[24] C.W. Tang. Two-layer organic photovoltaic cell. *Applied Physics Letters*, 48:183, 1986.

[25] G. Yu, J.C. Hummelen, F. Wudl, and A.J. Heeger. Polymer photovoltaic cells: Enhanced efficiencies via a network of internal donor-acceptor heterojunctions. *Science*, 270:1789, december 1995.

[26] Fabian Etzold, Ian A. Howard, Nina Forler, Don M. Cho, Michael Meister, Hannah Mangold, Jie Shu, Michael Ryan Hansen, Klaus Müllen, and Frédéric Laquai. The effect of solvent additives on morphology and excited-state dynamics in pcpdtbt:pcbm photovoltaic blends. *Journal of the American Chemical Society*, 134(25):10569–10583, 2012. PMID: 22612417.

[27] Almantas Pivrikas, Helmut Neugebauer, and Niyazi Serdar Sariciftci. Influence of processing additives to nano-morphology and

efficiency of bulk-heterojunction solar cells: A comparative review. *Solar Energy*, 85:1226–1237, 2011.

[28] Pascal Hoeben, Freek J. M.and Jonkheijm, E. W. Meijer, and Albertus P. H. J. Schenning. About supramolecular assemblies of pi-conjugated systems. *Chemical Reviews*, 105:1491–1546, 2005.

[29] Mariano Campoy-Quiles, Toby Ferenczi, Tiziano Agostinelli, Pablo G. Etchegoin, Youngkyoo Kim, Thomas D. Anthopoulos, Paul N. Stavrinou, Donal D. C. Bradley, and Jenny Nelson. Morphology evolution via self-organization and lateral and vertical diffusion in polymer:fullerene solar cell blends. *Nature Materials*, 7:158–164, january 2008.

[30] Jiun-Tai Chen and Chain-Shu Hsu. Conjugated polymer nanostructures for organic solar cell applications. *Polymer Chemistry*, 2:2707, 2011.

[31] Pierre-Olivier Schwartz, Laure Biniek, Elena Zaborova, Benoit Heinrich, Martin Brinkmann, Nicolas Leclerc, and Stephane Mery. Perylenediimide-based donor-acceptor dyads and triads: Impact of molecular architecture on self-assembling properties. *Journal of the American Chemical Society*, 136:5981–5992, 2014.

[32] Tracey M. Clarke and James R. Durrant. Charge photogeneration in organic solar cells. *Chemical Reviews*, 110:6736–6767, November 2010.

[33] Simon Gélinas, Akshay Rao, Abhishek Kumar, Samuel L. Smith, Alex W. Chin, Jenny Clark, Tom S. van der Poll, Guillermo C. Bazan, and Richard H. Friend. Ultrafast long-range charge separation in organic semiconductor photovoltaic diodes. *Science*, 343(6170):512–516, 2014.

[34] Stoichko D. Dimitrov and James R. Durrant. Materials design considerations for charge generation in organic solar cells. *Chemistry of Materials*, 26(1):616–630, 2014.

[35] Artem A. Bakulin, Akshay Rao, Vlad G. Pavelyev, Paul H. M. van Loosdrecht, Maxim S. Pshenichnikov, Dorota Niedzialek, Jérôme Cornil, David Beljonne, and Richard H. Friend. The role of driving energy and delocalized states for charge separation in organic

semiconductors. *Science*, 335(6074):1340–1344, 2012.

[36] Veaceslav Coropceanu, Jérôme Cornil, Demetrio A. da Silva Filho, Yoann Olivier, Robert Silbey, and Jean-Luc Brédas. Charge transport in organic semiconductors. *Chemical Reviews*, 107(4):926–952, 2007. PMID: 17378615.

[37] William Shockley and Hans J. Queisser. Detailed balance limit of efficiency of p-n junction solar cells. *Journal of Applied Physics*, 32(3), 1961.

[38] Hideo Ohkita, Steffan Cook, Yeni Astuti, Warren Duffy, Steve Tierney, Weimin Zhang, Martin Heeney, Iain McCulloch, Jenny Nelson, Donal D. C. Bradley, and James R. Durrant. Charge carrier formation in polythiophene/fullerene blend films studied by transient absorption spectroscopy. *Journal of the American Chemical Society*, 130(10):3030–3042, 2008. PMID: 18278911.

[39] Koen Vandewal, Steve Albrecht, Eric T. Hoke, Kenneth R. Graham, Johannes Widmer, Marcel Douglas, Jessica D.and Schubert, William R. Mateker, Jason T. Bloking, George F. Burkhard, Alan Sellinger, Jean M. J. Fréchet, Aram Amassian, Moritz K. Riede, Michael D. McGehee, Dieter Neher, and Alberto Salleo. Efficient charge generation by relaxed charge-transfer states at organic interfaces. *Nature Materials*, 13:63–68, 2014.

[40] G. Grancini, M. Maiuri, D. Fazzi, A. Petrozza, H-J. Egelhaaf, D. Brida, G. Cerullo, and G. Lanzani. Hot exciton dissociation in polymer solar cells. *Nature Materials*, 12:29–33, 2013.

[41] Ajay Ram Srimath Kandada, Giulia Grancini, Annamaria Petrozza, Stefano Perissinotto, Sai Santosh Kumar Fazzi, Danieleand Raavi, and Guglielmo Lanzani. Ultrafast energy transfer in ultrathin organic donor/acceptor blend. *Scientific Reports*.

[42] Thomas Bura, Nicolas Leclerc, Sadiara Fall, Patrick Lévêque, Thomas Heiser, Pascal Retailleau, Sandra Rihn, Antoine Mirloup, and Raymond Ziessel. High-performance solution-processed solar cells and ambipolar behavior in organic field-effect transistors with thienyl-bodipy scaffoldings. *Journal of the American Chemical Society*, 134:17404–17407, October 2010.

[43] Jean Roncali, Philippe Leriche, and Philippe Blanchard. Molecular materials for organic photovoltaics: Small is beautiful. *Advanced Materials*, 26(23):3821–3838, 2014.

[44] Yuze Lin, Yongfang Li, and Xiaowei Zhan. Small molecule semiconductors for high-efficiency organic photovoltaics. *Chem. Soc. Rev.*, 41:4245–4272, 2012.

[45] Amaresh Mishra and Peter Bäuerle. Small molecule organic semiconductors on the move: Promises for future solar energy technology. *Angewandte Chemie International Edition*, 51(9):2020–2067, 2012.

[46] Alexander W. Hains, Ziqi Liang, Michael A. Woodhouse, and Brian A. Gregg. Molecular semiconductors in organic photovoltaic cells. *Chemical Reviews*, 110(11):6689–6735, 2010. PMID: 20184362.

[47] Steffan Cook, Hideo Ohkita, Youngkyoo Kim, Jessica J. Benson-Smith, Donal D.C. Bradley, and James R. Durrant. A photophysical study of {PCBM} thin films. *Chemical Physics Letters*, 445(4–6):276 – 280, 2007.

[48] Steffan Cook, Akihiro Furube, Ryuzi Katoh, and Liyuan Han. Estimate of singlet diffusion lengths in {PCBM} films by time-resolved emission studies. *Chemical Physics Letters*, 478(1–3):33 – 36, 2009.

[49] Matt Gevaert and Prashant V. Kamat. Photochemistry of fullerenes: excited-state behavior of c60 and c70 and their reduction in poly(methyl methacrylate) films. *The Journal of Physical Chemistry*, 96(24):9883–9888, 1992.

[50] David S. Germack, Calvin K. Chan, Behrang H. Hamadani, Lee J. Richter, Daniel A. Fischer, David J. Gundlach, and Dean M. DeLongchamp. Substrate-dependent interface composition and charge transport in films for organic photovoltaics. *Applied Physics Letters*, 94(23):–, 2009.

[51] S.J. Strickler and R.A. Berg. Relationship between absorption intensity and fluorescence lifetime of molecules. *The Journal of Chemical Physics*, 37:814–822, August 1962.

[52] C. Geskes and J. Heinze. A spectroelectrochemical cell for mea-

surements in highly purified solvents. *Journal of Electroanalytical Chemistry*, 418(1–2):167 – 173, 1996.

[53] Andrew C. Benniston, Sophie Clift, Jerry Hagon, Helge Lemmetyinen, Nikolai V. Tkachenko, William Clegg, and Ross W. Harrington. Effect on charge transfer and charge recombination by insertion of a naphthalene-based bridge in molecular dyads based on borondipyrromethene (bodipy). *ChemPhysChem*, 13(16):3672–3681, 2012.

[54] Jian-Yong Liu, Mohamed E. El-Khouly, Shunichi Fukuzumi, and Dennis K. P. Ng. Photoinduced electron transfer in a ferrocene–distyryl bodipy dyad and a ferrocene–distyryl bodipy–c60 triad. *ChemPhysChem*, 13(8):2030–2036, 2012.

[55] Inchan Hwang and Gregory D. Scholes. Electronic energy transfer and quantum - coherence in π-conjugated polymers. *Chemistry of Materials*, 23(3):610–620, 2011.

[56] Henry M. Heitzer, Brett M. Savoie, Tobin J. Marks, and Mark A. Ratner. Organic photovoltaics: Elucidating the ultra-fast exciton dissociation mechanism in disordered materials. *Angewandte Chemie International Edition*, 53(29):7456–7460, 2014.

[57] Arun Aby Paraecattil and Natalie Banerji. Charge separation pathways in a highly efficient polymer: Fullerene solar cell material. *Journal of the American Chemical Society*, 136(4):1472–1482, 2014. PMID: 24437495.

[58] M. Scarongella, A. A. Paraecattil, E. Buchaca-Domingo, J. D. Douglas, S. Beaupre, T. McCarthy-Ward, M. Heeney, J.-E. Moser, M. Leclerc, J. M. J. Frechet, N. Stingelin, and N. Banerji. The influence of microstructure on charge separation dynamics in organic bulk heterojunction materials for solar cell applications. *J. Mater. Chem. A*, 2:6218–6230, 2014.

[59] Raphael Tautz, Enrico Da Como, Thomas Limmer, Jochen Feldmann, Hans-Joachim Egelhaaf, Elizabeth von Hauff, Vincent Lemaur, David Beljonne, Seyfullah Yilmaz, Ines Dumsch, Sybille Allard, and Ullrich Scherf. Structural correlations in the generation of polaron pairs in low-bandgap polymers for photovoltaics.

Nat Commun, 3:970, 2012.

[60] Obadiah G. Reid, Ryan D. Pensack, Yin Song, Gregory D. Scholes, and Garry Rumbles. Charge photogeneration in neat conjugated polymers. *Chemistry of Materials*, 26(1):561–575, 2014.

[61] ChristopherS. Foote. Photophysical and photochemical properties of fullerenes. In Jochen Mattay, editor, *Electron Transfer I*, volume 169 of *Topics in Current Chemistry*, pages 347–363. Springer Berlin Heidelberg, 1994.

[62] Thomas W. Ebbesen, Katsumi Tanigaki, and Sadanori Kuroshima. Excited-state properties of {C60}. *Chemical Physics Letters*, 181(6):501 – 504, 1991.

[63] Mose Casalegno, Stefano Zanardi, Francesco Frigerio, Riccardo Po, Chiara Carbonera, Gianluigi Marra, Tommaso Nicolini, Guido Raos, and Stefano Valdo Meille. Solvent-free phenyl-c61-butyric acid methyl ester (pcbm) from clathrates: insights for organic photovoltaics from crystal structures and molecular dynamics. *Chem. Commun.*, 49:4525–4527, 2013.

[64] Juan Cabanillas-Gonzalez, Giulia Grancini, and Guglielmo Lanzani. Pump-probe spectroscopy in organic semiconductors: Monitoring fundamental processes of relevance in optoelectronics. *Advanced Materials*, 23(46):5468–5485, 2011.

[65] Ian A. Howard, Ralf Mauer, Michael Meister, and Frédéric Laquai. Effect of morphology on ultrafast free carrier generation in polythiophene:fullerene organic solar cells. *Journal of the American Chemical Society*, 132(42):14866–14876, 2010. PMID: 20923187.

[66] Floris B. Kooistra, Valentin D. Mihailetchi, Lacramioara M. Popescu, David Kronholm, Paul W. M. Blom, and Jan C. Hummelen. New c84 derivative and its application in a bulk heterojunction solar cell. *Chemistry of Materials*, 18(13):3068–3073, 2006.

[67] V. D. Mihailetchi, L. J. A. Koster, P. W. M. Blom, C. Melzer, B. de Boer, J. K. J. van Duren, and R. A. J. Janssen. Compositional dependence of the performance of poly(p-phenylene vinylene):methanofullerene bulk-heterojunction solar cells. *Advanced Functional Materials*, 15(5):795–801, 2005.

[68] Dirk Veldman, Özlem İpek, Stefan C. J. Meskers, Jörgen Sweelssen, Marc M. Koetse, Sjoerd C. Veenstra, Jan M. Kroon, Svetlana S. van Bavel, Joachim Loos, and René A. J. Janssen. Compositional and electric field dependence of the dissociation of charge transfer excitons in alternating polyfluorene copolymer/fullerene blends. *Journal of the American Chemical Society*, 130(24):7721–7735, 2008. PMID: 18494472.

[69] R. Diller. Primary reactions in retinal proteins. In Markus Braun, Peter Gilch, and Wolfgang Zinth, editors, *Ultrashort Laser Pulses in Biology and Medicine*, Biological and Medical Physics, Biomedical Engineering, pages 243–277. Springer Berlin Heidelberg, 2008.

[70] Akira Kawanabe and Hideki Kandori. Photoreactions and structural changes of anabaena sensory rhodopsin. *Sensors*, 9(12):9741–9804, 2009.

[71] Flavio Lumento, Vinicio Zanirato, Stefania Fusi, Elena Busi, Loredana Latterini, Fausto Elisei, Adalgisa Sinicropi, Tadeusz Andruniów, Nicolas Ferré, Riccardo Basosi, and Massimo Olivucci. Quantum chemical modeling and preparation of a biomimetic photochemical switch. *Angewandte Chemie International Edition*, 46(3):414–420, 2007.

[72] Julien Briand, Olivier Bram, Julien Rehault, Jeremie Leonard, Andrea Cannizzo, Majed Chergui, Vinizio Zanirato, Massimo Olivucci, Jan Helbing, and Stefan Haacke. Coherent ultrafast torsional motion and isomerization of a biomimetic dipolar photoswitch. *Phys. Chem. Chem. Phys.*, 12:3178–3187, 2010.

[73] Euan R. Kay, David A. Leigh, and Francesco Zerbetto. Synthetic molecular motors and mechanical machines. *Angewandte Chemie International Edition*, 46(1-2):72–191, 2007.

[74] Andrew A. Beharry and G. Andrew Woolley. Azobenzene photoswitches for biomolecules. *Chem. Soc. Rev.*, 40:4422–4437, 2011.

[75] Jose Berna, David A. Leigh, Monika Lubomska, Sandra M. Mendoza, Emilio M. Perez, Petra Rudolf, Gilberto Teobaldi, and Francesco Zerbetto. Macroscopic transport by synthetic molecular machines. *Nature Materials*, 4:704 – 710, 2005.

[76] Joel M. Kralj, Daniel R. Hochbaum, Adam D. Douglass, and Adam E. Cohen. Electrical spiking in escherichia coli probed with a fluorescent voltage-indicating protein. *Science*, 333(6040):345–348, 2011.

[77] Philipp Schoenenberger, Yan-Ping Zhang Schärer, and Thomas G. Oertner. Channelrhodopsin as a tool to investigate synaptic transmission and plasticity. *Experimental Physiology*, 96(1):34–39, 2011.

[78] Daniel R Hochbaum, Yongxin Zhao, Samouil L Farhi, Nathan Klapoetke, Christopher A Werley, Vikrant Kapoor, Peng Zou, Joel M Kralj, Dougal Maclaurin, Niklas Smedemark-Margulies, Jessica L Saulnier, Gabriella L Boulting, Christoph Straub, Yong Ku Cho, Michael Melkonian, Gane Ka-Shu Wong, D Jed Harrison, Venkatesh N Murthy, Bernardo L Sabatini, Edward S Boyden, Robert E Campbell, and Adam E Cohen. All-optical electrophysiology in mammalian neurons using engineered microbial rhodopsins. *Nature Methods*, 11:825– 833, 2014.

[79] Joel M. Kralj, Adam D. Douglass, Daniel R. Hochbaum, Dougal Maclaurin, and Adam E. Cohen. Optical recording of action potentials in mammalian neurons using a microbial rhodopsin. *Nature Methods*, 9:90– 95, 2012.

[80] Wenjing Wang, Zahra Nossoni, Tetyana Berbasova, Camille T. Watson, Ipek Yapici, Kin Sing Stephen Lee, Chrysoula Vasileiou, James H. Geiger, and Babak Borhan. Tuning the electronic absorption of protein-embedded all-trans-retinal. *Science*, 338(6112):1340–1343, 2012.

[81] RW Schoenlein, LA Peteanu, RA Mathies, and CV Shank. The first step in vision: femtosecond isomerization of rhodopsin. *Science*, 254(5030):412–415, 1991.

[82] H.J.A. Dartnall. The photosensitivities of visual pigments in the presence of hydroxylamine. *Vision Research*, 8(4):339 – 358, 1968.

[83] Qing Wang, Robert W Schoenlein, Linda A Peteanu, Richard A Mathies, and Charles V Shank. Vibrationally coherent photochemistry in the femtosecond primary event of vision. *Science*, pages 422–422, 1994.

[84] R H Lozier, R A Bogomolni, and W Stoeckenius. Bacteriorhodopsin: a light-driven proton pump in halobacterium halobium. *Biophysical Journal*, 15:955–962, 09 1975.

[85] P. Scherrer, M. K. Mathew, W. Sperling, and Walther Stoeckenius. Retinal isomer ratio in dark-adapted purple membrane and bacteriorhodopsin monomers. *Biochemistry*, 28(2):829–834, 1989.

[86] Amir Wand, Noga Friedman, Mordechai Sheves, and Sanford Ruhman. Ultrafast photochemistry of light-adapted and dark-adapted bacteriorhodopsin: Effects of the initial retinal configuration. *The Journal of Physical Chemistry B*, 116(35):10444–10452, 2012. PMID: 22329764.

[87] T. Kouyama, Jr Kinosita, K., and A. Ikegami. Excited-state dynamics of bacteriorhodopsin. *Biophysical Journal*, 47.

[88] B. Schmidt, C. Sobotta, B. Heinz, S. Laimgruber, M. Braun, and P. Gilch. Excited-state dynamics of bacteriorhodopsin probed by broadband femtosecond fluorescence spectroscopy. *Biochimica et Biophysica Acta (BBA) - Bioenergetics*, 1706(1–2):165 – 173, 2005.

[89] S. Haacke, S. Schenkl, S. Vinzani, and M. Chergui. Femtosecond and picosecond fluorescence of native bacteriorhodopsin and a nonisomerizing analog. *Biopolymers*, 67(4-5):306–309, 2002.

[90] T. Ye, N. Friedman, Y. Gat, G. H. Atkinson, M. Sheves, M. Ottolenghi, and S. Ruhman. On the nature of the primary light-induced events in bacteriorhodopsin: Ultrafast spectroscopy of native and c13=c14 locked pigments. *The Journal of Physical Chemistry B*, 103(24):5122–5130, 1999.

[91] Q. Zhong, S. Ruhman, M. Ottolenghi, M. Sheves, N. Friedman, G. H. Atkinson, and J. K. Delaney. Reexamining the primary light-induced events in bacteriorhodopsin using a synthetic c13c14-locked chromophore. *Journal of the American Chemical Society*, 118(50):12828–12829, 1996.

[92] S. Schenkl, E. Portuondo, G. Zgrablic, M. Chergui, S. Haacke, N. Friedman, and M. Sheves. Ultrafast energy relaxation in bacteriorhodopsin studied by time-integrated fluorescence. *Phys. Chem. Chem. Phys.*, 4:5020–5024, 2002.

[93] Sanford Ruhman, Bixue Hou, Noga Friedman, Michael Ottolenghi, and Mordechai Sheves. Following evolution of bacteriorhodopsin in its reactive excited state via stimulated emission pumping. *Journal of the American Chemical Society*, 124(30):8854–8858, 2002. PMID: 12137538.

[94] Federico Melaccio, Nicolas Ferre, and Massimo Olivucci. Quantum chemical modeling of rhodopsin mutants displaying switchable colors. *Phys. Chem. Chem. Phys.*, 14:12485–12495, 2012.

[95] Giovanni Bassolino, Tina Sovdat, Matz Liebel, Christoph Schnedermann, Barbara Odell, Timothy D.W. Claridge, Philipp Kukura, and Stephen P. Fletcher. Synthetic control of retinal photochemistry and photophysics in solution. *Journal of the American Chemical Society*, 136(6):2650–2658, 2014. PMID: 24479840.

[96] Goran Zgrablić, Stefan Haacke, and Majed Chergui. Heterogeneity and relaxation dynamics of the photoexcited retinal schiff base cation in solution. *The Journal of Physical Chemistry B*, 113(13):4384–4393, 2009. PMID: 19249846.

[97] Julien Briand, Jérémie Léonard, and Stefan Haacke. Ultrafast photo-induced reaction dynamics in bacteriorhodopsin and its trp mutants. *Journal of Optics*, 12(8):084004, 2010.

[98] Rinat Rozin, Amir Wand, Kwang-Hwan Jung, Sanford Ruhman, and Mordechai Sheves. ph dependence of anabaena sensory rhodopsin: Retinal isomer composition, rate of dark adaptation, and photochemistry. *The Journal of Physical Chemistry B*, 118(30):8995–9006, 2014. PMID: 25003828.

[99] Alessandro Cembran, Fernando Bernardi, Massimo Olivucci, and Marco Garavelli. Counterion controlled photoisomerization of retinal chromophore models: a computational investigation. *Journal of the American Chemical Society*, 126(49):16018–16037, 2004. PMID: 15584736.

[100] Goran Zgrablić, Stefan Haacke, and Majed Chergui. Vibrational coherences of the protonated schiff base of all-trans retinal in solution. *Chemical Physics*, 338(2–3):168–174, 2007.

[101] Remedios González-Luque, Marco Garavelli, Fernando Bernardi,

Manuela Merchán, Michael A. Robb, and Massimo Olivucci. Computational evidence in favor of a two-state, two-mode model of the retinal chromophore photoisomerization. *Proceedings of the National Academy of Sciences*, 97(17):9379–9384, 2000.

[102] S. Schenkl, F. van Mourik, G. van der Zwan, S. Haacke, and M. Chergui. Probing the ultrafast charge translocation of photoexcited retinal in bacteriorhodopsin. *Science*, 309(5736):917–920, 2005.

[103] Piero Altoè, Alessandro Cembran, Massimo Olivucci, and Marco Garavelli. Aborted double bicycle-pedal isomerization with hydrogen bond breaking is the primary event of bacteriorhodopsin proton pumping. *Proceedings of the National Academy of Sciences*, 107(47):20172–20177, 2010.

[104] Jérémie Léonard, Erwin Portuondo-Campa, Andrea Cannizzo, Frank van Mourik, Gert van der Zwan, Jörg Tittor, Stefan Haacke, and Majed Chergui. Functional electric field changes in photoactivated proteins revealed by ultrafast stark spectroscopy of the trp residues. *Proceedings of the National Academy of Sciences*, 106(19):7718–7723, 2009.

[105] Clarence Zener. Non-adiabatic crossing of energy levels. *Proceedings of the Royal Society of London A: Mathematical, Physical and Engineering Sciences*, 137(833):696–702, 1932.

[106] R. M. Weiss and A. Warshel. A new view of the dynamics of singlet cis-trans photoisomerization. *Journal of the American Chemical Society*, 101(20):6131–6133, 1979.

[107] Gerd. G. Kochendoerfer and Richard A. Mathies. Spontaneous emission study of the femtosecond isomerization dynamics of rhodopsin. *The Journal of Physical Chemistry*, 100(34):14526–14532, 1996.

[108] R. W. Schoenlein, L. A. Peteanu, Q. Wang, R. A. Mathies, and C. V. Shank. Femtosecond dynamics of cis-trans isomerization in a visual pigment analog: isorhodopsin. *The Journal of Physical Chemistry*, 97(46):12087–12092, 1993.

[109] L A Peteanu, R W Schoenlein, Q Wang, R A Mathies, and C V

Shank. The first step in vision occurs in femtoseconds: complete blue and red spectral studies. *Proceedings of the National Academy of Sciences*, 90(24):11762–11766, 1993.

[110] J Léonard, J Briand, S Fusi, V Zanirato, M Olivucci, and S Haacke. Isomer-dependent vibrational coherence in ultrafast photoisomerization. *New Journal of Physics*, 15(10):105022, 2013.

[111] Tina Sovdat, Giovanni Bassolino, Matz Liebel, Christoph Schnedermann, Stephen P. Fletcher, and Philipp Kukura. Backbone modification of retinal induces protein-like excited state dynamics in solution. *Journal of the American Chemical Society*, 134(20):8318–8320, 2012. PMID: 22536821.

[112] Amir Wand, Rinat Rozin, Tamar Eliash, Kwang-Hwan Jung, Mordechai Sheves, and Sanford Ruhman. Asymmetric toggling of a natural photoswitch: Ultrafast spectroscopy of anabaena sensory rhodopsin. *Journal of the American Chemical Society*, 133(51):20922–20932, 2011. PMID: 22066688.

[113] Jérémie Léonard, Igor Schapiro, Julien Briand, Stefania Fusi, Riccardo Rossi Paccani, Massimo Olivucci, and Stefan Haacke. Mechanistic origin of the vibrational coherence accompanying the photoreaction of biomimetic molecular switches. *Chemistry – A European Journal*, 18(48):15296–15304, 2012.

[114] Amir Wand, Itay Gdor, Jingyi Zhu, Mordechai Sheves, and Sanford Ruhman. Shedding new light on retinal protein photochemistry. *Annual Review of Physical Chemistry*, 64(1):437–458, 2013. PMID: 23331307.

[115] Dario Polli, Piero Altoe, Oliver Weingart, Katelyn M. Spillane, Cristian Manzoni, Daniele Brida, Gaia Tomasello, Giorgio Orlandi, Philipp Kukura, Richard A. Mathies, Marco Garavelli, and Giulio Cerullo. Conical intersection dynamics of the primary photoisomerization event in vision. *Nature*, 467.

[116] Elena N. Laricheva, Samer Gozem, Silvia Rinaldi, Federico Melaccio, Alessio Valentini, and Massimo Olivucci. Origin of fluorescence in 11-cis locked bovine rhodopsin. *Journal of Chemical Theory and Computation*, 8(8):2559–2563, 2012.

[117] Luis Manuel Frutos, Tadeusz Andruniów, Fabrizio Santoro, Nicolas Ferré, and Massimo Olivucci. Tracking the excited-state time evolution of the visual pigment with multiconfigurational quantum chemistry. *Proceedings of the National Academy of Sciences*, 104(19):7764–7769, 2007.

[118] Oleg A. Sineshchekov, Vishwa D. Trivedi, Jun Sasaki, and John L. Spudich. Photochromicity of anabaena sensory rhodopsin, an atypical microbial receptor with a cis-retinal light-adapted form. *Journal of Biological Chemistry*, 280(15):14663–14668, 2005.

[119] Kwang-Hwan Jung, Vishwa D. Trivedi, and John L. Spudich. Demonstration of a sensory rhodopsin in eubacteria. *Molecular Microbiology*, 47(6):1513–1522, 2003.

[120] Yoichiro Wada, Akira Kawanabe, Yuji Furutani, Hideki Kandori, and Hiroyuki Ohtani. Quantum yields for the light adaptations in anabaena sensory rhodopsin and bacteriorhodopsin. *Chemical Physics Letters*, 453(1–3):105 – 108, 2008.

[121] Angela Strambi, Bo Durbeej, Nicolas Ferré, and Massimo Olivucci. Anabaena sensory rhodopsin is a light-driven unidirectional rotor. *Proceedings of the National Academy of Sciences*, 107(50):21322–21326, 2010.

[122] Igor Schapiro and Sanford Ruhman. Ultrafast photochemistry of anabaena sensory rhodopsin: Experiment and theory. *Biochimica et Biophysica Acta (BBA) - Bioenergetics*, 1837(5):589 – 597, 2014. Retinal Proteins.

[123] Akira Kawanabe, Yuji Furutani, Kwang-Hwan Jung, and Hideki Kandori. Photochromism of anabaena sensory rhodopsin. *Journal of the American Chemical Society*, 129(27):8644–8649, 2007. PMID: 17569538.

[124] Kazumi Shimono, Yukako Ikeura, Yuki Sudo, Masayuki Iwamoto, and Naoki Kamo. Environment around the chromophore in pharaonis phoborhodopsin: mutation analysis of the retinal binding site. *Biochimica et Biophysica Acta (BBA) - Biomembranes*, 1515(2):92 – 100, 2001.

[125] Akira Kawanabe, Yuji Furutani, Kwang-Hwan Jung, and Hideki

Kandori. Ftir study of the photoisomerization processes in the 13-cis and all-trans forms of anabaena sensory rhodopsin at 77 k†. *Biochemistry*, 45(14):4362–4370, 2006. PMID: 16584171.

[126] A. Cheminal, J. Léonard, S.Y. Kim, K.-H. Jung, H. Kandori, and S. Haacke. Steady state emission of the fluorescent intermediate of anabaena sensory rhodopsin as a function of light adaptation conditions. *Chemical Physics Letters*, 587(0):75 – 80, 2013.

[127] Oshrat Bismuth, Pavel Komm, Noga Friedman, Tamar Eliash, Mordechai Sheves, and Sanford Ruhman. Deciphering excited state evolution in halorhodopsin with stimulated emission pumping. *The Journal of Physical Chemistry B*, 114(8):3046–3051, 2010. PMID: 20143798.

[128] Anat Kahan, Omer Nahmias, Noga Friedman, Mordechai Sheves, and Sanford Ruhman. Following photoinduced dynamics in bacteriorhodopsin with 7-fs impulsive vibrational spectroscopy. *Journal of the American Chemical Society*, 129(3):537–546, 2007. PMID: 17227016.

[129] Ron Siewertsen, Jan Boyke Schonborn, Bernd Hartke, Falk Renth, and Friedrich Temps. Superior z [rightward arrow] e and e [rightward arrow] z photoswitching dynamics of dihydrodibenzodiazocine, a bridged azobenzene, by s1(n[small pi]*) excitation at [small lambda] = 387 and 490 nm. *Phys. Chem. Chem. Phys.*, 13:1054–1063, 2011.

[130] Arun Aby Paraecattil, Serge Beaupré, Mario Leclerc, Jacques-E. Moser, and Natalie Banerji. Intensity dependent femtosecond dynamics in a pbdttpd-based solar cell material. *The Journal of Physical Chemistry Letters*, 3(20):2952–2958, 2012.

Alexandre CHEMINAL

Processus de conversion d'énergie ultra-rapide dans des protéines photo-sensibles et nanostructures organiques à visée photovoltaïque

Résumé

Les techniques de spectroscopie femtoseconde permettent d'étudier les processus de conversion d'énergie dans les système organiques. Elles permettent d'étudier les populations photo-générées et leur évolution à l'échelle de ces photoréactions. Elles permettent de comprendre les transferts d'énergie et de charge intra- et inter-moléculaires à l'origine du fonctionnement de ces systèmes.

La protéine de rétinal Anabaena sensroy Rhodopsin est un photocommutateur naturel, qui est étudié afin de comprendre les paramètres à l'origine de l'efficacité quantique d'isomérisation. Nous avons pu déterminer cette efficacité quantique pour les deux formes stables du rétinal ainsi que leur dynamique d'isomérisation dans les mêmes conditions expérimentales.

La génération de charge dans des couches actives pour le photovoltaique organique est étudiée dans un système composé d'un mélange de PCBM et d'un donneur organique dérivé du colorant BODIPY. L'influence de la nanostructuration de la couche active sur la génération de charge est étudiée. La génération de charge est limitée dans ce système par la recombinaison des charges générées et par la diffusion des excition aux interfaces donneur-accepteur. Ces observations indiques que l'amélioration de la nanostructuration de la couche active peut permettre d'augmenter les rendements de photo-génération de charge.

Mots-clés : Photochimie – transfert de charge – photovoltaïque organique – spectroscopie ultrarapide – protéine de rétinal – isomérisation – optique non linéaire - photonique

Résumé en anglais

Femtosecond transient spectroscopies are used to investigate photonic energy conversion in organic systems. These techniques allow to observe the ground and excited states of the molecules at the timescale of the photoreactions. It is used to understand the inter- and intramolecular energy and charge transfers leading to the desired photochemical process.

The natural photoswiching retinal protein Anabaena sensory Rhodopsin is studied to understand the key parameters ruling the isomerisation quantum yield. We could determine the isomerisation quantum yield of both stable forms and their dynamics in the very same experimental conditions.

Charge generation is investigated in small molecule bulk heterojunction active layers for organic solar cells made of PCBM and a BODIPY dye-derivative donor. The influence of the active layer morphology on charge generation is studied. The charge generation is limited by charge recombination but also by exciton diffusion to the donor-acceptor interface. The active layer morphology has to be improved to achieve more efficient organic solar cells with these materials.

Keywords: Photochemistry – charge transfer – isomerization – ultrafast spectroscopy – organic photovoltaics – retinal proteins – nonlinear optics